1983

EXCITATION STUDIES IN THE RARE GASES AND SIMPLE MOLECULES USING A HIGH RESOLUTION ELECTRON SPECTROMETER.

HENRICUS W. DASSEN

University of Windsor

CANADIAN THESES ON MICROFICHE

I.S.B.N.

THESES CANADIENNES SUR MICROFICHE

NOTICE

The quality of this microfiche is heavily dependent
upon the quality of the original thesis submitted for
microfilming. Every effort has been made to ensure
the highest quality of reproduction possible.

If pages are missing, contact the university which
granted the degree.

Some pages may have indistinct print especially
if the original pages were typed with a poor typewriter
ribbon or if the university sent us a poor photocopy.

Previously copyrighted materials (journal articles,
published tests, etc.) are not filmed.

Reproduction in full or in part of this film is gov-
erned by the Canadian Copyright Act, R.S.C. 1970,
c. C-30. Please read the authorization forms which
accompany this thesis.

AVIS

La qualité de cette microfiche dépend grandement de
la qualité de la thèse soumise au microfilmage. Nous
avons tout fait pour assurer une qualité supérieure
de reproduction.

S'il manque des pages, veuillez communiquer
avec l'université qui a conféré le grade.

La qualité d'impression de certaines pages peut
laisser à désirer, surtout si les pages originales ont été
dactylographiées à l'aide d'un ruban usé ou si l'univer-
sité nous a fait parvenir une photocopie de mauvaise
qualité.

Les documents qui font déjà l'objet d'un droit
d'auteur (articles de revue, examens publiés, etc.) ne
sont pas microfilmés.

La reproduction, même partielle, de ce microfilm
est soumise à la Loi canadienne sur le droit d'auteur,
SRC 1970, c. C-30. Veuillez prendre connaissance des
formules d'autorisation qui accompagnent cette thèse.

Canada

EXCITATION STUDIES

IN THE RARE GASES AND SIMPLE MOLECULES

USING A HIGH RESOLUTION ELECTRON SPECTROMETER

by

© Henricus W. Dassen

A Dissertation
submitted to the Faculty of Graduate Studies
through the Department of
Physics in Partial Fulfillment
of the Requirements for the Degree of
Doctor of Philosophy at
the University of Windsor

Windsor, Ontario, Canada

- 1983 -

792944

ABSTRACT

A high resolution electron spectrometer has been used to perform electron scattering studies with both atomic and molecular targets. Work has been done on negative ion resonance production in the rare gases and on polarization correlation measurements in diatomic molecules.

High resolution metastable excitation function measurements have been made in the doubly excited state region for Ne, Ar and Kr targets. Comparison of the spectra obtained suggests that the gross features are due to negative ion resonances. Previous techniques which have proved successful in the identification and classification of resonances in the rare gases at energies below the first ionization threshold are shown to be applicable in this energy region also and assignments for a number of resonances are suggested. Where appropriate, comparisons have been made with data obtained by other techniques. The modified Rydberg formula has been used to predict energies for both doubly and triply excited configurations.

Polarization correlation measurements have been made with the target molecules N_2 and H_2. In H_2 the radiation resulting from excitation of the $C^1\Pi_u$ $v'=0$ band was studied. In N_2, excitation of the $C_4^1\Sigma_u^+$ $v'=0$ band was studied. Pseudo-threshold polarization measurements were made for these targets and comparisons with theoretical predictions were made. Systematic polarization correlation data for electron scattering angles up to 20 degrees have also been obtained

and preliminary attempts have been made to analyze these.

ACKNOWLEDGMENTS

> The Son is the radiance
> of God's glory and the
> exact representation of
> His being, sustaining all
> things by the word of His
> power.
>
> Hebrews 1:3a

-v-

TABLE OF CONTENTS

LIST OF TABLES

LIST OF FIGURES

CHAPTER 1

INTRODUCTION

Before the advent of high resolution electron spectrometers very little was known about the finer details of electron scattering processes in atoms and molecules. These details were smeared out by the poor energy resolution of simple electron sources. The resolution, or energy spread, inherent in the electron beams produced by these devices is on the order of 500 meV to several eV. Thus, atomic or molecular states separated in energy by say 50 or 100 meV could not be isolated and investigated.

With the introduction of high resolution electron sources and analyzers, this problem was significantly reduced. High resolution electron spectrometers are capable of producing and analyzing electron beams with resolutions on the order of 10 to 100 meV, enabling experimental physicists to study electron-atom and electron-molecule scattering in much more detail than was possible before. These devices quickly found applications in a variety of experiments, such as ejected electron spectra, differential elastic and inelastic scattering measurements, studies of excitation cross-sections, and most importantly, electron-photon coincidence experiments. In the latter type of experiment, it is essential that the target atoms (or molecules) be prepared in a well defined excited state, a task for which the spectrometer is much better suited than a simple electron gun. In addition to electrons, ions can also be used with these devices and this fact was exploited to the full in a variety of experiments. One other advantage of the electron spectrometer is its ability to simulate photo-excitation and photo-

ionization in energy regimes where photon sources are non-
existent or simply not intense enough to work with. These
properties make the high resolution electron spectrometer an
ideal tool for the study of electron scattering using atomic
and molecular targets.

In the present work, the electron spectrometer was used
in two different ways. The first was as a high resolution
source of electrons to study the production of metastable
species of Ne, Ar and Kr in the doubly excited state region.
The formation of negative ion resonances was examined in
this phase of the work. The second way was as a combined
high resolution source and analyzer for use in electron-pho-
ton polarization correlation studies in molecules. In the
present work N_2 and H_2 were used as target gases.

This work is divided into three self-contained chapters.
Chapter 2 describes the apparatus used in the experiments.
A description of the vacuum system is given, and a detailed
discussion of the electron spectrometer is also presented.
Chapter 3 presents the work done on negative ion resonances
in the rare gases. A discussion of resonance formation and
the analysis techniques used is first given, followed by a
description of the experiment itself, and then the results
are presented and discussed. Chapter 4 describes the work
done on polarization correlation measurements using simple
molecules as targets. A review of the atomic case is pre-
sented first, and then the current theories for the molecu-
lar case are discussed. Polarization of molecular radiation

at the excitation threshold and the use of 'pseudo-threshold' techniques are discussed, as well as the framework used to analyze the data obtained. The experimental procedure is described in detail, followed by the results obtained with N_2 and H_2 as target gases.

CHAPTER 2

THE EXPERIMENTAL DETAILS

2.1 INTRODUCTION

This chapter is intended to provide a complete description of each component used in the present work. Note that it contains information relevant to both parts of this work.

The apparatus can be categorized into three sections:

(1) The Vacuum System

(2) The Electron Spectrometer

(3) The Detection Systems

Each of these categories will be discussed in detail, with diagrams and tables to illustrate the construction, performance and operation of each part, with the exception of the detection systems, which will be discussed in chapters 3 and 4.

2.2 THE VACUUM SYSTEM

The vacuum system is, of course, common to both experiments and is therefore discussed first. Each component of the system, with the exception of the chamber housing the spectrometer, is commercially available and Table 2.1 contains the relevant information about them. Figure 2.1 shows a schematic diagram of the vacuum system and its various components.

2.2.1 The Vacuum Chamber

The vacuum chamber consists of a 20" x 20" x 20" aluminum box with each of its six panels removable for easy access to the interior. Each panel is bolted into place to a welded aluminum framework, and vacuum sealing is done with O-ring seals. With the exception of the top and bottom panels, each one has provisions for three 4" accessory ports, also sealed with O-rings. As indicated in Figure 2.1, five of the 12 ports are used to attach the following:

(a) a roughing valve directly to the chamber so that it could be pumped out to the foreline pressure without having to go through the diffusion pumps.

(b) a gas inlet valve to leak a target gas into the collision region. This inlet system is also attached to the foreline so that it can also be pumped directly.

(c) an ionization gauge tube to monitor the pressure inside the chamber. The controller and

Table 2.1
Vacuum System Components

```
-------------------------------------------------------------------

Vacuum Pumps:
    Rotary      -     Edwards ED-660
    Diffusion   -     (2) Edwards 6M3A (Mercury Vapour)

Pressure Monitors:
    Foreline    -     Veeco TG-7 Controller/DV-1M
                      Thermocouple Gauge (0-1000mTorr)
    Gas Inlet   -     Veeco TG-27 Controller/DV-4AM
                      Thermocouple Gauge (0-20 Torr)
    Chamber     -     Veeco RG-830 Controller/RG-75P
                      Ionization Gauge

Isolation Valves:
    Foreline    -     (3) Edwards 1" valves
                -     (2) Edwards 1/2" valves (to chamber)
                -     (1) Edwards 1" Magnetic (Air Admittance)
    High Vacuum       (2) Vacuum Generators D1216 Valves
                      (2) Edwards QSB6 6" Butterfly Valves

Gas Inlet Valve:

                      Vacuum Generators MD1871 Needle Valve

Traps and Baffles:
                      (2) Edwards NTN6 Liquid Nitrogen
                        Cold Traps
                      (2) Edwards DCB4 Thermoelectrically
                        Cooled Baffles
```

gauge tube used is indicated in Table 2.1.
Typical chamber pressures (without a target
gas) were on the order of 1×10^{-6} torr.

(d) an electrical feedthrough to provide power to
2 quartz-halogen heating lamps, used to keep
the interior of the chamber at a slightly ele-
vated temperature. This was done primarily to
reduce the formation of insulating layers on
the electrodes in the spectrometer. It was
found that operating the experiment with the
lamps on improved the long term stability of
the apparatus.

(e) a small glass viewing port. The purpose of
this was to be able to verify that the baking
lamps were indeed operating.

The other 7 ports were simply blanked off and not used in
the present set of experiments. The top flange has nine
accessory ports which have electrical feedthroughs on them
to connect the spectrometer to the outside world. It also
has two rotary vacuum feedthroughs, one of which is used to
rotate a polarizer, and the other to rotate the analyzer
half of the electron spectrometer. The top flange was also
used to hold the entire framework of the spectrometer and
the magnetic shielding box. Using this arrangement it was
possible to remove the entire spectrometer from the vacuum
chamber without disturbing any electrical connections bet-
ween the feedthroughs and the spectrometer. This was a dis-
tinct advantage when the spectrometer had to be removed for

Electrical Feedthroughs to Spectrometer

T.C. Gauge Tube

Gas Inlet

High Vacuum Isolation Valves

Ion Gauge Tube

Vacuum Chamber

μ-Metal Shield

Electrical Feedthrough for Baking Lamps

Butterfly Isolation Valves

Liquid Nitrogen Cold Traps

Thermo-Electrically Cooled Baffles

Mercury Vapour Diffusion Pumps

Foreline Isolation Valves

Thermocouple Gauge Tube

Zeolite Oil Trap Magnetic Valve

To Rotary Pump

FIG 2.1   THE VACUUM SYSTEM

Diffusion Pumps

Magnetic Valve

Rotary Pump

220 VAC

110 VAC

"Agastat" Time Delay Relay

Energize

Auxiliary Relay

FIG. 2.2 AGASTAT CONTROL CIRCUIT

cleaning or installation of major parts. It should be
pointed out, however, that because of the foresight in the
design of the chamber, it was rarely necessary to remove the
spectrometer in order to work on it. Removal of one or two
of the side panels allowed easy access to the spectrometer
for most occasions.

It was essential to the operation of the spectrometer
that stray magnetic fields be kept out of the interior of
the vacuum chamber. This was accomplished by enclosing the
entire spectrometer in a box constructed from u-metal
shielding. This box was suspended from the top of the cham-
ber, with four of its six sides removable. The shielding box
was held together with self-tapping, non-magnetic stainless
steel sheet metal screws. The bottom of the box was drilled
out with an array of 0.5 inch diameter holes to allow the
interior to be pumped efficiently. Measurements of the resi-
dual magnetic field inside the chamber indicated that it was
fairly uniform throughout, with a field strength of about 10
milligauss.

2.2.2 The Pumping System

The essential elements used to pump the vacuum chamber
are listed in Table 2.1 and shown in Fig. 2.1, so only the
following points need to be noted:

(1) Mercury vapour diffusion pumps were used to
maintain the high vacuum for the simple reason
that with an oil vapour pumping system the
possibility exists that some residual oil

might reach the spectrometer and cause the formation of insulating layers. These layers could charge up when exposed to the electron beam and degrade the performance of the instrument. Mercury, being a conductor, would not cause this type of problem. To prevent mercury from getting into the collision region, a combination of thermoelectrically cooled baffles and liquid nitrogen cold traps were used on each diffusion pump. The baffles enabled the system to be kept on continuously for months at a time, unlike the situation which arises without them - the mercury vapour freezes on the cold surface of the traps until there is none left in the pumps. When this happens the entire system must be shut down to allow the mercury to thaw and fall back into the pumps. With the present system (and no baffling) this would happen on a weekly basis, making long term stability difficult to maintain.

(2) Oil vapour in the foreline was removed by a trap containing activated alumina (Zeolite). This prevented backstreaming of oil from the rotary pump into the diffusion pumps.

(3) The foreline pressures attained by the rotary pump were between 10 and 20 millitorr as measured by the thermocouple gauge unit.

(4) Butterfly valves were used to isolate the vacuum chamber from the pumping system when it became necessary to shut the system down and open it up. This also prevented the mercury in the diffusion pumps from slowly evaporating.

.(5) To prevent the system from turning on again after a power failure of more than 10 secs duration, an Agastat power fail protection device was used to control power to the rotary pump and the diffusion pumps. The magnetic valve would then seal off the rotary pump from the foreline, thus preventing oil from being sucked into the line and then into the diffusion pumps. Figure 2.2 shows the schematic diagram of the Agastat control circuit.

2.3 THE ELECTRON SPECTROMETER

Since the electron spectrometer is _the_ most important piece of equipment used in the present work, it is worth-while to discuss the details of its design, construction and operation. The design of the spectrometer has already been discussed extensively in the literature[1-3], and the material presented here is an overview of these.

A general description of the spectrometer will be presented first, followed by a discussion of the criteria necessary to design the device, and lastly, the operation and performance of the spectrometer is discussed. Appendix 2.4 contains construction details other than what is discussed here.

2.3.1 General Description

The spectrometer consists of two independent halves: the _selector_, which produces an almost monoenergetic electron beam, and the _analyzer_, used to energy analyze scattered electrons. These are schematically illustrated in Figures 2.3(a) and 2.3(b), respectively. As can be seen from these diagrams the spectrometer consists of the following basic elements:

(1) an electron source - filament, grid and anode.
The filament is a heated tungsten wire bent into a hairpin shape, and is housed in a stainless steel holder which can be removed from Lens Stack 1 without having to dismantle
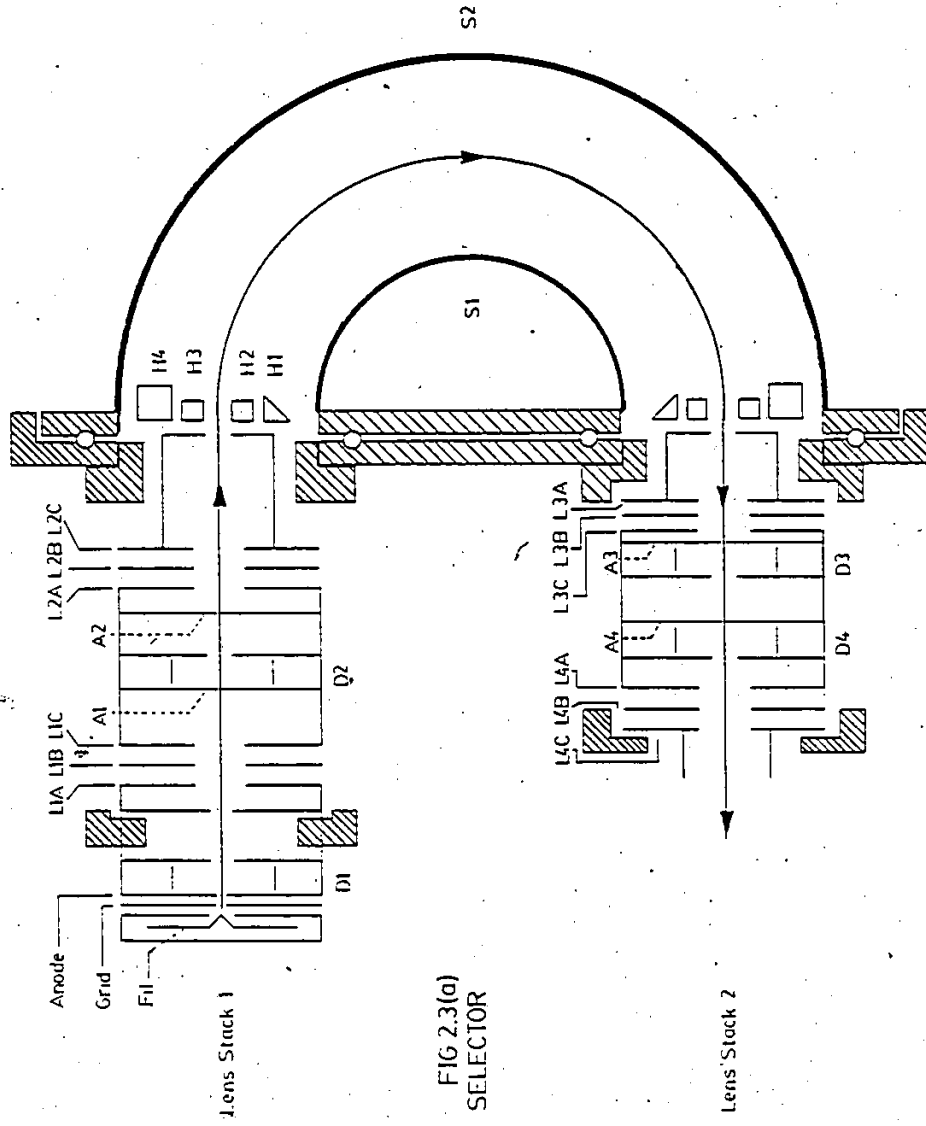
FIG 2.3(a)
SELECTOR
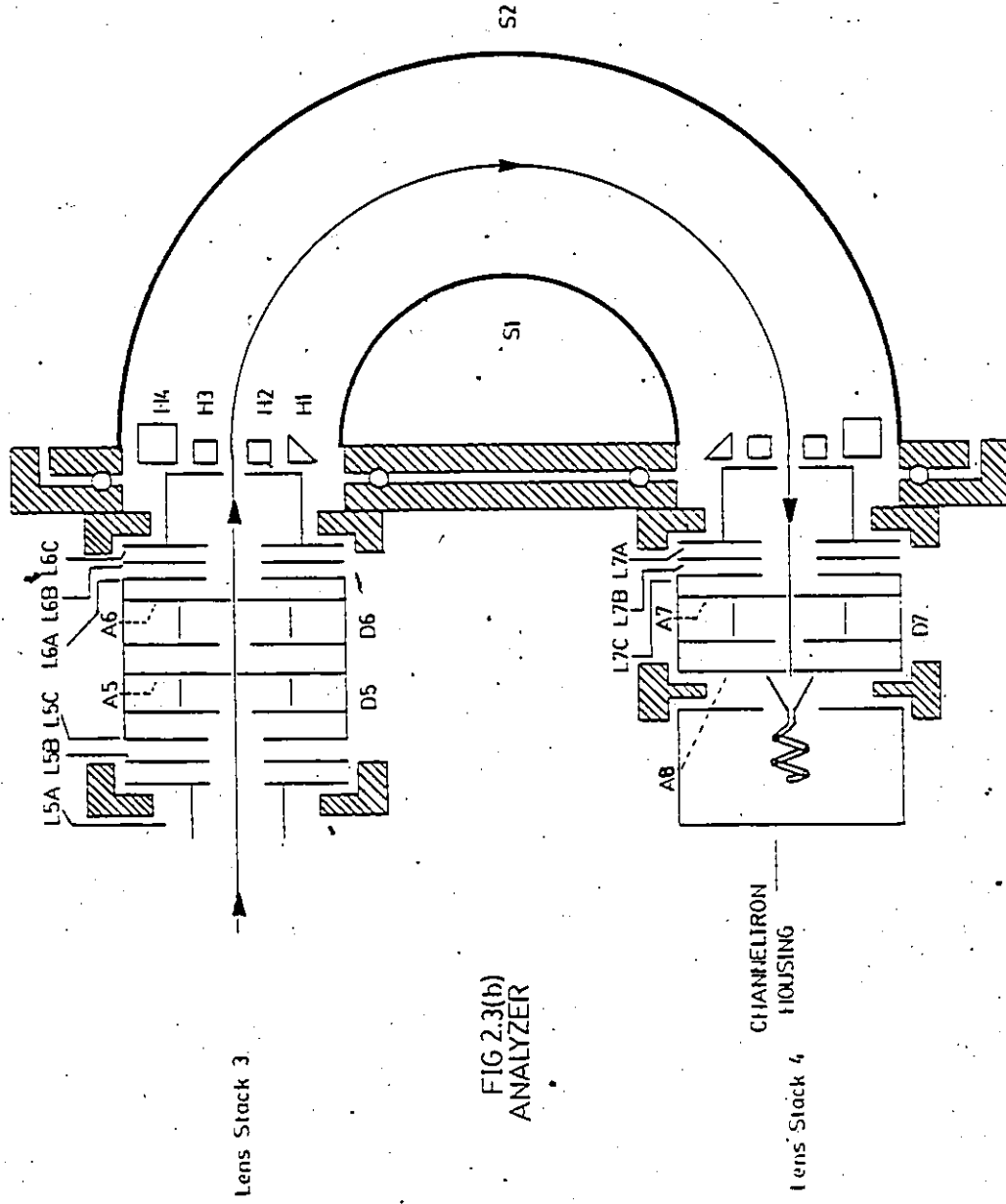
FIG 2.3(b)
ANALYZER

the entire stack (see Appendix 2.4).

(2) seven 3 element aperture lenses (L1-L7), used to focus the electron beam within the spectrometer. Lenses L4 and L5 are focussed on the target region.

(3) pinhole apertures (A1-A8) used to define the electron beam. Apertures A1-A6 are also used to monitor the beam current at various points in the spectrometer.

(4) deflector assemblies (D1-D7) to steer the beam in the x and y directions, the z direction being defined by the beam itself (see Appendix 2.4).

(5) fringe field correctors at the entrance and exit planes of the hemispheres. These are used to match the fields of the final lens elements (L2C, L3A, L6C, L7A) to the hemisphere fields and to correct for the field distortion at the gaps in the hemispheres.

(6) double hemispheres (S1 and S2) which energy analyze the electron beam, resulting in an almost monoenergetic final beam.

(7) a channel electron multiplier, or Channeltron(*), to detect electrons scattered into the analyzer. Note that the channeltron cone is kept at the potential on L7C.

(*) Trademark of Galileo Electro-Optics, Inc.

Figures 2.4 and 2.5 show schematic diagrams of the elec-
tronics used to control the selector and analyzer, respec-
tively. Table 2.2 lists the components used in these cir-
cuits. These circuits are self-explanatory for the most
part. Note the capacitors on the deflectors and on some of
the lens elements; these are used to eliminate 'ripple' vol-
tages and improve the stability of the electron beam. As
will be discussed later, it is essential that the hemisphere
voltages, the hoop voltages and the voltage on L2C (or L6C)
be kept at a fixed ratio to each other. To ensure that this
is the case, the scale power supply is used to adjust the
potentials simultaneously. Not indicated on the diagrams
are the jacks used to monitor the potentials on each ele-
ment. Also, lens elements indicated on Fig.'s 2.3(a) and
2.3(b) which are not indicated in the schematics are inter-
nally connected to other lens elements at the spectrometer
itself. The following table summarizes those internal con-
nections.

SELECTOR	ANALYZER
L1A – Anode.	L5A – L4C (Target)
L2A – L1C	L6A – L5C
L3A – L2C	L7A – L6C
L4A – L3C	

A summary of the materials used in the construction of
the spectrometer is in order at this point to give the
reader an idea of what is involved.
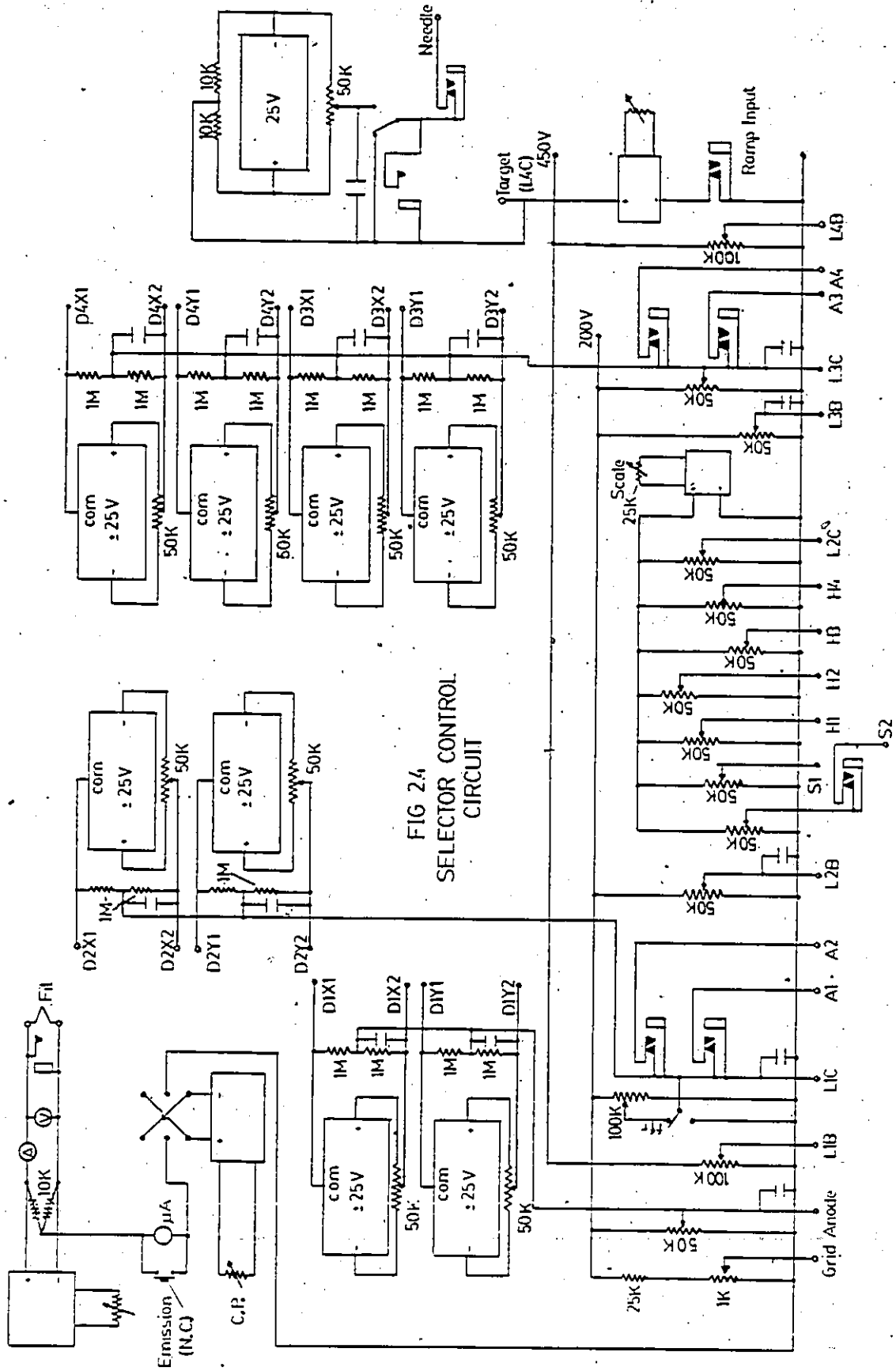
FIG 24.
SELECTOR CONTROL
CIRCUIT
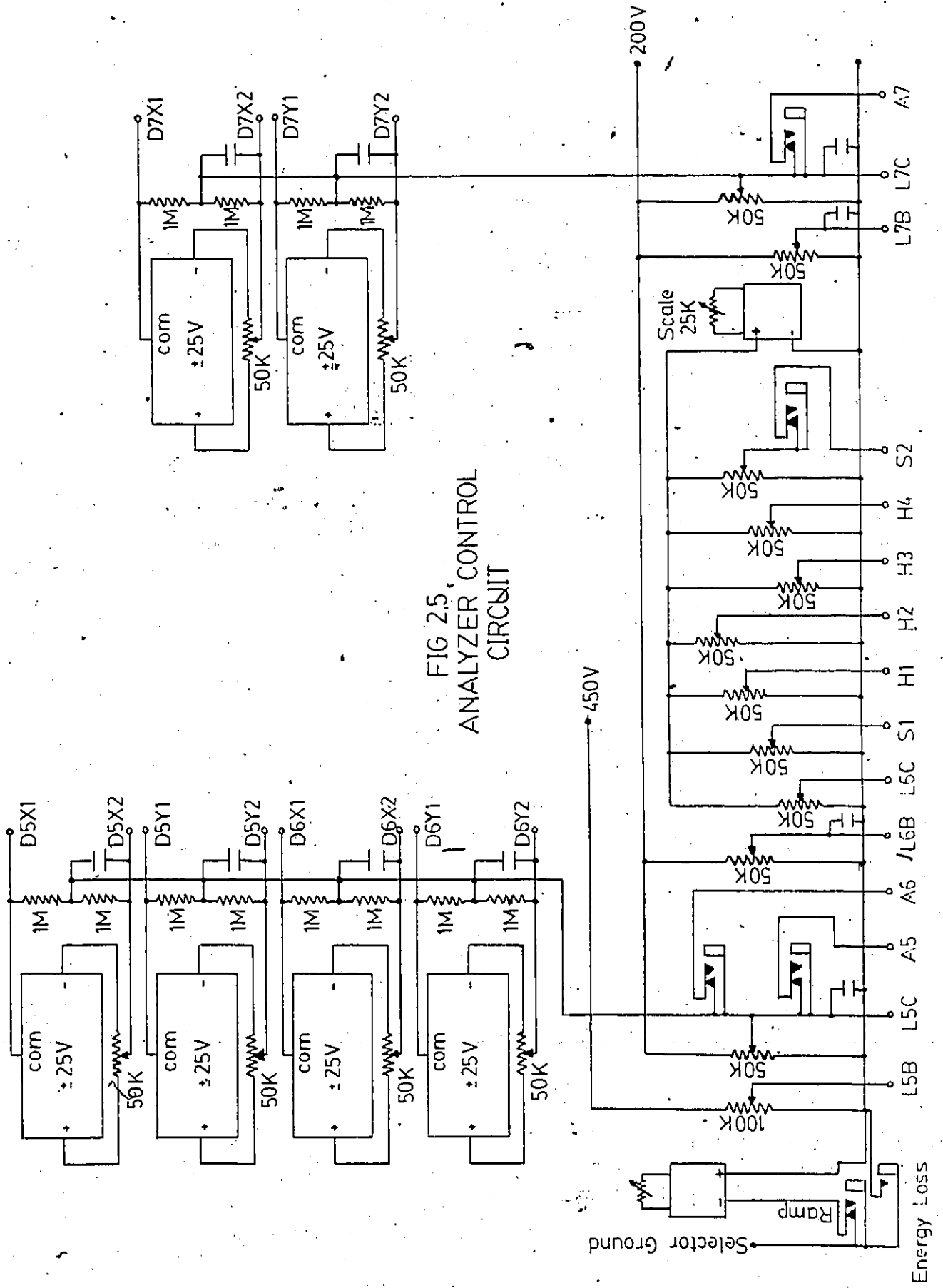
FIG 2.5
ANALYZER CONTROL
CIRCUIT

Table 2.2
Spectrometer Electronics

Potentiometers: Bourns 10 turn Helipots

Power Supplies:

Filament Supply: Lambda LCS-2-02 (0-18 volts Reg.)
Contact Potential: Lambda LCS-C-01 (0-7 VDC Reg.)
Scale Supply: Lambda LCS-2-04 (0-60 VDC Reg.)
Lens Elements: Lambda LPD-425A-FM (Dual 0-250 VDC Reg.)
Deflectors: Power One HAA-24-6 (+24 VDC Reg.)
Target Energy: Kepco ABC-100-0.2 M (0-100 VDC Prog., Reg.)
Energy Loss: Kepco HB-2AM (0-325 VDC Reg.)
Needle Bias: Power One B24-12 (0-24 VDC Reg.)

Voltage Monitor: Hewlett-Packard 3439A Digital Voltmeter

Current Monitor: Keithley 602 Solid State Electrometer

(1) Molybdenum - used for components exposed to the electron beam: lens elements, deflectors, field correctors, and the hemispheres. The target region was also constructed out of this material. Molybdenum was chosen because it is non-magnetic, and is not subject to oxidation or corrosion.

(2) Non-magnetic stainless steel - for lens stack ends, support rods, filament holder, deflector assemblies, the baseplates (and associated hardware), channeltron mounting assemblies, as well as all screws, nuts and bolts.

(3) Ceramic - for the three lens stack alignment rods used in the 4 lens stacks.

(4) Macor, a machinable fiberglass - used to construct spacers of appropriate length to achieve the required element separation in the stacks. It was also used to insulate the screws holding the filament, deflectors, corrector hoops, and the hemispheres. The target region was also mounted on Macor to insulate it from the chamber. The channeltrons were insulated from their mounting assemblies by holders constructed out of this material.

(5) Aluminum - used to construct the supporting framework which holds the spectrometer to the top plate of the vacuum chamber. It was also used to construct the mounting bracket for the

target region assembly.

Electrical connections to the spectrometer were made by spot-welding wires from each element to pins mounted in insulating blocks attached to the selector and analyzer baseplates. From there, wires were spot-welded to the feedthroughs on the top plate of the chamber. Insulation of these connections was done by using teflon sleeving at the spectrometer, and glass fiber sleeving to the feedthroughs.

To minimize the amount of electron scattering from the lens elements and apertures, the area around the holes in these was coated with a fine layer of scot. The hemispheres (S1 - outer surface; S2 - inner surface) and the field corrector hoops were also coated with soot, as was the entire target region.

The analyzer half of the spectrometer could be rotated about the target region through about 95 degrees. This was accomplished by a rotary feedthrough placed on the axis of rotation on the top plate of the chamber. To allow for the placement of a detector immediately above the interaction region, the bracket connecting the analyzer to the rotary feedthrough was diverted through 90 degrees near the top of the chamber. To ensure that the rotation was smooth, small teflon pads were attached to the underside of the analyzer mounting assembly to reduce friction.

The detector was held above the interaction region by a framework attached to the supporting rods of the spectrometer assembly. To allow rotation of the detector (needed for

a polarization sensitive one) another rotary feedthrough, offset from the axis of rotation, was placed on the top plate. A set of two gears were then used inside the chamber to couple the rotary feedthrough to the detector.

2.3.2 Design Criteria

There are many things which must be taken into account when designing any electron optical system, and these are especially important in the design of a high resolution electron spectrometer. Various effects present in electron optics put limitations on the available current and energy resolution, as well as beam definition, that a device is capable of achieving. The beauty of the present spectrometer lies in the fact that its designers (Read and his co-workers at the University of Manchester) have expended a great deal of time and effort in the task of minimizing these effects and producing an optimized design. In doing so, they have accounted for effects which were not taken into consideration in previous designs, and thus have been able to achieve very high resolution electron beams (10- 20 meV or better) with reasonable target currents (on the order of nanoamps).

Figure 2.6(a) is a schematic diagram of a typical electron optical system. The system consists of 4 basic elements: an electron source (cathode); a combination of lenses and collimators to focus the source into an energy selector; the energy selector, which provides the high energy resolution; and another set of lenses and collimators to focus the

RADIUS: r_k
PENCIL ANGLE: θ_k
VOLTAGE: V_k

CATHODE

LENSES and COLLIMATORS

r_s
θ_s
V_s

ENERGY SELECTOR

LENSES and COLLIMATORS

r_t
θ_t
V_t
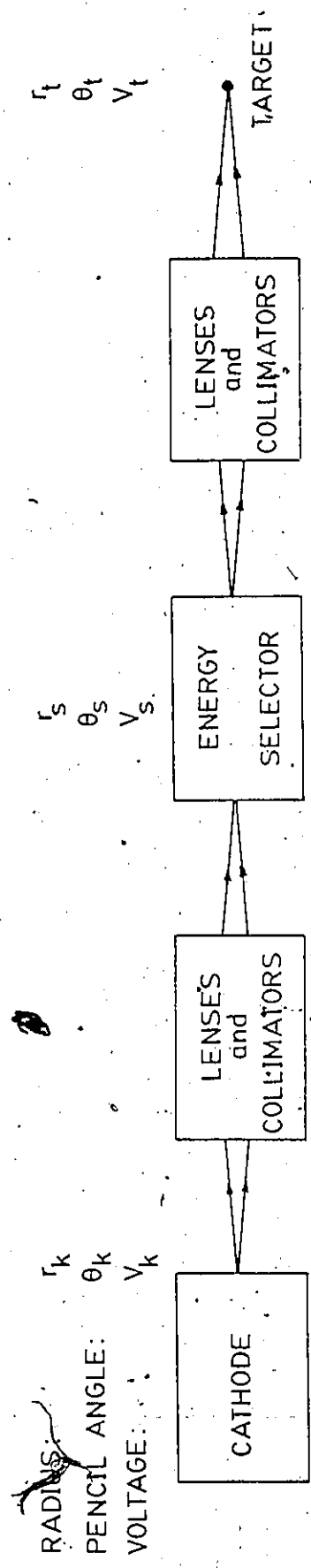
TARGET

SCHEMATIC REPRESENTATION OF AN ELECTRON OPTICAL SYSTEM

FIG 2.6(a)

final beam into the target region. The goal in designing a
working system is to produce the maximum current at the tar-
get for a given target energy and energy resolution. In
addition the target beam must be spatially well defined, and
the system should be able to keep these properties constant
for a wide range of target energies. We shall first discuss
the effects present in electron optical systems which place
constraints on the design parameters and the 'quality' of
the final electron beam. These are:

 (1) Removal of electrons by defining apertures and
  the energy selector.

 (2) Space-charge repulsion and inter-electron
  interactions.

 (3) Gun limitations.

 (4) Lens, collimator and deflector aberrations.

 (5) Aberrations of energy selectors.

(1) Removal of Electrons by Apertures and the Selector

A necessary part of any decent electron optical system is
one or more sets of defining apertures or <u>collimators</u> which
are used to spatially define the electron beam. Figure
2.6(b) shows a typical set of defining apertures. As can be
seen, this set consists of a <u>window</u> to limit the diameter of
the beam, and a <u>pupil</u> to define the beam angle θ_B and the
pencil angle θ_p. As we shall see later, these angles play
important roles in the proper design of the system. The
collimator will remove electrons from the beam, so that not
all electrons emitted by the cathode will reach the selec-
tor. This happens in two ways. First, electrons which are

PUPIL

WINDOW

θ_P

θ_B

r
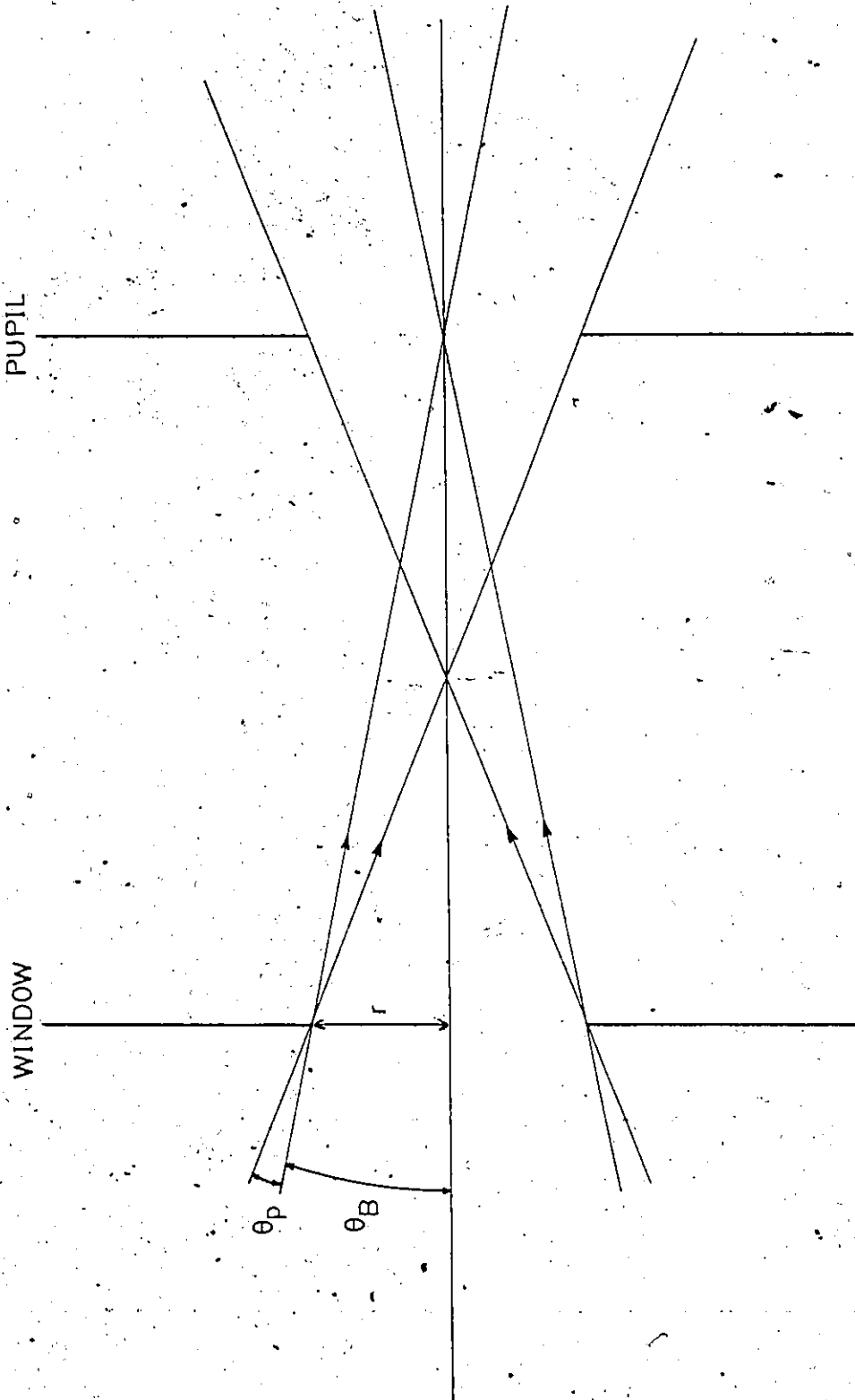
DEFINING APERTURES

FIG 2.6(b)

emitted too far from the beam axis will simply be screened out, and second, electrons which have a _transverse momentum_ which is too large will be stopped by the time they reach the collimator. Because of this second effect, the collimator will alter the energy distribution of electrons in the beam, a fact which was not considered in previous designs. Before discussing this aspect of collimators, we must examine the relationship between beam energy, beam radius and the beam pencil angle.

The above mentioned quantities are related to each other by the _Helmholtz-Lagrange_ equation:

$$rE^{1/2}\sin\theta_p = const. \qquad\qquad (2.3.1)$$

Thus, for the schematic diagram of Fig. 2.6(a), equation 2.3.1 gives:

$$r_K E_K^{1/2}\sin\theta_K = r_S (E_K + eV_S)^{1/2}\sin\theta_S = r_T (E_K + eV_T)^{1/2}\sin\theta_T$$

where:

r_K is the radius of that part of the electron source which is finally imaged at the target.

E_K is the beam energy at the cathode.

θ_K is the beam pencil angle at the cathode.

r_S is the beam radius at the selector entrance and exit.

V_S is the potential of the selector region (with respect to the cathode).

θ_S is the pencil angle at the selector.

r_T is the beam radius at the target.

V_T is the target potential.

θ_T is the pencil angle at the target.

Note that equation 2.3.1 implies that the pencil angle can never be made arbitrarily small, and therefore the angular divergence of the beam, $\theta_B + \theta_P$ will always be non-zero. When using collimators equation 2.3.1 must always be kept in mind.

Returning now to the effect that collimators have on the energy distribution of the electron beam, Fig. 2.6(c) shows this. Curve (a) on Fig. 2.6(c) is the (assumed) Maxwellian distribution of electrons emitted from the cathode at an effective temperature T_K. Curve (b) shows the distribution after passing through the collimator. This is obtained by defining a critical energy, E_C, given by[2]:

$$E_C = \frac{eV_T M_T^2 \sin^2 \theta_T}{1 - M_T^2 \sin^2 \theta_T} \approx eV_T M_T^2 \sin^2 \theta_T \qquad (2.3.2)$$

where $M_T = r_T / r_K$ is the linear magnification at the target. Electrons with energies less than E_C will be transmitted by the collimator, whereas only a fraction of the electrons with energies greater than this will be transmitted. This fraction is given by:

$$f_{coll} = 1 - \frac{eV_T \exp(-E_C / kT_K)}{E_C + eV_T} \qquad (2.3.3)$$

As can be seen from Fig. 2.6(c), the energy distribution is

FIG 2.6(c)

ELECTRON ENERGY DISTRIBUTIONS
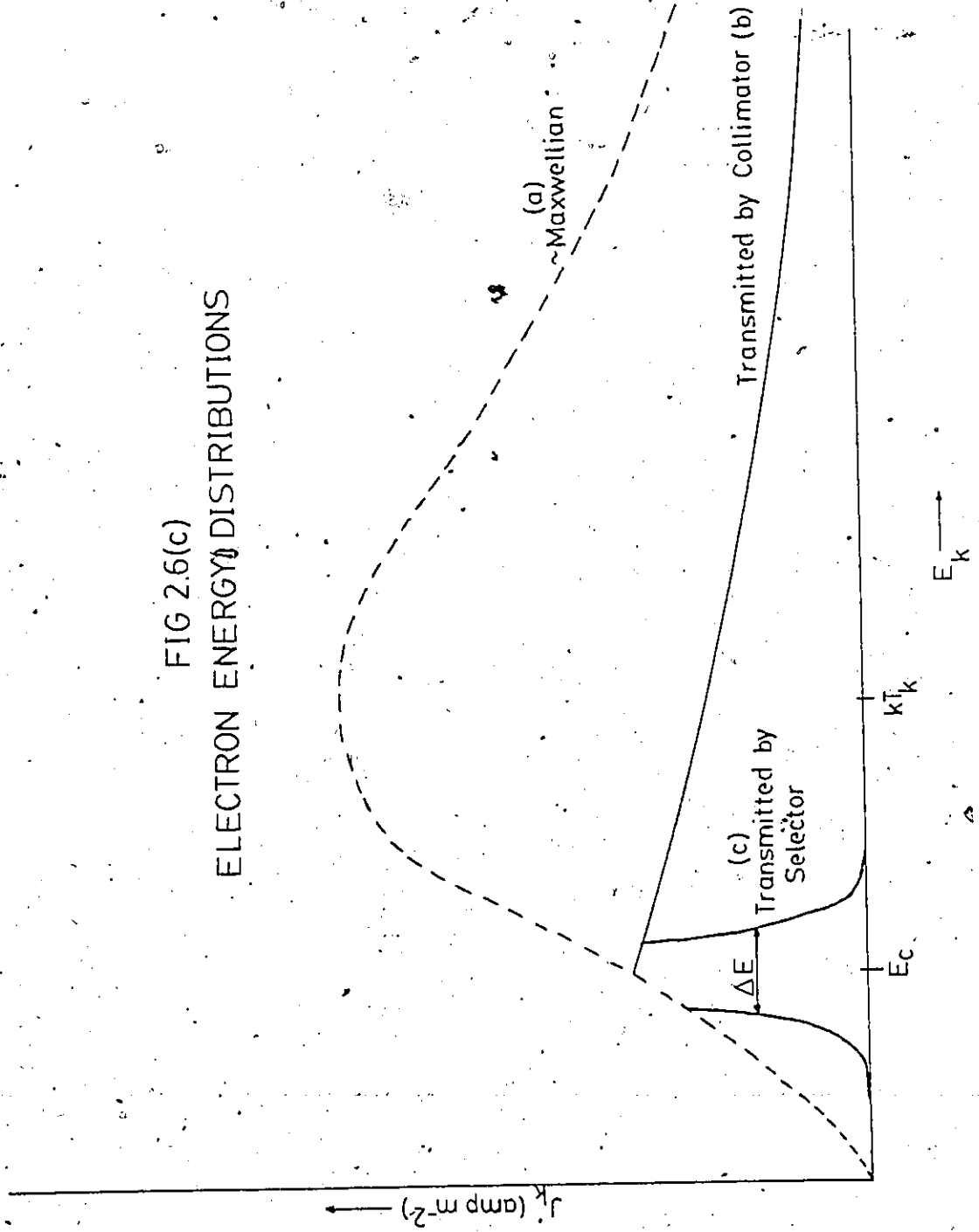
altered significantly by the collimators.

Two additional points about collimators should be mentioned:

, (1) If more than one set of defining apertures are used in the system, the energy distribution of the beam should be determined by only one set; the extra collimators and their image sizes should be larger than the primary collimator and its image. If this is not done, then the center of the beam will be 'brighter' than the edges (vignetting) and as a result there will be an unnecessary loss of current.

(2) It is desirable to place the primary collimator as soon after the cathode as possible, and definitely before the energy selector, to reduce the effects of too much current at the selector entrance. Also, placing the defining apertures early in the system has the advantage of starting with a well defined beam from the beginning, which will reduce the effects of aberrations later on in the system.

The energy selector also removes electrons from the beam, so that not all electrons entering it will reach the target. Electrons whose energies are too high or too low will not pass through the selector. i.e. the selector will only pass an energy $E_0 \pm \Delta E$. Curve c on Fig. 2.6(c) shows the energy distribution of the electron beam after passing through the

hemispherical energy selector. In the past E_0 was taken to be $E = kT_K$, the energy of the maximum in the Maxwellian distribution. Clearly, the presence of the collimator changes this, especially when E_0 and ΔE are much less than kT_K. The mean energy transmitted by the selector is instead E_C, and the fraction of electrons transmitted by the selector is:

$$f_{sel} = \frac{(E_C/kT_K)\exp(-E_C/kT_K)\Delta E}{(1 - \exp(-E_C/kT_K))kT_K} \qquad (2.3.4)$$

The transmission of the entire system is the product of the collimator and selector transmissions, and is:

$$f_{trans} = \frac{E_C\ E\exp(-E_C/kT_K)}{(kT_K)^2} \qquad (2.3.5)$$

for $\Delta E \ll E_C$. As indicated by equation 2.3.4, the fraction of current transmitted by the selector increases as ΔE increases. For $E_C \ll kT_K$, equation 2.3.4 can be written as:

$$f_{sel} = (1 - \frac{E_C}{kT_K})\frac{\Delta E}{kT_K}.$$

Thus a slight increase in transmission can be gained by decreasing E_C, but (shown later), E_C and ΔE are proportional, so E_C cannot be reduced too far.

(2) Space Charge Repulsion and Inter-Electron Interactions

The electrostatic repulsion between electrons in the beam has two effects: on the spatial distribution of the beam, and on the energies of individual electrons in the beam.

The repulsion between electrons means that a lens cannot focus the electron beam to a point on the 'optical' axis of the system(or anywhere, for that matter); i.e. the beam radius can never be zero anywhere in the system. The best that can be achieved is focussing the beam to some minimum radius, which depends in a complex way on the initial radius, the beam current, the distance from the lens, and the beam energy. Alternatively, this can be viewed as putting a constraint on the maximum amount of current that can be passed through a radius r_2 at a distance z away from the lens for a given beam energy(determined by the beam voltage V) and initial beam radius r_1. This maximum current is given by:

$$I_{max} = \frac{38.5 \times 10^{-6}}{\ln(r_1/2r_2)} \, V^{3/2} \left(\frac{r_1}{z}\right)^2 \qquad (2.3.6a)$$

which is accurate to about 20% for $0.0035 \leq r_2/r_1 \leq 0.027$ and

$$I_{max} = 38.5 \times 10^{-6}\left(0.3 + 3.7\frac{r_2}{r_1}V^{3/2}\left(\frac{r_1}{z}\right)\right)^2 \qquad (2.3.6b)$$

which is accurate to about 20% for $0.04 \leq r_2/r_1 \leq 1.0$. The expression used in past designs is:

$$I_{max} = 38.5 \times 10^{-6} V^{3/2} (2r_1/z)^2$$

which is the maximum amount of current that can be forced through a tube of length z and radius r_1. Read et al[2] point out that this is simply not accurate enough to account for all of the space charge repulsion, and does not agree with experimentally determined data. It should also be noted that the minimum radius of the beam is always subject to the constraints imposed by the Helmholtz-Lagrange equation (2.3.1).

The effect of inter-electron interactions can change the energies of individual electrons. This results in an anomalous energy spread in the beam, known as the Boersch effect. This energy spread is given by:

$$\Delta E_B = \frac{1}{r\theta_P} \chi(Ir/V^{1/2}) \qquad (2.3.7)$$

where $\chi(x)$ is a function which varies from about 10^{-10} for $x = 10^{-15}$ (SI units) to about 3×10^{-6} for $x = 10^{-9}$ (SI units) (see graphs in ref 2). This effect can be neglected at the

selector entrance since it will be much smaller than the 'natural' energy spread in the electrons coming from the cathode. After the beam leaves the selector, however, this must be taken into account. For example, suppose that the final set of lens elements is rather poorly designed, and that the beam radius at the target is 0.5mm, the pencil angle is 0.025 rads, and I and V are such that X has the value 10^{-7}. The Boersch energy spreading is then 8 meV, which is certainly non-negligible if one desires final resolutions of 10 or 20 meV. Thus the selector to target lens system must be designed to keep this effect at a minimum (1 or 2 orders of magnitude lower than the above example would do nicely).

(3) Gun Limitations

Space charge effects also put a limit on the maximum current that can be obtained from a plane parallel diode arrangement. This is given by:

$$J_K^{max} = 2.33 \times 10^{-6} \, d_K^{-2} \, V_A^{3/2} \quad (ampm^{-2}) \qquad (2.3.8)$$

where d_K is the distance between the cathode and anode and V_A is the anode potential. This then also limits the available current at the target, given by the product of the transmission of the system (equation 2.3.5) and equation 2.3.8, in the absence of other effects. There is not much one can do to overcome this limitation. The maximum current can be increased by making V_A large and d_K as small as pos-

sible, and the use of a triode arrangement will improve the situation to some degree. This limitation on the system, however, is less important than limitations from other causes.

(4) Lens, Deflector and Collimator Aberrations

Electrostatic lenses and associated elements introduce aberrations into the electron beam which have the effect of increasing the size, beam angle and pencil angle throughout the system. This results in a less well defined beam at the target, a loss of current, and an increase in the overall energy spread in the beam.

As in light optics, electron optics suffer from spherical aberration, coma, astigmatism, curvature of field, and other distortions as well. These aberrations are mainly due to non-uniformities in the lens fields near the edges of the elements, as well as the inability of the lens to focus the beam to a point. Thus it is desirable to keep the beam away from the edges of the lens elements, i.e., to make the lens diameter much larger than the beam diameter, and to make certain that the beam is on the optical axis.

Lens aberrations are usually discussed in terms of a quantity called the filling factor of the lens. This is defined to be the ratio of the beam diameter inside the lens to the lens diameter. The spherical aberration of a two-element cylinder lens, for example, due to the filling factor (η) is given by:

$$\Delta r / D = 0.1 \eta^3$$

where Δr is the radius or the image disc on the axis due to the aberration of a point source, and D is the lens diameter. For real objects, the aberration is generally much worse. The lenses used in the present spectrometer are all 3 element aperture lenses, and the aberrations of these are usually greater than those of 2 element lenses, particularly if the center element is at a lower potential than the other two. Thus the center element of a 3 element lens should always be operated at a higher potential than the outer elements. The aberrations of various types of lenses have been tabulated by Harting and Read[4], and this reference can be used when designing an electron optical system to determine the aberrations of lens elements that one could expect.

It is immediately clear that a defining aperture has a filling factor of 1.0 by definition. This has two important consequences: one, that a lens cannot also be used as a defining aperture without introducing severe aberrations into the image, and two, defining apertures must be placed in field-free regions lest they act as terribly aberrated lenses. It is also advisable to place defining apertures in regions of high potential, where the beam energy is large, to further minimize the effects of any aberrations that may occur.

Deflectors used to steer the beam within the system can also cause aberrations if the deflecting voltages used are too high. Thus the maximum deflector voltages should be

high enough to be able to push the electron beam around, but not so high as to distort the fields around them. Deflectors should also be placed in field-free regions, and to minimize any field distortion, the deflecting potentials should float on top of the potential within the region.

(5) Aberrations of Energy Selectors

Energy selectors suffer from what might be called 'chromatic' aberration, in that different energies are focussed at different points in the exit plane of the selector. Thus a finite energy spread will still remain in the final beam after passing through the selector. The base width of this energy spread is given by[2]:

$$\Delta E_b = E_S(\alpha\frac{r_S}{L_S} + \beta\theta_S^n + \gamma\phi_S^2) \qquad (2.3.9)$$

where:

E_S is the beam energy at the selector entrance (also called the analysis energy).

r_S is the beam radius in the selector.

L_S is the distance in a straight line between the selector entrance and exit positions.

θ_S, ϕ_S are the half angles of the beam in two perpendicular directions at the selector entrance.

α, β and γ are constants which depend on the selector geometry.

The following table lists the values of L_S, α, β, n and γ for various types of selectors.

SELECTOR TYPE	L	α	β	γ	n
180 degree Hemispherical	2R	4.0	1.0	0	2
127 degree Cylindrical	1.79R	7.2	1.33	1.0	2
Parallel Plate Mirror	R*	4.0	2.0	1.0	2
Cylindrical Mirror with 2nd order focus	3.39R*	6.5	5.54	0	3

R is the mean radius of the orbit
R* is the maximum radius of the orbit

From this table it is clear that the hemispherical analyzer is a good choice for an energy selector. The energy spread for this device is:

$$\Delta E_b = E_S (2\frac{r_S}{R} + \theta_S^2) \qquad (2.3.10)$$

Thus, for a fixed r_S, R and E_S, it is desirable to make θ_S, the angular divergence of the beam, as small as possible. This can be done by arranging that the beam angle is zero; i.e. using a real window and a virtual (at infinity) pupil before the selector. Then θ_S will be given by the pencil angle of the beam. Since θ_S, r_S and E_S are related by the Helmholtz-Lagrange equation, r_S cannot be made arbitrarily small, so it is also desirable to make R>>r_S.

The quantity that is to be optimized at the target is not the base width of the final energy distribution, but the FWHM. This is not quite one-half of the base width, but is given by:

$$\Delta E_{1/2} = E_S(\alpha_{1/2}\frac{r_S}{2L_S} + \beta_{1/2}\theta_S^2) \qquad (2.3.11)$$

where $\alpha_{1/2}$ and $\beta_{1/2}$ are empirically determined parameters[2] which depend on the ratio of $\beta\theta_S^2/(\alpha r_S/L_S)$. It turns out that $\alpha_{1/2}$ is about equal to $\alpha/2$, but $\beta_{1/2} < \beta/2$.

The hemispherical energy selector also suffers from aberrations due to fringe fields in the gap between the hemispheres. This is due to the fact that half of each sphere is missing, and this must be corrected somehow so that the field in the gap has the proper $1/r$ dependence around the mean orbital radius of the beam. This is done by setting the potential of the last lens element to the mean energy of the beam in the selector and by introducing correction elements to modify the field in the gap. This will be discussed in greater detail in the next section.

(6) Optimization

Having discussed the various details of aberrations and limitations inherent in an electron optical system, it is clear that these effects are interrelated in some complex fashion. Thus the effects cannot be considered and minimized independently, but some sort of optimization must be performed for a given set of specifications of the system. This has been very carefully and thoroughly done by the Manchester group[1], and has resulted in spectrometer systems such as the one used in this work. The focussing properties of various types of lenses have also been tabulated by Hart-

ing and Read[4] and these tables can be used in conjunction with the principles discussed above to design the optimum system to meet one's requirements.

2.3.3 Design of the Present Spectrometer

It is worthwhile to examine the design of spectrometer used in this work in the light of the previous section to see how it has been optimized. A complete discussion of this can be found in ref. 1 so only an overview will be given here.

Lens Elements

A brief discussion of thick lenses is included here to provide a basis for understanding the material that follows. Figure 2.7 shows a representation of a thick lens. As indicated, PF_1 and PF_2 are the first and second principal foci, PP_1 and PP_2 are the first and second principal planes, and R is the reference plane. P and Q are the object and image distances, respectively. As in light optics, the relationship between these quantities is given by:

$$(P-F_1)(Q-F_2) = f_1 f_2 \qquad (2.3.12)$$

and the linear magnification is given by:

$$M = -f_1/(P-F_1) = -(Q-F_2)/f_2 \qquad (2.3.13)$$

The behaviour of these lenses is determined by the voltage ratios between each lens element. Figure 2.8 (taken from Harting and Read[4]) illustrates this for a typical 3 element aperure lens.
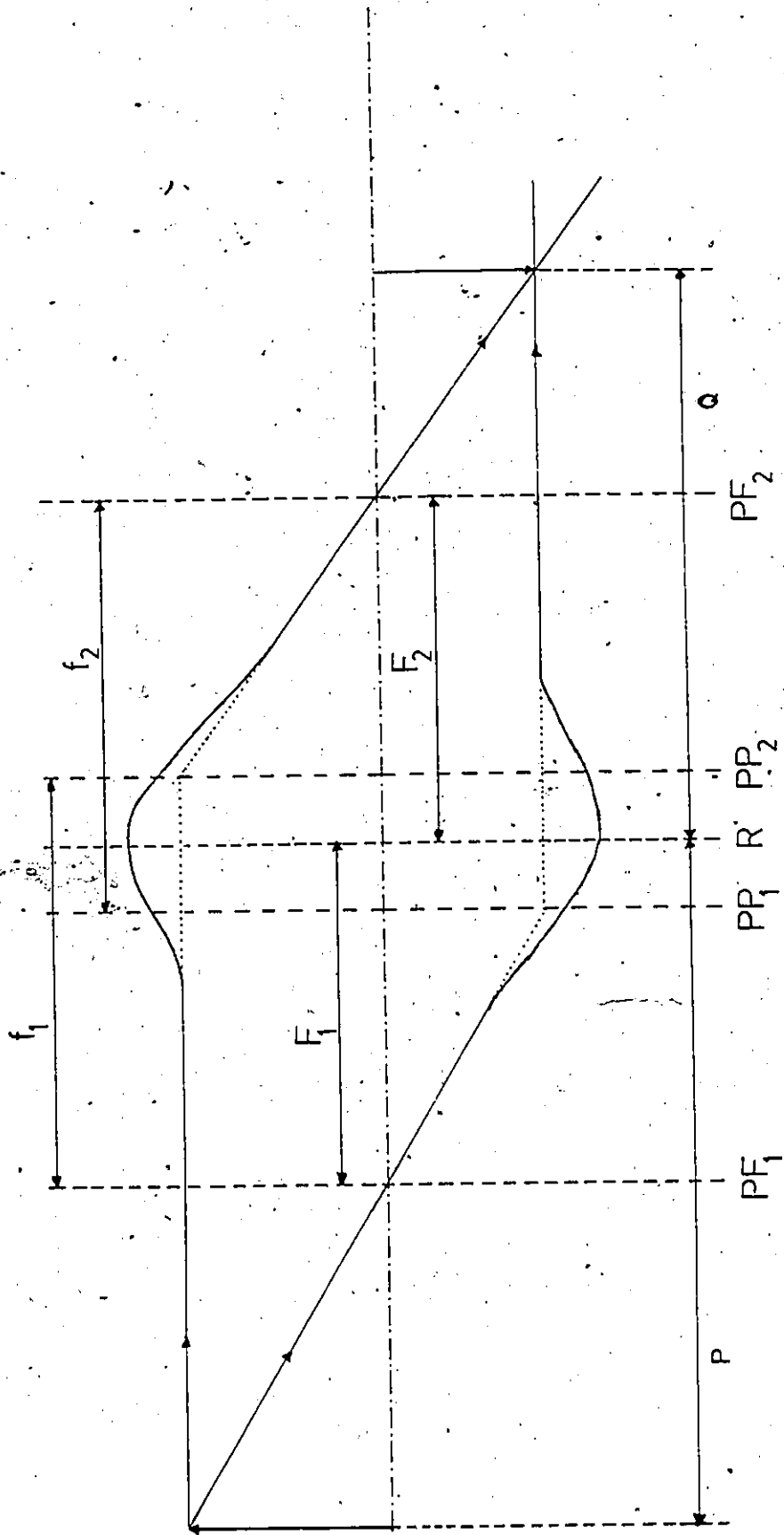
FIG. 2.7 THICK LENS SCHEMATIC

V3/V1- 5.0

THREE APERTURE LENS.A/D=0.5
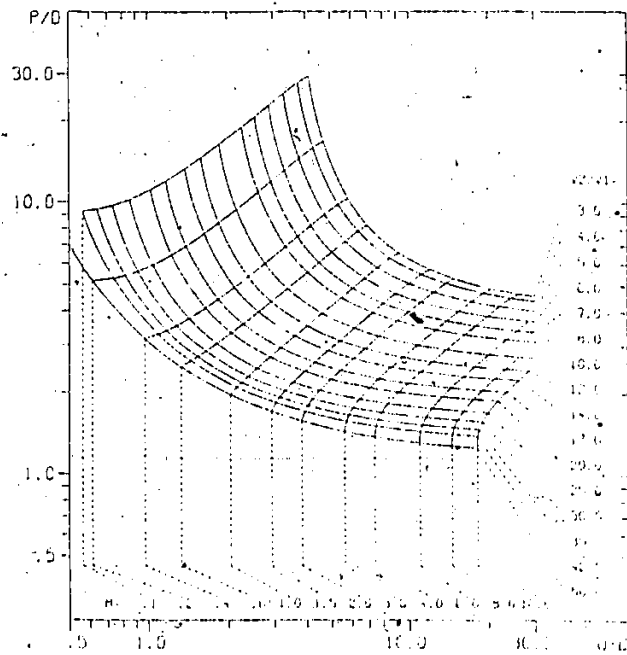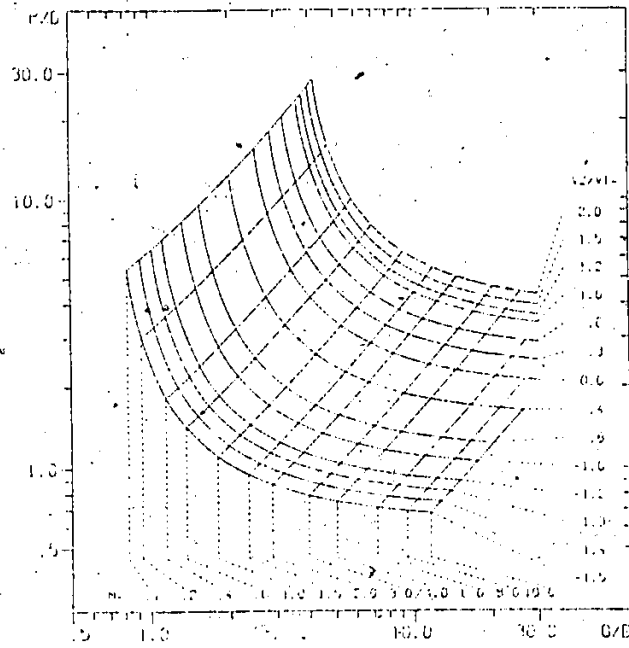
FIG 2.8

FIG 2.9 LENS STACK 1 PARAMETERS
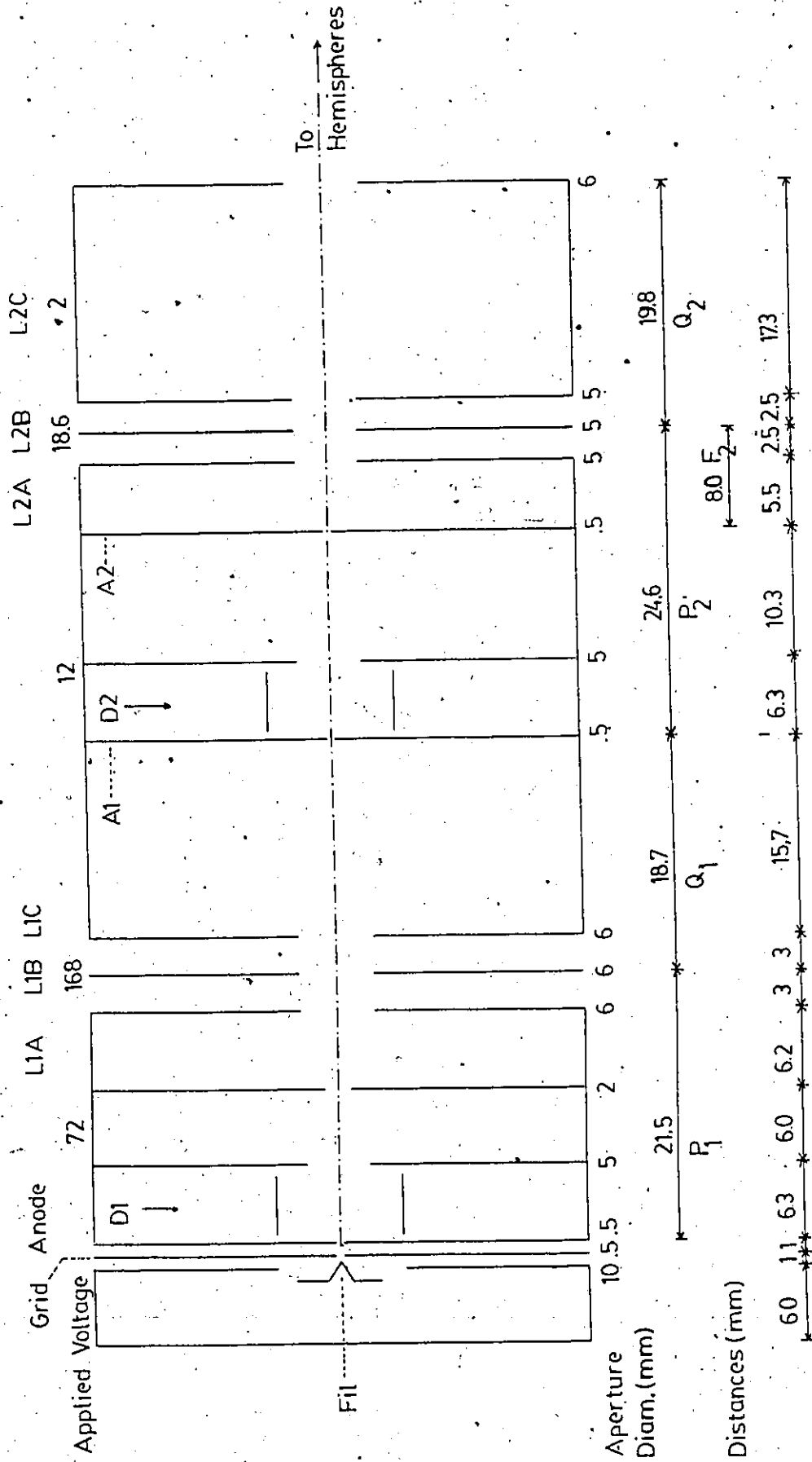
Selector: Lens Stack 1

A schematic diagram of Lens Stack 1 is shown in Fig. 2.9. Indicated on this diagram are the voltages applied to each lens element (calculated for an analysis energy of 2.0 eV), the diameters of all apertures, the spacing between each element, and the calculated object and image distances for each lens. Several points should be noted about the design:

(1) The electron source consists of a filament, grid and an anode, a triode configuration instead of a simple diode one. This enables one to extract somewhat more current from the cathode than would be possible with a diode. The presence of the grid, however, means that the effective position of the object is somewhat ill defined. For this reason, two oversize apertures are placed before lens L1 to limit the size of the beam and avoid problems caused by overfilling that lens.

(2) Although a single lens could have been used to image the source onto the hemisphere's entrance plane, this would have meant that one of the defining apertures would not be in a field free region. Thus two lenses were used instead. Lens L1 focusses the source onto aperture A1, and L2 focusses A1 into the hemispheres. Aperture A2 is placed at the first focal point of L2, and is imaged at infinity. This ensures that the beam angle going into

the hemispheres is zero, as required.

(3) The center elements of lenses L1 and L2 were operated at higher potentials than their respective outer elements to minimize lens aberrations. The potentials on L1A, L1C and L2C were usually kept fixed, and focussing was done by varying L1B and L2B. This also provided some freedom of adjustment to correct for space charge effects, minor mechanical misalignment, and to minimize aberrations at the hemisphere entrance plane.

(4) With the diameter of 'the defining apertures fixed at 0.5 mm, the pencil angle of the beam at the energy selector was 0.037 rads for the lens potentials indicated on Fig. 2.9.

Selector: Lens Stack 2

A schematic diagram of Lens Stack 2 is shown in Fig. 2.10. As indicated on this diagram, Lens Stack 3 (on the analyzer) is the mirror image of Lens Stack 2; that is to say, Lens Stack 3 works the same way as Lens Stack 2, except in reverse. This can be done because electrostatic lenses are symmetric with respect to time reversal operations*.

Lens Stack 2 is designed to provide a well defined beam at the target for a wide range of final energies. Again, two lenses are used to ensure that defining apertures are always placed in field free regions, and also eliminate the problems associated with placing a defining aperture too

FIG 2.10   LENS STACKS 2 & 3 PARAMETERS
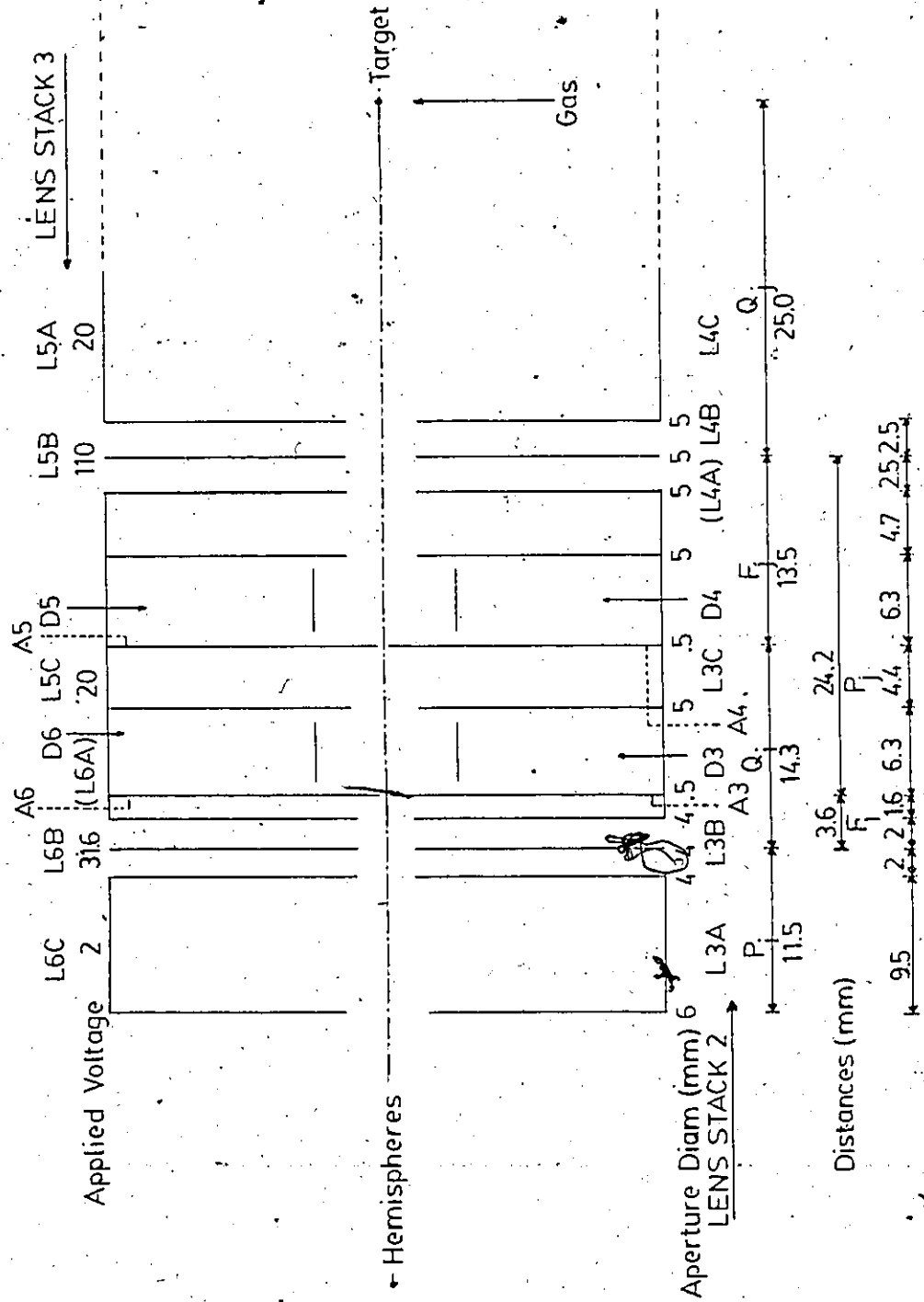
close to the energy selector. It is also difficult to
maintain the beam quality at the target with a single lens
and still be able to 'zoom' the final energy. Note that the
selector exit plane is imaged onto aperture A4, and aperture
A3 is imaged at the target. Aperture A3 is placed at the
second focal point of L3, and this quarentees that the beam
angle at the target is close to zero. This arrangement in
Lens Stack 3 also ensures that the beam angle going into the
hemispheres is zero.

The last lens on the stack, L4, (first lens on stack 3 of
the analyzer, L5) operates as a 'zoom' lens. It will oper-
ate over a wide range of target energies(up to 100 eV) while
keeping the final beam properly focussed at the target.
Calculations have indicated that the lens properties remain
constant for V(L4C)/V(L3C) > 1.5, provided V(L4B)/V(L3C) is
chosen properly[14]. This is shown in Fig. 2.11, taken from
ref. 1.

One additional point about Lens Stacks 2 and 3 is that
they were designed to minimize the Boersch energy spreading
at the target, making it negligible compared to the desired
resolution. At a target energy of 50 eV and a beam current
of 1nA, the Boersch energy spreading is on the order of 0.01
meV for this spectrometer.

Analyzer: Lens Stack 4

Figure 2.12 shows a schematic diagram of Lens Stack 4,
used to focus the exit plane of the hemispheres into the
channeltron. A single lens is sufficient for this, since at

FIG 2.11
ZOOM LENS CHARACTERISTICS
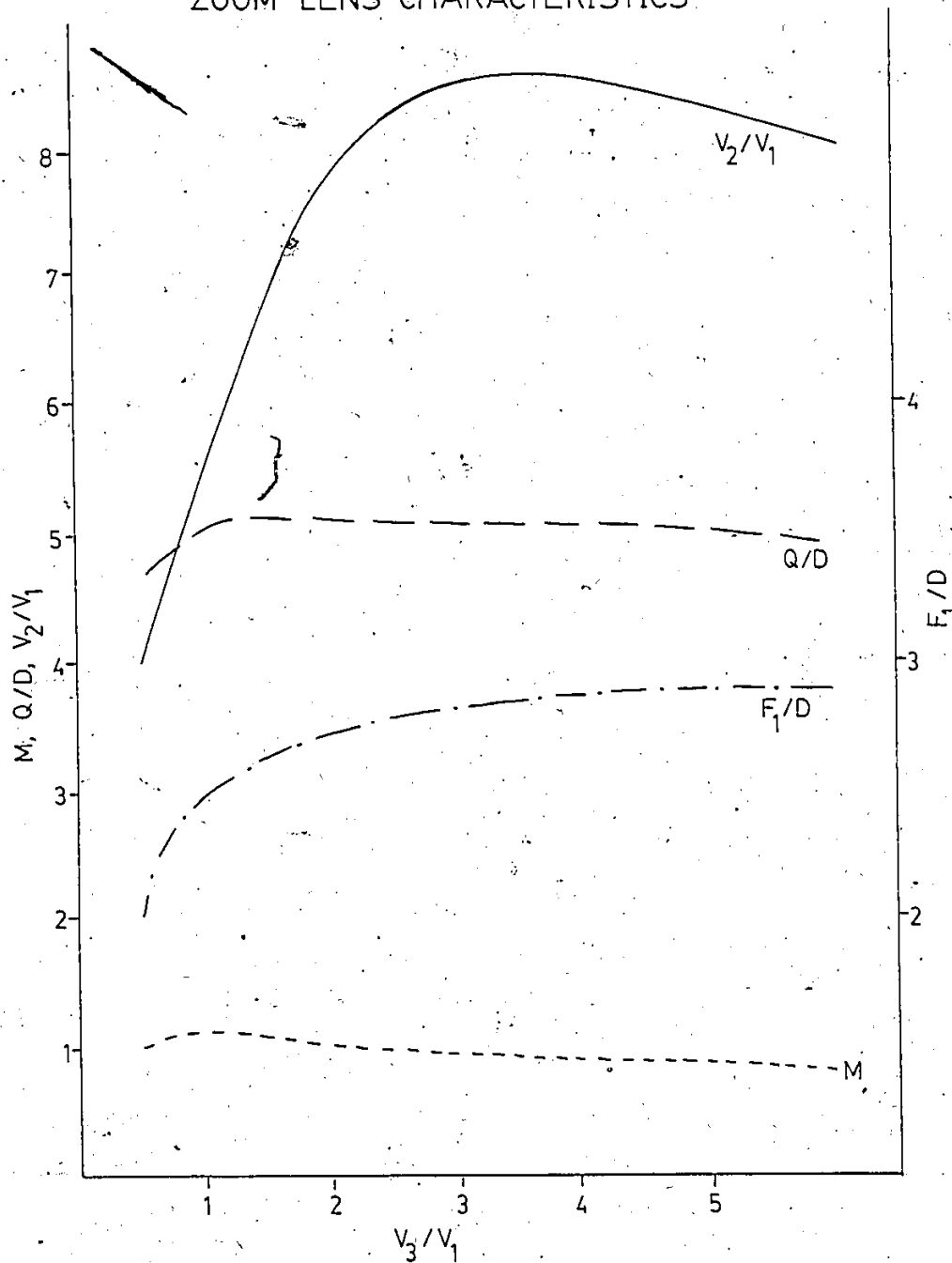
M: Linear Magnification
D: Lens Diameter
V_1, V_2, V_3: Potentials Applied to L3C, L4B, Target

LENS STACK 4 PARAMETERS

	L7A	L7B	L7C	
Applied Voltage	2	31.6	20	

-A7
-A8

D7

From Hemispheres ———— Channeltron

Aperture Diam.(mm): 6   .4 .4 .4 .5   5   .5

Distances (mm):
11.5 — 14.3
P — Q
9.5 — .2 .2 — 6.3 — 4.4
1.6
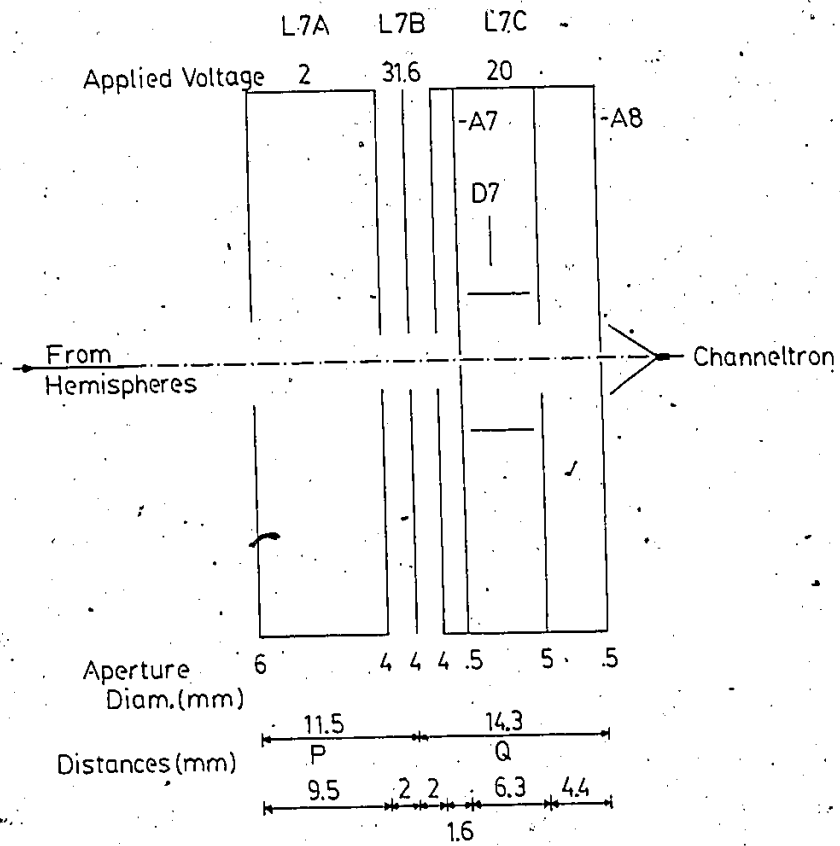
FIG 2.12

this point one is more concerned about getting as much cur-
rent to the channeltron as possible without overfilling the
lens and accepting only those electrons from the hemispheres
which have been properly energy selected than anything else.
Thus one still requires defining apertures to limit the beam
radius.

The Correcting Hoops

The correcting hoops are used to adjust the field in the
gaps between the hemispheres so that it has the correct 1/r
dependence throughout. Figure 2.13(a) shows the details of
the correcting hoops, and Figure 2.13(b) shows how they
modify the field in the gaps. The potentials indicated on
Fig. 2.13(b) have been calculated for an analysis energy of
1.0 eV, by numerically solving Laplace's equation in the
gaps with the shapes and potentials of the hoops as adjusta-
ble parameters.

The problem of field correction at the hemisphere gaps is
an important one, and must be dealt with if the energy
selector is to function properly. This is especially so in
the present design, since the spacing between the hemi-
spheres has been made rather large to minimize the effects
of surface irregularities on the hemispheres(which would
cause field distortion). The fringe field in the gap also
becomes more of a problem, however, as the spacing
increases. The use of 4 correcting hoops gives some freedom
to obtain satisfactory field adjustment within the mechani-
cal constraints of the hemispheres, and, since the potential
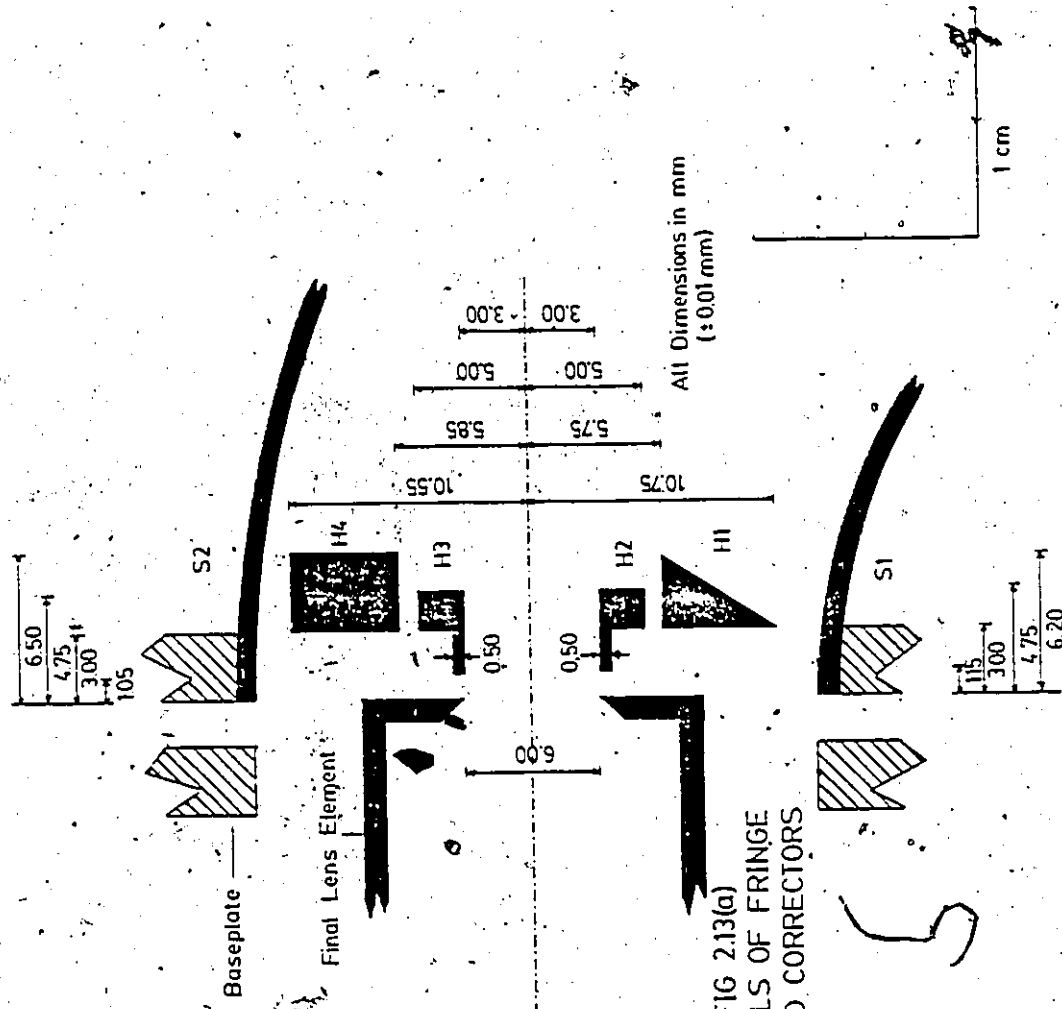
FIG 2.13(a)
DETAILS OF FRINGE
FIELD CORRECTORS

All Dimensions in mm
(±0.01 mm)

1 cm

S2
H4
H3
H2
H1
S1

Baseplate

Final Lens Element

3.00
3.00
5.00
5.00
5.85
5.75
10.55
10.75

6.50
4.75
3.00
1.05

1.15
3.00
4.75
6.20

0.50
0.50

6.00

0.7603

1 mm

0.8737

0.800

0.850

0.900

0.950

0.992

1.008

1.050

1.100

1.1395

1.150

1.200

1.281
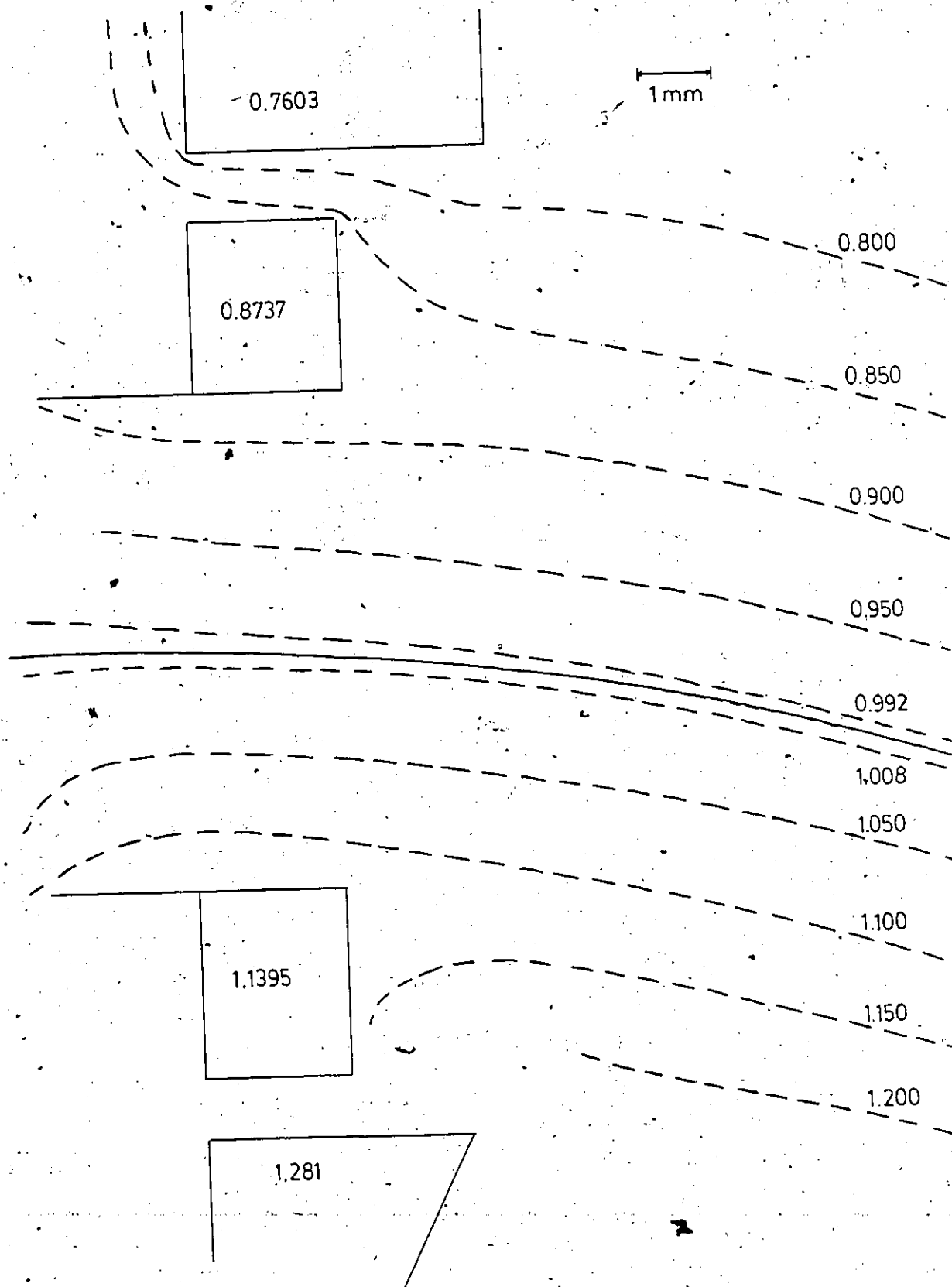
FIG 2.13(b)

on each hoop can be varied independently, minor adjustments
can be made to correct for various misalignments and devia-
tions from the calculated operating conditions if necessary.

2-3.4 The Hemispherical Energy Selector

Since the 180 degree energy selector is at the heart of
the spectrometer it is important to have some understanding
of its principle of operation. Figure 2.14 shows a sche-
matic diagram of the energy selector. Hemispheres S_1 and S_2
are kept at potentials V_1 and V_2, respectively. In the pre-
sent spectrometer $R_2 = 2R_1$ and R_0, the radius of the 'equi-
librium' orbit, is given by:

$$R_0 = (R_1 + R_2)/2 = 3R_1/2$$

In the following discussion we shall ignore the effects of
the field in the gaps at the entrance and exit planes, as
this is assumed to be corrected by the hoops.

The potential between the hemispheres is found by solv-
ing:

$$\nabla^2 \phi = 0$$

with the boundary conditions:

$$\phi(r=R_1) = V_1$$

$$\phi(r=R_2) = V_2$$

$$V_2 < V_1$$

Because of the spherical symmetry involved, the potential is
a function of r only, and is given by:

H4

H3

H2

H1

Ruby Ball
(1 of 3)

R_2

S_2

R_0

R_1

S_1

Baseplate

Clamping
Screw
(1 of 3)
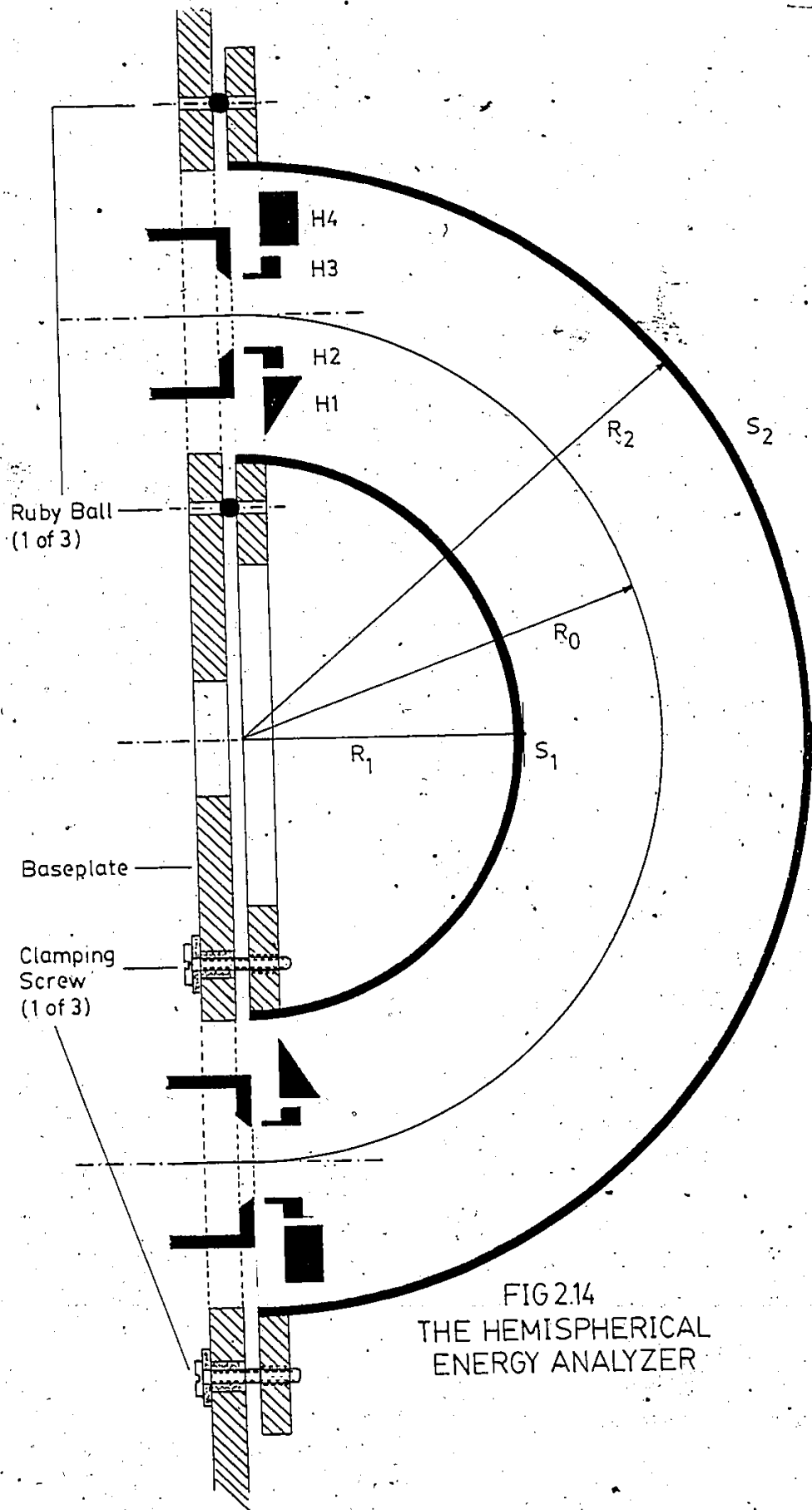
FIG 2.14
THE HEMISPHERICAL
ENERGY ANALYZER

$$\Phi(r) = \frac{(V_2 - V_1)}{r} \frac{R_1 R_2}{(R_2 - R_1)} + \frac{R_2 V_2 - R_1 V_1}{R_2 - R_1} \qquad (2.3.4.1)$$

The electric field is then given by:

$$\vec{E}(\hat{r}) = -\frac{d\Phi}{dr}\hat{r} = -\frac{(V_2 - V_1)}{r^2} \frac{R_1 R_2}{(R_2 - R_1)} \hat{r} \qquad (2.3.4.2)$$

If the incoming beam has an energy E_0 and enters at a radius R_0, then for a circular orbit, equating the electrostatic force on the electrons to the centripetal force yields the transmitted energy:

$$E_0 = -\frac{(V_2 - V_1)}{2R_0} \frac{R_1 R_2}{(R_2 - R_1)} \qquad (2.3.4.3)$$

Expressing R_1 and R_2 in terms of R_0, equation 2.3.4.3 becomes:

$$E_0 = -2(V_2 - V_1)/3$$

Thus, to transmit an energy of 2.0 eV, for example, requires a potential difference of 3 volts between the hemispheres. It is advisable to choose V_1 and V_2 close to the analysis energy to minimize the distortion of the field in the gaps, and so putting $V_1 = 4$ volts and $V_2 = 1$ volt will satisfy this condition.

Another property of the hemispherical energy selector is

that it will focus the entrance plane onto an exit plane
which is 180 degrees 'away' (hence the name). To see this,
one writes down the Lagrangian of the system and solves the
equations of motion in the limit of small deviations from
the equilibrium orbit. The results are equations of the
form:

$$\frac{d^2(\Delta X)}{dt^2} + \omega_0^2(\Delta X) \simeq 0$$

where

$$\omega_0 = (2eE_0/mR_0^2)^{1/2}$$

is the angular frequency of the electrons inside the hemis-
pherical region. Thus, when $\omega_0 t = \pi$ rads, the electrons
will have travelled through 180 degrees, and will be
focussed on a plane at this point.

2.3.5 Operation and Performance of the Spectrometer

Operating the spectrometer can be defined as transporting
the electron beam from the cathode, through the selector,
and into the target region. If scattered electrons are to
be detected, then they must be transported from the target
region, through the analyzer, and into the channeltron. All
of this must be done in such a way as to achieve the optimum
current and energy resolution for a given set of operating
potentials, both at the target and at the channeltron.

The spectrometer can be 'tuned up' by monitoring the cur-
rent on the apertures A1-A6. This can best be illustrated
by way of an example. First, the potential on L2C is set to
the desired analysis energy by adjusting the SCALE poten-

FIG 2.15
Ne METASTABLE SPECTRUM

Signal (× 10⁴)

Incident Electron Energy (eV)
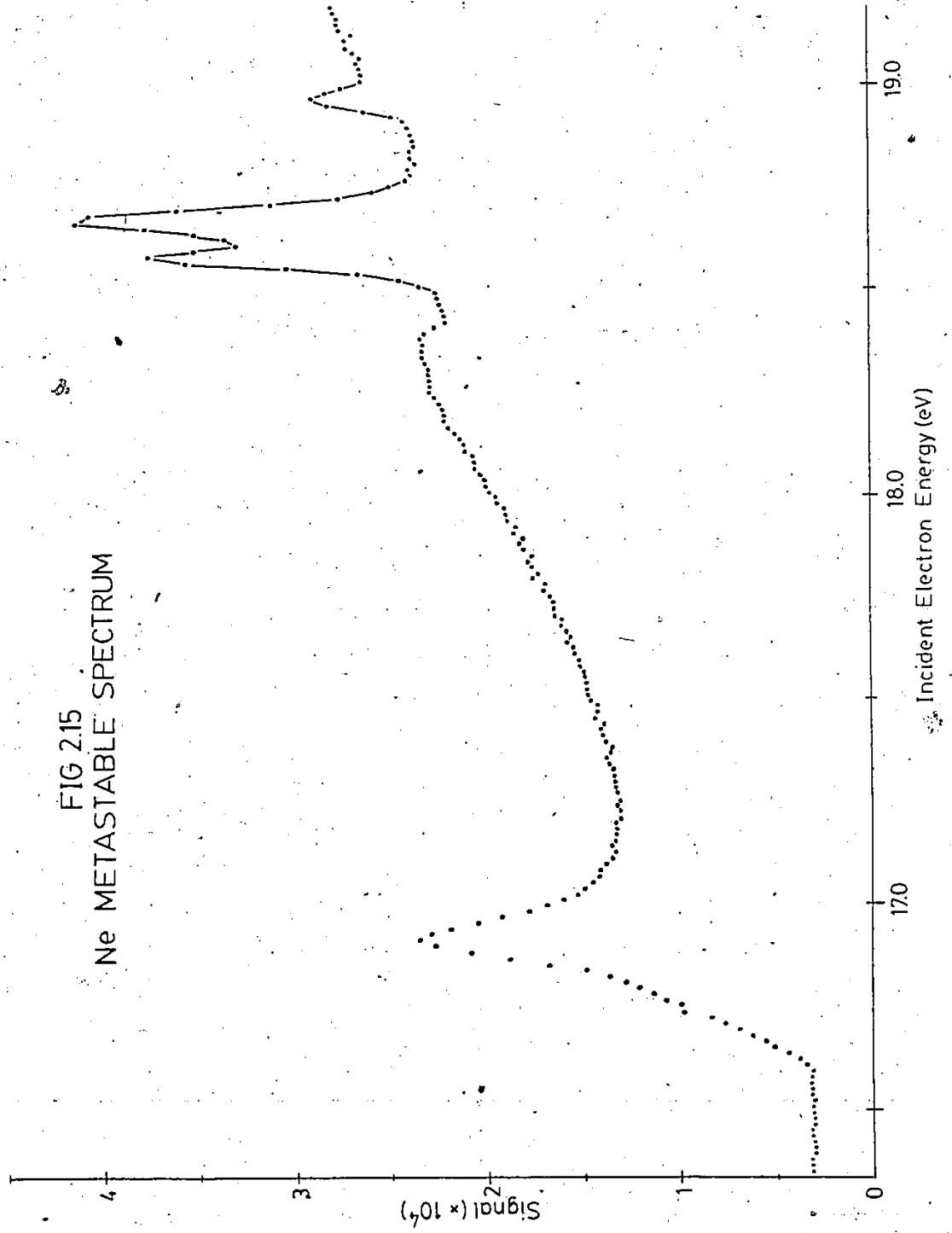
Table 2.3
Spectrometer Operating Conditions

Target Gas: Neon — Metastable Excitation Spectrum		
Parameter	Theoretical Value	Actual Value
Fil		4.554
C.P.		+0.243
Grid		1.29
Anode	90.0	66.49
D1X		+24.27
D1Y		+11.58
L1B	210.0	158.6
L1C	15.00	15.87
D2X		+10.37
D2Y		-1.865
L2B	23.25	38.44
L2C	2.500	2.500
S1	5.000	5.000
S2	1.250	1.250
H1	3.202	3.202
H2	2.849	2.849
H3	2.184	2.184
H4	1.901	1.901
L3B	32.85	18.49
D3X		+2.838
D3Y		+21.50
D4X		-23.19
D4Y		-4.841
H3C	25.00	24.31
L4B	82.5	124.0
Resolution	12.5meV	20.meV
Peak Rate		35.kHz

tiometer. This determines the resolution of the final beam. The rest of the lens elements are then set at or near the calculated operating potentials. These potentials scale linearly with the analysis energy; i.e., if the analysis energy is changed from 2 volts to 4 volts, say, then the potentials of the rest of the lens elements must be doubled from the calculated values (at 2 eV analysis energy). The filament is turned on and enough current is sent through it to give a reasonable amount of emission (10 uA, for instance). One then adjusts the deflectors and lens elements to maximize the current on A1 and then A2. The potential on S1 is temporarily set to 0 to allow all the electrons entering the hemispheres to be collected on S2. The CONTACT POTENTIAL is adjusted to maximize the current on S2, as are the deflectors and lens elements. After this is done, S1 is reset to the correct potential, and the current on A3 is then maximized. The current reaching A4 is maximized, and then one attempts to look for signal coming from the interaction region. Suppose that one desires to look for metastable atoms in Neon, for example. With a suitable Ne gas pressure, the electron beam is focussed into the target region at an energy where a known peak in the metastable spectrum exists. Once a real signal is found, one then attempts to maximize the signal to noise ratio as well as acheiving the optimum energy resolution of the spectrometer. This can be done by making small adjustments to the lens element potentials and the deflector potentials until a satisfactory compromise between resolution and signal-to-

noise is found. A typical metastable excitation spectrum in Ne(see Chapter 3 for one in Ar) is s~~hown~~ in Fig. 2.15, and Table 2.3 shows the operating characteristics of the spectrometer associated with this spectrum.

The spectrometer is also capable of energy analyzing scattered electrons. This is done by determining the amount of energy lost by electrons in collisions with target atoms. The energy loss power supply is used to add energy to the scattered electrons before enetering the analyzer by floating the analyzer ground above the selector ground. The analyzer is tuned to accept only those electrons which have the correct energy, namely the energy set by the target potential. Electrons which have lost energy in collisions will reach the detector only if the amount of energy lost is equal to the potential difference between the analyzer and selector grounds. This energy loss can be varied by a ramp voltage from a multichannel analyzer, for instance, and an energy loss spectrum is obtained in this way. As with the selector, the analyzer half must be adjusted to maximize the signal-to-noise ratio, as well as acheiving an optimum resolution. Energy loss spectra in N_2 and H_2 are shown in Chapter 4. These are by no means high resolution spectra; the estimated overall resolution is 100 meV. The spectrometer is certainly capable of much better resolutions; overall resolutions of about 30 meV were obtained routinely in initial testing of the device.

2.4 APPENDIX

This appendix contains additional construction details of
the spectrometer in the form of scale diagrams. They are
not necessary to the understanding of the device, and thus
were not included earlier. It was felt, however, that it
would be useful to include them for future reference pur-
poses.
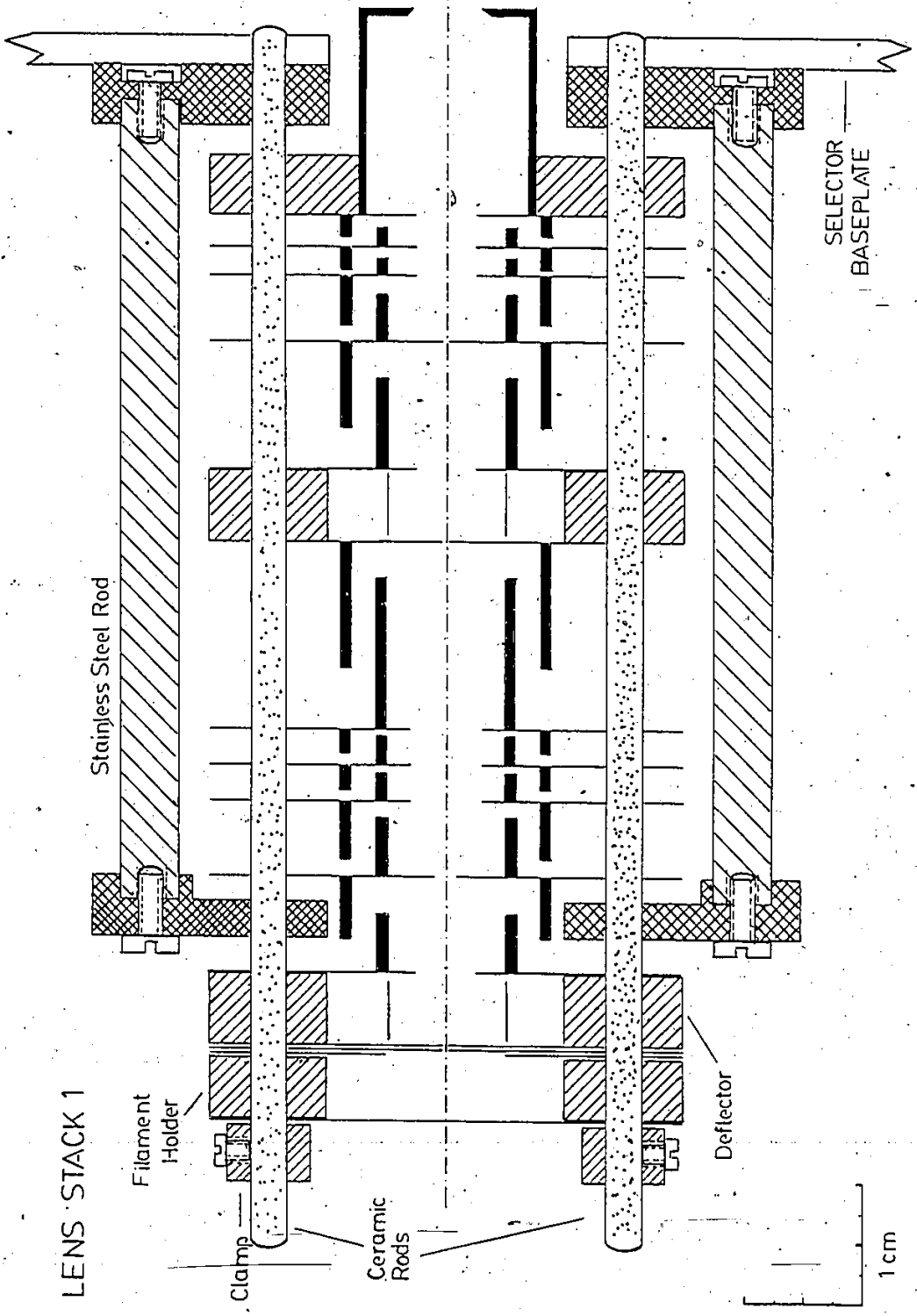
LENS STACK 1

Filament Holder

Stainless Steel Rod

Clamp

Ceramic Rods

Deflector

SELECTOR BASEPLATE

1 cm

Ceramic Rods

BASEPLATE

Stainless Steel Rod

Molybdenum
Shielding Ring

LENS STACKS
2 & 3

1 cm

LENS STACK 4

Ceramic Rods

ANALYZER
BASERLATE

Stainless Steel Rod

Channeltron
Mounting Assembly

Cone

+HV

Macor

1cm

(b) TYPICAL LENS ELEMENT

Aperture

Ceramic Rod Clearance Hole

Mo Shielding Rings

0.075mm Mo Sheet

1cm
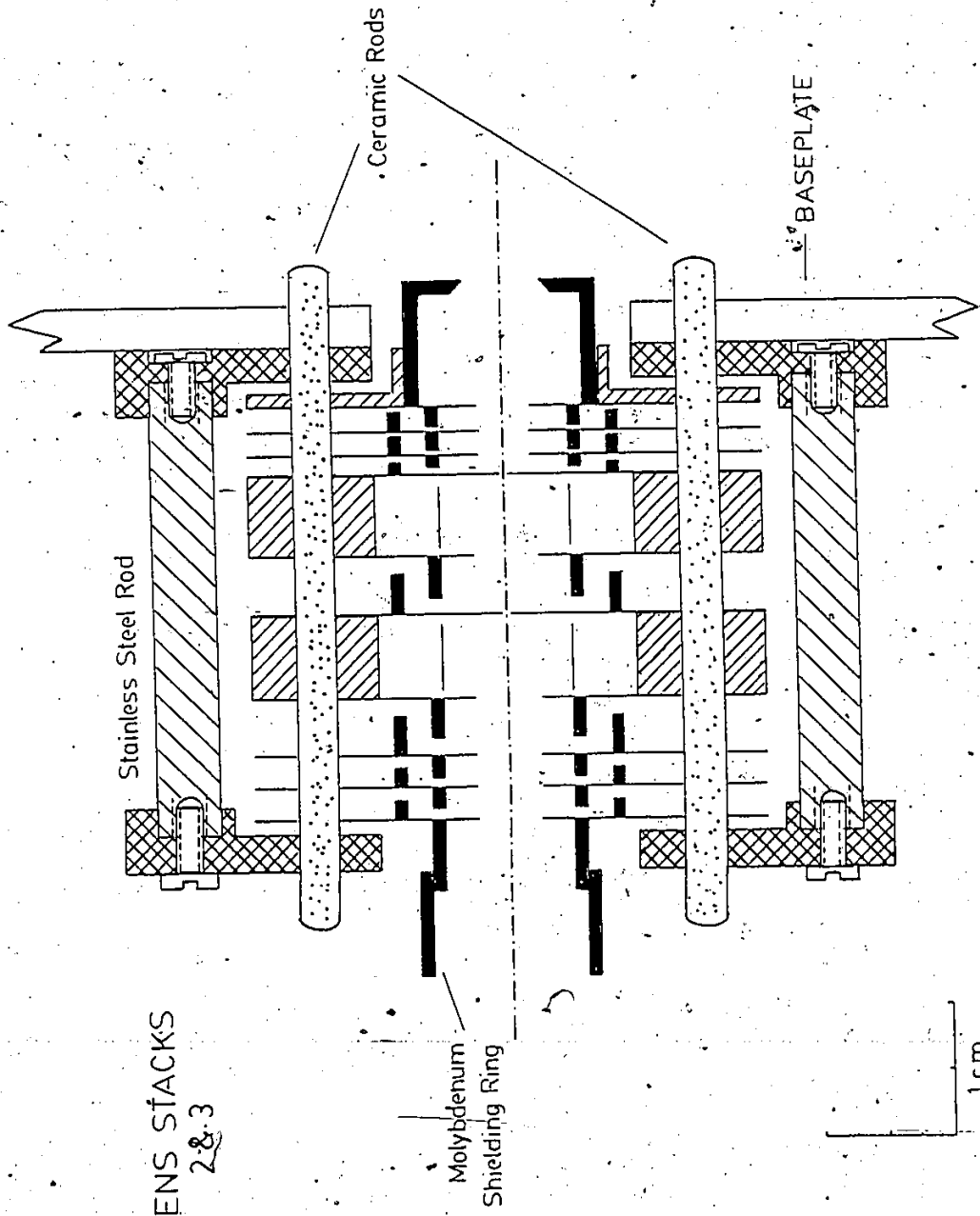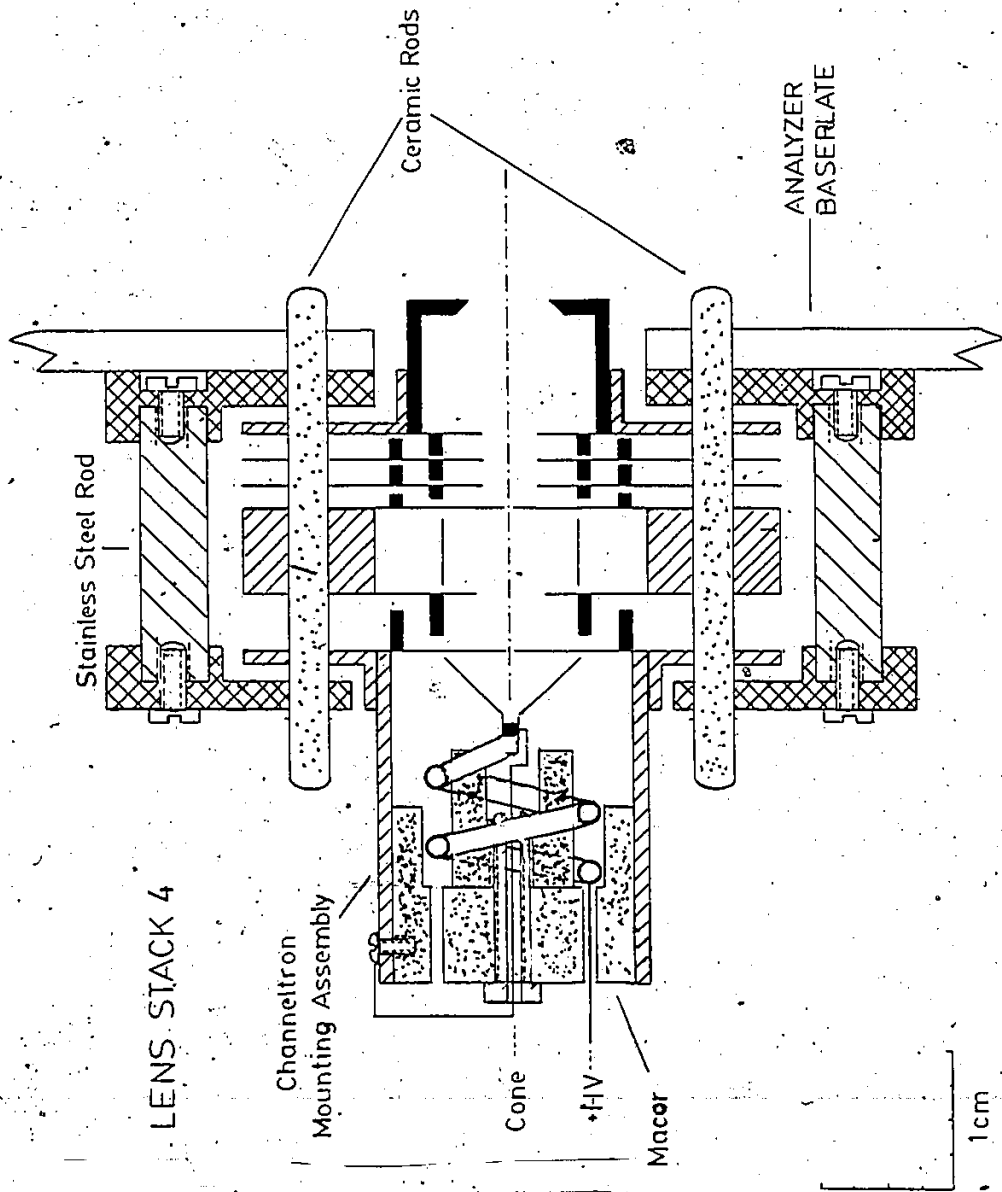
(a) LENS STACK ENDS
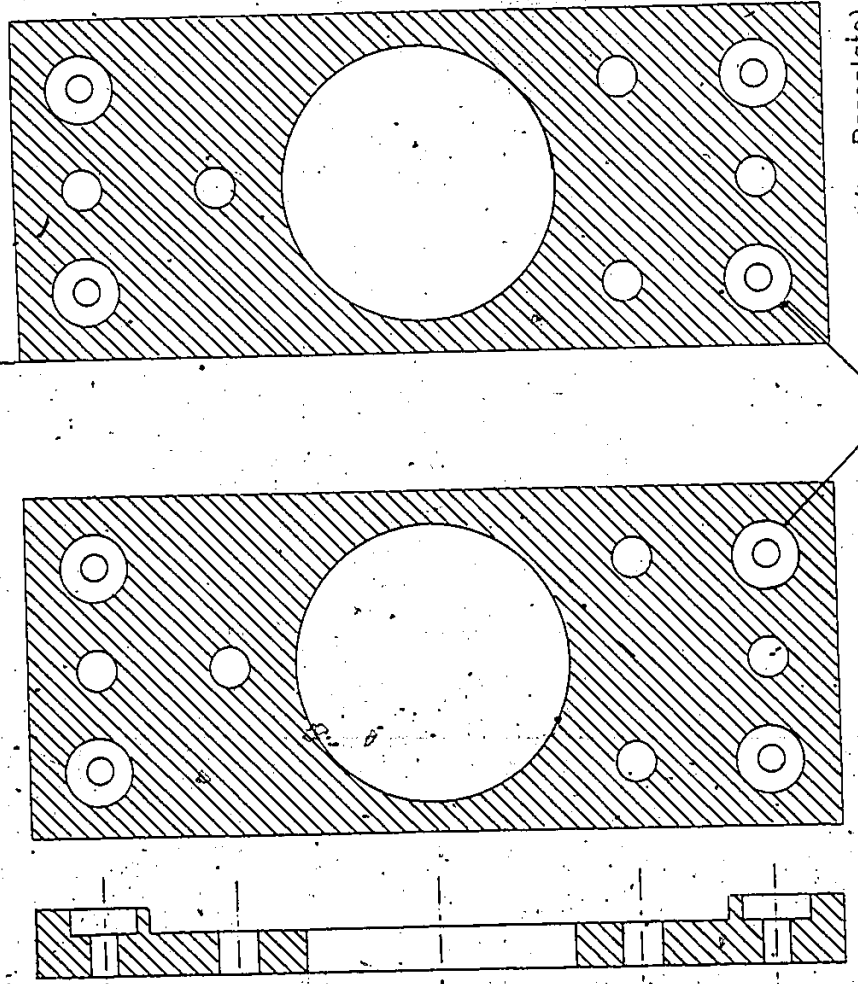
Top

Bottom (on Baseplate)

Holes for Stainless Steel Rods
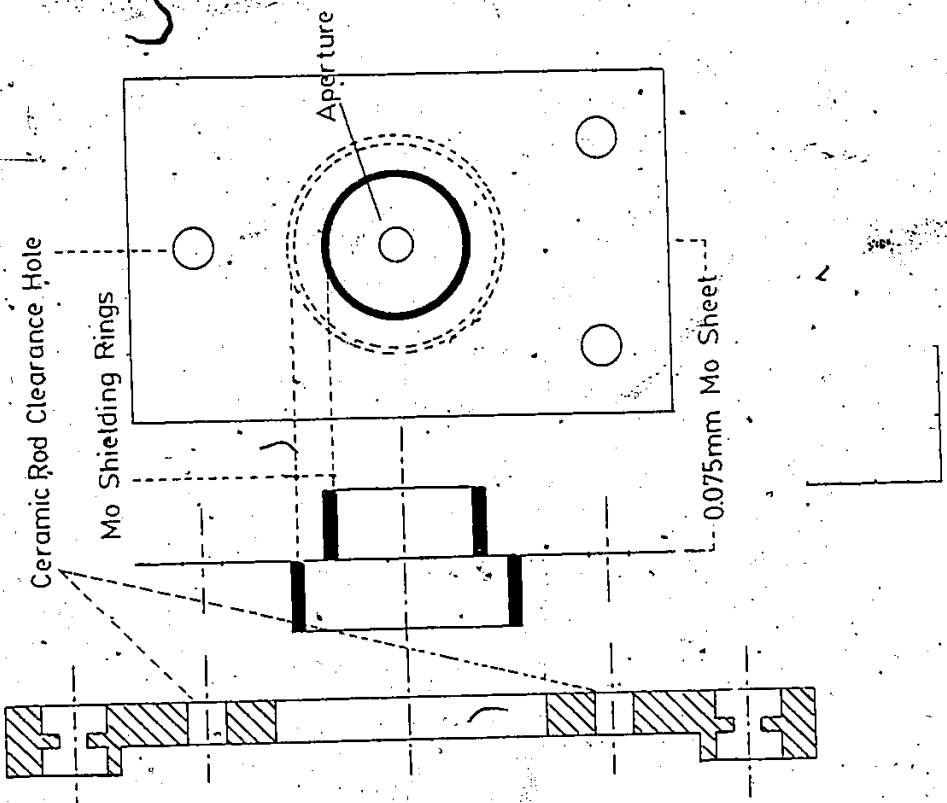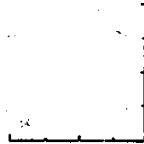
Stainless Steel

Macor

Ceramic Rod
Clearance Hole

1cm

Y1

X1

X2

Y2

Mo Plates

(a) DEFLECTOR SYSTEM

Cu Fil Supports

W Fil

Mo Plates

(b) FILAMENT HOLDER

Mounting Holes

Lens Stack Mounting Hole

Ceramic Rod Clearance Hole

Field Corrector Mounting Hole (on hoops)

Ruby Ball

Clamping Screw

BASEPLATE ASSEMBLY

Section A–A'

S2 H4 H3 H2 H1 S1

Baseplate

Macor
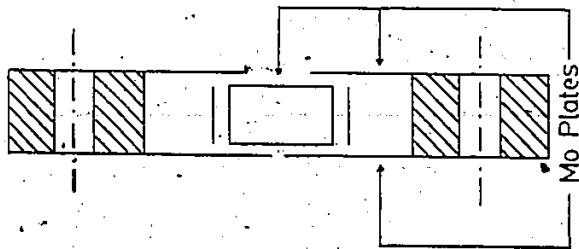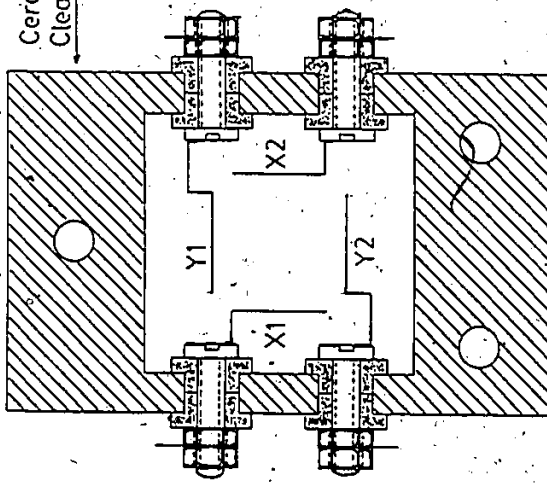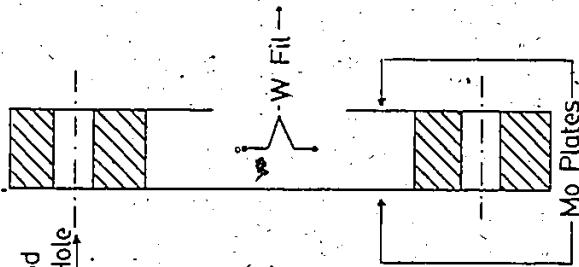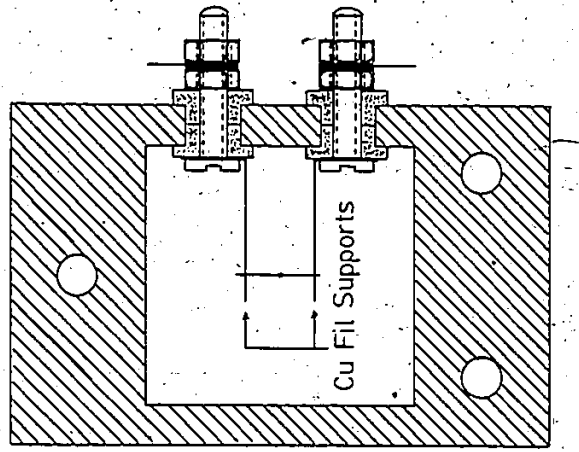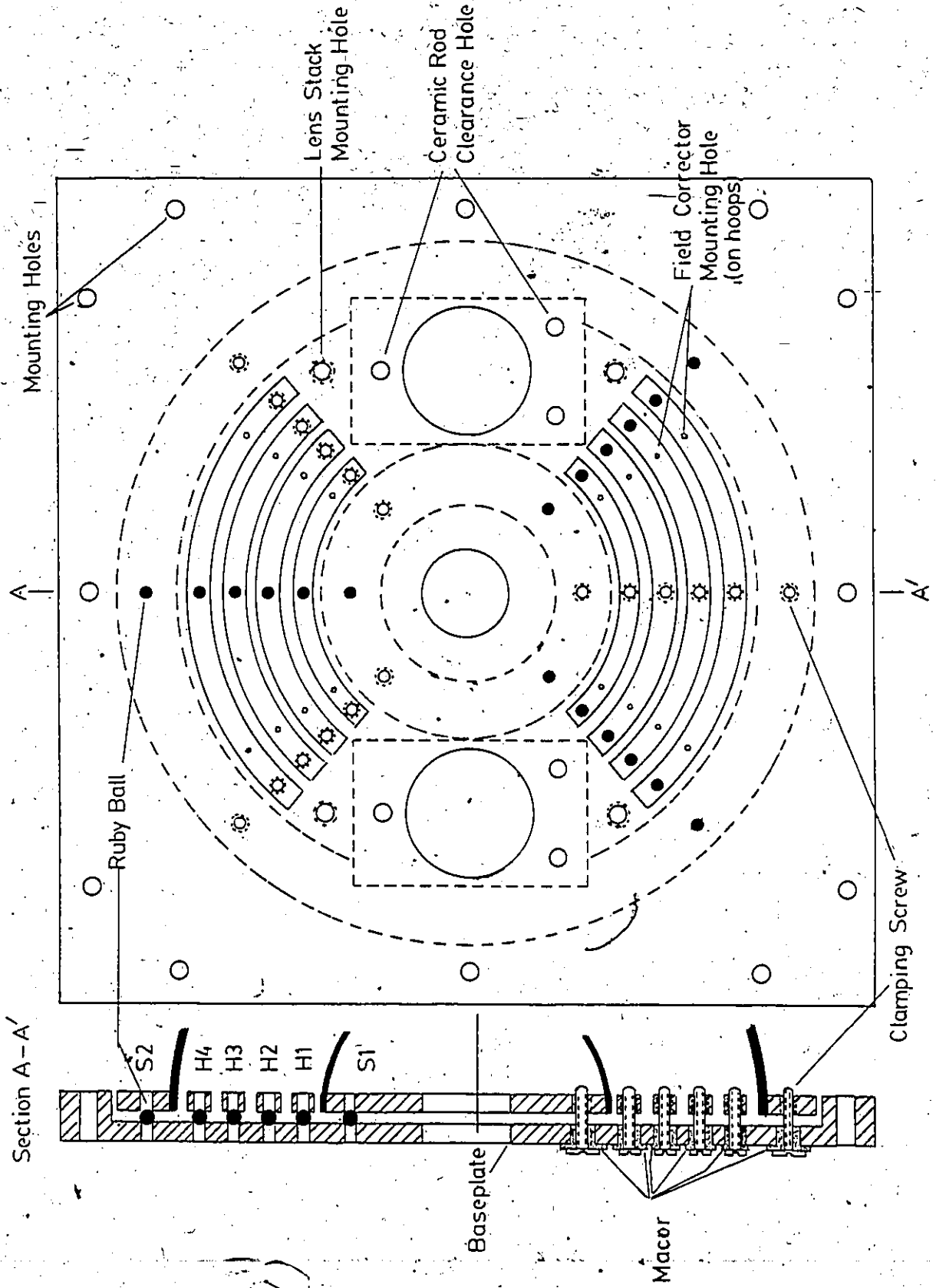
CHAPTER 3
NEGATIVE ION RESONANCES IN THE RARE GASES

3.1 INTRODUCTION

This chapter discusses the production of resonance struc-
tures in the metastable excitation spectra of the rare gases
and the analysis and interpretation of these structures.
The energy region of interest in the present work lies in
the doubly excited state region (above the first ionization
threshold). The region below the first ionization threshold
has been extensively studied, and in the metastable channel
the definitive work is that of Brunt et al[5] who were able to
resolve a wealth of structure with the aid of a high resolu-
tion electron spectrometer. The doubly excited state region
has also been the subject of intensive study using a variety
of techniques and observation channels. In Ne, for example,
measurements have been made on ion production[6], differential
electron scattering[7], electron transmission[8], trapped elec-
tron production[9,10], broadband photon production[11] and meta-
stable production[12]. In recent years many of these authors
have applied their methods to the other rare gases as well.
In many cases a large number of structures have been
observed and accurate identification has proved difficult,
particularly since the energy ranges covering the inner
shell and doubly excited states exhibit much overlap. Two
factors have emerged, however, which lead to a simplifica-
tion of the situation. First, it appears that in certain
observation channels the features are predominantly due to
negative ion resonance formation rather than neutral auto-
ionizing states, for example. Second, it has been found
possible to unambiguously identify the resonances involved

in Ne[10].

A comparison between the lower energy (i.e. below the first I.P.) data of Sanche and Schulz[8] and Brunt et al[5] reveals that essentially every feature in the former data can be identified with a negative ion resonance. In the higher energy region, a comparison can also be made in Ne with the data of Spence[10] and again it is found that negative ion resonances dominate Sanche and Schulz's data. It is reasonable to suppose that this conclusion is valid for the other rare gases as well. In addition, it would appear that the differential inelastic scattering data[7,13-15] are also dominated by negative ion resonances and show an almost one-to-one correspondence with the data of Sanche and Schulz. In the light of all this, Spence's conclusion[10], based on an analysis of possible resonance decay modes, that low-n excitation functions should demonstrate structures preferentially due to negative ion resonances, would seem to be justified. High-n excitation functions, on the other hand, are more likely to display auto-ionization features since these states are more closely coupled to this channel via post-collision-interaction (PCI) effects[16].

Based on these ideas it was felt that a good channel to search for negative ion resonances in the rare gases in the doubly excited state region would be the metastable excitation channel. This possesses certain advantages and simplifications from an experimental point of view, and has been demonstrated to be very rich in resonance structures at

lower energies[5]. Previous studies in this channel have been limited to some low resolution work in Ne[12] and a much more extensive study in Ar[17].

The present work presents high resolution data for Ne, Ar and Kr, and a discussion of the analysis and identification of the observed structures is also undertaken. Two reports have already been presented previously[18,19].

The rest of this chapter is divided into four sections. Section 3.2 provides a theoretical framework for the understanding of resonance formation and the analysis of the resonance data. Section 3.3 describes the experimental details involved: the interaction region, energy calibration, and data collection. Section 3.4 presents the data and results of the analysis, and section 3.5 presents conclusions drawn and suggestions for further research.

3.2 THEORETICAL BACKGROUND

3.2.1 Resonance Formation

For reasons of simplicity this discussion of resonance formation will be limited to the metastable excitation channel only. Clearly the metastable channel is not the only one available in which to study resonances, but, as mentioned in the introduction, it is certainly rich in these structures.

Basically a negative ion resonance forms when an electron interacts with a target atom in such a way as to be captured by it for a short time, creating a temporary negative ion. The ion eventually decays, leaving the atom in some final state (not necessarily the same as the initial state) and releasing the captured electron. This phenomenon generally results in a rather pronounced change in the cross-section being measured, and is characterized by the _shape_ and also the _width_ of the feature, as well as the energy at which it occurs. The width of the feature is characteristic of the _lifetime_ of the resonant state. The process involved in forming the resonance can either be _elastic_ (no excitation of the atom) or _inelastic_ (the atom undegoes excitation before the resonance is formed). The latter is the case in the present situation, where the process of interest is:

$$e^- + X[ns^2np^6(^1S_0)]$$
$$\downarrow$$
$$X^-([nsnp^6](^2S)\,ml\,ml')$$
$$\downarrow$$
$$X([ns^2np^5](^2P)(n+1)s(^{2S+1}P_{2,0})) + e^-$$

(3.2.1a)

and/or:

$$e^- + X[ns^2np^6(^1S_0)]$$
$$\downarrow$$
$$X^-(ns^2np^4(^3P,^1D,^1S)\,mlml'ml'') \qquad (3.2.1b)$$
$$\downarrow$$
$$X([ns^2np^5](^2P)(n+1)s(^{2S+1}P_{?,0})) + e^-'$$
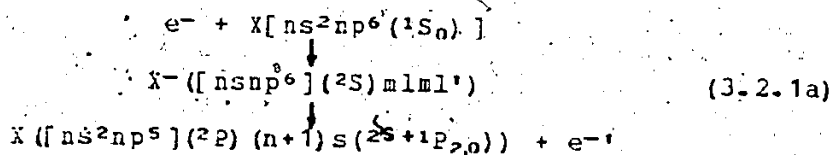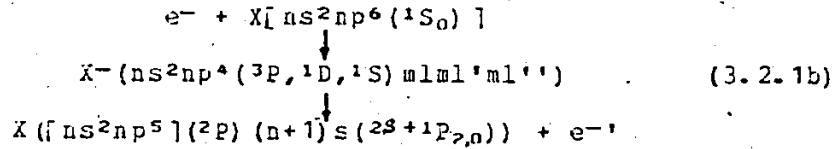
where $X[ns^2np^6](^1S_0)$ denotes a rare gas atom in its ground state and $X[ns^2np^5](^2P_{3/2,1/2})(n+1)s$ is the metastable state which is finally detected. Note that equation 3.2.1a denotes inner shell excitation and that equation 3.2.1b denotes two electron excitation. Direct production of the metastable state is also possible and this will form a continuous background upon which resonance structures are superimposed. In addition to this, there is also the possibility of Rydberg metastable species contributing to the observed signal and producing structures which might erroneously be attributed to negative ion resonances. This results in at least six channels which can contribute to the observed metastable signal, not to mention additional channels(eg. auto-ionization) which may also be present. The overlapping of these channels leads to interference effects in the metastable cross-section, making identification and classification of features difficult and often ambiguous. This state of affairs is clearly reflected in the present state of the literature, as any survey of the problem will show.

To understand how resonance formation affects the behaviour of the metastable cross-section generally requires the use of multi-channel scattering theory. The large number of

available channels makes this a formidable problem to solve, but it is possible to greatly simplify the situation in some cases.

Consider the case of one resonance channel well separated from all other channels. This reduces the problem to essentially a single channel one, which is dealt with in most texts dealing with scattering theory (see, for example, Taylor[20], for a complete discussion).

By using a partial wave analysis, the scattering cross-section can be written as:

$$\sigma = \sum_{\ell} 4\pi (2\ell+1) \left| f_{\ell}(p) \right|^2 \qquad (3.2.2)$$

where

$$f_{\ell}(p) = \frac{e^{i\delta_{\ell}(p)} \sin\delta_{\ell}(p)}{p}$$

is the _scattering amplitude_ and $\delta_{\ell}(p)$ is the _scattering phase shift_ for the l-th partial wave. Now a resonance usually has a well-defined orbital angular momentum associated with it, and so one partial wave in particular will dominate the scattering process near the resonance. Thus the scattering cross-section is:

$$\sigma_{\ell} = \frac{4\pi}{p^2} (2\ell+1) \sin^2 \delta_{\ell}(p) \qquad (3.2.3)$$

It is the behaviour of the scattering phase shift which det-

ermines the behaviour of the resonance; $\delta_\ell(p)$ is composed of two parts: a resonant part, $\delta_\ell^{res}(p)$, which varies rapidly with p; and a background part, $\delta_\ell^{bg}(p)$, which varies slowly with p. Figure 3.1 illustrates typical resonance profiles for different values of the background phase shift. Near the center of the resonance, the resonant phase shift is:

$$\sin\delta_\ell(p) = \frac{\Gamma/2}{((E-E_R)^2 + (\Gamma/2)^2)^{1/2}} \qquad (3.2.4)$$

where Γ is the width of the resonance and E_R is the resonance energy. Using the fact that the phase shift is composed of two parts, we can write:

$$\sin\delta_\ell(p) = \sin(\delta_\ell^{res}(p) + \delta_\ell^{bg}(p))$$

which is:

$$\sin\delta_\ell(p) = \sin\delta_\ell^{res}(p)\sin\delta_\ell^{bg}(p)(\cot\delta_\ell^{res}(p) + \cot\delta_\ell^{bg}(p))$$

Define:

$$q = \cot\delta_\ell^{bg}(p)$$

$$\varepsilon = \cot\delta_\ell^{res}(p) = 2(E-E_R)/\Gamma$$

Then the scattering cross-section is given by:

$$\sigma = \frac{4\pi}{p^2}(2\ell+1)\frac{(q+\varepsilon)^2}{(1+\varepsilon)^2} \qquad (3.2.5)$$

This is the usual Fano formula for the behaviour of the cross-section near a resonance. If q=0, then the result is the familiar Breit-Wigner formula.
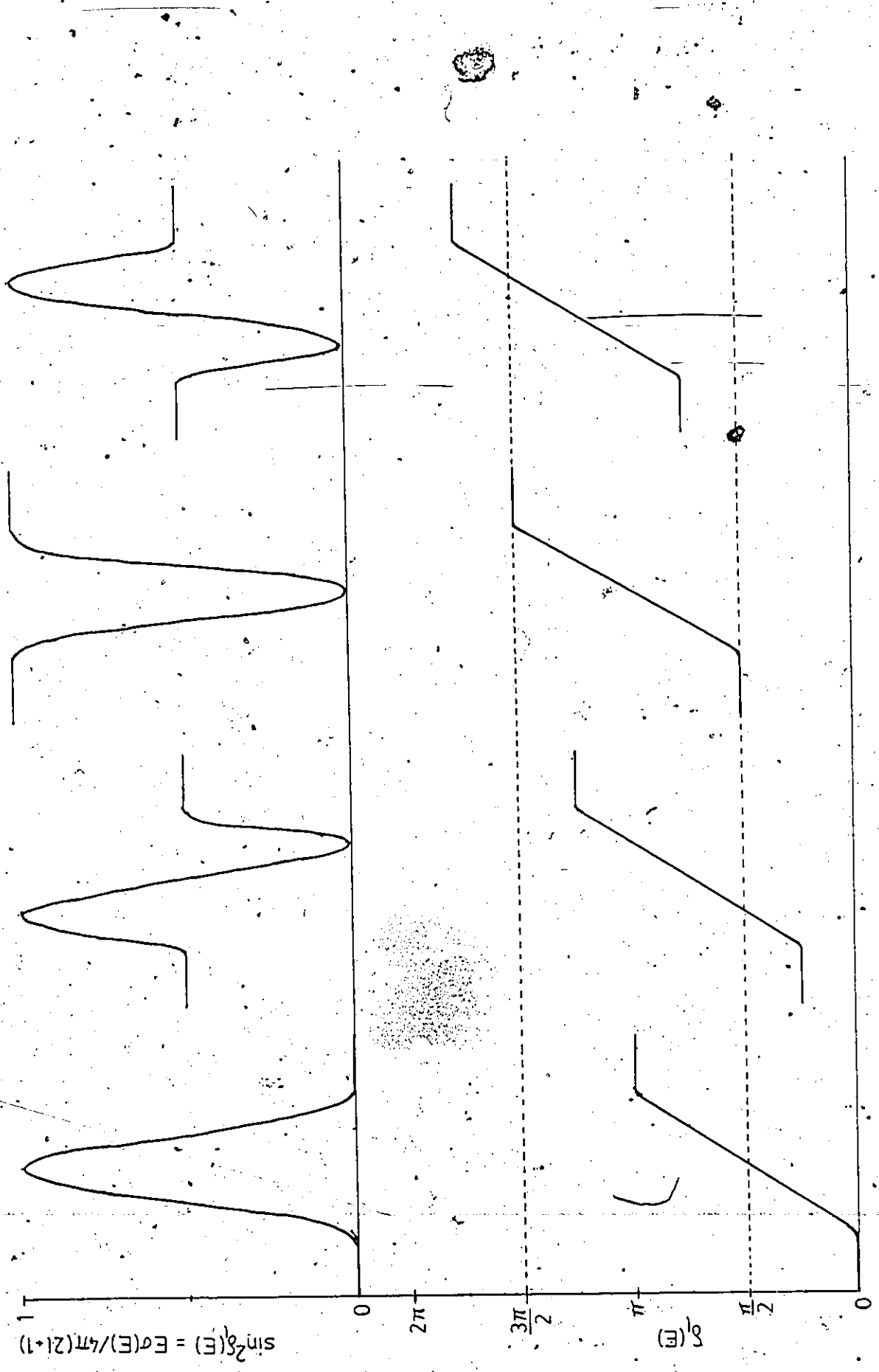
FIG 3.1

Equation 3.2.5 is often parametrized and is then used to fit experimental data to obtain the various parameters. This parametrization is:

$$f(\vec{a};x) = a_1 \frac{(a_2 + \varepsilon)^2}{(1 + \varepsilon)^2} + a_5; \quad \varepsilon = \frac{2(x-a_3)}{a_4} \qquad (3.2.6)$$

where

a_1 = amplitude of the feature

a_2 = shape parameter (due to background)

a_3 = resonance position

a_4 = resonance width

a_5 = amplitude away from resonance

In order to extract the values of these parameters from the experimental data it is first necessary to convolute equation 3.2.6 with the energy profile of the incident electron beam. The apparatus profile is written as a Gaussian distribution:

$$g(x) = \frac{1}{a_6} \frac{\ln 2}{\pi} \exp(-x^2 \ln 2 / a_6^2) \qquad (3.2.7)$$

where a_6 is the FWHM of the profile. A fitting routine which included the apparatus profile was developed and applied to some of the more isolated features in the spectra(*). The results of the fitting procedure are discussed

----

(*) Routine developed by William van Wijngaarden

in section 3.4

3.2.2 Analysis Techniques Used

Once the sharp features in a metastable excitation cross-section have been positioned in energy, the task of deducing the identification of these features begins. As mentioned in the introduction, this is a rather complicated task, but there are some significant observations which simplify matters somewhat.

(1) The metastable channel is dominated by negative ion resonances thereby eliminating much of the complications due to neutral states.

(2) The negative ion resonances have been unambiguously identified in Ne.

(3) There is a systematic behaviour involved for equivalent resonances in the different rare gases. Much of this is due to the fact that the coupling between the excited electrons is the same for equivalent resonances, and that the influence of the core is not the dominant effect. Thus it is possible to establish simple relationships linking the energies of equivalent resonances in the different rare gases to the corresponding binding energies relative to the positive ion cores involved.

Two techniques which make use of the simple relationships are available at the present time. These give some insight into the nature and validity of the proposed relationships,

and are aids in classifying features in the metastable exci-
tation spectra. The first approach is a graphical one due
to Spence[21]. This techique was previously found useful for
classifying negative ion resonances in molecules. The sec-
ond approach, suggested by Heddle[22], and developed exten-
sively by Read[23], who devised a "Modified Rydberg" formula
to predict the energies of resonances in different gases.
These two techniques will be discussed in turn to illustrate
how they can be used in the present situation.

The Graphical Approach

This technique has as its basis the idea that the ener-
gies of equivalent resonances in the heavy rare gases could
be represented by an equation of the form:

$$E = AI + B \qquad (3.2.8)$$

where I is the appropriate ionization potential (of the
core), A is a constant close to unity, and B is another
constant. To gain some insight into the significance of
this it is instructive to apply such an analysis to the data
of Codling and co-workers.[24-27] They measured photo-absorp-
tion cross-sections in the heavy rare gases using a synchro-
tron radiation source and observed a number of reso-
nance (autoionizing) structures in their spectra. Let us
examine the behaviour of the $[nsnp^6](^2S)(n+k)p$ (k=1 to 6)
states in the different rare gases. Figure 3.2(a) shows a
plot of _ionization potential_ vs energy for this series, and
it can be seen that very good straight lines can be drawn
joining equivalent configurations. This illustrates the
behaviour indicated by equation 3.2.8. Now, turning to Fig.

3.2(b), which is a plot of binding energy (of the resonance) vs energy for the same series, once again it can be seen that good straight lines join equivalent resonances(note that the data of Fig. 3.2(b) are equivalent to that of Fig. 3.2(a), but that the vertical scale is much finer, allowing one to see any deviations from a linear relationship). The notable exception to the linear relationship is Ar; the deviation increases as the outer electron gets closer to the core. The other bit of information apparent on Fig. 3.2(b) is the decrease in the slopes of the lines joining equivalent resonances as the value of k increases. The numerical values of the slopes are indicated beside each line on Fig. 3.2(b). The slope is largest for the the $(n+1)$p configuration and practically zero for the $(n+6)$p· configuration. This behaviour has an immediate interpretation, namely, the slope of the line joining equivalent resonances must reflect the amount or interaction the outer electron has with the core, and that this interaction increases as one progresses from Ne to Xe. Thus, the energy of the $(n+m)$p states could be written as:

$$E_{nl} = I_n - \langle nl|V|nl \rangle - \langle nl|V'|core \rangle \qquad (3.2.9)$$

where I_n is the ionization potential appropriate to each gas, $\langle nl|V|nl \rangle$ represents the interaction of the electron with the pure Coulomb field of the ion core, and $\langle nl|V'|core \rangle$ represents the other interactions the electron has with the core. It should be pointed out that equation 3.2.9 is simply another way of expressing the normal Rydberg-Ritz equation. The other interactions are contained in

FIG 3.2(a): I.P. vs Energy: $[nsnp6]^+ (^2S)(n+k)p$

Ionization Potential (eV)

Energy (eV)

Ne⁺

Ar⁺

Kr⁺

Xe⁺

(n+1)p
(n+2)p
(n+3)p
(n+4)p
(n+5)p
(n+6)p

50.0

40.0

30.0

20.0

50.0

40.0

30.0

20.0

$[nsnp^6]^+(^2S)(n+k)p$

$(n+1)p$ 1.391×10^{-2}

$(n+2)p$ 0.691×10^{-2}

$(n+3)p$ 0.304×10^{-2}

$(n+4)p$ 0.143×10^{-2}

$(n+5)p, 0.097 \times 10^{-2}$

$(n+6)p$ 0.060×10^{-2}

Ne$^+$

Ar$^+$

Kr$^+$

Xe$^+$

Binding Energy (eV)

3.0

2.0

1.0

0.0

Energy (eV)

20.0   30.0   40.0   50.0
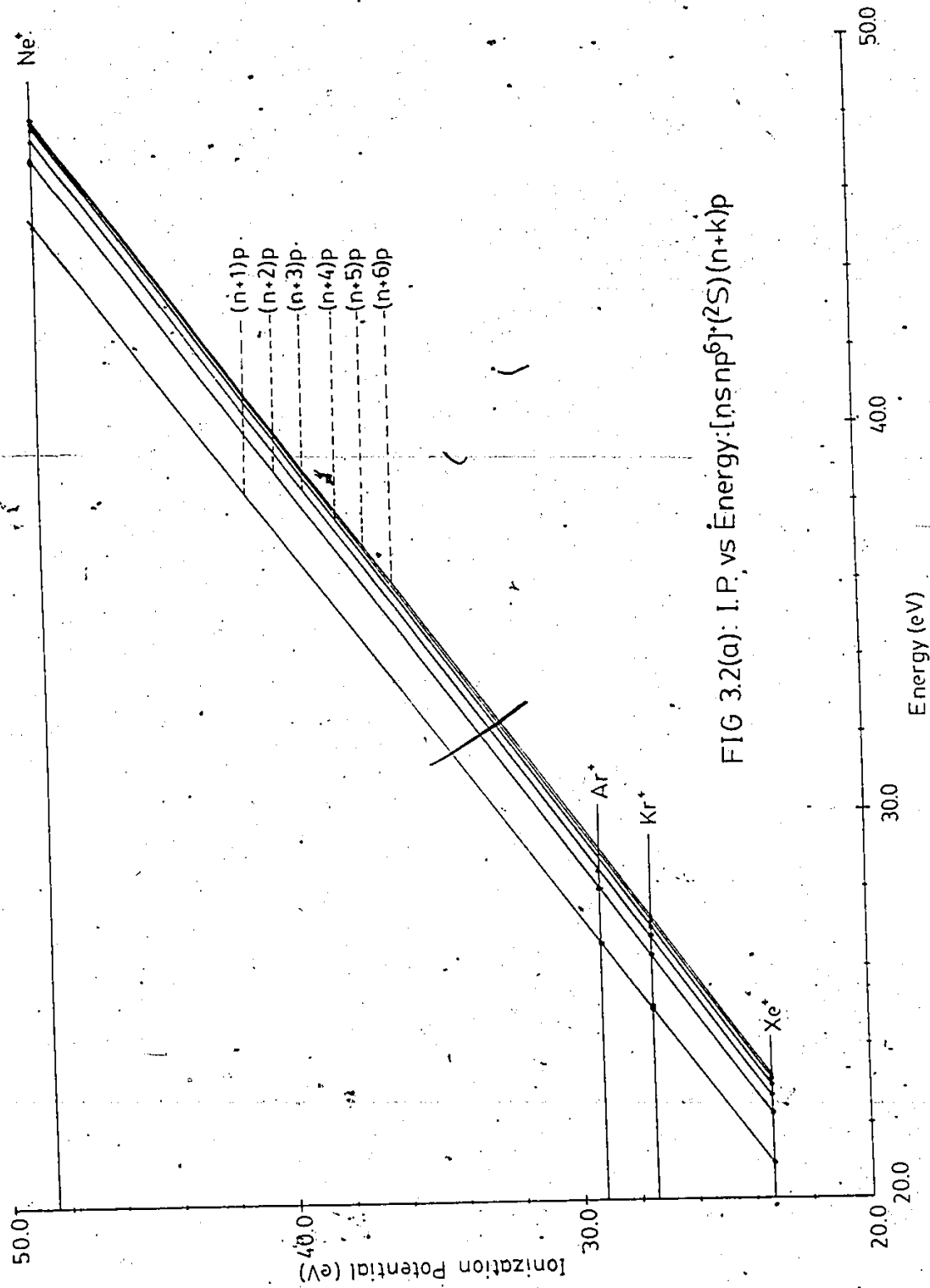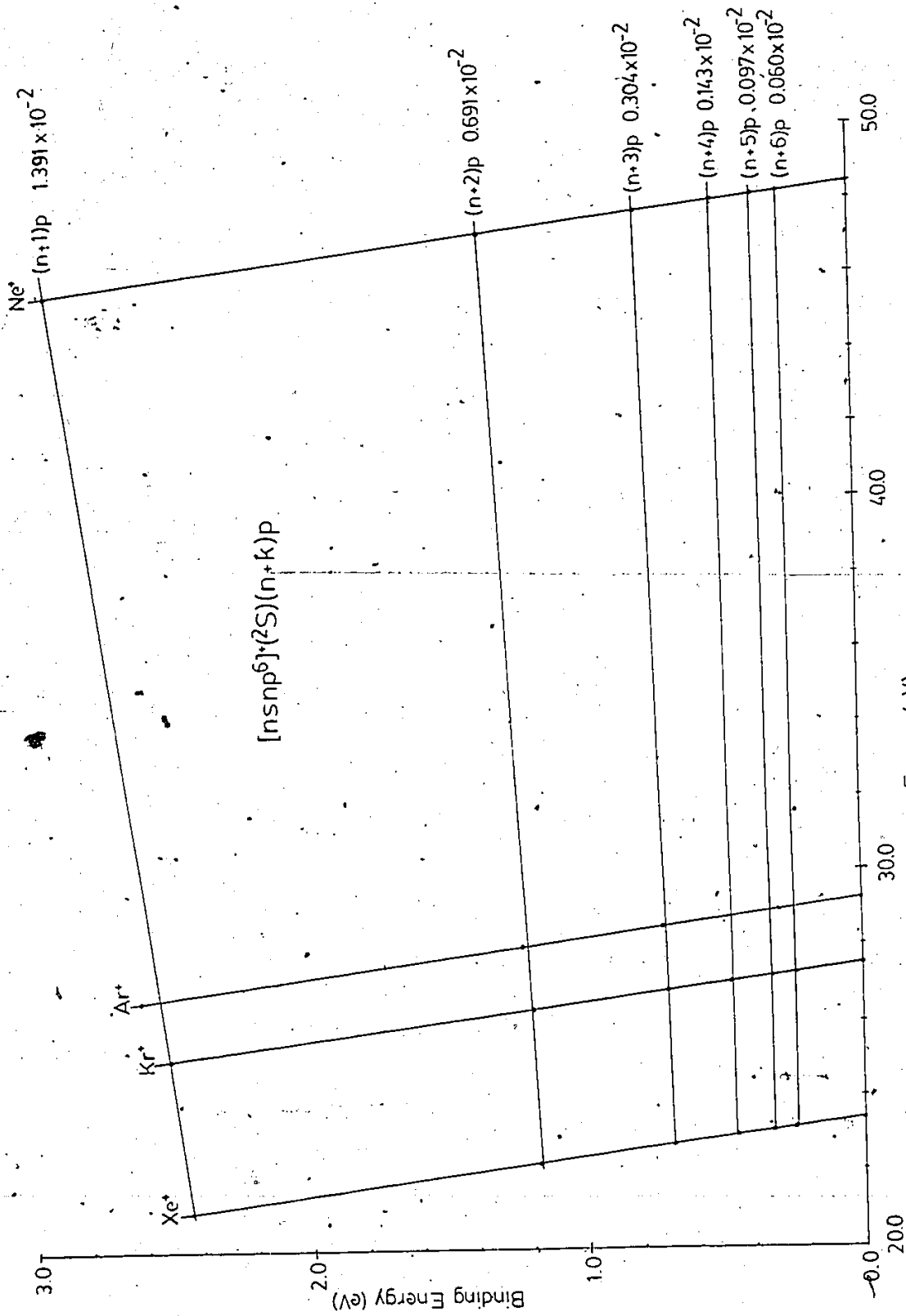
FIG 3.2(b)

the quantum defect of the electron in this case. Equation
3.2.9 also sheds light on the deviation of Ar from this
"rule". The systematic behaviour is "violated" because the
Ar⁺ core has a much greater influence on the outer electron
than the other gases do.

The other interactions between the electron and the core
would be dominated by the penetration of the electron into
the core (the essence of quantum defect theory), but the pec-
uliar behaviour of Ar suggests that an additional term is
present. The nature of this additional term is probably
related to configuration interaction effects, which are
known to be strong in Ar. These effects are normally accom-
panied by a mutual repulsion of the states involved. Thus
the Ar term considered here could acquire a larger binding
energy.

The deviations from the linear relationship are not appa-
rent on Fig. 3.2(a) because the scale is too coarse to high-
light them. It would appear that this technique is good as
a first approximation to determine the energies, and to at
least identify the configuration of the features observed.

Having seen that the "graphical" approach is useful for
the simple case of one excited electron, the next question
to ask is, "How does it work for two excited electrons"?
This has been dealt with by Spence[21], who used the data of
Sanche and Schulz[8] and Brunt et al[5] to demonstrate the use-
fulness of equation 3.2.8. He did not plot binding energy
vs resonance energy for the data used, however, but did

demonstrate the applicability of the graphical approach. Thus it is proposed that a similar equation for the resonance energy can be written down for two electrons as was the case for a single electron, namely:

$$E_{nlnl'} = I_n - <nlnl'|V|nlnl'> - <nlnl'|V'|core> \cdot \qquad (3.2.10)$$

where I_n is again the appropriate ionization potential, $<nlnl'|V|nlnl'>$ represents the interaction of two electrons with the core Coulomb field, and $<nlnl'|V'|core>$ represents the other interactions of the electrons with the core. The normal Coulomb interaction term would presumably also include electron-electron interactions, and the strength of the other term is reflected in the slope of the line joining equivalent resonances.

When one considers the case of three excited electrons outside of a doubly ionized core, there is no data available to make an analysis of this type at the moment. However, having established the significance of the linear relationship and the deviations from it, it would seem to be a reasonable approach to use when attempting to analyze the present data. The success of this approach, then, remains to be seen for this case.

Thus, to analyze the data obtained in the present experiment, the graphical approach will be used as outlined above. It is reasonable to suppose that it will work above the first ionization threshold, as it did for resonances below the threshold. Even if the linear relationship is not strictly valid, the deviations from it are themselves signi-

ficant and can be used to gain insight into the _physics_ of
resonance formation in this energy region. Also, the fact
that the graphical approach works as a first approximation
means that it can be used to identify major features or at
least put limits on the possible classifications.

The Modified Rydberg Formula

This is an intuitive extension(proposed by Read[23]) of the
familiar Rydberg-Ritz equation:

$$E_{nl} = I_n - \frac{RZ^2}{(n - \delta_{nl})^2} \qquad (3.2.11)$$

where:

I is the ionization potential

R is the Rydberg constant (13.606 eV)

Z is the charge of the core

n,l are the radial and angular momentum quantum numbers

δ_{nl} is the quantum defect

For the case of two excited electrons, the modified Rydberg
equation is:

$$E_{nln l'} = I_n - R(Z-\sigma)^2 ((n-\delta_{nl})^{-2} + (n-\delta_{nl'})^{-2}) \qquad (3.2.12)$$

The assumptions involved in this extension are:

(1) The two outer electrons will screen each other
to some extent from the core, and that both
electrons experience the same amount of
screening, independent of the value of l (i.e.

the screening is the same for nl and nl' elec-
trons). Thus each electron experiences an
effective charge Z-σ, where σ is the screening
constant.

(2) The presence of the second electron does not
influence the penetration of the first elec-
tron into the core. Thus, the quantum defects
for the nl and nl' electrons are the same as
they would be for a single nl (or nl') electron
outside of the same core. The quantum defects
can then be obtained from the [core]nl ener-
gies using equation 3.2.11, after taking into
account the level splittings due to exchange
and magnetic interactions.

The screening constant is related to the amount of corre-
lation between the two electrons(see Appendix 3.6.2). For
completely correlated electrons, the screening constant has
the value of 0.25, and for completely uncorrelated elec-
trons, it has the value of 0.5. The recent work of Lin[29] on
electron correlations indicates that the two electrons would
tend to stay on *opposite* sides of the core, and thus, a high
degree of correlation is to be expected in this case. In
fact, Read found that the average value of the screening
constant was 0.254 for two excited electrons in a variety of
gases using his analysis.

For the case of three excited electrons outside the core,
with the configuration [core]nlnl'nl'', the extension pro-

posed by Read is:

$$E_{nln1'nl''} = I_n - R(Z-2\sigma)^2 ((n-\delta_{nl})^{-2} + (n-\delta_{nl'})^{-2}$$
$$+ (n-\delta_{nl''})^{-2})$$

(3.2.13)

For completely correlated electrons (on the vertices of an equilateral triangle), the screening constant has the value of 0.289.

To use the modified Rydberg formula in the present case, one first determines the quantum defects for each electron in each gas using the normal Rydberg-Ritz equation. Then the screening constants for each configuration in Ne are deduced from the resonance data, and these are used to predict the energies of equivalent resonances in the other gases. The results of this are discussed in section 3.4.

3.3 DESCRIPTION OF THE EXPERIMENT

3.3.1 The Interaction Region

Figure 3.3 shows a scale diagram of the interaction region used to detect metastable atoms. Note that the gas beam enters the interaction region from below the electron beam and drifts up into the detector. Only metastable atoms (and in principle, VUV photons) are detected in this arrangement. All non-metastable excited atoms decay long before they reach the channeltron and charged particles are kept out of the detector by suitably biased grids - positive ions are discriminated against by a grid kept at a potential of about +20 volts, and negative ions/electrons are kept out by biassing the channeltron cone at -250 volts.

The gas beam itself was produced by a single capillary needle made from platinum-iridium alloy (non-magnetic), and gas simply effused out of the capillary under pressure (1 to 5 torr) into the interaction region. A single capillary was used instead of a multi-channel array for the gas source to minimize the total gas load on the vacuum system. The electron beam passed through the gas just above the end of the needle, through the region of highest density, thus ensuring high signal rates.

The interaction region was kept field free by the use of a molybdenum shielding arrangement kept at the same potential as L4C and L5A. The needle, although the facility to bias it with respect to the target region was available, was

also kept at the same potential as the target.

3.3.2 Data Collection and Calibration

Figure 3.4 shows a block diagram of the electronics used
in the collection of the data, and Table 3.1 lists the rele-
vant components. The TN-1710 multichannel analyzer was used
in conjunction with the TN-1251 ramp generator to vary the
incident electron energy to obtain a metastable excitation
spectrum.

As mentioned above, the possibility of detecting VUV pho-
tons exists, but solid angle limitations and the lower quan-
tum effeciency of the channeltron for photons restricted
this to less than 0.1 percent, whereas the detection effi-
ciency for metastable atoms approached 100 percent. In
addition to this, a comparison of the present Ar data to
that of Marchand and Cardinal[17] reveals an almost one-to-one
correspondence between the two sets of data. These authors
used a pulsed excitation technique to discriminate against
photons, so this comparison suggests that photons contribu-
tions to our observed signal were indeed negligible. Thus,
no attempts were made to discriminate against photons in the
present work.

The absence of any structure near the ionization thres-
hold in the present data and that of Brunt et al[5] suggests
that high-n Rydberg species represented only a minor contri-
bution to the observed signal.

H.V.

Cone

Channeltron
Mounting
Assembly

Grid

Mo Mesh

e⁻ Beam

Needle

Lens
Stack 3

Lens
Stack 2

Gas Inlet

1 cm
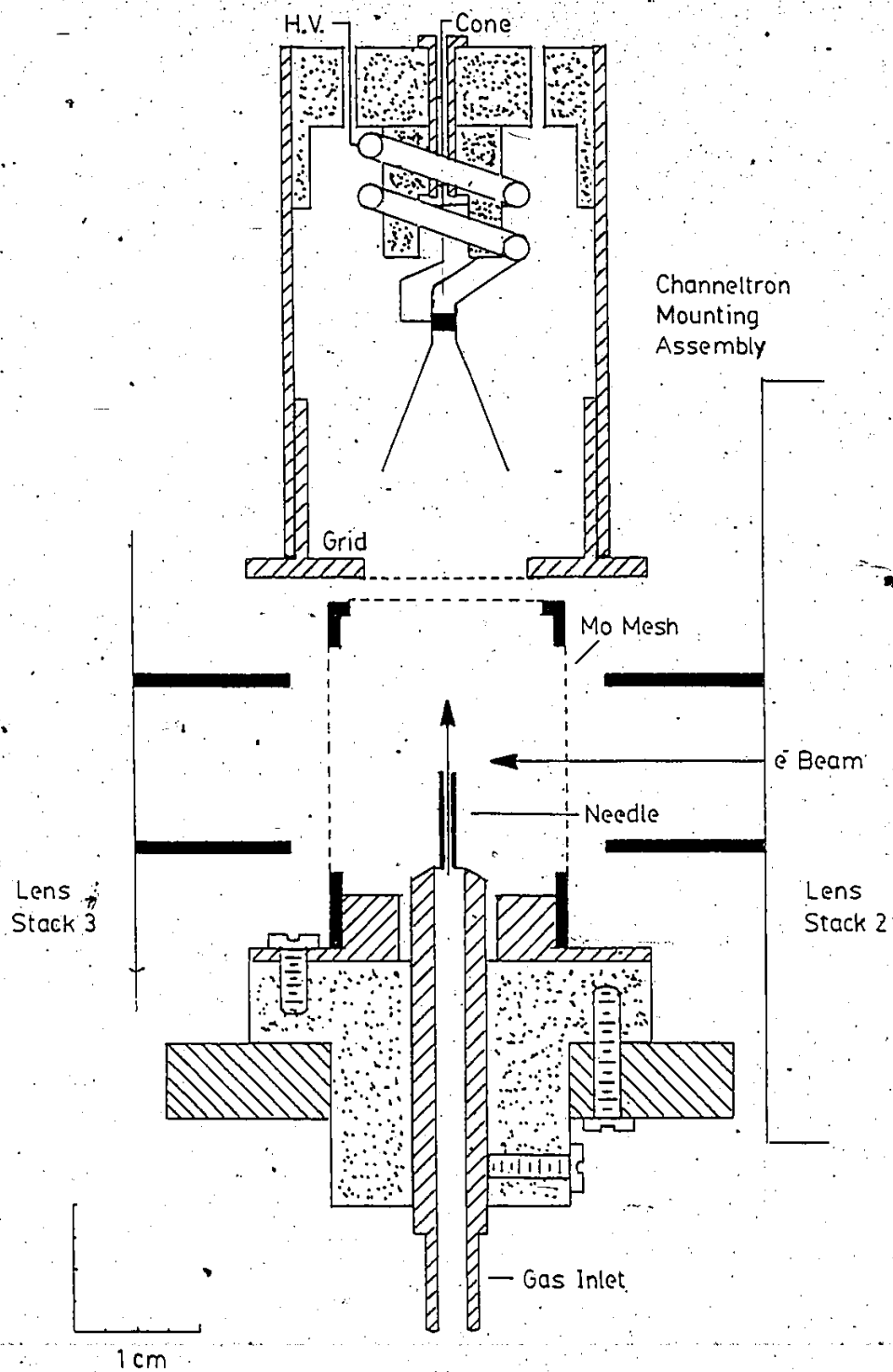
INTERACTION REGION: METASTABLE DETECTION

FIG 3.3
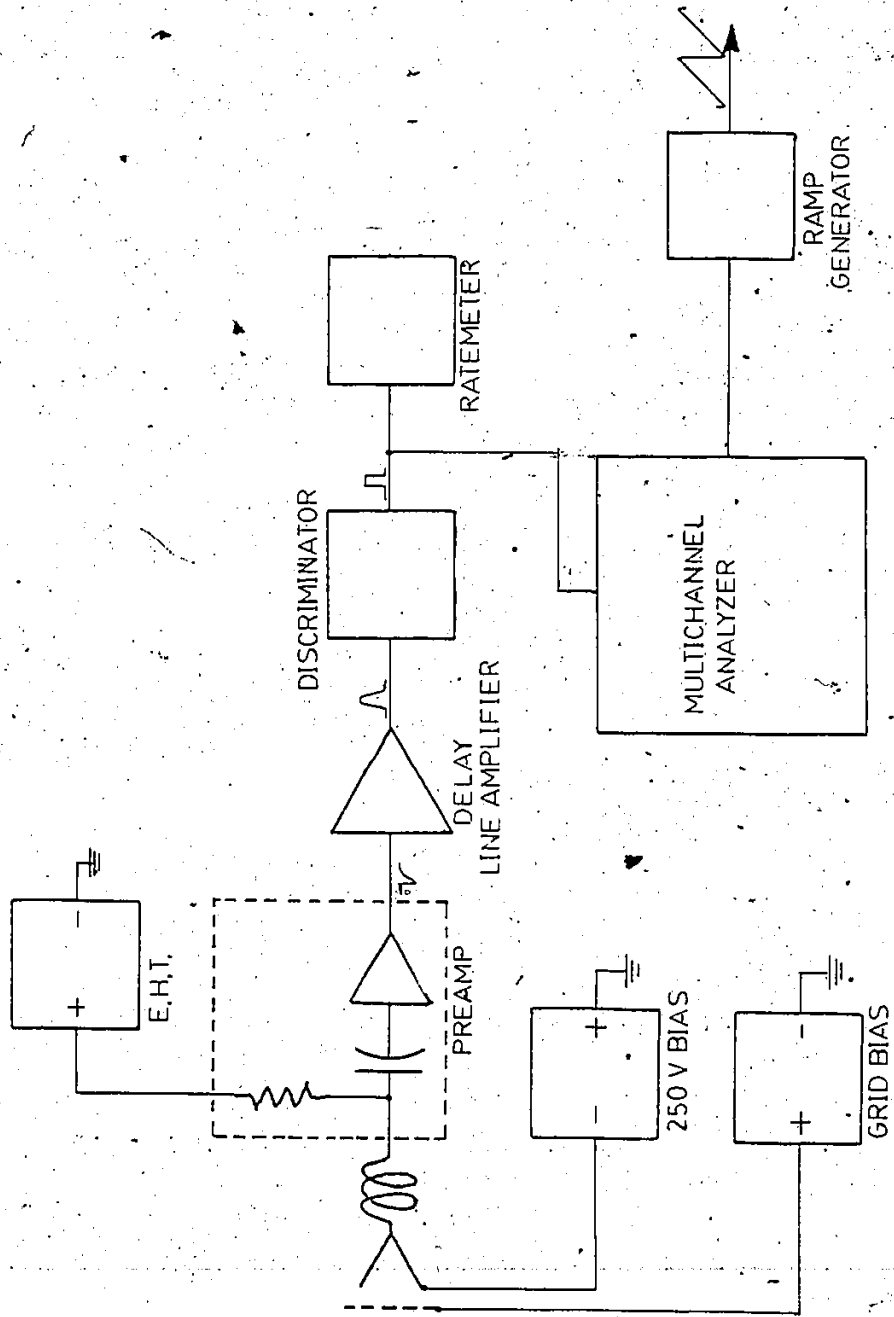
FIG 34

METASTABLE DETECTOR ELECTRONICS

FIG 3.5 Ar Calibration Spectrum
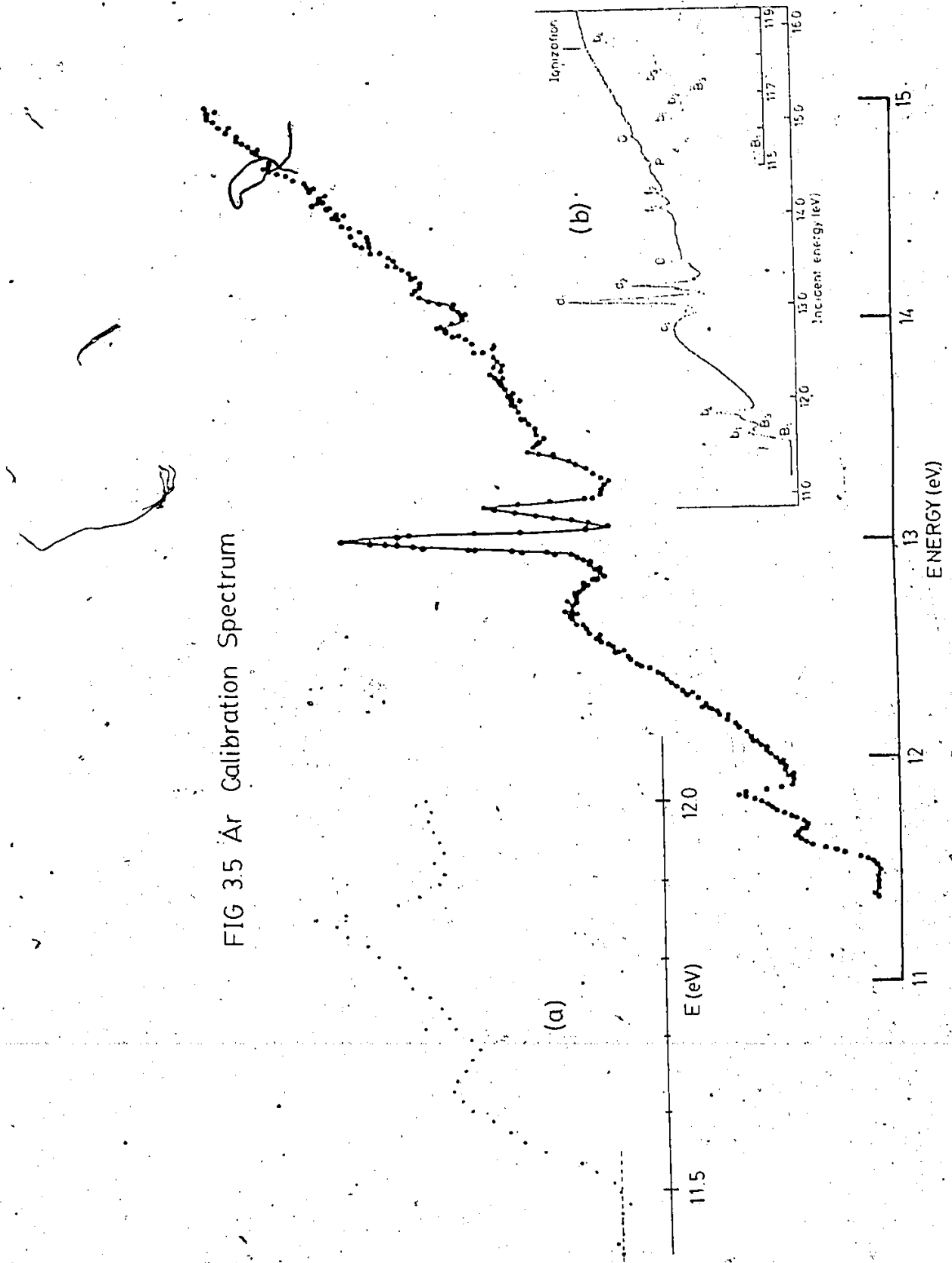
Table 3.1
Components - Metastable Detection Electronics

Component	Function
Kepco HB2AM Power Supply	Grid Bias
Power-One 250 VDC Supply	Channeltron Cone Bias
Tennelec AEC-5000 Power Supply	Channeltron High Voltage Supply
Ortec 460 NIM Module	Delay Line Amplifier
Ortec 421 NIM Module	Integral Discriminator
Ortec 441 NIM Module	Ratemeter
Tracor Northern TN-1710	Multi-Channel Analyzer
Tracor Northern TN-1251	Ramp Generator (0-10 v)

Typical counting rates approaching 100kHz were readily obtainable in the present set-up and the energy resolution of the incident electron beam was estimated to be 20-30 meV at the most. This value was arrived at by examining the initial fast rise in the metastable spectrum of Fig. 3.5 (see inset a). Also shown in Fig. 3.5 is a similar spectrum (inset b) taken from Brunt et al[5], using a similar spectrometer but operated at a much higher resolution. Since the features of interest represented a small fraction (about 10^{-3}) of the total signal, data collection times were 2 to 3 days in order to gain statistical significance. The data was then transferred to a PDP-8/E computer for analysis and plotting. In order to highlight the features present in the spectra the large background was removed. In some cases a constant or linear background was removed, while in others a subtraction routine which removed the low frequency oscillations from the data was used (see Appendix 3.6.3).

Accurate energy calibration of the spectra was achieved by using the known positions of the sharp features below the first ionization threshold[5]. A calibration spectrum was taken before the data was acquired and also after data collection was stopped. This allowed the energy per channel to be determined as well as the 'contact potential' or difference between the starting value of the incident energy (measured as target potential) and the actual value. The positions of the sharp features could then be determined

to 25 meV or better in this way.   The energies given in the
tables of the next section are averages obtained from a num-
ber of spectra for each gas.   A typical calibration spectrum
is shown in Fig. 3.5, taken with Ar as the target gas.

3.4 RESULTS AND DISCUSSION

3.4.1 Introduction and Analysis

The data obtained are displayed in figures 3.6.(a), 3.7 and 3.8, which show metastable excitation spectra for Ne, Ar and Kr, respectively. As can be seen a large number of features are evident, and the most prominent of these are listed in Tables 3.2, 3.3 and 3.4. These tables also include data from other authors for comparison purposes, and also some widths for the more isolated features (where a reasonable curve fitting procedure (see section 3.2.1) could be applied). It should be stressed at this point that the current analysis seeks to provide a framework for the major features observed; no attempt was made to discuss the fine detail superimposed on the larger features, as has been done by other authors[17,29].

As a first step in the analysis consider the Ne spectrum of Fig 3.6(a), where the features are all fairly distinct and well separated. A comparison of this data with that of Spence[10] reveals the following significant facts:

(1) An exact one to one correspondence occurs in the position of each feature (see Table 3.2).

(2) Good correspondence is obtained if a visual comparison of the respective profiles in both sets of data is made. Such a comparison is justified since something close to a total cross-section is being measured in both cases.

(3) Although this is probably not as significant

Ne

FIG 36(a)

Energy (eV)

42   44   46   48   50

3s²3p

3s²

3s 3p

3s²3p

3s 3p²

3s²3p

3p²

4s

4s 4p

3s 3p²

[2s2p⁶]²S

3s²3p²

[2s²2p⁴] ³P
          ¹D
          ¹S

a b c d e f g h i j k l m n

Ne

(a)

(b)

A B C D E F G H I J K

(c)

E(eV)
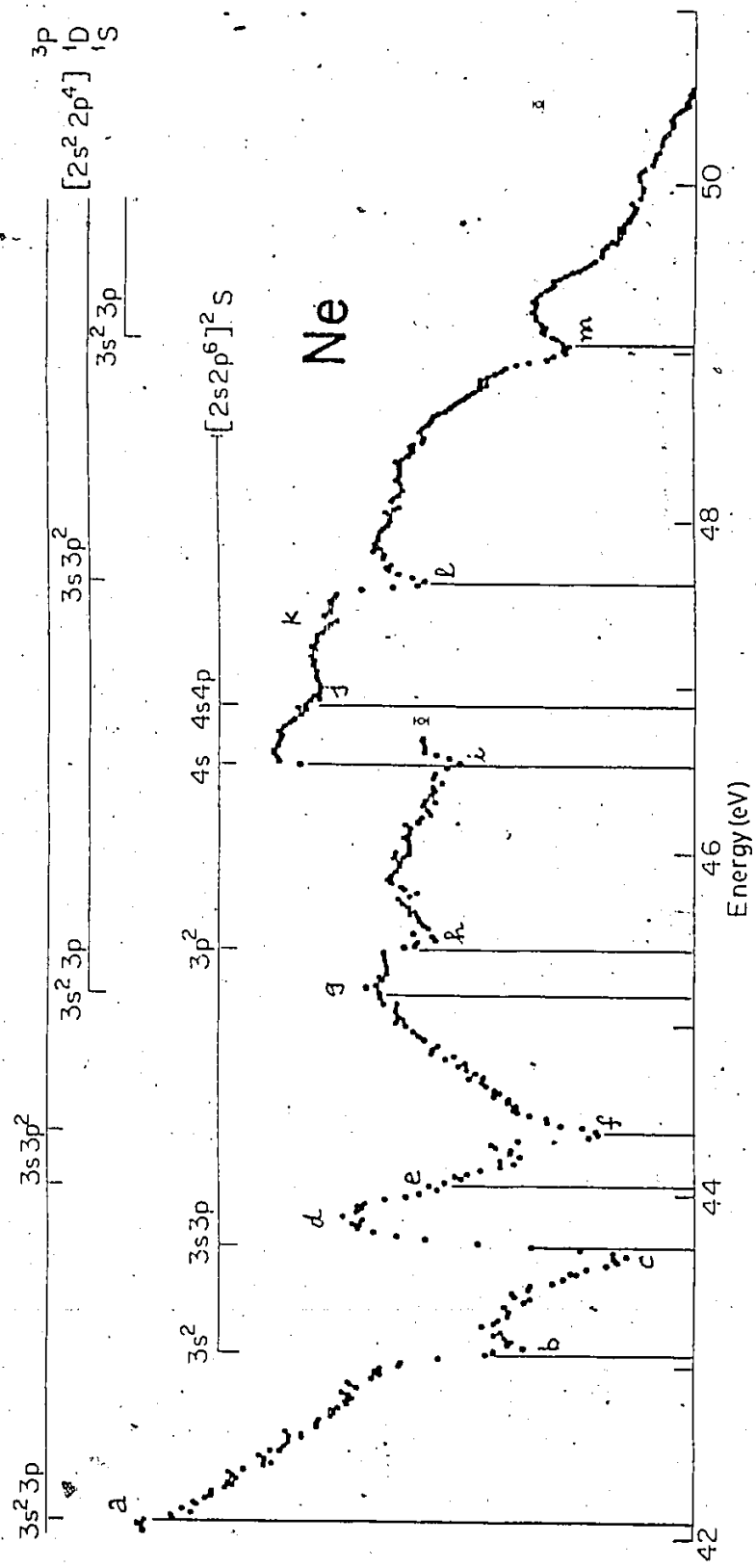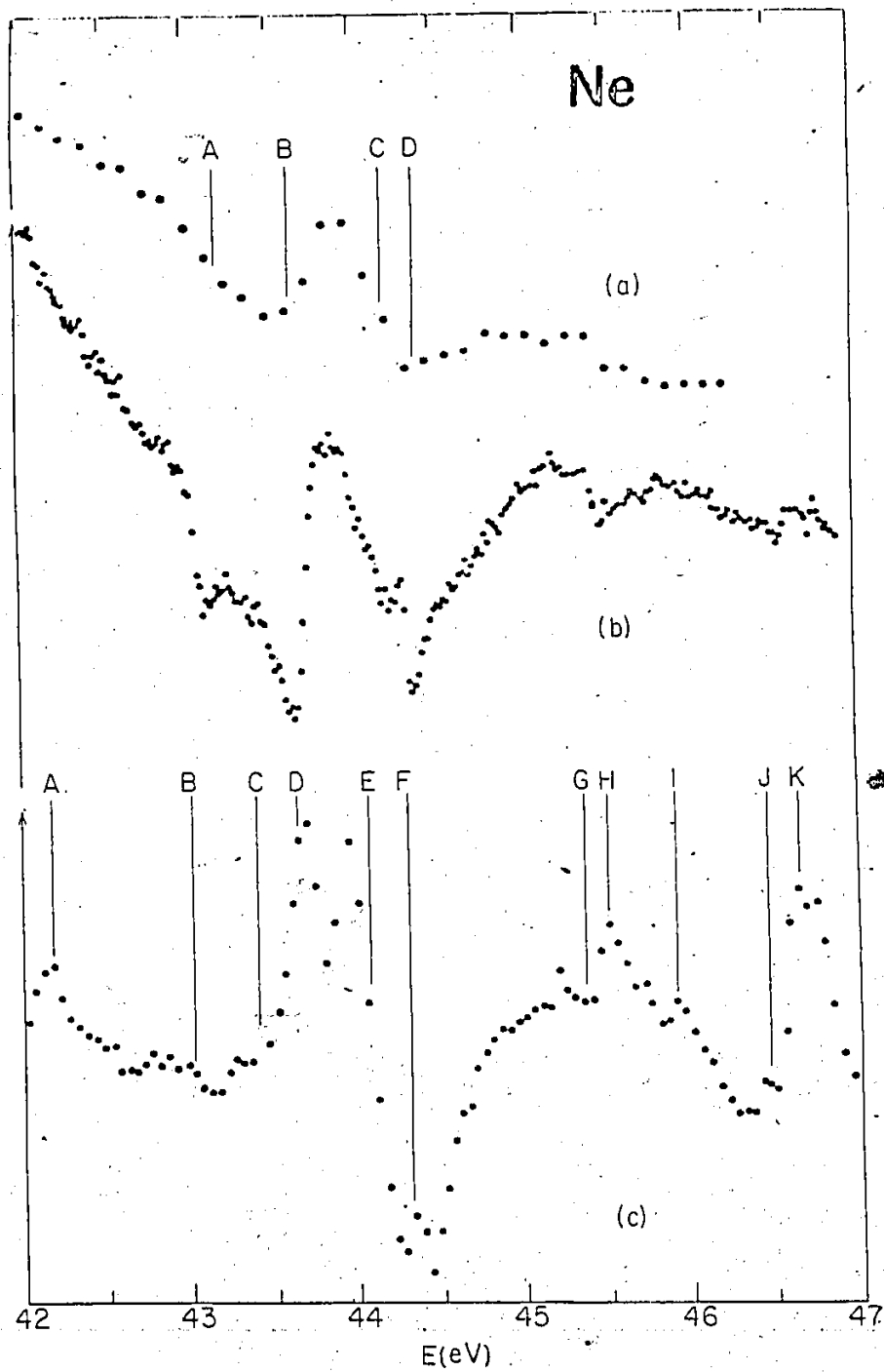
FIG 3.6(b)

TABLE 3.2 Neon Data

Feature	Present Data (eV) Energy	Config.	Spence[10] (1) Energy	Spence[10] (1) Config.	Width[a] (eV)
a	42.11	$[^3P]^{++}3s^2 3p$	42.08	$[^3P]^{++}3s^2 3p$	0.070±0.020
b	43.10	$[^2S]^{+}3s^2(^2S)$	43.06	$[^2S]^{+}3s^2(^2S)$	
c	43.67	$[^2S]^{+}3s3p$	43.69	$[^2S]^{+}3s3p$	
d	43.86				
e	44.07	$[^3P]^{++}3s3p^2$	44.05	$[^3P]^{++}3s3p^2$	0.050±0.020
f	44.36	$[^3P]^{++}3s3p^2$	44.37	$[^3P]^{++}3s3p^2$	
q	45.25	$[^1D]^{++}3s\,3p$	45.17	$[^1D]^{++}3s^2 3p$	
h	45.45	$[^2S]^{+}3p^2$	45.42	$[^2S]^{+}3p^2$	0.035±0.010
i	46.53	$[^2S]^{+}4s^2$	46.52	$[^2S]^{+}4s^2(^2S)$	
j	46.97	$[^2S]^{+}4s4p$	46.88	$[^2S]^{+}4s4p$	
k	47.38	$[^1D]^{++}3s3p^2$			
l	47.64	$[^1D]^{-}3s3p^2$	47.60	$[^2S]^{+}5s5p$	
m	49.02	$[^1S]^{++}3s^2 3p^2$	49.04	$[^1S]^{++}3s^2 3p$	

(a) These widths were obtained by fitting a Fano profile to the observed data (see text).
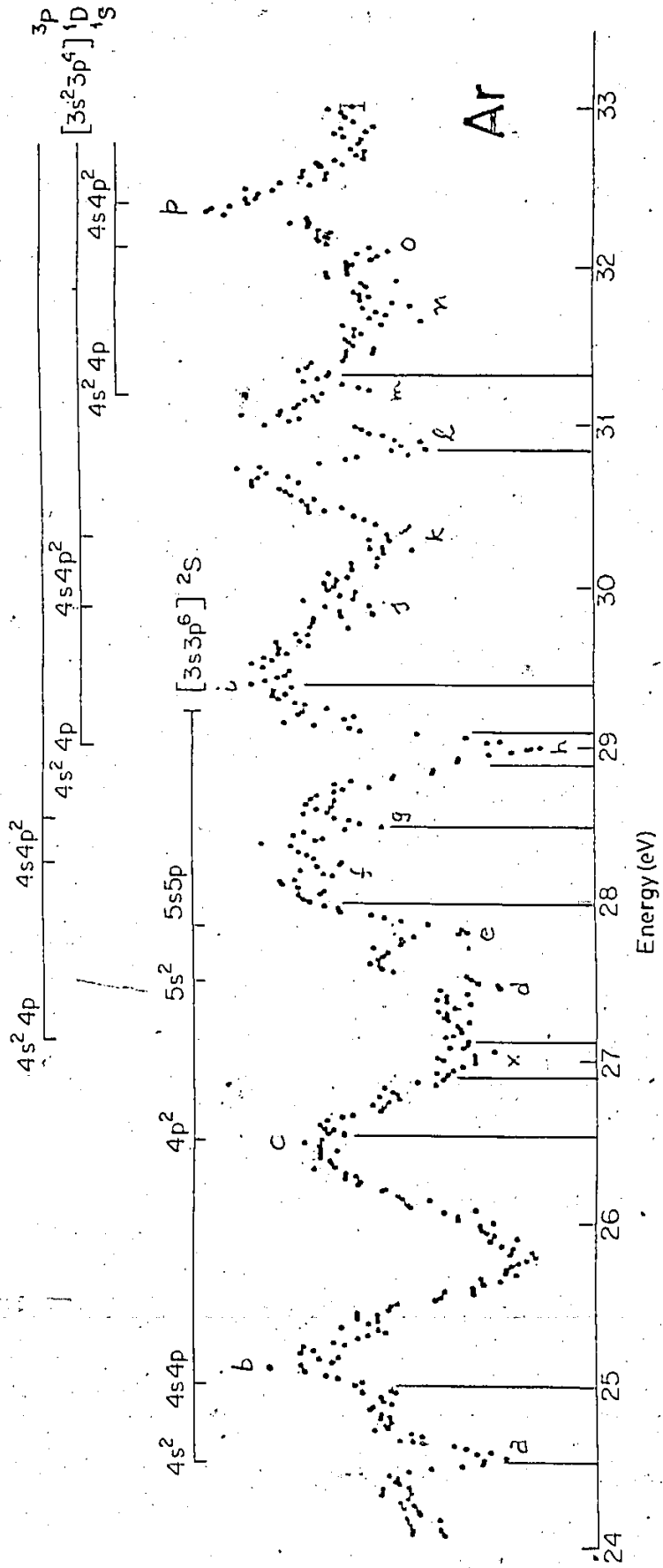
FIG 3.7

TABLE 3.3 Argon Data

Present Work		Predicted Value (see text)	Tentative Classification	Sanche & Schultz [8]	Roy and Carette [13]	Marchand & Cardinal [17]	Bolduc et al. [6]	Lefaivre & Marmet [31]	Width (meV) (c)
a	24.54	24.48	$[3s3p^6](^2S)4s^2(^2S)$	24.48-24.58	24.49-24.65	24.55	24.44	-	90±15
b	24.99-25.10	25.03	$[3s3p^6](^2S)4s4p(^2P)$	25.03	24.94-25.04	[24.95/25.20]	[24.96/25.25]	-	
c	26.45	26.54	$[3s3p^6](^2S)4p^2(^2D)$	26.55	26.50	[26.65]	-	-	
x	27.08		$[3s^23p^4](^3P)4s^24p$	26.84-26.90/27.07	26.92/27.15	[26.95]	-	-	70±10
d	27.57-27.72	27.50	$[3s3p^6](^2S)5s^2(^2S)$	[27.4]	-	[27.65]	[27.61]	-	75±10
e	27.88	27.81	$[3s3p^6](^2S)5s5p(^2P)$	27.95-28.08	27.87-27.95	[27.95]	-	[28.05]	
f	28.30		$[3s^23p^4](^3P)4s4p^2$	-	-	[28.25-28.40]	-	[28.36]	
g	28.57	28.44	$[3s3p^6](^2S)6s6p$	28.33-28.53	28.41-28.58	-	-	[28.67]	120±20
h	28.98		$[3s^23p^4](^3P)4s4p^2$	28.82-28.98	28.88/29.10	[29.05]	-	[29.10]	
i	29.44		$[3s^23p^4](^1D)4s4p$	29.36	29.39-29.49	[29.60]	-	[29.58]	
j	29.86		$[3s^23p^4](^1D)4s4p^2$	29.82^b	-	[30.01]	-	-	
k	30.33		$[3s^23p^4](^1D)4s4p^2$	30.0/30.2^b	-	[30.?/30.45]	-	-	
l	30.90		?	30.75-30.86	30.93	[30.90]	-	-	
m	31.30		$[3s^23p^4](^1S)4s^24p$	31.2/31.4^b	31.28-31.37	31.4	-	31.38	
n	31.71		-			31.75			
o	32.12		$[3s^23p^4](^1S)4s4p^2$			32.25		[32.34]	
p	32.40		$[3s^23p^4](^1S)4s4p^2$			32.4			

Brackets placed around an energy indicate that a different designation was given by the authors.

(a) Because of the very close correspondence between this data and our own, we have included the energies of the features which most closely correspond to the equivalent features in our data. These authors list and discuss many other smaller features which are apparent on their spectra.

(b) Features not tabulated by authors but apparent on graphs.

(c) These widths were obtained by fitting a Fano profile to the data.

Kr

$5s^2 5p$ $5s 5p^2$

$5s^2 5p$ $5s 5p^2$ $5s 5p^2$

$5s^2 5p$ $5s^2 5p$ $5s 5p^2$ $5s 5p^2$

$6s^2$ $6s 6p$

$[4s 4p^6]\ ^2S$

$5s^2 5p$ $5s 5p^2$

$[4s^2 4p^4]\ ^3P$ ^1D ^1S

$5p^2$

Energy(eV)

FIG 3.8

a b c d e f g h i j k l m
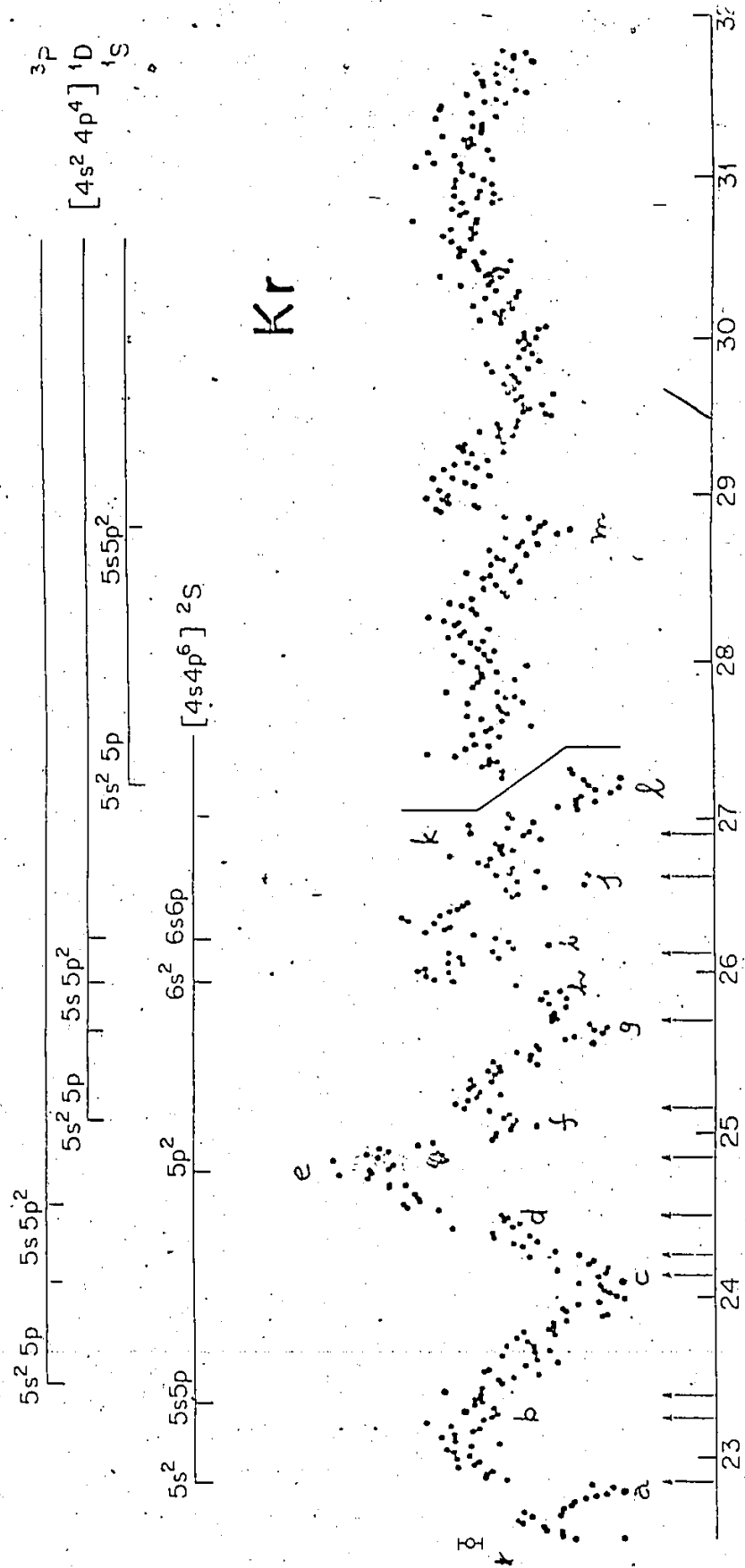
TABLE 3.4 Krypton Data

Present Work		Prediction	Tentative Classification	Sanche & Schultz[8]	Roy et al.[14]	Valin & Marmet[31][a]	Boulay & Marchand[29][a]	Width (meV)[c]
a	22.79	22.86	$[4s4p^6](^2S)5s^2(^2S)$	22.76–22.87	22.85–22.97		22.90	65±10
b	23.27	23.36	$[4s4p^6](^2S)5s5p(^2P)$	23.30	23.14–23.26		23.17	
c	24.08		$[4s^24p^4](^3P)5s\,5p^2$ $[4s^24p^4](^3P)5s5p^2$	23.39 $24.13/24.25^b$	23.33–23.50	22.68 24.03	23.80	
d	24.51		$[4s^24p^4](^3P)5s5p^2$	24.46–24.54	[24.43–24.58]	[24.5]		
e	24.74	24.85	$[4s4p^6](^2S)5p^2$	24.78–24.91	[24.81–24.99]	[24.92]		
f	25.04		$[4s^24p^4](^1D)5s\,5p^2$	25.13^b	[25.11–25.18]			
g	25.59		$[4s^24p^4](^1D)5s5p^2$	25.70^b	25.68		[25.40]	
h	25.92	25.80	$[4s4p^6](^2S)6s^2(^2S)$ $[4s^24p^4](^1D)5s5p^2$		[25.95–26.17]	25.88		
i	26.20	26.11	$[4s4p^6](^2S)6s6p$	26.18	[25.95–26.17]			
j	26.55		$[4s^24p^4](^1D)5s5p^2$	26.56–26.68				
k	26.89			26.90	[26.90]			
l	27.19		$[4s^24p^4](^1S)5s^25p$					
m	28.80		$[4s^24p^4](^1S)5s5p^2$					

(a) Only those features designated to be resonances by the authors have been listed.

(b) Features not tabulated by authors but apparent on their figure.

(c) Obtained by fitting a Fano profile to the data.

Brackets around an energy indicate that a different designation was given by the authors.

as (1) and (2), there seems to be a good correspondence between the relative strengths of features based on the same core in both sets of data.

These facts strongly suggest that the features in Ne are due to negative ion resonances, rather than to autoionization, for example. In some cases there is no possible ambiguity since there are no neutral excited states in the vicinity. Feature b and c(Fig 3.6(a) and Table 3.2) fall into this category. Further support for the identification of the Ne features with resonances comes from the data of Sanche and Schulz[8] and the data of Roy et al[7]. In both cases, techniques were used which are known to be sensitive to the detection of resonances, and the close correspondence between the present data and that of these authors is very convincing evidence for our identifications. Thus, assuming that our features are due to Ne⁻ resonances and that Spence's classifications as given in Table 3.2 are valid, it is reasonable to suppose that similar features will probably occur in the other rare gases. This would be consistent with the situation found at lower energies[5]. Using the graphical approach discussed in section 3.2.2 it was found possible to identify which features might correspond to which resonance configurations. This is illustrated in Figures 3.9(a) and (b), and 3.10(a) and (b), which show that very good straight lines can be drawn through equivalent resonances in the doubly excited state region, as was the case for lower energies. Figure 3.9(a) shows a plot of ionization potential vs reso-
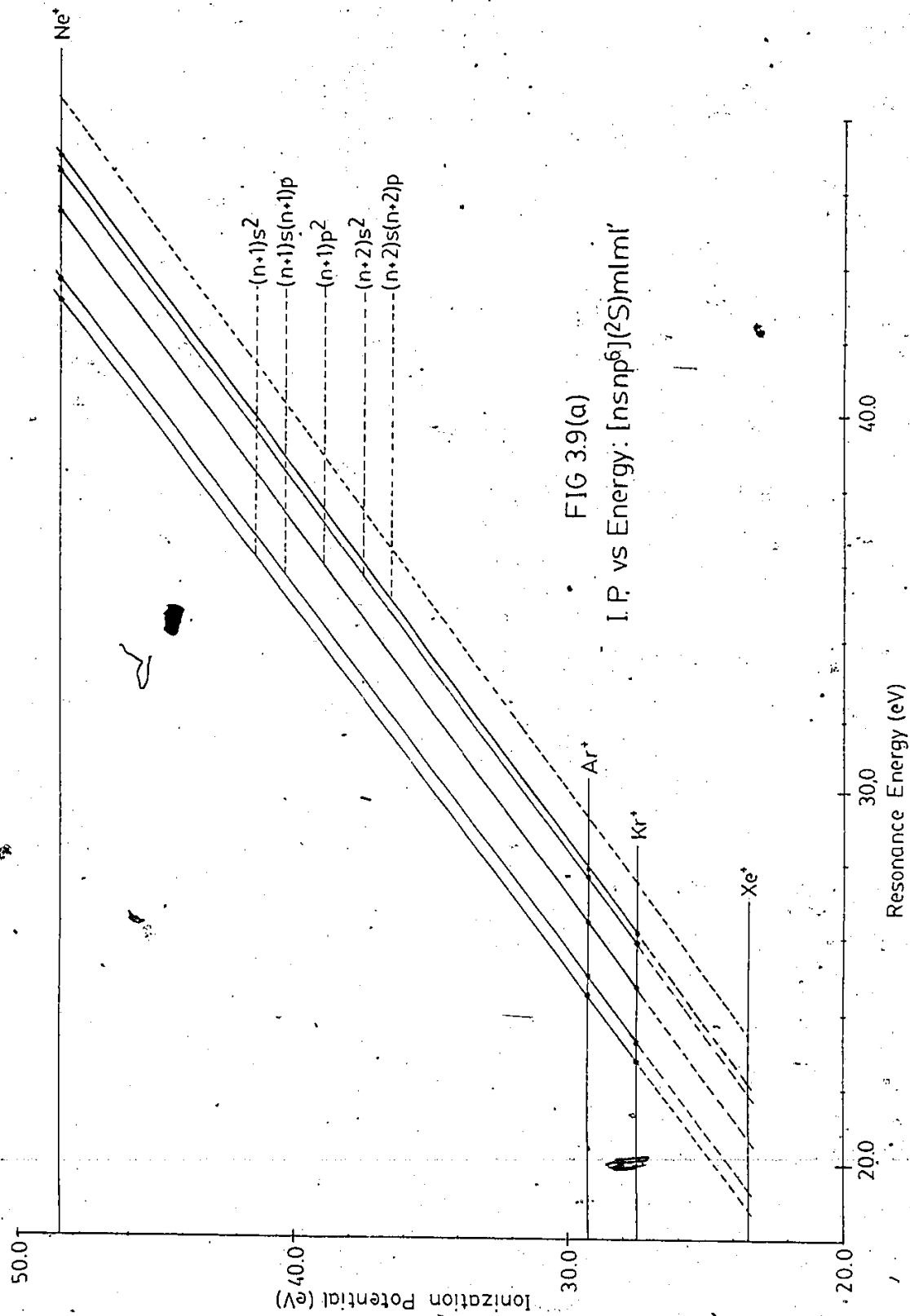
FIG 3.9(a)

I.P. vs Energy: [nsnp⁶](²S)mlml'

$(n+1)s^2$
$(n+1)s(n+1)p$
$(n+1)p^2$
$(n+2)s^2$
$(n+2)s(n+2)p$

Ne⁺

Ar⁺

Kr⁺

Xe⁺

Resonance Energy (eV)

20.0   30.0   40.0

Ionization Potential (eV)

20.0   30.0   40.0   50.0

FIG 3.9(b): B.E. vs Energy
[nsnp^6](^{2}S)mlml' States

(n+1)s^2 3.339x10^{-2}

(n+1)s(n+1)p 2.933x10^{-2}

(n+1)p^2 1.180x10^2

(n+2)s^2 1.712x10^{-2}

(n+2)s(n+2)p 0.811x10^{-2}

Ne$^+$

Ar$^+$

Kr$^+$

Xe$^+$

Resondnce Energy (eV)

20.0   30.0   40.0

Binding Energy (eV)

0.0   1.0   2.0   3.0   4.0   5.0   6.0
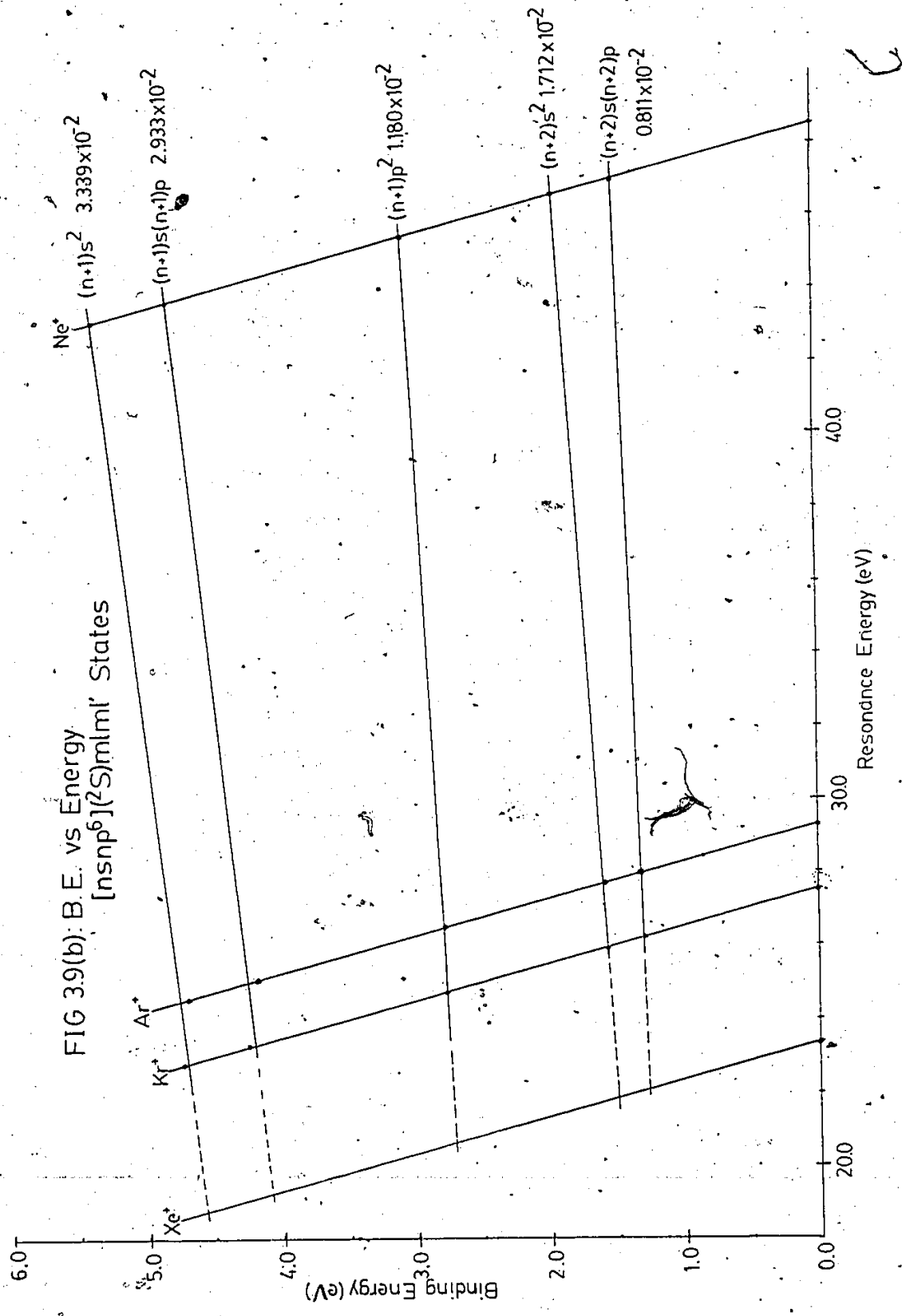
nance energy for the singly ionized cores(inner shell excitation) and Fig. 3.9(b) shows the equivalent plot of binding energy vs resonance energy for the same configurations. Also indicated on these figures are the slopes of the lines connecting equivalent resonances. The lines are best fits to the data points. These states have a $^2S_{12}$ configuration and no fine structure splitting. Five different states have been positively identified in Ne, and the three lowest energy features in Ar have also been unambiguously identified by many authors. Also, the two lowest energy features in Kr and Xe have been identified. Fig 3.9(a) illustrates that the equivalent resonances [core]$^+$(n+1)s^2 and [core]$^+$(n+1)s(n+1)p are connected by excellent straight lines. Now if a straight line joining the [core]$^+$(n+1)p^2 configurations is drawn and extrapolated to Kr, it is immediately seen that the Kr$^-$ feature at 24.74 eV may be identified with this configuration. It is interesting to note that a p^2 resonance gives rise to a broad feature in the spectra of Fig's 3.6(a) to 3.8. It is also noted that the feature 5-5' of Sanche and Schulz[8] at 24.78-24.91 eV and that of Roy et al[4] near 24.85 eV might also to be identified with this resonance. Furthermore, if the feature observed at 24.45 eV by Roy et al(which they identify with a p^2 resonance) is plotted on Fig 3.9(a), it would not fall on the straight line connecting the p^2 configuration. Of course, the p^2 configuration is split into a number of terms, and it is possible that one term may decay into the metastable channel while another decays into the channel

observed by Roy et al. Now if the line is extrapolated back to Xe, the Xe$^-$ p^2 resonance should occur at an energy of about .20.8 eV. Delage et al[15] observe a feature at 20.89-21.10 eV, but they classify it as a neutral autoionizing state rather than as a resonance. Having established that these resonances lie on straight lines, the other features in Ar and Kr can be plotted and joined to the equivalent resonances in Ne. The slopes of these lines must lie between 1 (appropriate to the bare core, indicated by the dashed line on Fig 3.9(a)) and the larger slope of the (n+1) s^2 configuration. This restriction enables the features to be identified with little effort..

Now consider the plot of binding energy vs resonance energy in Fig 3.9(b). Note that because of the more sensitive scale used, the straight line fit does not appear to be quite so good. This is due to either inaccuracies in assigning energies to the features or the effects of configuration interaction causing departures from the linear relationship. As discussed in section 3.2.2 the significant bit of information to note is the slope of the lines connecting equivalent configurations. It can be seen at once that the core perturbations are greatest for the (n+1) s^2 states and the least for the (n+2) s (n+2) p states. By comparing the slopes of each line, the relative strengths of the core perturbations can be deduced as V((n+1)s^2) > V((n+1) s (n+1) p) > V((n+2) s^2) > V((n+1) p^2) > V((n+2) s (n+2) p). It should also be noted that the straight line fit is the poorest for the (n+1) s^2 and (n+1) s (n+1) p configurations.

This probably reflects the influence of configuration inter-
action effects on these states. If this is indeed the case,
then it might be concluded that configuration interaction is
negligible for the other states.

The next bit of information to look at is the possibility
of a systematic behaviour of the slopes of the lines con-
necting equivalent resonances. Figure 3.9(c) shows a plot
of slope vs principal quantum number for the photoabsorption
data of Codling and co-workers[24-27] as indicated by the
appropriate configurations. A clear trend is apparent for
the $[nsnp^6](^2S)mp$ series. Turning to the negative ion data
it can be seen that similar trends exist, namely, a sharp
decrease in slope as the principal quantum number of the
excited electrons increases. It is not possible to use the
photoabsorption data to give more than a rough estimate of
the slopes for the negative ion data, since electron-elec-
tron interactions are not present for that data. Without
more series terms for the negative ion data it is also not
possible to determine the quantitative behaviour of the
slopes.

One other problem associated with this or any approach is
due to the considerable amount of overlap of features, as
can be seen in Fig's 3.6(a), 3.7 and 3.8. Thus, even allow-
ing that all of the observed features are due to negative
ions, the overlap between different channels can make it
difficult to decide which feature belongs to which channel.
Also, the interference effects make accurate assignment of a

particular feature difficult in some cases. Little help can be expected at the moment from theoretical considerations because of the complexity of the problem (a large number of available and overlapping channels).

It should be pointed out that no attempt has been made to position the $(^2S) nd^2$ resonances. These should occur at energies close to the equivalent $(n+2)s^2$ resonances and may account for some of the observed strength of these features in the metastable spectra. In the lower energy region, however, the nd^2 resonances were found to be much weaker than the $(n+2)s^2$ ones[30].

The main usefulness of the graphical approach is in the area of classification of features. It may not always be possible to provide an unambiguous classification, but is certainly able to limit the possiblities.

Now consider Fig's 3.10(a) and (b). These plots are based on the $[ns^2np^4]^{++}$ cores, and the situation is now more difficult to sort out. The core configuration is split into 5 terms: $^3P_{2,1,0}$, $^1D_2$ and $^1S_0$. In Ne the ^3P splitting is small, but this is not the case with the other gases; the splitting in Xe covers 1.21 eV. This is indicated in Fig. 3.10(a) and Fig. 3.10(b). Thus there are effectively five ionization potentials to deal with for each gas, and resonances could be associated with each of these. This inevitably leads to some overlap in the spectral features resulting from different configurations.

FIG 3.9(c) Slope vs k

$[nsnp^6](^2S)^+$ Core

$(n+k)s^2$

$(n+k)p^2$

$(n+k)s(n+k)p$

$(n+k)p$

Slope $(\times 10^{-2})$

k

FIG 3.10(a): I.P. vs. Energy
$[ns^2 np^4]({}^3P)mlml'ml''$ States

Resonance Energy (eV)

Ionization Potential (eV)

Ne^{++}

Ar^{++}

Kr^{++}

Xe^{++}

$(n+1)s^2(n+1)p$

$(n+1)s(n+1)p^2$
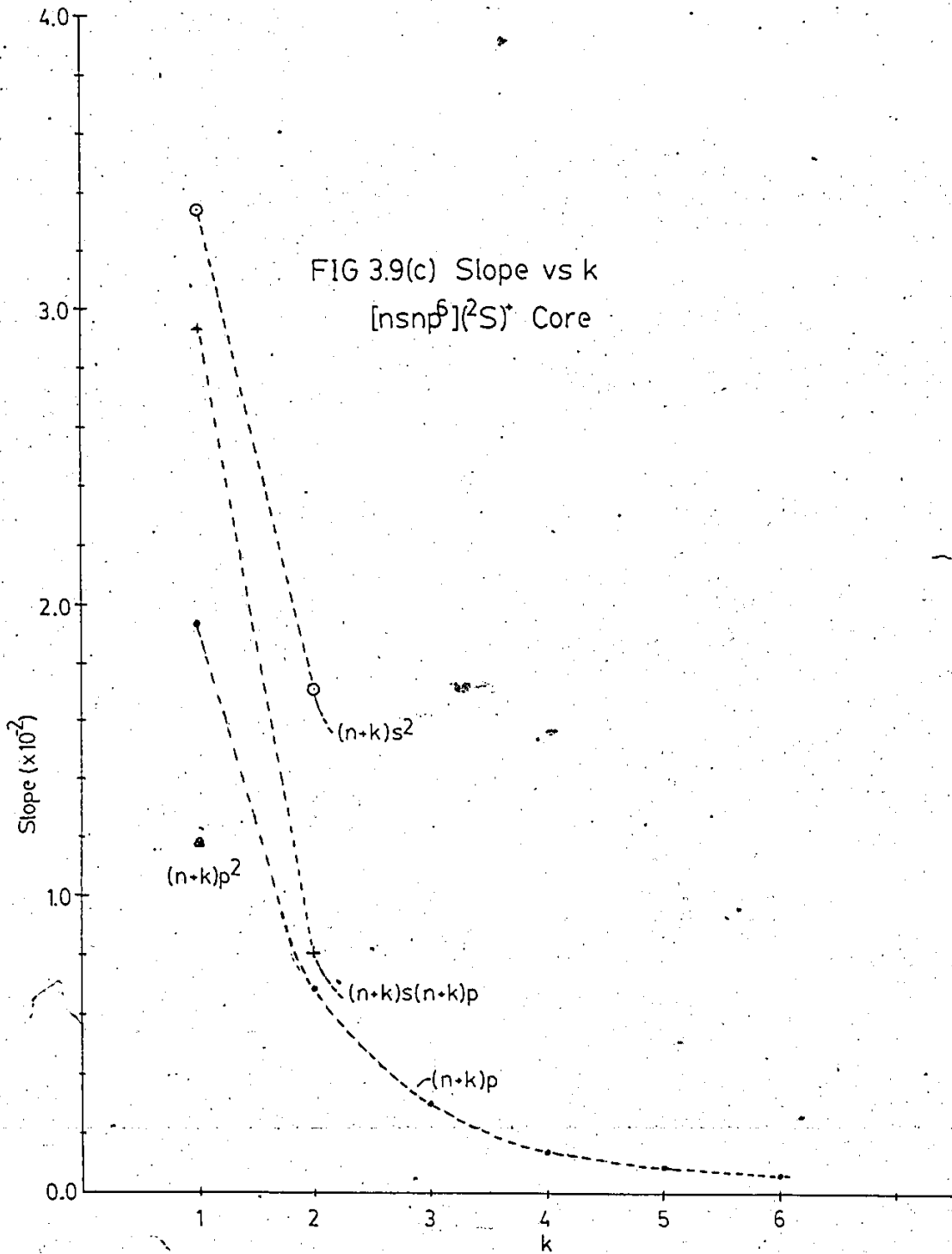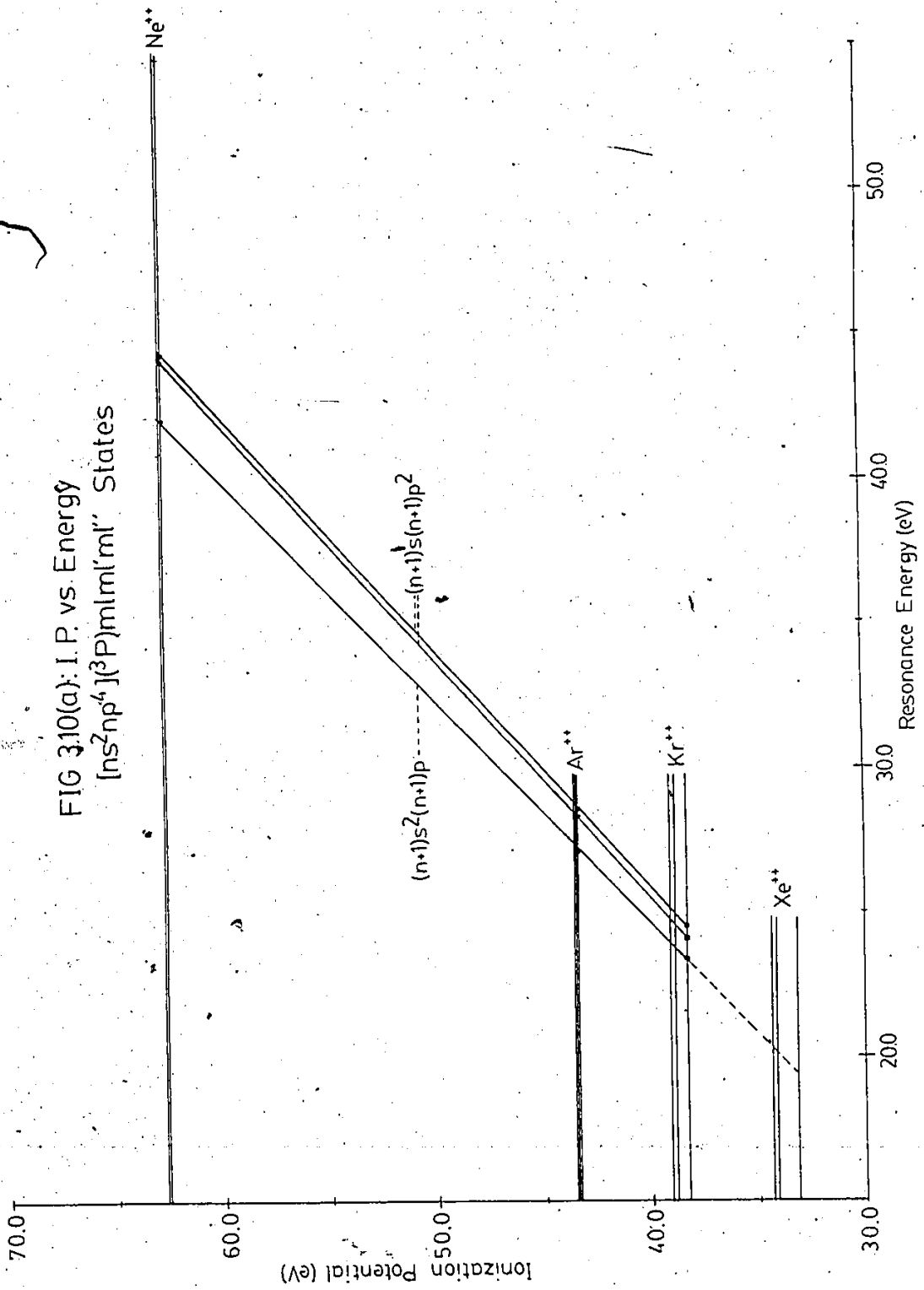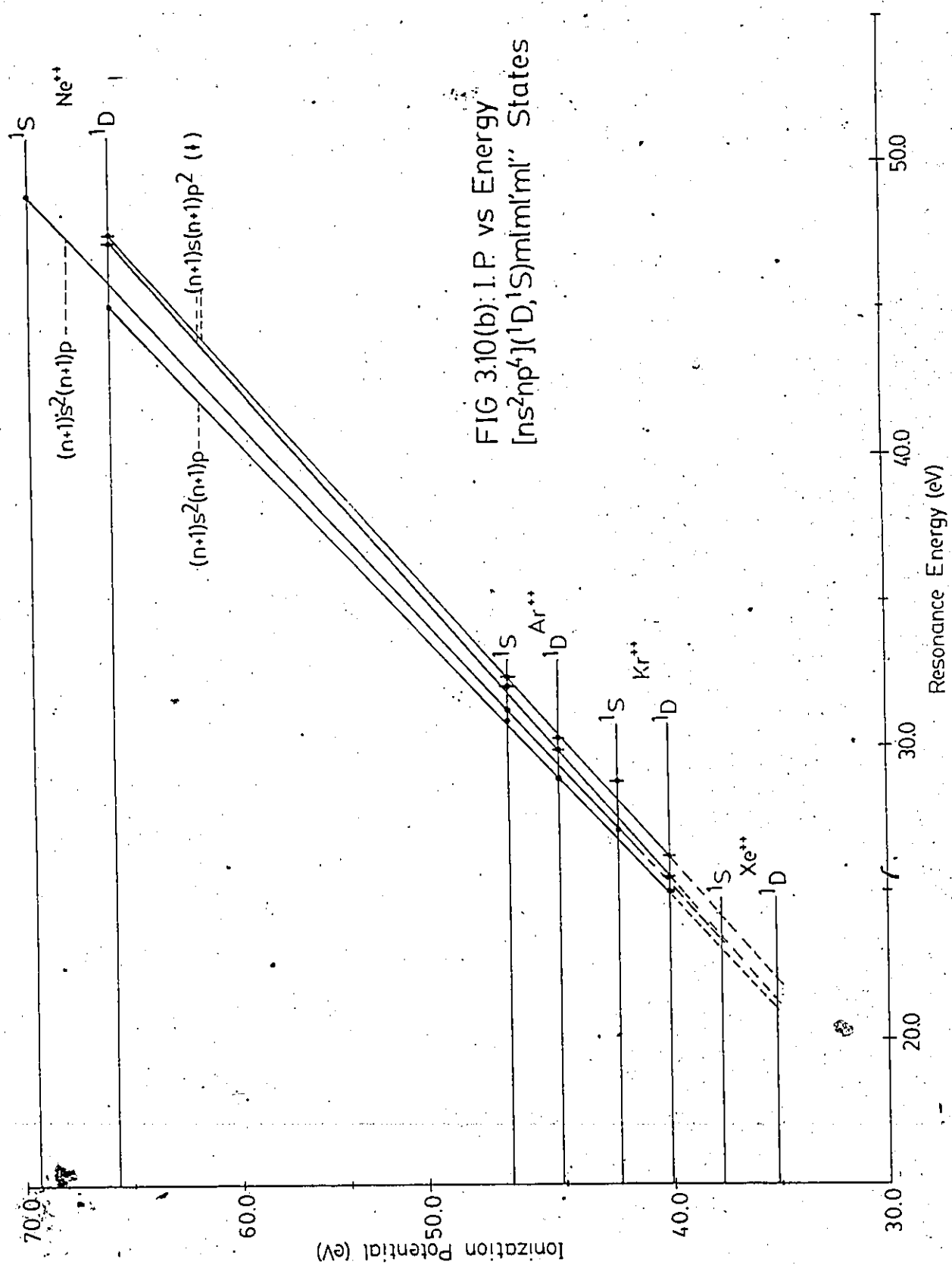
FIG 3.10(b): I.P. vs Energy
[ns²np⁴]('D,'S)ml ml'ml'' States

Ionization Potential (eV)

Resonance Energy (eV)

FIG 3.10(c): B.E. vs Energy
[ns²np⁴](³P,¹D,¹S)mℓmℓ'mℓ'' States

Line	Configuration	Slope(x10¹)
a	(³P)ms²mp	2.857
b	(¹D)ms²mp	2.647
c	(¹S)ms²mp	2.274
d	(³P)msmp²	2.113
e	''	2.158
f	(¹D)msmp²	1.734
g	''	1.911

(m = n+1)

Resonance Energy (eV)

Binding Energy (eV)

Ne⁺⁺

³P ¹D ¹S

Ar⁺⁺

³P ¹D ¹S

Kr⁺⁺

³P ¹D ¹S
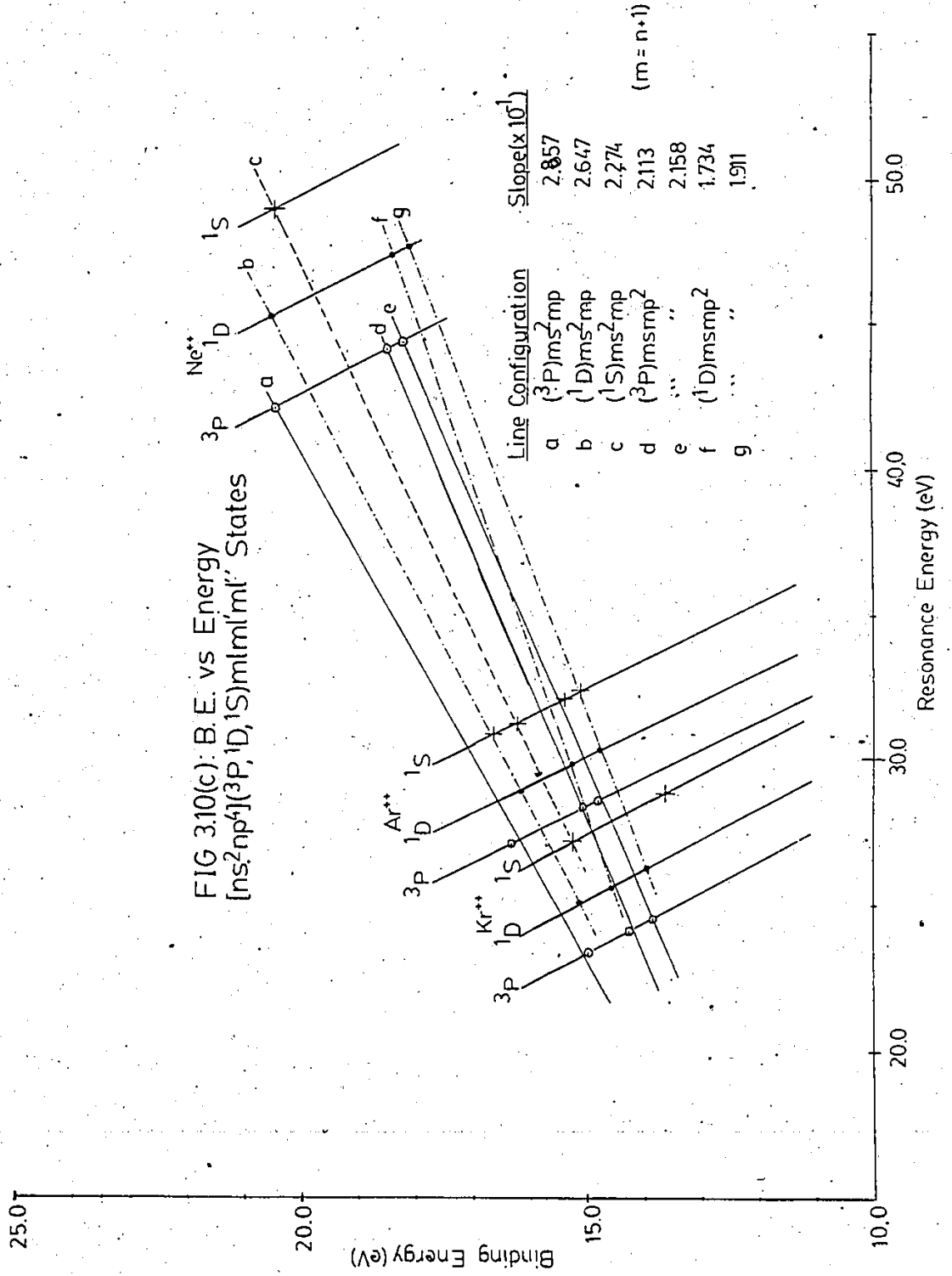
To establish the validity of the graphical approach for the doubly ionized cores it would be preferable to consider the first resonances in the family, namely the $[^3P]^{++}(n+1)s^2(n+1)p$ ones. Unfortunately, these resonances seem to decay rather weakly into the metastable channel, so only the Ne- member could be positioned at 42.10 eV. Suggested positions for the other members of this family by other authors are scarce. For example, no other author has claimed to observe the $[^3P]^{++}4s^24p$ resonance in Ar at the present time; the $[^3P]^{++}5s^25p$ resonance in Kr has been positioned at 22.68 eV[31] and near 23.4 eV[14]; in Xe the $[^3P]^{++}6s^26p$ resonance is possibly observed at 19.10 eV[15].

Another complication which enters the problem when working with the doubly ionized core states is that of configuration interaction. This is highlighted by the work of Codling et al[24-27], who pointed out the large amount of configuration interaction occuring in neutral states based on this core, so much so that they were unable to classify many of their observed features, especially in Kr and Xe. These effects will almost certainly be present in the resonance states based on this core, so the present assignments must be considered tentative.

The $[^3P]^{++}(n+1)s(n+1)p^2$ terms seem to be the best ones to consider using the graphical approach. Two features have been classified in Ne[10] at 44.05 eV and 44.37 eV. These features occur strongly in the present data, particularly the one at higher energy, so it is very probable that simi-

lar features will occur in the other gases. In Ar two strong features are observed at 28.30 and 28.57 eV, and in Kr, two features are apparent at 24.08 and 24.51 eV, making them possible candidates for this classification. As can be seen from Fig. 3.10(a), rather good straight lines can be drawn to link these points. Fig 3.10(c) shows the plot of binding energy vs resonance energy for these core configurations. The straight lines linking equivalent resonances are lines of best fit to the data. It should be noted that the slopes are much larger for the doubly ionized core states than they were for the singly ionized core states, and that the fit is not as good. This reflects the increased difficulties in assignments, the increased influence of core penetration effects, and probably also increased correlation effects.

At higher energies the $[^1D]^{++}$ and $[^1S]^{++}$ configurations will become involved and probable resonances based on these cores are included in the tables. These will be discussed in the following sections.

In order to carry out a more detailed comparison with the data of other authors, it is helpful to consider each gas separately, as has been done in previous literature.

3.4.2 Neon

This is the most widely studied of the heavy rare gases and classification of the major resonances is reasonably sure, as discussed previously. A few additional points,

however, might be made:

(1) The inaccuracies in the widths given in Table 3.2 are largely due to difficulties in properly fitting the data. Considerable increase in the statistical accuracy of the data would be needed to gain any significant improvement here. Also, a more sophisticated fitting routine, one that could handle overlapping features, might give more reliable results.

(2) The only previous data obtained using the metastable channel is that of Huard et al[12]. Their data(curve a) is compared with a sample of the present data(curve b) in Fig. 3.6(b). The greatly increased resolution over their results is quite evident. Also shown in Fig. 3.6(b) is the broadband photon data of Veillette and Marchand[11](curve c). Although the overall shape of the photon spectrum is quite different from our data, there is an almost one to one correspondence in the number and position of the features. This adds weight to Spence's suggestion that these authors may be seeing much more negative ion resonance structure than they thought[32].

(3) The designations in Table 3.2 are taken from Spence[10] with one exception. The relative strength of the $[^3P]^{++}3s3p^2$ resonances seems to suggest that similar structures could be

associated with the $[^1D]^{++}$ core. It should be
noted from Fig. 3.10(c) that the binding ener-
gies of this configuration in Ne appear to be
independent of the core configuration. Thus,
knowing the $^3P-^1D$ splitting, it is possible to
make a good prediction of the energy of the
$[^1D]^{++}3s3p^2$ configuration. Feature 1 is there-
fore given this designation rather than the
$[^2S]^+5s5p$ designation given by Spence.

3.4.3 Argon

The spectrum obtained for this gas is given in Fig. 3.7
and is essentially identical to the one obtained by Marchand
and Cardinal[17]. Any small differences may be attributed to
the rather better energy resolution of the present work
and/or to the effect of background subtraction techniques
used in the two experiments.

Marchand and Cardinal assumed that the majority of their
features were due to the decay of doubly or singly excited
neutral states, but, based on our experience with Ne, a
different approach, with resonances being responsible for
the major features, is suggested.

To justify this first consider the results of the two
techniques known to be very sensitive to resonance detec-
tion, namely electron transmission spectroscopy[8] and differ-
ential inelastic electron scattering[13]. In the case of Ne
very good agreement was obtained between the present data

and that obtained with these techniques. A comparison of the work of the two groups mentioned reveals an almost one to one correspondence between the two sets of data with the exception that Sanche and Schulz[8] observe a sharp feature at 27.41 eV and also some unlisted features around 30 eV not seen by Roy and Carette[13]. This slight difference is probably due to the fact that Roy and Carette were using a single observation channel $(3p^54s(^1P))$, whereas Sanche and Schulz's technique integrated over all channels.

The vertical lines plotted on Fig. 3.7 are taken from the data observed by Sanche and Schulz and Roy and Carette and the close correspondence observed between their data and many of our features is evident. Therefore these features are denoted as resonances in Table 3.2 and the techniques discussed previously were used to aid in their classification.

Features Based On $[3s3p^6(^2S)]^+$ Cores

The features below 29.23 eV are candidates for states based on this core. The first three features, a, b and c, have all been recognized as resonances by Roy and Carette and were also noted by Sanche and Schulz. The classifications in Table 3.2 follow that of Roy and Carette[13]. It should be noted that in further support there is good agreement between the observed values and predictions based on the graphical approach(illustrated on Fig. 3.9(a) and (b)). Marchand and Cardinal[17] identify their feature A at 24.55 eV as a resonance but prefer neutral states for the other two

features.

Features d and e also seem to be good candidates for resonances based on this core, with classifications $5s^2(^2S)$ and $5s5p(^2P)$ respectively. Roy and Carette assign the possible $5s^2(^2S)$ classification to features which they observe at 26.92 and 27.15 eV but, assuming that the equivalent $4s^2(^2S)$ designation is correct in Ne, the graphical approach would suggest that these assignments are incorrect, and that this state must lie considerably higher in energy than these. It is more probable that the features they observe are resonances based on the $[3s^23p^4]^{++}(^3P)$ core as discussed later. Feature f could have a contribution from $[3s3p^6](^2S)6s6p$ which is predicted to occur at 28.44 eV, but quite likely there is overlap with the $[3s^23p^4](^3P)4s4p^2$ configuration which is expected in this region. Marchand and Cardinal suggest that their feature J at 27.95 eV could have a contribution from this configuration.

It should be noted that resonances where the two electrons have different principal quantum numbers or those involving d electrons have not been considered in this analysis, for reasons discussed in the literature[30,33].

Features Based On $[3s^23p^4]^{++}$ Cores

Both Sauche and Schulz and Roy and Carette observe a couple of features close to 27 eV. A dip in that region is consistently observed in the present data. It is designated x in Table 3.3 because of its weak statistical significance. Assuming that these features are resonances, for the reasons

given in the previous section, it is unlikely that they are associated with the ^2S core, as suggested by Roy and Carette. The only real alternative is the $[3s^23p^4](^3P)4s^24p$ configuration. Support for this identification comes from Fig. 3.10(a) and (b) where the slope of the line·linking the equivalent resonance in Ne with the feature at .27 eV in Ar is consistent with the slopes of the lines linking the known $(^3P)4s4p^2$ terms, with the slight change(in slope) reflecting the change in the core perturbation effects. A further bit of information in favour of this identification with the ^3P core is the fact that the splitting(close to 0.2 eV) observed by both Sanche and Schulz and Roy and Carette closely matches the known splitting (0.195 eV) of the $Ar^{++}(^3P)$ term. Finally, if the modified Rydberg equation is used to predict the energy of this configuration, a value close to 27 eV is obtained.

As mentioned earlier in section 3.4.1, it seems very plausible to associate features f and g with the $(^3P)4s4p^2$ configuration, although feature f may be a composite involving $(^2S)6s6p$ as discussed previously. The Rydberg analysis lends additional support to this designation. Marchand and Cardinal suggest that the $(^3P)4s4p^2$ configuration may contribute to their feature at 27.95 eV, a suggestion also put forward by Lefaivre and Marmet for their feature some 10 meV higher in energy[34].

An examination of Fig. 3.10(c) shows that the binding energy of equivalent resonances is almost independent of the

core configuration in Ne, and this suggests that the same would be true in the other rare gases as well. This approximation turns out to be less valid in the cases of Ar and Kr, but it does allow a rough estimate of the energies of resonances based on the ^1D and ^1S cores, knowing the core splittings of the parent ion. This suggests that the strong feature k, near 29 eV, and also the features observed by Sanche and Schulz and by Roy and Carette near this same energy should have the $(^1D)4s^24p$ classification. The relative strengths of this configuration based on the ^1D and ^3P cores is consistent with what was observed in Ne. The observed 2 eV splitting between the ^1D and ^3P terms is close to the known (1.74 eV) splitting of the core. It should be stressed that configuration interaction effects are known to be very strong for doubly excited states based on these cores, so this classification must be viewed as tentative.

In a similar fashion, the feature m, at 31.30 eV and those of Sanche and Schulz and Roy and Carette at about the same energy may be identified with the $(^1S)4s^24p$ configuration. Here the observed splitting is 4.22 eV, compared with the known $^3P-^1S$ splitting of 4.12 eV. Feature l is also a candidate for this classification.

The final assignments given in Table 3.3 are made by assuming that the separation of the $4s^24p$ and $4s4p^2$ configurations are approximately independent of the core. This is consistent with the approximate independence of the binding energies with the core configurations. Thus, based on the

previous identifications for the ^3P core, features j and k are linked with the ^1D core while o and p are linked with the ^1S core. Clearly, a lack of precise knowledge of the configuration interaction effects involved, along with the large number of possible states which could arise from a combination of three electrons, precludes more definitive statements about the classification. Lefaivre and Marmet[34] identify the $(^1D)4s4p^2$ term with their feature at 29.58 eV, somewhat lower in energy than suggested here.

Note that when the states identified as in Table 3.3 are plotted on Fig. 3.10(a) along with the equivalent state of Kr, rather good straight lines are obtained. This adds some support to the identification, as does the Rydberg analysis (done in section 3.4.6).

3.4.4 Krypton

The spectrum obtained for this gas is shown in Fig. 3.8 and the data for the most prominent features are tabulated in Table 3.4. Also given in the table are resonance data from other sources for comparison purposes. Table 3.4 reveals again the close correspondence between the electron transmission work of Sanche and Schulz[3] and the inelastic electron scattering data of Roy et al[14]. Thus, the same procedure as was used for Ar will be used for Kr, namely working under the assumption that the features observed by these authors were predominantly resonances rather than neutral autoionizing states. Where a feature in Fig. 3.8 corresponds to one observed by these workers it is assumed that

a resonance is responsible and the techniques discussed previously are used to aid in the identification. Two other techniques which employ electron impact, namely electroionization measurements[31] and broadband photon yield measurements[29], have revealed a wealth of structure most of which has been attributed to neutral autoionizing states. The resonances observed by these authors are also listed in Table 3.4.

Features Based On $[4s4p^6]^+(^2S)$ Cores

If it is assumed that the graphical approach works reasonably well with this core (as it did with Ar), then Fig. 3.9(a) and Fig. 3.9(b) can be used to predict where resonances based on this core will occur. These are listed in the second column of Table 3.4 and enable features a, b, e, h and i to be identified with the $5s^2$, $5s5p$, $5p^2$, $6s^2$ and $6s6p$ resonances respectively. Note that this classification agrees with Roy et al[14] for the first two features but not thereafter. They identify feature d, some 0.23 eV lower than e, with the p^2 resonance and suggest that the $6s^2$ resonance occurs at 25.35 eV, 0.45 eV below the predicted value and inconsistent with the trends of Fig. 3.9(a). Valin and Marmet[31] only suggest one resonance, the $4d^2$, based on this core. They identify a feature at 24.92 eV with this configuration. Boulay and Marchand[29] identify resonances $5s^2$ and $5s5p$ in good agreement with our features a and b, but suggest that the $6s^2$ resonance may occur at 25.40 eV in agreement with Roy et al[14].

In Kr there is clearly even more overlap of features based on different parent or grandparent cores than in the case of Ar, so precise identification becomes correspondingly more difficult. Feature h is probably a composite, and in fact both Sanche and Schulz[8] and Roy et al[14] identify two resonances in this region, probably one with a two electron configuration based on the ^2S core, and the other with a three electron configuration based on the ^3P core.

Features Based On The $[4s^2 4p^4]^{++}$ Cores

Because of the large core splitting involved here and also the large amount of configuration interaction which is to be expected[25], accurate identification of the features is very difficult. The overlap of different channels mentioned above introduces still further complications. For these reasons the proposed identifications given for the features in Table 3.4 should be regarded as fairly speculative. However, in spite of this, comparison of the Kr spectrum with those of Ne and Ar suggests some approaches which may be helpful. For example, experience with the other two gases indicated that resonances of the type $(^1D)(n+1)s^2(n+1)p$ and $(^1S)(n+1)s^2(n+1)p$ should show up quite strongly. In addition, if the binding energies of these configurations are approximately independent of the core configuration (as in Ne and Ar - see Fig. 3.10(c)) then these resonances should be separated by the $^1D-^1S$ core splitting of the parent ion. The known position of the $(^3P)5s^2 5p$ resonance near 23.4 eV helps to position approximately the resonances based on the ^1D and ^1S cores. These ideas suggest that the strong fea-

tures f at 25.04 eV and l at 27.19 eV can be identified in
this way. Their splitting of 2.15 eV can be compared with
the 2.28 eV splitting of the parent core. The Rydberg ana-
lysis also suggests that feature k at 26.89 eV should also
be considered with l for this classification.

Again analogously with Ne and Ar it is expected that a
pair of $(^3P)(n+1)s(n+1)p^2$ resonances, with the higher energy
one predominating, should be seen. By classifying features
c and d in this way we have a basis for identifying the same
outer configuration but based on the ^1D and ^1S cores. A ^1S
configuration can almost certainly be identified with fea-
ture m since it is the only strong feature in the expected
region above 28 eV. The ^1D ones are much more difficult to
identify because they will lie in a region where there is
much overlap with the resonances based on the ^2S core. All
features between 25.5 and 26.5 eV, namely g, h, i and j
should be considered for this identification, as indicated
in Table 3.4. Clearly, much further experimental and theor-
etical work is required to help elucidate this situation.

It should be added that the restriction to resonances
where the principal quantum numbers of all the excited elec-
trons are the same, a situation which seemed to hold for Ne
and Ar, may not be a valid assumption for Kr and Xe. In
addition, the discrimination against possible significant
contributions from neutral states may be an over-simplifica-
tion.

The present assignments are rather different from those of Roy et al[14] for all of the resonances based on these cores with the exception of $(^3P)5s^25p$ and $(^1D)5s5p^2$. They suggest a $(^2S)4d^2$ assignment for the strong feature, f, near 25 eV (compared with $(^2S)6s^2$ at 25.36 eV). They assign a $(^1D)5s4d^2$ configuration at 26 eV, and their other assignments include a number of Wigner cusps associated with neutral states.

Valin and Marmet[31] have suggested resonance assignments based on this core for some of their features observed in the total ionization yield and these are noted in Table 3.4. They assign $(^3P_2)5s^25p$ to the feature they observe at 22.68 eV. Roy et al[14] suggest that their feature at 23.33-23.50 eV, some 0.7 eV higher in energy, has a similar outer configuration, but is based on the $(^3P_{0,1})$ cores. The separation is fairly consistent with the splitting (~0.6 eV) between the $^3P_2$ and $^3P_{0,1}$ terms of the bare core. No feature near 22.7 eV was observed in the present work, but this is not suprising since the $(^3P)5s^25p$ resonances decay weakly into the metastable channel. Valin and Marmet[31] agree with the present identification of the $5s5p^2$ configuration based on the ^3P and ^1D cores as indicated in Table 3.4. Their other resonance feature at 24.5 eV is attributed to $(^1D)5s^25p$ based on their assignment of the $(^3P_2)5s^25p$ resonance at 22.68 eV and the expected splitting of the terms.

Boulay and Marchand[29] also observe numerous features in this energy region in their integrated photon yield. How-

ever, they only attribute one of these (at 23.80 ev) to the
resonance $(^3P_2)$ 5s5p^2 based on this core. This is in reason-
able agreement with the present assignment of the feature
near 24 eV in Fig. 3.3.

None of the other authors suggest that any of their fea-
tures could be due to resonances based on the ^1S core.

3.4.5 Extension to Xe

Although no measurements were made with Xe as a target
gas it is possible to make some predictions based on the
graphical analysis. The work indicates that resonances
based on the $[nsnp^6](^2S)$ cores are more or less well behaved
and that the graphical approach works fairly well with them.
Thus Fig. 3.9(a) can be used to predict the energies of the
Xe$^-$ resonances based on this core. The results of this are
given in Table 3.5, along with the data of Sanche and
Schulz[8] and Delage et al[15] for comparison purposes.

It is obvious from Table 3.5 that there is good agreement
between the prediction for the $6s^2$ resonance and the obser-
vations of both sets of authors. This adds weight to the
other predictions since the identification of the $6s^2$ reso-
nance is well established. The present prediction also con-
firms the assignment of Delage et al of their feature at
19.38-19.55 eV as $6s6p(^2P)$ and at the same time rules out
their suggested designation of the same configuration to a
feature at the significantly lower energy of 19.1 eV. This
illustrates the usefulness of the technique.

Table 3.5
Predicted and Observed Resonances in Xenon

Resonance Configuration	Predicted Energy (from Fig. 3.9)	Sanche and Schulz[8]	Delage et al. [15]
$[5s5p^6](^2S)6s^2(^2S)$	18.84	18.85-18.96	18.88-18.95
$[5s5p^6](^2S)6s6p(^2P)$	19.37	19.4(a)	19.38-19.55
$[5s5p^6](^2S)6p^2$	20.81		[20.89-21.10]
$[5s5p^6](^2S)7s^2$	21.73		[21.64-21.79]
$[5s5p^6](^2S)7s7p$	22.02		[22.04-22.26]

(a) Feature not listed by authors but apparent on figure.

Energies in brackets indicate that a different designation was given by the authors.

It can also be suggested that their designation of $(^2S)6p^2$ to their feature 6-6' at 20.48-20.62 eV would be more appropriate to their feature 7-7' at 20.89-21.10 eV. They should probably also consider the $7s^2$ and $7s7p$ configurations for their features 9-9' and 10-10' in addition to the other possibilities which they list.

Making predictions for resonances based on the $[5s^25p^4]^{++}$ cores will be far less reliable than they were for the ^2S core since configuration interaction effects will almost certainly cause significant deviations from the simple relationships used. However, for the sake of completeness, these predictions are listed in Table 3.6, along with observations of other authors where they see features at or near the predicted energy. It should be stressed that these predictions are only speculative and indicate the approximate positions of these resonances that one might expect.

Future experiments are being planned to study the metastable excitation spectrum of Xe to examine the validity of some of these suggestions. However, it does seem clear from the work of Roy et al[14] and Delage et al[15] that as one progresses to the heavier rare gases, decay of neutral states becomes more significant in the inelastic scattering channel as compared to the decay of resonances. Clearly there remains a great deal of work to be done on this problem.

Table 3.6

Predicted and Observed Resonances in Xe:[$5s^25p^4$]++ Cores

Resonance Configuration	Predicted Energy (eV)	Sanche and Schulz[8]	Delage et al (ref 15)
(^3P) $6s^26p$	19.22		19.10
(^3P) $6s6p^2$	19.79	19.78-19.88	[19.73-19.87]
(^3P) $6s6p^2$	20.10-20.17		[20.05-20.19]
(^1D) $6s^26p$	21.15		
(^1D) $6s6p^2$	21.41		[21.25-21.40]
(^1D) $6s6p^2$	22.05		[22.04-22.26]
(^1S) $6s^26p$	23.17		[23.22]

Energies in brackets indicate that a different designation was given by the authors.

3.4.6 Application of the Modified Rydberg Equation

The framework of this equation was discussed in section
3.2.2, and now its application to the present data will be
examined.

Application to [nsnp⁶](²S)mlml' States

As discussed in section 3.2.2, one first requires a know-
ledge of the quantum defects for the ml and ml' electrons.
These can be deduced from the corresponding singly excited
neutral states, such as [core]+nl, for example, by using the
normal Rydberg equation. If the neutral state is split into
several components by magnetic interactions and exchange
effects, the center of gravity of the multiplet structure
must be used, as discussed by Read[23].

One of the significant things observed by Read was that
the value of σ, the screening constant, remained almost
constant for a given configuration in various gases. His
values of σ are listed in Table 3.7 for Ne, Ar, and Kr based
on the np⁵ cores. Notice that the value of σ is fairly
constant for equivalent configurations in each gas. This
suggests that one could evaluate the screening constants for
the $(n+1)s^2$, $(n+1)s(n+1)p$, $(n+1)p^2$, $(n+2)s^2$ and $(n+2)s(n+2)p$
configurations in Ne, and then use these values to predict
the energies of the equivalent resonances in the other rare
gases. These predictions are given in column 5 of Table
3.7. Also shown in Table 3.7 are the energies predicted
using the graphical approach (last column). As can be seen

TABLE 3.7

Observed and Predicted Energies: Singly Ionized-Cores

Gas	Configuration	Observed Energy (eV)	Screening Constants Present Data	Read (23)	Rydberg Analysis	Graphical Analysis
Neon	$(^2S)\,3s^2$	43.10	0.267	0.254		43.11
	$(^2S)\,3s3p$	43.67	0.225	0.216		43.68
	$(^2S)\,3p^2$	45.45	0.290	0.295		45.45
	$(^2S)\,4s^2$	46.53	0.291			46.53
	$(^2S)\,4s4p$	46.97	0.326			46.97
Argon	$(^2S)\,4s^2$	24.54		0.252	24.77	24.50
	$(^2S)\,4s4p$	25.05		0.225	25.07	24.99
	$(^2S)\,4p^2$	26.45		0.286	26.43	26.45
	$(^2S)\,5s^2$	27.57-27.72			27.50	27.63
	$(^2S)\,5s5p$	27.88			27.87	27.89
Krypton	$(^2S)\,5s^2$	22.79		0.252	23.46	22.83
	$(^2S)\,5s5p$	23.27		0.220	23.65	23.32
	$(^2S)\,5p^2$	24.74		0.276	24.83	24.74
	$(^2S)\,6s^2$	25.92			25.89	25.93
	$(^2S)\,6s6p$	26.20			26.23	26.18

Table 3.8
Observed and Predicted Energies: Doubly Ionized Cores

Gas	Configuration	Observed Energy	Screening Constants	Rydberg Analysis	Graphical Analysis
Neon	$(^3P)3s^23p$	42.11	0.262		42.09
	$(^3P)3s3p^2$	44.05	0.261		44.06
	$(^3P)3s3p^2$	44.36	0.268		44.35
	$(^1D)3s^23p$	45.25	0.262		45.25
	$(^1D)3s3p^2$	47.38	0.265		47.39
	$(^1D)3s3p^2$	47.64	0.270		47.64
	$(^1S)3s^23p$	48.02	0.263		48.98
Argon	$(^3P)4s^24p$	27.08		27.45	27.20
	$(^3P)4s4p^2$	28.30		28.88	28.26
	$(^3P)4s4p^2$	28.57		28.88	28.61
	$(^1D)4s^24p$	28.98		28.92	28.96
	$(^1D)4s4p^2$	29.86		30.46	29.83
	$(^1D)4s4p^2$	30.33		30.46	30.34
	$(^1S)4s^24p$	30.90		31.28	
	$(^1S)4s^24p$	31.30		31.28	31.12
	$(^1S)4s4p^2$	32.12		32.94	
	$(^1S)4s4p^2$	32.40		32.94	
Krypton	$(^3P)5s^25p$	23.39		23.27	23.29
	$(^3P)5s5p^2$	24.08		24.74	24.11
	$(^3P)5s5p^2$	24.51		24.74	24.48
	$(^1D)5s^25p$	25.04		24.56	25.05
	$(^1D)5s5p^2$	25.59		26.10	25.61
	$(^1D)5s5p^2$	26.20		26.10	26.19
	$(^1S)5s^25p$	27.19		26.77	27.01
	$(^1S)5s5p^2$	28.80		28.31	

there is rough agreement between the observed energies and those predicted by the modified Rydberg equation, and that the graphical approach appears to work much better in most cases.

The reason that the modified Rydberg formula approximates the resonance energies is of course, that the screening is deduced from the data, and that the core interaction is built into the quantum defects. What this formula will not handle well at all is the fact that configuration interaction will probably have an effect on the screening constants as one goes from Ne to Kr, and and also, the interaction of the core with two electrons will not be quite the same as a core-one electron case.

Application to Doubly Ionized Cores

The present work also provides an opportunity to test an extension of the modified Rydberg equation to a system of three electrons attached to a positive ion core. It should be pointed out, however, that correlation effects will probably make this approach somewhat unreliable.

Proceeding as in the case of the ^2S core, the quantum defects for the [core]$^{++}$nl electrons are deduced from known data[35] and then the screening constants for Ne are calculated. These constants are then used to predict the resonance energies in the other gases, and the results are given in Table 3.8. As can be seen from the table, surprisingly good agreement between predicted and observed values is obtained, considering the possible problems mentioned above.

3.5 CONCLUSIONS AND SUGGESTIONS

3.5.1 Conclusions

Metastable excitation spectra in the doubly excited state region have been obtained for the rare gases Ne, Ar and Kr. The most prominent features in these spectra have been identified with negative ion resonances based on the $[nsnp^6]({}^2S)$ and $[ns^2np^4]({}^3P, {}^1D, {}^1S)$ cores, and similarities between equivalent resonances in the different gases have been demonstrated.

The graphical approach used by Spence to analyze negative ion resonances below the first ionization threshold in these gases has been extended to the higher energy region and has been shown to work very well in the present case. The method works particularly well for features based on the ${}^2S$ cores and hence the identification of these resonances is reasonably sure. This approach has been shown to work for features based on the ${}^3P$, ${}^1D$ and ${}^1S$ cores, but because of the effects of configuration interaction and the large number of possible terms involved, the classifications of these features must be regarded as tentative.

In addition to demonstrating the power of the graphical approach as a tool for identifying resonances, the deviations from the linear behaviour of binding energy vs resonance energy have been considered and were suggested to be related to perturbations of the outer electrons by the positive ion core. The significance of the slope of the line

joining equivalent resonances in such a plot has also been considered, and has been shown to be related to the amount of interaction between the core and the outer electrons.

The modified Rydberg equation proposed by Read has been applied to the present data. Effective screening constants were deduced from the Ne data, and following Read, these were used to predict the energies or equivalent resonances in Ar and Kr. It was found that the predicted energies were not as good as energies given by the graphical approach, differing from the experimentally determined energies by several hundred meV in some cases. It was also found that the effective screening constants deduced from the data were close to the values expected for completely correlated electrons, particulary when two outer electrons were considered. From this result it can be concluded that a high degree of correlation between the outer electrons is to be expected for these resonances.

Based on the relative success of the graphical approach in Ne, Ar, and Kr, the energies of the equivalent resonances in Xe were predicted. A comparison of these predicted energies with the results of other authors indicated that there were indeed features present at or near the predicted energy, although in many instances the observed features were not classified as negative ion resonances by these authors.

Comparisons of the present data were made with the data of other authors. In many cases there was disagreement bet-

ween the present classification scheme and the classifica-
tions given to similar features by these authors. Agreement
was found between our data and the data of authors who used
techniques which were sensitive to the detection of negative
ion resonances, thus adding weight to the present conclu-
sions.

Finally, widths were determined for some of the more iso-
lated features in the spectra. Because of the statistical
uncertainty in the data it was not possible to determine the
widths with any great precision. Also, uncertainties were
introduced because of the overlapping of features in some
instances.

3.5.2 Suggestions for Future Research

It can be seen that there is still a great deal of work
to be done with the rare gases in connection with negative
ion resonances. Several avenues of approach can be envi-
sioned for future experimental work:

(1) A study of the metastable excitation functions
for Xe in the doubly excited state region.
This can be used to test the predictions of
the graphical approach for this gas, as well
as to look for a continuation of the similari-
ties between equivalent resonances as was
found for Ne, Ar and Kr. Because the metasta-
ble excitation energies are lower in Xe than
the other rare gases, a special low-workfunc-
tion detector is currently being developed for

use with this target gas.

(2) A continuation of the present work with the aim of obtaining a significant improvement in the statistical accuracy of the data, allowing an examination of the finer details superimposed on the major features to be carried out.

(3) An extension of the present work to even higher impact energies. It would be useful to look for higher lying members of the Rydberg series based on the ^2S core in particular, so that a true multichannel quantum defect theory could be used to analyze the data.

(4) To further aid in the identification and classification of resonances, differential inelastic scattering studies will be performed. This type of experiment will also allow the contributions of different partial waves to the scattering process to be evaluated, as well as the branching ratios into different decay channels.

(5) To aid in the assignment of energies to features observed in the metastable channel, more sophisticated data analysis techniques should be developed. In particular, a technique which would be able to handle overlapping spectral features would be extremely useful.

3-6 APPENDICES

3.6.1 Ionization Potentials for the Rare Gases

Gas	Configuration	Ionization Potential (eV)
Neon	$[2s2p^6](^2S)+$	48.463
	$[2s^22p^4](^3P_2)++$	62.512
	$[2s^22p^4](^3P_1)++$	62.593
	$[2s^22p^4](^3P_0)++$	62.627
	$[2s^22p^4](^1D_2)++$	65.712
	$[2s^22p^4](^1S_0)++$	69.422
Argon	$[3s3p^6](^2S)+$	29.231
	$[3s^23p^4](^3P_2)++$	43.375
	$[3s^23p^4](^3P_1)++$	43.513
	$[3s^23p^4](^3P_0)++$	43.570
	$[3s^23p^4](^1D_2)++$	45.112
	$[3s^23p^4](^1S_0)++$	47.458
Krypton	$[4s4p^6](^2S)+$	27.507
	$[4s^24p^4](^3P_2)++$	38.350
	$[4s^24p^4](^3P_1)++$	38.914
	$[4s^24p^4](^3P_0)++$	39.009
	$[4s^24p^4](^1D_2)++$	40.165
	$[4s^24p^4](^1S_0)++$	42.450
Xenon	$[5s5p^6](^2S)+$	23.395
	$[5s^25p^4](^3P_2)++$	33.110
	$[5s^25p^4](^3P_1)++$	34.324
	$[5s^25p^4](^3P_0)++$	34.106
	$[5s^25p^4](^1D_2)++$	35.230
	$[5s^25p^4](^1S_0)++$	37.746

3.6.2 Calculation of σ

This appendix briefly describes the relationship between the screening constant used in the Modified Rydberg Formula and electron correlations. To illustrate this we will confine ourselves to the situation where the outer electrons are _completely_ correlated.

$$-e \bullet \!\!-\!\!-\!\!-\!\!-\!\!-\!\!-\!\!\underbrace{r_1}\!\!-\!\!-\!\!-\!\!-\!\!-\!\!-\!\! \left(+Ze\right) \!\!-\!\!-\!\!-\!\!-\!\!-\!\!-\!\!\underbrace{r_2}\!\!-\!\!-\!\!-\!\!-\!\!-\!\!-\!\! \bullet -e$$
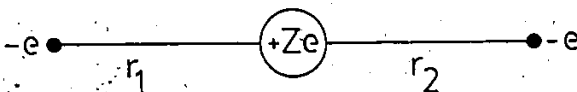
$$r_1 = r_2 = r$$

Consider first the case for two outer electrons, as shown above. The electrons are on opposite sides of the core, and at the same distance from the core. The potential energy of this system is given by:

$$V(r) = -\frac{Ze^2}{r_1} - \frac{Ze^2}{r_2} + \frac{e^2}{r_1+r_2} \qquad (3.6.1)$$

where Z is the charge of the core. Using the fact that the radii are equal yields:

$$V(r) = -\frac{2(Z-0.25)e^2}{r}$$

(3.6.2)

Thus the effective charge seen by each electron is $Z-0.25$, and so the screening constant has the value of 0.25.
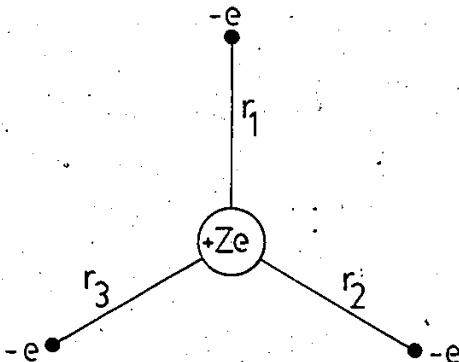
$$r_1 = r_2 = r_3 = r$$

Now consider the case of three correlated electrons, as shown above. These should sit on the "vertices of an equilateral triangle", and the potential energy of the system is:

$$V(r) = -\frac{Ze^2}{r_1} - \frac{Ze^2}{r_2} - \frac{Ze^2}{r_3} + \frac{e^2}{r_{12}} + \frac{e^2}{r_{13}} + \frac{e^2}{r_{23}}$$

(3.6.3)

and the separation between each electron is:

$$r_{ij} = \sqrt{3}\, r$$

Thus the effective potential seen by one electron (due to the core field and the other two electrons) is

$$V(r) = -(Z-2(0.289))e^2/r$$

(3.6.4)

which gives the screening constant a value of 0.289.

3.6.3 Background Subtraction

Recall from section 3.3.2 that the features of interest in the metastable excitation spectra were highlighted by removal of the large background present in the data. In many cases, this background was highly "non-linear", so a subtraction routine was written that would remove the low frequency oscillations(see ref. 36). This was done by an averaging routine which replaced the point $y(i)$ by:

$$y(i) \longleftarrow [y(i-1) + 2y(i) + y(i+1)]/4$$

except for the endpoints of the spectrum, which were obtained by:

$$y(1) \longleftarrow [y(1) + y(2)]/2$$

$$y(n) \longleftarrow [y(n-1) + y(n)]/2$$

This was repeated a large number of times, usually 100-1000 passes through the data, and then this smoothed data was subtracted from the original data, leaving behind the small features to be studied.

CHAPTER 4

POLARIZATION CORRELATION EXPERIMENTS WITH SIMPLE MOLECULES

4.1 INTRODUCTION

The subject of electron-photon coincidence experiments has received a great deal of attention over the past 12 years since the initial theoretical work of Macek and Jaecks[37]. A massive effort has been put into angular and polarization correlation studies[38-50] and related topics[51,52], both experimentally and theoretically. Electron-photon coincidence studies yield basic information about the magnitudes and relative phases of the scattering amplitudes which describe the scattering process, and also information about the elements of the density matrix which describes the excited state. Such studies provide the most sensitive tests of existing theoretical approximations.[53-58]

Most of the experimental work has been concentrated on He[41-47,59], because the situation is relatively simple. He can be described by LS coupling, and there are no fine or hyperfine structure effects to contend with. Some work has also been done with Ne[46], Ar[48,60,61], as well as with atomic hydrogen[49,50,65]. Some work has also been performed with Hg as a target gas[66], as well as with Kr[62] and the heavy rare gases[63]. Spin polarization effects have also been under investigation in electron-photon coincidence experiments[64]. Very little work has been done with molecules. The only previous study has been a preliminary investigation of polarization correlation in H_2 by McConkey and Malcolm[61]. On the theoretical side, the only treatment which exists is the density matrix formalism of Blum and Jakubowicz for

molecules obeying Hund's Case (b) coupling[67].

The present work examines the excitation of the $C4\,^1\Sigma_u^+$ state of N_2 and the $C^1\Pi_u$ state of H_2 using the electron-polarized photon coincidence technique. Two Stokes' parameters of the emitted radiation were measured as a function of incident electron energy and electron scattering angle. Because the radiation lies in the VUV spectral range, no measurements of circular polarization were possible.

This work begins with a theoretical framework necessary to understand the coincidence experiments. This is done in section 4.2. Section 4.3 describes the details of the experiment and the reduction of coincidence spectra to obtain the Stokes' parameters. Section 4.4 contains the experimental results and a discussion of the data obtained. Lastly, section 4.5 puts forward some conclusions and suggestions for future research.

4.2 THE THEORETICAL FRAMEWORK

4.2.1 Introduction

In this section a discussion of the theory upon which an electron-photon coincidence experiment is based is presented. The first topic of discussion is polarized light and the Stokes' parameters and how they can be determined by a series of polarization measurements. Next a review of coincidence experiments with He is given, using the density matrix formalism, followed by the density matrix approach applied to molecules. Lastly, a discussion of threshold polarization of molecular radiation and pseudo-threshold polarization measurements is presented.

4.2.2 Polarized Light and the Stokes' Parameters

Consider the diagram illustrated in Fig. 4.1. This shows schematically a source of polarized light being observed from the y-direction. In this case, the light source consists of two dipole oscillators, one oscillating along the z-direction, and one oscillating along the x-direction. In general the two dipoles can be described by both a magnitude and a phase angle. Now this light source can be character- ized by 4 quantities known as the Stokes' parameters. These parameters are:

(1) The total unpolarized intensity, I, of light observed in the y-direction.

(2) The degree of linear polarization, S_3, mea- sured with respect to the two orthogonal axes

$$\hat{e}(\beta) = \cos\beta\,\hat{z} + \sin\beta\,\hat{x}$$

$$\bar{p}_z = a_z e^{i\phi_z}\hat{z}$$

$$\bar{p}_x = a_x e^{i\phi_x}\hat{x}$$
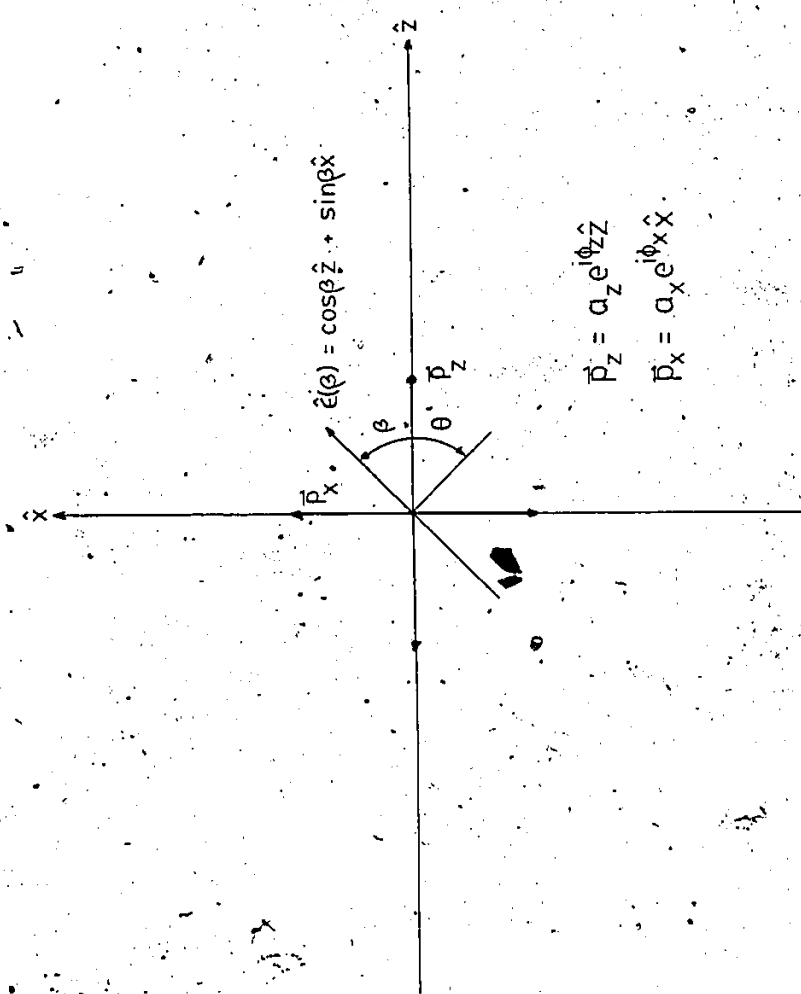
FIG. 4.1, Polarized Light Source

z and x.

(3) The degree of linear polarization, s_1, mea-
sured with respect to two orthogonal axes
oriented at 45 degrees to z and x.

(4) The degree of circular polarization, s_2.

The first three parameters can be determined by placing a linear polarizer between the source and the detector. If the 'polarization vector' of the polarizer, $\hat{e}$, is rotated through an angle β with respect to the z axis, then:

$$\hat{e}(\beta) = \cos\beta\, \hat{z} + \sin\beta\, \hat{x} \qquad (4.2.2.1)$$

If $E(y)$ is the observed electric field along the y axis, then the observed intensity transmitted by the polarizer is given by:

$$I(\beta) = |E(y)\hat{e}(\beta)|^2 \qquad (4.2.2.2)$$

and the Stokes' parameters are given by:

$$I = I(0)+I(90)$$
$$Is_3 = I(0)-I(90)$$
$$Is_1 = I(45)-I(135)$$

The degree of circular polarization can be measured by inserting a quarter-wave plate in front of the linear polarizer and measuring the intensities at 45 and 135 degrees, and it is given by:

$$Is_2 = I(RHC)-I(LHC)$$

where $I(RHC)$ is the intensity of Right Hand Circularly polarized light, and $I(LHC)$ is the intensity of Left Hand Circularly polarized light.

The electric field along the y direction produced by the two dipole oscillators is given by:

$$\vec{E}(\hat{y},t) = e^{i\omega t}(a_z e^{i\phi z}\,\hat{z} + a_x e^{i\phi x}\,\hat{x})\qquad(4.2.2.3)$$

If the x component of the electric field is subject to a retardation η (by a quarter-wave plate, for example), the field is then given by:

$$\vec{E}(\hat{y},t) = e^{i\omega t}(a_z e^{i\phi z}\,\hat{z} + a_x e^{i(\phi x+\eta)}\,\hat{x})\qquad(4.2.2.4)$$

Using this in equation 4.2.2.2 along with eq 4.2.2.1 gives the intensity of light transmitted by the polarizer:

$$I(\beta;\eta) = a_z^2\cos^2\beta + a_x a_z\cos(\delta-\eta)\sin2\beta + a_x^2\sin^2\beta\qquad(4.2.2.5)$$

where δ is the relative phase (apart from the retardation η) between the z component and the x component of the field. Equation 4.2.2.5 can now be used to express the Stokes' parameters in terms of the oscillator amplitudes and the relative phase. With $\eta = 0$, the first three parameters are given by:

$$I = a_z^2 + a_x^2\qquad(4.2.2.6a)$$

$$Is_3 = a_z^2 - a_x^2\qquad(4.2.2.6b)$$

$$Is_1 = 2a_z a_x\cos\delta\qquad(4.2.2.6c)$$

The insertion of a quarter wave plate is equivalent to putting the retardation η to $\pi/2$, and the circular polarization is then given by:

$$Is_2 = 2a_z a_x \sin\delta \qquad (4.2.2.6d)$$

By measuring the Stokes' parameters, the oscillator ampli-
tudes and their relative phase can be determined. Once this
is done the complete angular distribution of the emitted
radiation can be found. From electrodynamics, the electric
field of a dipole observed in the direction $\hat{n}$ is given by (in
the radiation zone):

$$\vec{E}(\hat{n}) = \vec{p} - \hat{n}(\hat{n}\cdot\vec{p})$$

Now the dipole moment is given by:

$$\vec{p} \sim a_z \hat{z} + a_x e^{i\delta}\hat{x}$$

and the unit vector $\hat{n}$ (in spherical polar coordinates) is:

$$\hat{n} = \sin\theta \cos\phi\, \hat{x} + \sin\theta \sin\phi\, \hat{y} + \cos\theta\, \hat{z}$$

The intensity is proportional to $|E|^2$, and is given by:

$$(4.2.2.7)$$
$$I(\theta,\phi) = a_z^2\sin^2\theta + a_x^2(1-\sin^2\theta\cos^2\phi)-a_z a_x\cos\delta\sin2\theta\cos^2\phi$$

The intensity pattern in the x-z plane is of particular
interest in coincidence experiments, and this is given when
$\phi=0$:

$$I(\theta) = c\,(a_z^2\sin^2\theta - a_z a_x\cos\delta\sin2\theta + a_x^2\cos^2\theta)$$

where c is an appropriate constant. For 'historical' rea-
sons, the angle θ in the x-z plane is measured in the clock-
wise direction instead of the counterclockwise direction,
and this means that θ is negative in the above equation.
Thus the intensity is given by:

$$I(\theta) = c(a_z^2\sin^2\theta + a_z a_x\cos\delta\sin2\theta + a_x^2\cos^2\theta) \quad (4.2.2.8)$$

This sign convention is now firmly entrenched in the literature, so to avoid any confusion it will be maintained throughout all subsequent discussions.

Another quantity of interest in coincidence experiments is the orientation of the radiation pattern in the x-z plane. This is specified by the angle at which the minimum intensity is observed. Differentiating eq 4.2.2.8 with respect to θ and setting the derivative equal to zero gives:

$$\tan2\theta = -\frac{2a_z a_x\cos\delta}{a_z^2 - a_x^2} \quad (4.2.2.9a)$$

Comparing eq. 4.2.2.9a with equations 4.2.2.6b and c, the orientation angle is given by:

$$\tan2\theta_{min} = -s_1/s_3 \quad (4.2.2.9b)$$

It is apparent from equation 4.2.2.8 that the oscillator amplitudes and the magnitude of their relative phase can be determined by measuring the angular distribution of the radiation in the x-z plane. This is equivalent to measuring the Stokes' parameters I, s_1 and s_3. In an electron-photon coincidence experiment, measuring the angular distribution of the radiation is known as _angular correlation_ and measuring the Stokes' parameters is known as _polarization correla-_

tion.   Note that only the magnitude of the circular polarization can be determined from angular correlations, and not its sign.

It should be emphasized that the above discussion assumed that the radiation was completely monochromatic.   If the radiation is quasi-monochromatic or made up of a large number of different frequencies then a time averaging must be performed on the observed intensity.   In such a situation the time-averaged amplitudes and relative phase must be used in the expressions for the Stokes' parameters.

One further point which should be noted is that the above example is completely coherent, in the sense that the total polarization, given by:

$$P = (s_1^2 + s_2^2 + s_3^2)^{1/2}$$
(4.2.2.10)

is equal to 1.   In general this is not the case, since there may be a large unpolarized contribution to the intensity. In this case the total polarization will be less than 1. This is equivalent to saying that the radiation is composed of an incoherent superposition of polarization states.

4.2.3 Coincidence Experiments With Atoms

To illustrate the usefulness of electron-photon coincidence experiments we now turn our attention to the atomic case.   Since angular correlation experiments are equivalent to polarization correlations experiments, the discussion will be restricted to the latter type of experiment.   We

shall further restrict the discussion to the density matrix
formalism and outline the steps necessary to arrive at
expressions for the Stokes' parameters. A complete discus-
sion can be found in Karl Blum's book Density Matrix Theory
and Applications which gives an excellent presentation of
the subject[68]. An excellent review article by Blum and
Kleinpoppen[69] also discusses this material.

Consider first the experimental geometry shown schemati-
cally in Fig. 4.2. The z axis is defined by the incident
electron beam and is used as the quantization axis. The
scattering plane is defined by the momenta of the incident
and scattered electrons, p and p'. Note that the scattering
plane is taken to be the x-z plane. Photons emitted by
atoms excited by collisions are observed in the y-direction
after passing through a linear polarizer which is rotated
about the y axis. The scattered electrons are analyzed for
both energy and scattering angle, determining the magnitude
and direction of p'. The measured coincidence rate between
the photons and scattered electrons thus comes from a suben-
semble of atoms that have been excited to the same state by
electrons scattered into the direction p'.

Having defined the experimental geometry we can now dis-
cuss the excitation process in terms of the density matrix
formalism. A number of assumptions are made in this discus-
sion, and these are:

  (1) The excitation and decay processes can be
      treated independently. This means that the

Scattered
Electrons

$\hat{z}$

θ_e

SCATTERING PLANE

$\hat{x}$

$\hat{\epsilon}(\beta)$ Polarizer

β

ϕ_γ

θ_γ

$\hat{y}$

Gas "Beam"

Incident Electrons
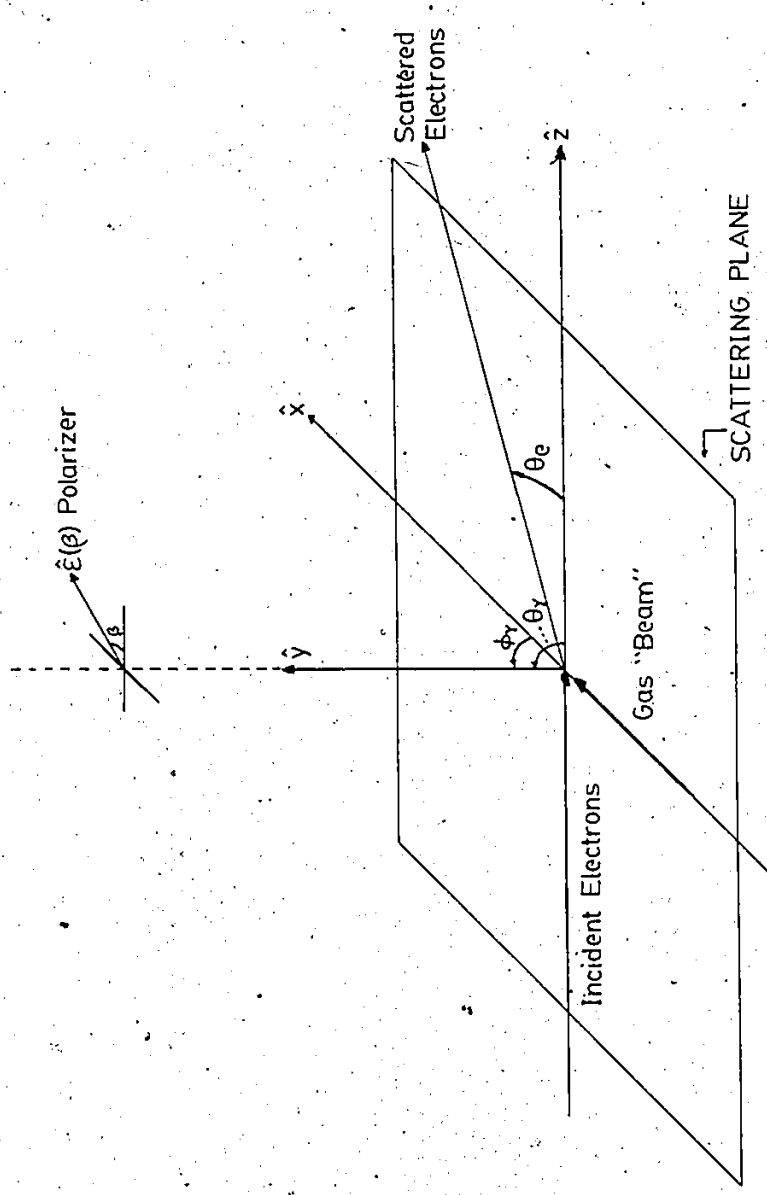
EXPERIMENTAL GEOMETRY

FIG 4.2

excitation is 'instantaneous'; i.e., it takes

place in a time which is much shorter than the

lifetime of the excited state and any spin-or-

bit precession times.

(2) The Hamiltonian describing the scattering pro-

cess contains no explicit spin dependent

— terms. Thus a change in spin can only occur

by electron exchange, which we shall not con-

sider.

(3) LS coupling is adequate to describe the atomic

states.

(4) No observation of initial and final spins of

*any particle is made.

(5) Both the incident electron beam and the ini-

tial atomic ensemble are unpolarized.

(6) The initial atomic ensemble has $L_0=0$ and all

atoms are in the ground state.

The states of the system are described by:

INITIAL STATE:

Atoms: $|n_0 L_0 S_0 M_{L_0} M_{S_0} > = |\alpha_0 S_0 M_{S_0} >; L_0 = M_{L_0} = 0$

Electrons: $|p_0 m_0 >$

EXCITED STATE:

Atoms: $|n_1 L_1 S_1 M_{L_1} M_{S_1} > = |\alpha_1 S_1 M_{L_1} >$

Electrons: $|p_1 m_1 >$

where m_0 and m_1 refer to the z component of the orbital

angular momentum of the incident and scattered electrons,

respectively.

The density matrix of the combined system of atoms+electrons

for the initial state is:

$$\rho_0 = \frac{1}{2(2S_0+1)(2L_0+1)} \sum_{m_0 M_{L_0} M_{S_0}} |\alpha_0 S_0 P_0 M_{S_0} m_0 \rangle \langle \alpha_0 S_0 P_0 M_{S_0} m_0|$$

With the restriction that $L_0=0$, ρ_0 can be written as:

$$\rho_0 = \frac{1}{2(2S_0+1)} \sum_{m_0 M_{S_0}} |\alpha_0 S_0 P_0 M_{S_0} m_0 \rangle \langle \alpha_0 S_0 P_0 M_{S_0} m_0| \qquad (4.2.3.1)$$

and its matrix elements are given by:

$$\langle \alpha_0 S_0 P_0 M'_{S_0} m'_0 | \rho_0 | \alpha_0 S_0 P_0 M_{S_0} m_0 \rangle = \frac{\delta_{m'_0 m_0} \delta_{M'_{S_0} M_{S_0}}}{2(2S_0+1)} \qquad (4.2.3.2)$$

The scattering process is characterized by the <u>scattering amplitudes</u> $f(n_1 L_1 S_1 M_{L_1} M_{S_1} m_1; P_1 \Leftarrow n_0 S_0 M_{S_0} m_0; P_0)$ which are the matrix elements of the corresponding transition operator T. The density matrix describing the excited state is given by:

$$\rho_1 = T \rho_0 T^+ \qquad (4.2.3.3a)$$

and its matrix elements are given by:

$$\langle n_1 L_1 S_1 P_1 M'_{L_1} M'_{S_1} m'_1 | \rho_1 | n_1 L_1 S_1 P_1 M_{L_1} M_{S_1} m_1 \rangle =$$

$$\frac{1}{2(2S_0+1)} \sum_{m_0 M_{S_0}} f(n_1 L_1 S_1 M'_{L_1} M'_{S_1} m'_1; P_1 \leftarrow n_0 S_0 M_{S_0} m_0; P_0) \qquad (4.2.3.3b)$$

$$\times f^*(n_1 L_1 S_1 M_{L_1} M_{S_1} m_1; P_1 \leftarrow n_0 S_0 M_{S_0} m_0; P_0)$$

Since the spins of the scattered electrons and the excited atoms are not observed, the density matrix ρ_1 must be summed over the diagonal elements of the unobserved spin components M_{S_1} and m_1. The result is known as the <u>reduced density matrix</u> which describes the orbital states of the excited

atoms. This is given by:

$$\langle n_1 L_1 S_1 M'_{L_1}; p_1 | \rho_1 | n_1 L_1 S_1 M_{L_1}; p_1 \rangle = $$

$$(4.2.3.3c)$$

$$\langle f(n_1 L_1 S_1 M'_{L_1}; p_1 \leftarrow n_0 S_0 M_{S_0}; p_0) f^*(n_1 L_1 S_1 M_{L_1}; p_1 \leftarrow n_0 S_0 M_{S_0}; p_0) \rangle$$

where $\langle \ldots \rangle$ denotes the averaging over unobserved spins. For convenience of notation the dependence of the matrix elements on n_1, L_1, S_1, p_1, n_0, S_0 and p_0 will be suppressed since these are fixed. The reduced density matrix of the system is then given by:

$$\langle M'_{L_1} | \rho(L_1) | M_{L_1} \rangle = \langle f(M'_{L_1}) f^*(M_{L_1}) \rangle \qquad (4.2.3.4)$$

Note that the normalization of this density matrix is such that the trace is equal to the differential cross-section for exciting the state $|n_1 L_1 S_1\rangle$. For the case where $L_1=1$ the density matrix can be written out explicitly and is:

$$\rho_1(1) = \begin{pmatrix} \langle |f(+1)|^2 \rangle & \langle f(+1)f^*(0) \rangle & \langle f(+1)f^*(-1) \rangle \\ \langle f(0)f^*(+1) \rangle & \langle |f(0)|^2 \rangle & \langle f(0)f^*(-1) \rangle \\ \langle f(-1)f^*(+1) \rangle & \langle f(-1)f^*(0) \rangle & \langle |f(-1)|^2 \rangle \end{pmatrix}$$

It can be seen that the density matrix is Hermitian, and since the scattering amplitudes are complex, there are 6 independent parameters which are necessary to describe the density matrix, namely the magnitudes and relative phases of the scattering amplitudes. Symmetry considerations can be used to reduce the number of parameters needed. Because the scattered electrons are detected the symmetry of the system is reduced from axial to planar, and the system is invariant under reflections in the scattering plane. This gives the

condition that:

$$\langle M'|\rho|M\rangle = (-1)^{M'+M}\langle -M'|\rho|-M\rangle$$

for the density matrix and:

$$f(MM_{S_1}m_1,M_{S_0}m_0) = (-1)^{S_0+S_1-M} f(-M-M_{S_1}-m_1, -M_{S_0}-m_0)$$

for the scattering amplitudes. If spin conservation is also taken explicitly into account, the number of independent parameters needed to specify the density matrix is reduced to 4, and in the special case where $S_0=S_1=0$, the number is reduced to 3. In this case $f(M) = (-1)^M f(-M)$, and there is no need to perform a spin averaging. The density matrix is given by:

$$\langle M'|\rho_1|M\rangle = f(M') f^*(M) \qquad (4.2.3.5)$$

The parametrization used in the literature for this case is given by:

$$\sigma = f^2(0) + 2f^2(1)$$

$$\lambda = f^2(0)/\sigma$$

$$\cos \chi = \mathrm{Re}[f(0)f(1)]/\sigma$$

In general it is possible to excite states of different total angular momentum, and the density matrix must be written(in a $|JM\rangle$ basis) as:

$$\rho(J'J) = \sum_{M'M} \rho(J'M'JM)|J'M'\rangle\langle JM|$$

where the (J'M'JM) are the density matrix elements. The density matrix can be expressed in terms of its irreducible components, or _state multipoles_, by defining a new set of tensor operators $T(J'J)_{KQ}$:

$$T(J'J)_{KQ} = \sum_{M'M} (-1)^{J'-M'} (2K+1)^{1/2} \begin{pmatrix} J' & J & K \\ M' & -M & Q \end{pmatrix} |J'M'><JM| \quad (4.2.3.6)$$

The density matrix is expressed in terms of these operators as:

$$\rho = \sum_{J'JKQ} <T(J'J)_{KQ}^{\dagger}> T(J'J)_{KQ}$$

where $<T(J'J)_{KQ}^{\dagger}>$ are the state multipoles, given by:

$$<T(J'J)_{KQ}^{\dagger}> = \sum_{M'M} (-1)^{J'-M'} (2K+1)^{1/2} <J'M'|\rho|JM> \quad (4.2.3.7)$$
$$\times \begin{pmatrix} J' & J & K \\ M' & -M & -Q \end{pmatrix}$$

The state multipoles have the property:

$$<T(J'J)_{KQ}^{\dagger}> = (-1)^{K+Q} <T(J'J)_{K-Q}^{\dagger}>$$

For the case where the excited state has a well defined angular momentum $J'=J=L_1$, the state multipoles can be written as:

$$<T(L_1)_{KQ}^{\dagger}> = \sum_{M'_{L_1} M_{L_1}} (-1)^{L_1 - M'_{L_1}} (2K+1)^{1/2} \begin{pmatrix} L_1 & L_1 & K \\ M'_{L_1} & -M_{L_1} & -Q \end{pmatrix} \quad (4.2.3.8)$$
$$\times <f(M'_{L_1}) f^*(M_{L_1})>$$

Thus it can be seen that for $L_1=1$, the state multipoles $<T(1)_{00}^{\dagger}>$, $<T(1)_{11}^{\dagger}>$, $<T(1)_{20}^{\dagger}>$, $<T(1)_{21}^{\dagger}>$ and $<T(1)_{22}^{\dagger}>$ must be determined. Note that because of the symmetry properties of the state multipoles, $<T(J'J)_{K0}^{\dagger}>$ is 0 for odd K. Thus $<T(1)_{10}^{\dagger}>=0$.

The state multipoles have a much deeper physical signifi-

cance than the density matrix elements. For $K=0$, $\langle T(L)^{\dagger}_{00}\rangle$ is proportional to the differential cross-section and is:

$$\langle T(L)^{\dagger}_{00}\rangle = \sigma/(2L+1)^{1/2}$$

It can be shown for $K=1$ that:

$$\langle T(L)^{\dagger}_{1Q}\rangle \sim (3/(2L(L+1)(2L+1)))^{1/2}\sigma\langle L_Q\rangle$$

where L_Q are the spherical components of the orbital angular momentum. Thus the tensor with $K=1$ is related to the net amount of orbital angular momentum transferred to the atom during the collision. $\langle T(L)^{\dagger}_{1Q}\rangle$ are known as the components of the orientation vector. It turns out that only $\langle L_y\rangle$ is non-zero, and this is related to $\langle T(L)^{\dagger}_{11}\rangle$ by:

$$\langle T(L)^{\dagger}_{11}\rangle \sim -i\sigma/\sqrt{2}\,(3/(2L(L+1)(2L+1)))^{1/2}\langle L_y\rangle$$

Fig 4.3 illustrates a semiclassical model of grazing collisions, used to illustrate the production of orientation in atomic collisions. Electrons can be scattered into the direction of $\vec{p}_1$ by the long range attractive force due to the atomic polarizability as in Fig. 4.3(a), or by the short range repulsive force of the atomic electrons, as in Fig. 4.3(b). In the attractive case the atom acquires a net negative angular momentum and $\langle L_y\rangle < 0$. This will be the case for scattering into small angles. In the repulsive case, the atom acquires a net positive angular momentum and $\langle L_y\rangle > 0$. Scattering into large angles will be dominated by this effect.

Lastly, the tensors with $K=2$ can be shown to be:

$\vec{p}_{f_o}$
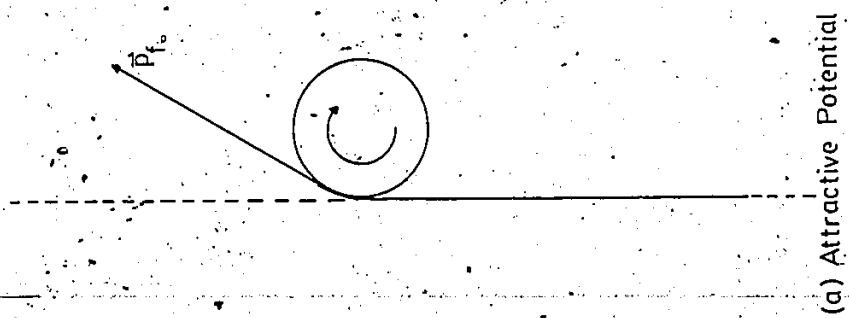
(a) Attractive Potential

$\vec{p}_f$
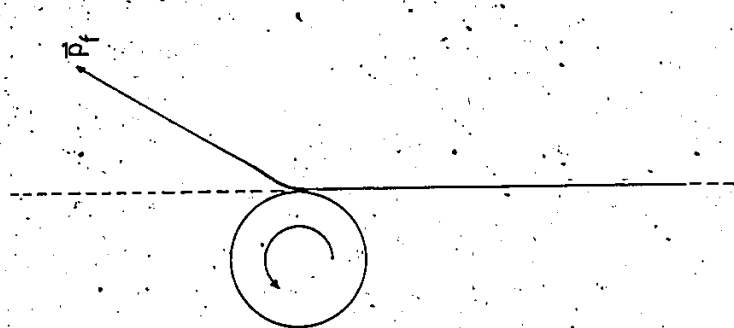
(b) Repulsive Potential

FIG 4.3 Semiclassical Grazing Collisions

$$\langle T(L)_{20}^{\dagger}\rangle \sim \langle 3L_z^2 - L^2\rangle\sigma/\sqrt{6}$$

$$\langle T(L)_{2\pm1}^{\dagger}\rangle \sim \pm\langle L_xL_z + L_zL_x\rangle\sigma/\sqrt{2}$$

$$\langle T(L)_{2\pm2}^{\dagger}\rangle \sim \langle L_x^2 - L_y^2\rangle\sigma/2$$

and these are known as the components of the <u>alignment</u> <u>tensor</u>. It will be shown later that the orientation vector is responsible for the production of circular polarization and that the alignment tensor is responsible for linear polarization.

Time Dependence of the State Multipoles

Because of the influence of fine and hyperfine structure and the finite lifetime of the excited state, the state multipoles (and of course, the density matrix) are not constant but are time dependent. It can be shown that the state multipoles evolve according to an equation of the form:

$$\langle T(j'j;t)_{kq}^{\dagger}\rangle = \sum_{J'JKQ} \langle T(J'J)_{KQ}^{\dagger}\rangle G(J'J,j'j;t)_{Kk}^{Qq}$$

where the $G(J'J,j'j;t)_{Kk}^{Qq}$ are known as perturbation coefficients which include the effects of fine and hyperfine structure and the finite lifetime of the excited state. For the case of fine structure only the perturbation coefficients can be shown to be:

$$G(L_1;t)_{Kk}^{Qq} = \frac{\delta_{Qq}\delta_{Kk}}{2S_1+1} \sum_{J'J} (2J'+1)(2J+1) \begin{Bmatrix} L_1 & J & K \\ J' & L_1 & S_1 \end{Bmatrix}^2 \qquad (4.2.3.9a)$$

$$\times \exp(i(E_J - E_{J'})t/h - (\gamma_J + \gamma_{J'})t/2)$$

These are independent of Q and can be written simply as

$G(L_1;t)_K$. Note that the complex terms in this expression implies the existence of quantum beats in the observed radiation. Now if the time resolution of the coincidence electronics is very large compared to the periods of the quantum beats, the beats cannot be observed, and this is equivalent to a time integration of equation 4.2.3.9a. If this is done it turns out that only states with $J'=J$ can contribute to the state multipoles; the contributions from states with J' different from J are negligible.

Finally, if states with zero spin are considered, the perturbation coefficients reduce to:

$$G(L_1;t)_K = \exp(-\gamma_{L_1}t) \qquad (4.2.3.9b)$$

The Radiative Decay Process

To consider the radiative decay process it is convenient to work in the helicity basis of the emitted photons. In this basis, the quantization axis is taken to be the direction of propagation, n. Since photons are massless, they have only two components of spin angular momentum along n, namely +1 and -1. A density matrix of the emitted photons can be constructed in this representation, and is given by:

$$\langle \lambda'|\rho|\lambda\rangle = \begin{pmatrix} \rho_{11} & \rho_{1-1} \\ \rho_{-11} & \rho_{-1-1} \end{pmatrix}$$

The density matrix is of course Hermitian, so $\rho_{-11}=\rho^*_{1-1}$. The Stokes' parameters can be expressed in terms of the density matrix elements, and are given by:

$$I = tr\rho = \rho_{11} + \rho_{-1-1}$$

$$Is_3 = -(\rho_{1-1} + \rho_{-11})$$

$$Is_1 = -i(\rho_{1-1} - \rho_{-11})$$

$$Is_2 = \rho_{11} - \rho_{-1-1}$$

By transforming the state multipoles from the collision (x,y,z) system into the helicity system (using a rotation matrix), the photon density matrix can be shown to be:

$$\rho_{\lambda'\lambda}(\hat{n},t) = C(\omega) \sum_{\substack{J'JJ_f \\ KQq}} \langle J_f||\vec{r}||J'\rangle\langle J_f||\vec{r}||J\rangle^* (-1)^{J+J_f+\lambda}(2K+1)^{1/2}$$

$$\times \exp(i(E_J-E_{J'})t/h - (\gamma_J+\gamma_{J'})t/2)\langle T(J'J)_{KQ}^\dagger\rangle \quad (4.2.3.10)$$

$$\times D(n)_{Qq}^K \begin{pmatrix} 1 & 1 & K \\ -\lambda' & \lambda & q \end{pmatrix} \begin{Bmatrix} 1 & 1 & K \\ J & J' & J_f \end{Bmatrix}$$

For the case of 0 spin the Stokes' parameters are finally given by:

$$I = \frac{C(\omega)}{\gamma} |\langle L_f||\vec{r}||L_1\rangle|^2 (-1)^{L_1+L_f} \left[\frac{2(-1)^{L_1+L_f}}{3(2L_1+1)^{1/2}} \langle T(L_1)_{00}^\dagger\rangle \right.$$

$$- \begin{Bmatrix} 1 & 1 & 2 \\ L_1 & L_1 & L_f \end{Bmatrix} (\langle T(L_1)_{22}^\dagger\rangle \sin^2\theta \cos2\phi$$

$$(4.2.3.11a)$$

$$- \langle T(L_1)_{21}^\dagger\rangle \sin2\theta \cos\phi$$

$$\left. + \langle T(L_1)_{20}^\dagger\rangle (3\cos^2\theta - 1)/\sqrt{6} \right]$$

$$Is_3 = \frac{C(\omega)}{\gamma} |\langle L_f||\vec{r}||L_1\rangle|^2 (-1)^{L_1+L_f} \begin{Bmatrix} 1 & 1 & 2 \\ L_1 & L_1 & L_f \end{Bmatrix}$$

$$\times (\langle T(L_1)_{22}^\dagger\rangle (1+\cos^2\theta)\cos2\phi + \langle T(L_1)_{21}^\dagger\rangle \sin2\theta \cos\phi$$

$$(4.2.3.11b)$$

$$\times (3/2)^{1/2} \langle T(L_1)_{20}^\dagger\rangle \sin^2\theta)$$

$$Is_1 = -\frac{C(\hat{\omega})}{\gamma} |<L_f||\vec{r}||L_1>|^2 (-1)^{L_1+L_f}$$

$$(4.2.3.11c)$$

$$\times \begin{Bmatrix} 1 & 1 & 2 \\ L_1 & L_1 & L_f \end{Bmatrix} 2(<T(L_1)^\dagger_{22}>\cos\theta\sin2\phi + <T(L_1)^\dagger_{21}>\sin\theta\sin\phi)$$

$$Is_2 = -2i\frac{C(\omega)}{\gamma}|<L_f||\vec{r}||L_1>|^2 (-1)^{L_1+L_f}$$

$$(4.2.3.11d)$$

$$\times \begin{Bmatrix} 1 & 1 & 1 \\ L_1 & L_1 & L_f \end{Bmatrix} <T(L_1)^\dagger_{11}>\sin\theta\sin\phi$$

where $C(\omega)$ is given by:

$$C(\omega) = \frac{e^2\omega^4 d\Omega}{2\pi c^3 h} \qquad (4.2.3.11e)$$

and $<L_f||\vec{r}||L_1>$ is the reduced matrix element (Edmonds' normalization) of the dipole transition operator from the excited state to the final state (L_f). As stated earlier, equations 4.2.3.11 show that the orientation vector is related to the circular polariation and the alignment tensor is related to the linear polarization.

Excitation of the n^1P States of He

As a specific example, the excitation of the n^1P state of He and the subsequent radiative decay to 1^1S will be considered. In this case $L_1=1$ and $L_f=0$. The state multipoles can be evaluated and are:

$$<T(1)^\dagger_{00}> = (a_0^2 + 2a_1^2)/(3)^{1/2}$$

$$\langle T(1)^\dagger_{11}\rangle = \sqrt{2}\ i\,\mathrm{Im}(a_0 a_1^*)$$

$$\langle T(1)^\dagger_{10}\rangle = \sqrt{2/3}\ (a_1^2 - a_0^2)$$

$$\langle T(1)^\dagger_{21}\rangle = -\sqrt{2}\ \mathrm{Re}(a_0 a_1^*)$$

$$\langle T(1)^\dagger_{22}\rangle = -a_1^2$$

where $f(0)$ has been denoted by a_0 and $f(1)$ by a_1. Using the expressions for the state multipoles in equations 4.2.3.11, evaluating the 6-j symbols, and using the fact the the observation direction is $\theta = \phi = 90$ degrees, the Stokes' parameters are given by:

$$I = C(\omega)\,|\langle 0||\vec{r}||1\rangle|^2\,(a_0^2 + 2a_1^2)/3 \qquad (4.2.3.12a)$$

$$s_3 = (a_0^2 - 2a_1^2)/(a_0^2 + 2a_1^2) \qquad (4.2.3.12b)$$

$$s_1 = -2\sqrt{2}\ \mathrm{Re}(a_0 a_1^*)/(a_0^2 + 2a_1^2) \qquad (4.2.3.12c)$$

$$s_2 = 2\sqrt{2}\ \mathrm{Im}(a_0 a_1^*)/(a_0^2 + 2a_1^2) \qquad (4.2.3.12d)$$

It can be shown that equations 4.2.3.12 are equivalent to the Stokes' parameters of the complex dipole oscillator given in section 4.2.2. This is done as follows. The excited state is composed of a coherent superposition of the magnetic substates, and can be written as:

$$|\psi\rangle = a_{-1}|1\ -1\rangle + a_0|1\ 0\rangle + a_1|1\ 1\rangle$$

The excited state wavefunction can also be written in the form (by changing to a Cartesian basis set):

$$|\psi\rangle = a_x|x\rangle + a_y|y\rangle + a_z|z\rangle$$

The Cartesian basis vectors can be transformed to the angular momentum basis by noting that $\langle x|LM\rangle = C_{LM}(\hat{r}) =$ normalized spherical harmonic. It turns out that $a_z = a_0$, $a_y = 0$, and $a_1 = -a_x \sqrt{2}$. Thus there is a one-to-one correspondence between the scattering amplitudes and the dipole oscillator amplitudes.

He n¹P Excitation and the Born Approximation

As a final example we shall consider the predictions of the Born approximation for the excitation of n^1P states of He. This can be done by making the following assumptions:

(1) The He target states are properly antisymmetrized linear combinations of products of hydrogenic wavefunctions.

(2) Spin and exchange effects are neglected.

(3) The incident electron interacts with the Coulomb field of a positive ion core + the other target electron. Now the interaction with the core does not contribute to excitation, so this simplifies the calculation.

The results of the Born calculation show that the scattering amplitudes are given by:

$$a_0 = I(ka) Y_{10}^*(\hat{k})$$

$$a_1 = I(ka) Y_{11}^*(\hat{k})$$

where $I(ka)$ is a radial integral and $\vec{k}$ is the momentum transfer vector $\vec{p}_1 - \vec{p}_0$. In the scattering plane $\phi_k = 0$ and so the scattering amplitudes are:

$$a_0 \sim \cos\theta_k$$

$$a_1 \sim \sin\theta_k / \sqrt{2}$$

Thus the Stokes' parameters are given by:

$$s_3 = \cos 2\theta_k$$

$$s_1 = -\sin 2\theta_k$$

$$s_2 = 0$$

Recall that the orientation angle of the radiation pattern in the scattering plane is given by:

$$\tan 2\theta^{\gamma}_{min} = -s_1/s_3 = \tan 2\theta_k$$

Thus the momentum transfer direction also specifies the orientation of the radiation pattern. The momentum transfer direction can be found from the electron scattering angle, the incident electron energy, and the scattered electron energy(see Appendix 4.6.2). For a fixed incident energy and scattered energy, the Stokes' parameters can be calculated as a function of electron scattering angle and compared with experiment. In the Born approximation the scattering amplitudes are real, and thus the relative phase between them is 0. Also, the circular polarization is predicted to be 0, and the emitted photons are completely polarized; i.e., the magnitude of the polarization vector is 1. A comparison with actual experimental data[69] shows that the Born approximation predicts the value of s_3 reasonably well for small electron scattering angles, but not s_1 or s_2. Also there is a noticeable difference between the momentum transfer direction and the orientation of the radiation pattern.

4.2.4 Coincidence Experiments with Molecules

Having seen how the density matrix formalism works for atomic excitation, we can now turn our attention to molecules. The basic approach is the same, but in molecules the situation is complicated by the fact that electronic, vibrational and rotational excitation must be considered. In addition to this, there is a Maxwellian distribution in the population of different rotational states in the molecular ground state, which is also affected by nuclear spin statis-

tics. Thus the excitation is more complicated than in the atomic case, since several rotational states can contribute to the same excited state. For the sake of brevity we shall simply list the assumptions involved in the calculation and give the expressions for the Stokes' parameters. The reader is referred to the work of Blum and Jakubowicz[67] for complete details of the calculation. Having done this we shall proceed to work out some simple examples and discuss some of the difficulties associated with the experimental aspects of working with molecules.

Assumptions Involved

Several assumptions are made in this calculation, most of which are similar to the ones made for atomic excitation. These are:

(1) The excitation process is much quicker than the radiative decay process and the characteristic vibrational and rotational periods of the molecule. This means that the molecule is essentially frozen during the collision (the Franck-Condon principle).

(2) The electronic motion and the nuclear motion can be considered separately, and electronic, vibrational and rotational motion can be separated (Born-Oppenheimer approximation).

(3) The molecule obeys Hund's case (b) coupling (see Appendix 4.6.1).

(4) The initial state of the molecular ensemble is such that Λ_0, v_0 and S_0 are fixed.

(5) The incident electron beam has fixed momentum P_0 and is unpolarized.

(6) The molecular ensemble is also unpolarized.

(7) The Hamiltonian describing the scattering process contains no explicit spin-dependent terms. Thus, as in the atomic case, spin changes can only occur by electron exchange, which is neglected.

(8) No observations of initial and final spins of any particles are made.

(9) Conservation of spin angular momentum is taken explicitly into account in the scattering amplitudes. This means that there are two channels with spin $S=S_0+1/2$ and $S_0-1/2$.

Results.

We now list the results obtained by Blum and Jakubowicz for the state multipoles, perturbation coefficients and the Stokes' parameters. The state multipoles $\langle T(N_1'N_1)^\dagger_{KQ}\rangle$ are given by:

$$\langle T(N_1'N_1)^\dagger_{KQ}\rangle = \frac{1}{2(2S_0+1)} \sum_{\substack{N_0 M_{N_0} S M_{N_1}' M_{N_1}}} (2S+1)(2K+1)^{1/2} W(N_0)/(2N_0+1)$$

$$\times (-1)^{N_1+K+Q-M_{N_1}} \begin{pmatrix} N_1 & N_1' & K \\ -M_{N_1} & M_{N_1}' & -Q \end{pmatrix} f^S_{N_1'M_{N_1}' N_0 M_{N_0}} f^{S*}_{N_1 M_{N_1} N_0 M_{N_0}}$$

$$(4.2.4.1)$$

where $W(N_0)$ is the rotational population distribution in the ground state, and is:

$$W(N_0) = (2N_0+1)\exp(-BhcN_0(N_0+1)/kT) \qquad (4.2.4.2)$$

k is Boltzmann's constant.

B is the rotational constant of the molecular ground state.

T is the temperature of the ensemble.

Note that $W(N_0)$ also must include the effect of nuclear spin statistics. The $f^S_{N_1 M_{N_1} N_0 M_{N_0}}$'s in equation 4.2.4.1 are the scattering amplitudes in the channel with total spin S (formed by coupling the molecular spin with the spin of the incident electron) for the process:

$$|\alpha_0 N_0 M_{N_0}> \rightarrow |\alpha_1 N_1 M_{N_1}>$$

Note also that it is possible to excite a number of rotational levels coherently, hence the appearance of N_1 and N_1' in the state multipoles.

The perturbation coefficients $G(t)^{Qq}_{Kk}$ due to the fine structure interaction and the lifetime of the excited state are given by:

$$G(t)^{Qq}_{Kk} = \frac{\delta_{Kk}\delta_{Qq}}{2S_1+1} \sum_{J'J} (2J'+1)(2J+1)\exp(i(E_J-E_{J'})t/h - (\gamma_J+\gamma_{J'})t/2)$$

$$\times \begin{Bmatrix} N_1' & J' & S_1 \\ J & N_1 & K \end{Bmatrix}^2 \qquad (4.2.4.3)$$

Once again, notice the appearance of quantum beat terms in this expression. As in the atomic case, if the time resolution of the electronics is large compared to the quantum beat periods, the beating cannot be observed, and a time integration must be carried out. This means that only states with $N_1'=N_1$ contribute in equation 4.2.4.3. Furthermore, if only singlet states are considered, the perturba-

tion coefficients reduce to:

$$G(t)_K = \frac{1}{Y} \delta_{N_1'N_1} \tag{4.2.4.4}$$

Finally, the Stokes' parameters are given by:

$$I = C(\omega)|\langle\alpha_f|r_{\Lambda_1-\Lambda_f}|\alpha_1\rangle|^2 \left[\sum_{N_1 N_f} W(N_f N_1 N_1)\left(\frac{2(-1)^{N_1+N_f}}{3(2N_1+1)^{1/2}}\right) \right.$$

$$\left. \times G(t)_0 \langle T(N_1'N_1)_{00}^\dagger\rangle\right) - \left[\sum_{N_1'N_1 N_f} W(N_f N_1 N_1') G(t)_2 \begin{Bmatrix} 1 & 1 & 2 \\ N_1 & N_1' & N_f \end{Bmatrix} \right.$$

$$\times (\langle T(N_1'N_1)_{22}^\dagger\rangle \sin^2\theta\cos2\phi - \langle T(N_1'N_1)_{21}^\dagger\rangle\sin\theta\cos\phi \tag{4.2.4.5a}$$

$$\left. + \langle T(N_1'N_1)_{20}^\dagger\rangle(3\cos^2\theta - 1)/\sqrt{6}\right]$$

$$Is_1 = -2C(\omega)|\langle\alpha_f|r_{\Lambda_1-\Lambda_f}|\alpha_1\rangle|^2 \sum_{N_1'N_1 N_f} W(N_f N_1 N_1') G(t)_2$$

$$\times \begin{Bmatrix} 1 & 1 & 2 \\ N_1 & N_1' & N_f \end{Bmatrix} (\langle T(N_1'N_1)_{22}^\dagger\rangle\cos\theta\sin2\phi \tag{4.2.4.5b}$$

$$+ \langle T(N_1'N_1)_{21}^\dagger\rangle\sin\theta\sin\phi)$$

$$Is_2 = -2iC(\omega) |<\alpha_f|r_{\Lambda_1-\Lambda_f}|\alpha_1>|^2 \sum_{N_1'N_1N_f} \hat{W}(N_fN_1N_1')G(t)_1$$

(4.2.4.5c)

$$x \begin{Bmatrix} 1 & 1 & 1 \\ N_1 & N_1' & N_f \end{Bmatrix} <T(N_1'N_1)^\dagger_{11}>\sin\theta\sin\phi$$

$$Is_3 = C(\omega) |<\alpha_f|r_{\Lambda_1-\Lambda_f}|\alpha_1>|^2 \sum_{N_1'N_1N_f} W(N_fN_1N_1')G(t)_2$$

$$x \begin{Bmatrix} 1 & 1 & 2 \\ N_1 & N_1' & N_f \end{Bmatrix} (<T(N_1'N_1)^\dagger_{22}>(1+\cos^2\theta)\cos2\phi$$

(4.2.4.5d)

$$+ <T(N_1'N_1)^\dagger_{21}>\sin2\theta\cos\phi + (3/2)^{1/2}<T(N_1'N_1)^\dagger_{20}>\sin^2\theta)$$

where $W(N_fN_1N_1')$ is given by:

$$W(N_fN_1N_1') = (-1)^{N_1+N_f}(2N_f+1)((2N_1+1)(2N_1'+1))^{1/2}$$

(4.2.4.5e)

$$x \begin{pmatrix} N_1 & N_f & 1 \\ \Lambda_1 & -\Lambda_f & \Lambda_f-\Lambda_1 \end{pmatrix} \begin{pmatrix} N_1' & N_1 & 1 \\ \Lambda_1 & -\Lambda_f & \Lambda_f-\Lambda_1 \end{pmatrix}$$

and $C(\omega)$ is the same as for the atomic case, except that ω is now the mean frequency of the emitted radiation, and $<\alpha_f|r_{\Lambda_1-\Lambda_f}|\alpha_1>$ is the matrix element describing a vibrational transition. The refer to all other quantum numbers necessary to describe the molecular states. If the rotational structure of a given vibrational band is not resolved in the experiment, a new set of state multipoles

$<T(t)^{\dagger}_{KQ}>$ can be defined by the formal summation:

$$<T(t)^{\dagger}_{KQ}> = \sum_{N_1'N_1N_f} W(N_fN_1N_1')G(t)_K \begin{Bmatrix} 1 & 1 & K \\ N_1 & N_1' & N_f \end{Bmatrix} <T(N_1'N_1)^{\dagger}_{KQ}> \qquad (4.2.4.6)$$

The Stokes' parameters are then given by (for the observation direction y):

$$I = A[<-2<T^{\dagger}_{20}>/\sqrt{3} + <T^{\dagger}_{22}> + <T^{\dagger}_{20}>/\sqrt{6}] \qquad (4.2.4.7a)$$

$$Is_1 = -2A<T^{\dagger}_{21}> \qquad (4.2.4.7b)$$

$$Is_2 = -2iA<T^{\dagger}_{21}> \qquad (4.2.4.7c)$$

$$Is_3 = A[-<T^{\dagger}_{22}> +\sqrt{3/2} <T^{\dagger}_{20}>] \qquad (4.2.4.7d)$$

where $A = C(\omega)|<\alpha_f|r_{\Lambda_1-\Lambda_f}|\alpha_i>|^2$

In the case where $S_0=S_1=S_f=0$, the formal summation 4.2.4.6 can be carried out over N_f, and the result for the state multipoles is:

$$<T(t)^{\dagger}_{KQ}> = \frac{(2K+1)^{1/2}}{\gamma} \quad (-1)^{Q+\Lambda_f} \begin{pmatrix} 1 & 1 & K \\ \Lambda_1-\Lambda_f & \Lambda_f-\Lambda_1 & 0 \end{pmatrix}$$

$$\times \sum_{N_0N_1M_0M_1M_1'} (-1)^{-M_{N_1}} (2N_1+1) \begin{pmatrix} N_1 & N_1 & K \\ \Lambda_1 & -\Lambda_1 & 0 \end{pmatrix} \begin{pmatrix} N_1 & N_1 & K \\ -M_{N_1} & M_{N_1}' & 0 \end{pmatrix} \qquad (4.2.4.8)$$

$$\times f_{N_1M_1'N_0M_0} f^*_{N_1M_1N_0M_0}$$

Note that the finite resolution time of the electronics has been taken into account and the assumption that the life-times are independent of N_1 has been made. Equation 4.2.4.8 shows that information about individual scattering ampli-tudes is lost when the rotational structure is unresolved.

Also, by not resolving the quantum beats, information about the coherence between states of different N_1 is lost.

Some Examples

Let us consider the situation where a single rotational line is resolved, say the strongest one in the band. In practice this will only be possible for the lightest molecules, so the case of H_2 $X^1\Sigma_g^+ \rightarrow C^1\Pi_u$ excitation will be considered. For this system the $Q(1)$ line is expected to be the strongest, and this comes from $N_0 = N_1' = N_f = 1$ only. The assumption that excitation and decay proceeds via a dipole route only has been made. Using equation 4.2.4.2 for the state multipoles, with $N_1' = N_1 = 1$, $N_0 = N_f = 1$, $\Lambda_0 = \Lambda = 0$ and $\Lambda_1 = 1$, $\langle T(1)_{00}^\dagger \rangle$ is given by:

$$\langle T(1)_{00}^\dagger \rangle = \frac{W(1)}{3\sqrt{3}} \sum_{M_{N_0} M_{N_1}} \left| f(1M_{N_1} 1M_{N_0}) \right|^2$$

The scattering amplitudes $f(1M_{N_1} 1M_{N_0})$ are denoted by $a(M_{N_1} M_{N_0})$, and reflection invariance in the scattering plane implies that $a(-M_{N_1} -M_{N_0}) = (-1)^{M_{N_1} + M_{N_0}} a(M_{N_1} M_{N_0})$. The summation over M_{N_0} can be performed first, giving a new set of amplitudes $\langle a(M_{N_1}) \rangle$. Then $\langle T(1)_{00}^\dagger \rangle$ is:

$$\langle T(1)_{00}^\dagger \rangle = (W(1)/3\sqrt{3})(\langle a^2(0) \rangle + 2\langle a^2(1) \rangle)$$

The other state multipoles are given by:

$$\langle T(1)_{11}^\dagger \rangle = (\sqrt{2}\, iW(1)/3) \operatorname{Im}[\langle a(0) a(1) \rangle]$$

$$\langle T(1)_{20}^\dagger \rangle = (2W(1)/3\sqrt{6})(\langle a^2(1) \rangle - \langle a^2(0) \rangle)$$

$$\langle T(1)_{21}^\dagger \rangle = (-\sqrt{2}\, W(1)/3) \operatorname{Re}[\langle a(0) a(1) \rangle]$$

$$\langle T(1)_{22}^\dagger \rangle = (-W(1)/3)\langle a^2(1) \rangle$$

The Stokes' parameters are then given by:

$$I = A \frac{W(1)}{12} (<a^2(0)> + 2<a^2(1)>)$$

$$Is_1 = -A \frac{W(1)}{6}\sqrt{2} \, Re(<a(0)a^*(1)>)$$

$$Is_2 = A \frac{W(1)}{6}\sqrt{2} \, Im(<a(0)a^*(1)>)$$

$$Is_3 = A \frac{W(1)}{12} (<a^2(0)> - 2<a^2(1)>)$$

where $A = \frac{C(\omega)}{\gamma}|<\alpha_f|r_{\Lambda_1-\Lambda_f}|\alpha_1>|^2.$

and:

$$s_1 = -2\sqrt{2} \, Re[<a(0)a^*(1)>]/(<a^2(0)>+2<a^2(1)>).$$

$$s_2 = 2\sqrt{2} \, Im[<a(0)a^*(1)>]/(<a^2(0)>+2<a^2(1)>)$$

$$s_3 = (<a^2(0)>-2<a^2(1)>)/(<a^2(0)>+2<a^2(1)>)$$

Thus the Stokes' parameters for the resolved $Q(1)$ line are somewhat similar to the n^1P case in He, except that the scattering amplitudes have been summed over the ground state magnetic sublevels.

In practice it is very difficult to resolve the rotational structure in a coincidence experiment because of the corresponding loss of intensity in the photon channel. Another approach would be to prepare the initial molecular ensemble in such a way that only one rotational level is populated. This can be done by using a supersonic nozzle arrangement. During the expansion the vibrational and rotational states are frozen out, and only the $N_0=0$ state is populated. In this case the only allowed dipole excitation route is to $N_1=1$, and the only allowed decay routes are to $N_f=0$ and 2, corresponding to the $R(0)$ and $P(2)$ branches. The state multipoles can be evaluated easily, and are given by:

$$\langle T(1)^{\dagger}_{00}\rangle = \left(\bar{w}(0)/\sqrt{3}\right)(a_0^2 + 2a_1^2)$$

$$\langle T(1)_{11}\rangle = \left(i\sqrt{2}\ \bar{w}(0)\right)Im(a_0 a_1)$$

$$\langle T(1)_{20}\rangle = \sqrt{2/3}\ \bar{w}(0)\ (a_1^2 - a_0^2)$$

$$\langle T(1)_{21}\rangle = -\sqrt{2}\ \bar{w}(0)\,Re(a_0 a_1)$$

$$\langle T(1)_{22}\rangle = -\bar{w}(0)\,a_1^2$$

where the scattering amplitudes $f(1100)$ and $f(1000)$ have been denoted by a_1 and a_0, respectively. The Stokes' parameters can be evaluated by summing equations 4.2.4.2 over $N_f = 0$ and 2, and are:

$$I = A\ \frac{16\sqrt{5} + 3}{36\sqrt{5}}\ (a_0^2 + 2a_1^2)$$

$$Is_1 = -A\ \frac{2(12\sqrt{5} + 9)}{18\sqrt{5}}\ Re(a_0 a_1^*)$$

$$Is_2 = A\ \frac{5\sqrt{2}}{6}\ Im(a_0 a_1^*)$$

$$Is_3 = A\ \frac{12\sqrt{5} + 9}{36\sqrt{5}}\ (a_0^2 - 2a_1^2)$$

where $A = C(\omega)\ \dfrac{W(0)}{\gamma}|\langle \alpha_f|r_1|\alpha_r\rangle|^2$.

Thus s_1, s_2 and s_3 are given by:

$$s_1 = \frac{12\sqrt{5} + 9}{16\sqrt{5} + 3}\ \frac{-2\sqrt{2}\ Re(a_0 a_1^*)}{a_0^2 + 2a_1^2}$$

$$s_2 = \frac{15\sqrt{5}}{16\sqrt{5} + 3}\ \frac{2\sqrt{2}\ Im(a_0 a_1^*)}{a_0^2 + 2a_1^2}$$

$$s_3 = \frac{12\sqrt{5} + 9}{16\sqrt{5} + 3}\ \frac{a_0^2 - 2a_1^2}{a_0^2 + 2a_1^2}$$

It can be seen that these parameters are the same as the ones obtained for the He n^1P case, apart from the numerical

factors.

It should be pointed out that the scattering amplitudes $f(N_1 M_{N_1}; p_1 \leftarrow N_0 M_{N_0}; p_0)$ depend on the orientation of the molecular axis with respect to p_0. The initial molecular ensemble contains all possible orientations, so the scattering amplitudes used in the above expressions must be integrated over all orientations of the molecules. It is expected that this will cause an overall reduction of the polarization, and it may also result in a change in the relative phases of the scattering amplitudes. It is difficult to ascertain the exact nature of the effect without knowing the explicit angular dependence of the scattering amplitudes.

4.2.5 Threshold and Pseudo-Threshold Polarization

Consider the situation where the scattered electron is not detected. This requires that the state multipoles must be integrated over all electron scattering angles. When this is done, only multipoles with Q=0 can contribute, and the new state multipoles are given by:

$$\langle T(N_1)^{\dagger}_{K0} \rangle = \sum_{N_0 M_{N_1}} W(N_0) (-1)^{N_1 - M_{N_1}} (2K+1)^{1/2} \begin{pmatrix} N_1 & N_1 & K \\ -M_{N_1} & M_{N_1} & 0 \end{pmatrix} Q(N_0 N_1)_{M_{N_1}} \quad (4.2.5.1)$$

where $Q(N_0 N_1)_{M_{N_1}}$ is the total cross-section for exciting the state $|\alpha N_1 M_{N_1}\rangle$, and is given by:

$$Q(N_0 N_1)_{M_{N_1}} = \frac{1}{2(2S_0+1)(2N_0+1)} \sum_{SM_{N_0}} \int |f^S_{N_1 M_{N_1} N_0 M_{N_0}}|^2 d\Omega_e \qquad (4.2.5.2)$$

In addition to integration over the scattered electron directions, not observing the scattered electrons means that the time at which photons are observed is not uniquely defined with respect to the time at which excitation took place, and an integration over all observation times must be performed. Blum and Jakubowicz give expressions for the total unpolarized intensity I and the intensity of light with polarization vector parallel to the z-axis, $I_{\parallel}$, as:

$$I \sim \sum_{N_1 N_f} \frac{(-1)^{N_1+N_f} W(N_f N_1 N_1)}{2N_1+1} \sum_{N_0 M_{N_1}} W(N_0) Q(N_0 N_1)_{M_{N_1}} \qquad (4.2.5.3a)$$

$$I_{\parallel} \sim \sum_{N_1 N_f K} (2K+1) W(N_f N_1 N_1) \begin{pmatrix} 1 & 1 & K \\ 0 & 0 & 0 \end{pmatrix} \begin{Bmatrix} 1 & 1 & K \\ N_1 & N_1 & N_f \end{Bmatrix}$$

$$\times \sum_J \frac{(2J+1)^2}{2S_1+1} \begin{Bmatrix} N_1 & J & S_1 \\ J & N_1 & K \end{Bmatrix}^2 \sum_{N_0 M_{N_1}} W(N_0) (-1)^{N_1-M_{N_1}} \begin{pmatrix} N_1 & N_1 & K \\ -M_{N_1} & M_{N_1} & 0 \end{pmatrix} Q(N_0 N_1)_{M_{N_1}} \qquad (4.2.5.3b)$$

For singlet transitions $I_{\parallel}$ reduces to:

$$I_{\parallel} \sim \sum_{N_1 N_f K} (2K+1) W(N_f N_1 N_1) \begin{pmatrix} 1 & 1 & K \\ 0 & 0 & 0 \end{pmatrix} \begin{Bmatrix} 1 & 1 & K \\ N_1 & N_1 & N_f \end{Bmatrix}$$

$$\quad (4.2.5.3c)$$

$$\times \sum_{N_0 M_{N_1}} W(N_0) (-1)^{N_1 - M_{N_1}} \begin{pmatrix} N_1 & N_1 & K \\ -M_{N_1} & M_{N_1} & 0 \end{pmatrix} Q(N_0 N_1)_{M_{N_1}}$$

and the sum over K can be performed explicitly, giving:

$$I_{\parallel} \sim \sum_{N_0 N_1 N_f} (-1)^{N_1 + N_f} W(N_0) W(N_f N_1 N_1) \sum_{M_{N_1}} \begin{pmatrix} N_1 & 1 & N_f \\ -M_{N_1} & 0 & M_{N_1} \end{pmatrix}^2 Q(N_0 N_1)_{M_{N_1}} \quad (4.2.5.4)$$

The polarization P is defined by:

$$P = \frac{3I_{\parallel} - I}{I_{\parallel} + I} \qquad (4.2.5.5)$$

Using the expressions for I and $I_{\parallel}$, the polarization is:

$$P = \frac{\displaystyle\sum_{N_0 N_1 N_f} (-1)^{N_1 + N_f} W(N_0) W(N_f N_1 N_1) \sum_{M_{N_1}} (3A^2 - 1/(2N_1+1)) Q(N_0 N_1)_{M_{N_1}}}{\displaystyle\sum_{N_0 N_1 N_f} (-1)^{N_1 + N_f} W(N_0) W(N_f N_1 N_1) \sum_{M_{N_1}} (A^2 + 1/(2N_1+1)) Q(N_0 N_1)_{M_{N_1}}}$$

$$\qquad (4.2.5.6)$$

$$A = \begin{pmatrix} N_1 & 1 & N_f \\ M_{N_1} & 0 & -M_{N_1} \end{pmatrix}$$

If the scattering amplitudes $f(N_1 M_{N_1} N_0 M_{N_0})$ are written as:

$$f(N_1 M_{N_1} N_0 M_{N_0}) = \sum_{kq} c_{kq} \langle \alpha_1 N_1 M_{N_1} | R_{kq} | \alpha_0 N_0 M_{N_0} \rangle$$

where R_{kq} represents an angular momentum change of $|kq\rangle$,

then the total cross section can be written as:

$$Q(N_0 N_1)_{M_{N_1}} = (2N_1+1)^2 (2N_0+1) \sum_{kk'q} c_{kq} c^*_{k'q} \int \langle \alpha_1 | R_k | \alpha_0 \rangle \langle \alpha_1 | R_{k'} | \alpha_0 \rangle^* d\Omega_e$$

$$\times \begin{pmatrix} N_1 & k & N_0 \\ M_{N_1} & -q & q-M_{N_1} \end{pmatrix} \begin{pmatrix} N_1 & k' & N_0 \\ M_{N_1} & -q & q-M_{N_1} \end{pmatrix} \begin{pmatrix} N_0 & N_1 & k \\ \Lambda_0 & -\Lambda_1 & \Lambda_1-\Lambda_0 \end{pmatrix} \begin{pmatrix} N_0 & N_1 & k' \\ \Lambda_0 & -\Lambda_1 & \Lambda_1-\Lambda_0 \end{pmatrix} \quad (4.2.5.7)$$

In particular if the excitation is restricted to dipole routes alone, then $k=k'=1$ and the result is:

$$Q(N_0 N_1)_{M_{N_1}} = (2N_1+1)^2 (2N_0+1) \int |\langle \alpha_1 | R_1 | \alpha_0 \rangle|^2 d\Omega_e$$

$$\times \sum_q |c_{1q}|^2 \begin{pmatrix} N_0 & N_1 & 1 \\ \Lambda_0 & -\Lambda_1 & \Lambda_1-\Lambda_0 \end{pmatrix}^2 \begin{pmatrix} N_1 & 1 & N_0 \\ M_{N_1} & -q & q-M_{N_1} \end{pmatrix}^2 \quad (4.2.5.8)$$

Now conservation of total angular momentum and its z component requires that:

$$N_0 + l_0 = N_1 + l_1 \qquad (4.2.5.9a)$$

and

$$M_{N_0} + m_0 = M_{N_1} + m_1 \qquad (4.2.5.9b)$$

where $k=l_1-l_0$, and $q=m_1-m_0$. The incident electron beam defines the z-axis, so m_0 is always 0. Consider what happens at the excitation threshold. The scattered electrons leave the collision with $p_1 \sim 0$ and carry away no angular momentum. Thus $m_1=0$ and we have the threshold selection rule:

$$M_{N_1} = M_{N_0} \qquad (4.2.5.10)$$

The threshold polarization is then given by:

$$P_{th} = \frac{\sum\limits_{N_0 N_1 N_f} (-1)^{N_1+N_f} W(N_0) W(N_f N_1 N_1) \sum\limits_{M_{N_0}} (3A^2 - 1/(2N_1+1)) Q(N_0 N_1)_{M_{N_0}}}{\sum\limits_{N_0 N_1 N_f} (-1)^{N_1+N_f} W(N_0) W(N_f N_1 N_1) \sum\limits_{M_{N_0}} (A^2 + 1/(2N_1+1)) Q(N_0 N_1)_{M_{N_0}}}$$

(4.2.5.11)

where $A = \begin{pmatrix} N_1 & 1 & N_f \\ M_{N_0} & 0 & -M_{N_0} \end{pmatrix}$.

Notice that the threshold polarization is not independent of the dynamics of the scattering process as would be the case for atoms. However, using equation 4.2.5.8 with $M_{N_1} = M_{N_0}$, P_{th} is given by:

$$P_{th} = \frac{\sum\limits_{N_0 N_1 N_f} (-1)^{N_1+N_f} W(N_0) W(N_f N_1 N_1) V(N_0 N_1) \sum\limits_{M_{N_0}} (3A^2 - 1/(2N_1+1)) B^2}{\sum\limits_{N_0 N_1 N_f} (-1)^{N_1+N_f} W(N_0) W(N_f N_1 N_1) V(N_0 N_1) \sum\limits_{M_{N_0}} (A^2 + 1/(2N_1+1)) B^2}$$

(4.2.5.12)

$$V(N_0 N_1) = (2N_1+1)^2 (2N_0+1) \begin{pmatrix} N_0 & N_1 & 1 \\ \Lambda_0 & -\Lambda_1 & \Lambda_1-\Lambda_0 \end{pmatrix}^2 \qquad B = \begin{pmatrix} N_0 & 1 & N_1 \\ M_{N_0} & 0 & -M_{N_0} \end{pmatrix} \quad A \text{ given in 4.2.5.11}$$

If N_0, N_1 and N_f are fixed, equation 4.2.5.11 is:

$$P_{th} = \frac{\sum\limits_{M_{N_0}} \left[3 \begin{pmatrix} N_1 & 1 & N_f \\ M_{N_0} & 0 & -M_{N_0} \end{pmatrix}^2 - \frac{1}{2N_1+1} \right] Q(N_0 N_1)_{M_{N_0}}}{\sum\limits_{M_{N_0}} \left[\begin{pmatrix} N_1 & 1 & N_f \\ M_{N_0} & 0 & -M_{N_0} \end{pmatrix}^2 + \frac{1}{2N_1+1} \right] Q(N_0 N_1)_{M_{N_0}}}$$

(4.2.5.13a)

and equation 4.2.5.12 is:

$$
P_{th} = \frac{\displaystyle\sum_{M_{N_0}} \left[3 \begin{pmatrix} N_1 & 1 & N_f \\ M_{N_0} & 0 & -M_{N_0} \end{pmatrix}^2 - \frac{1}{2N_1+1} \right] \begin{pmatrix} N_0 & 1 & N_1 \\ M_{N_0} & 0 & -M_{N_0} \end{pmatrix}^2}{\displaystyle\sum_{M_{N_0}} \left[\begin{pmatrix} N_1 & 1 & N_f \\ M_{N_0} & 0 & -M_{N_0} \end{pmatrix}^2 + \frac{1}{2N_1+1} \right] \begin{pmatrix} N_0 & 1 & N_1 \\ M_{N_0} & 0 & -M_{N_0} \end{pmatrix}^2}
\tag{4.2.5.13b}
$$

Equation 4.2.5.13b is identical to the results obtained if excitation with linearly polarized light is considered.

Consider for the moment the general expression for the threshold polarization for fixed rotational quantum numbers given by equation 4.2.5.13a. The predicted polarization cannot be evaluated unless the cross-sections are known or some additional selection rules can be invoked to eliminate the dependence on the cross-sections. This problem has been discussed extensively in the literature[70-78], so only a brief summary will be given here.

The Approach of Jette and Cahill

These authors[76] made the assumption that _electronic_ orbital angular momentum was conserved during the collision. Thus, in particular for the z component:

$$
\langle v_0 \Lambda_0 N_0 M_{N_0} | L_z | v_0 \Lambda_0 N_0 M_{N_0} \rangle = \langle v_1 \Lambda_1 N_1 M_{N_1} | L_z | v_1 \Lambda_1 N_1 M_{N_1} \rangle
$$

The matrix element can be evaluated and is:

$$
\frac{M_{N_0} \Lambda_0^2}{N_0(N_0 + 1)} = \frac{M_{N_1} \Lambda_1^2}{N_1(N_1 + 1)}
$$

For a Σ to Π transition, $\Lambda_0 = 0$ and $\Lambda_1 = 1$, implying that only the $M_{N_1} = 0$ substate will be populated. Then only the $M_{N_0} = 0$

term contributes in equation 4.2.5.13a and the dependence on the cross-section vanishes. It should be pointed out that conservation of L_z does not agree with the threshold selection condition. The predicted threshold polarizations obtained in this way do not agree with the experimentally determined values[73], and this approach has been discredited.

The Approach of Baltayan and Nedelec.

These authors[77,78] used the united atom approximation and a partial wave analysis to determine the cross-sections $Q(N_1 N_0)_{M_N}$. In this approximation the electronic orbital angular momentum, l, is a good quantum number, and results in the additional coupling rule:

$$l_0 + L_0 = l_1$$

where L_0 refers to the L_0-th partial wave. With $l_0 = 0$, only the partial wave $L_0 = 1$, contributes to the excitation. The resulting expression for the threshold polarization is identical to equation 4.2.5.13b, and this was found to give reasonably good agreement with experiment.

The Approach of Malcolm, Dassen and McConkey

These authors[75] applied the symmetry rules of Dunn[79] to the excitation process to determine the threshold polarization. Basically, Dunn's symmetry rules relate the transition probability to the orientation of the molecule with respect to the incident electron beam. For a Σ_g^+ to Σ_u^+ transition, the transition probability is a maximum when the molecular axis is parallel to the incident beam, and zero when the axis is perpendicular to it. For a Σ_g^+ to Π_u tran-

sition, the reverse is true. The transition probability is zero when the axis is parallel to the incident beam and a maximum when the axis is perpendicular to it. Thus, for Σ_g^+ to Σ_u^+ transitions, states with $M_{N_1}=0$ should then be preferentially populated, and for Σ_g^+ to Π_u transitions, states with $M_{N_1}=\pm N_0$ should be preferentially populated. These predictions gave results which agreed with experiment much better than the predictions of Jette and Cahill, but it must be emphasized that the selection rules are not strictly obeyed because of the distribution of orientations of the molecular axes. For the Σ_g^+ to Π_u case, the cross-sections would have a $\sin^2\theta$ dependence, and thus only $M_{N_0}=0$ would be excluded from the expression 4.2.5.13a. Blum[70] has developed these ideas in a rigorous fashion and has obtained an expression for the scattering amplitudes which depend on the orientation of the molecular axis. This is given by:

$$A(\hat{n}) = (4\pi)^{-3/2} ((2N_0+1)(2N_1+1))^{1/2} D^*(\hat{n})^{N_1}_{\Lambda_1 M_{N_1}}$$
$$\times (\Sigma_{L_0} (-1)^{\Lambda_1-\Lambda_0} Y^{L_0}_{\Lambda_1-\Lambda_0}(\hat{n}) P_{L_0}(\cos\theta) <v_1\Lambda_1\Pi_1|T|v_0\Lambda_0\Pi_0 L_0\Lambda_1-\Lambda_0>) \qquad (4.2.5.14)$$
$$\times D(\hat{n})^{N_0}_{\Lambda_0 M_{N_0}}$$

where $D(\hat{n})^{N}_{\Lambda M_N}$ is a rotation matrix, $\hat{n}$ is the orientation of the molecular axis with respect to z, and L_0 refers to the L_0-th partial wave. Blum shows that for Σ_g^+ to Σ_u^+ transitions states with values of $M_{N_1}=0$ are preferentially populated. For Σ_g^+ to Π_u transitions, it can be shown that the amplitudes vanish if the axis is parallel to z, and that they will vanish if the axis is perpendicular to z unless

$M_{N_1} = \pm N_0$. It can also be shown that the amplitudes vanish if $M_{N_1} = 0$.

The cross-sections $Q(N_1 N_0)_{M_N}$ can be determined by integrating the scattering amplitude over all orientations of the axis, squaring the result, and integrating over all electron scattering angles. If this is done, the cross-sections are given by:

$$Q(N_0 N_1)_{M_{N_0}} = \frac{a^2}{4\pi} (2N_1+1) \begin{pmatrix} N_1 & L_0 & N_0 \\ -\Lambda_1 & \Lambda_1-\Lambda_0 & \Lambda_0 \end{pmatrix}^2 \begin{pmatrix} N_1 & L_0 & N_0 \\ M_{N_0} & 0 & -M_{N_0} \end{pmatrix}^2 \quad (4.2.5.15)$$

where $a = \langle v_1 \Lambda_1 \Pi_1 | T | v_0 \Lambda_0 \Pi_0 L_0 \Lambda_1 - \Lambda_0 \rangle$ and we have assumed that only one partial wave contributes to the excitation. This result applies only at the excitation threshold. The threshold polarization can be determined, and is given by:

$$P_{th} = \frac{\sum\limits_{N_0 N_1 N_f} (-1)^{N_1+N_f} W(N_0) W(N_f N_1 N_1) A^2 \sum\limits_{M_{N_0}} (3B^2 - 1/(2N_1+1))C^2}{\sum\limits_{N_0 N_1 N_f} (-1)^{N_1+N_f} W(N_0) W(N_f N_1 N_1) A^2 \sum\limits_{M_{N_0}} (B^2 + 1/(2N_1+1))C^2} \quad (4.2.5.16)$$

$$A = \begin{pmatrix} N_1 & L_0 & N_0 \\ -\Lambda_1 & \Lambda_1-\Lambda_0 & \Lambda_0 \end{pmatrix} \qquad B = \begin{pmatrix} N_1 & 1 & N_f \\ M_{N_0} & 0 & -M_{N_0} \end{pmatrix} \qquad C = \begin{pmatrix} N_1 & L_0 & N_0 \\ M_{N_0} & 0 & -M_{N_0} \end{pmatrix}$$

Note that equation 4.2.5.16 is very similar to equation 4.2.5.8 when $L_0=1$. Table 4.1 lists the predicted threshold polarizations for the P, Q and R branches of the H_2 $X^1\Sigma_g^+$ to $C^1\Pi_u$ Werner bands, and the P and R branches of the N_2 $X^1\Sigma_g^+$ to $C^1\Sigma_u^+$ bands. The first column gives the predicted values of equation 4.2.5.12, and the second column gives the pred-

Table 4.1
Predicted Threshold Polarizations in H_2 and N_2

Hydrogen $C^1\Pi_u - X^1\Sigma_g^+$ Rotational Line	Predicted Polarization From eq 4.2.5.12	From eq 4.2.5.16
P(2)	0.105	0.133
P(3)	0.135	0.139
P(4)	0.141	0.142
P(5)	0.142	0.143
P(6)	0.143	0.143
Q(1)	0.333	0.333
Q(2)	0.447	0.447
Q(3)	0.474	0.474
Q(4)	0.484	0.484
Q(5)	0.490	0.490
R(0)	0.800	0.951
R(1)	0.426	0.437
R(2)	0.318	0.319
R(3)	0.268	0.268
R(4)	0.239	0.239

Nitrogen $C_4^1\Sigma_u^+ - X^1\Sigma_g^+$ Rotational Line	Predicted Polarization From eq 4.2.5.12	From eq 4.2.5.16
P(2)	0.054	0.061
P(3)	0.085	0.086
P(4)	0.099	0.100
P(5)	0.108	0.108
P(6)	0.114	0.114
R(0)	0.466	0.512
R(1)	0.277	0.280
R(2)	0.228	0.228
R(3)	0.205	0.206
R(4)	0.193	0.193

icted values of equation 4.2.5.16.

The Approach of MacPherson et al

MacPherson et al[80] used a semiclassical approach to pred-
ict the polarization of molecular radiation. Their pred-
icted polarizations should be approached for high values of
the rotational quantum number. The predicted polarization
is given by:

$$P = \frac{3\cos^2\gamma - 1}{\cos^2\gamma + 3}$$

where γ is the average angle between the dipole moment for
absorption, $\vec{\mu}_{abs}$, and the dipole moment for emission, $\vec{\mu}_{em}$.
For Σ to Π transitions (R and P branches), both $\vec{\mu}_{abs}$ and $\vec{\mu}_{em}$
lie in a plane perpendicular to the internuclear axis with
no correlation between them. The average angle γ is then 45
degrees, and the predicted polarization is 0.143. For the Q
branch, $\vec{\mu}_{abs}$ and $\vec{\mu}_{em}$ both lie along the rotation vector,
and hence the value of γ is 0, and the predicted polariza-
tion is 0.5. For Σ to Σ transitions, there are only the R
and P branches to consider, and $\vec{\mu}_{abs}$ and $\vec{\mu}_{em}$ lie in the
plane of the internuclear axis with no correlation between
them. Thus the average value of γ is 45 degrees and the
predicted polarization is 0.143.

Pseudo-Threshold Polarization

Estimating the threshold polarization from straightfor-
ward polarization measurements is often difficult because of
intensity limitations near the threshold and cascade contri-
butions from higher lying states. In addition to these, the
assumption of impulse excitation is questionable close to

threshold; the possiblities of electron correlations[81] and near threshold resonances exist. These effects would cause the measured polarization to vary rapidly with energy, making extrapolation to threshold somewhat dubious. If these effects are known to be occuring, it is possible to estimate the threshold polarization from energies well above threshold[71], but the accuracy of the estimate may be questionable. It is possible to _simulate_ the threshold selection rule (eq. 4.2.5.10) by use of the _pseudo-threshold_ measurement suggested by King et al[82]. In this type of measurement the photons are detected in coincidence with the _forward scattered_ electrons, forcing $m_1 = 0$. The work by Wykes[38] on the angular dependence of the scattering amplitudes shows that setting the scattering angle equal to 0 forces the selection rule $\Delta M_N = 0$, since they contain an associated Legendre polynomial. At $\theta_e = 0$, only $P_0^{\Delta N}(\cos\theta_e)$ is non-zero. This measurement can be performed at energies well away from threshold, where intensity is no problem and impulse excitation is a valid assumption. Also, the measurement is rendered cascade-free because of the coincidence nature of the experiment. King et al[82] used this technique to measure the 'threshold' polarization of the He 2^1P radiation and obtained a value of 1, the expected theoretical value. They did however find that it was important to accept only those electrons scattered very close to $\theta_e = 0$. The finite angular resolution of any spectrometer results in the usefulness of this technique being limited to incident energies less than approximately three times the threshold excitation energy.

Above this 'critical energy' the measured value of P_{th} decreased rapidly with increasing energy. More will be said about this later.
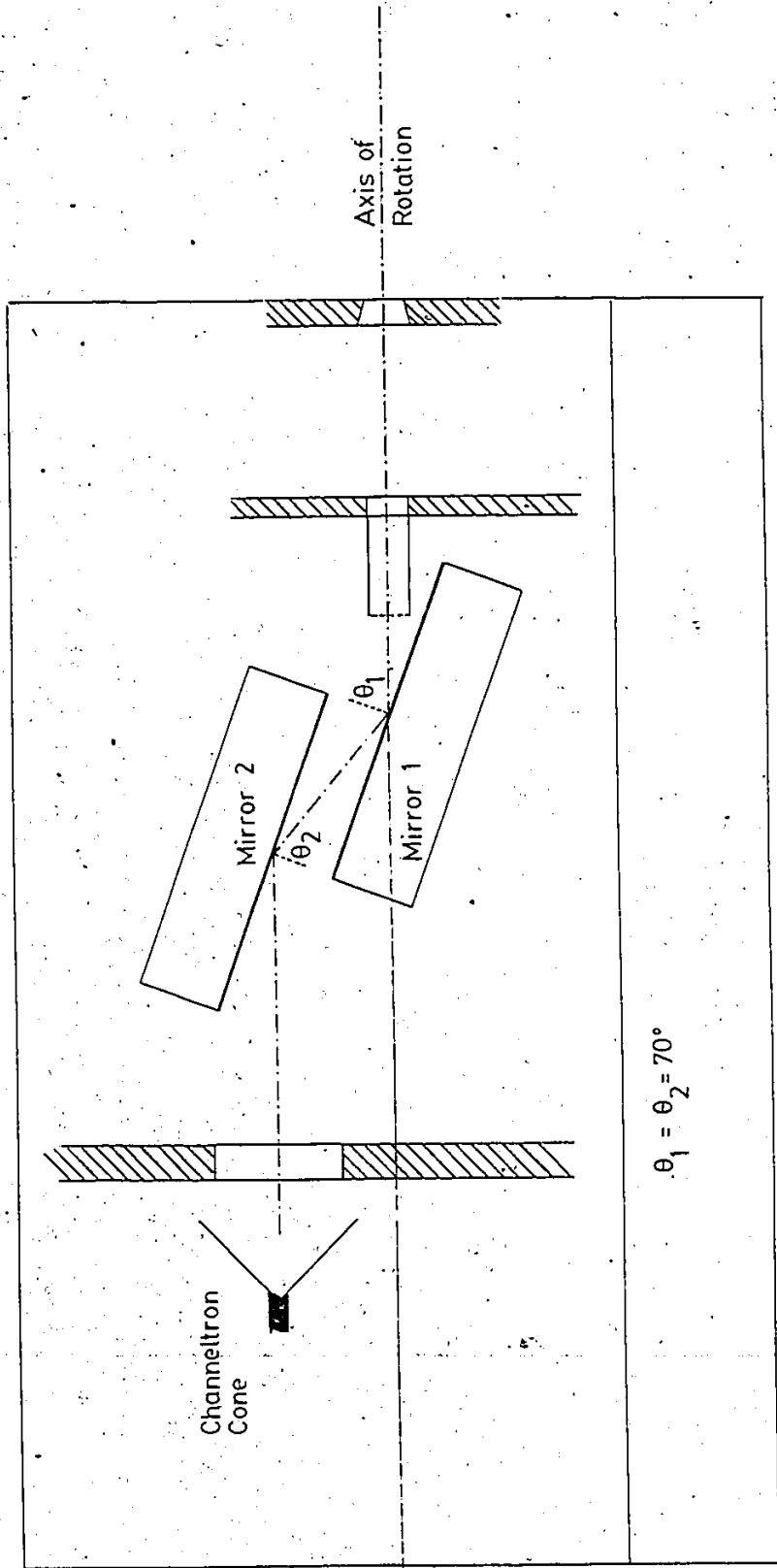
4.3 DESCRIPTION OF THE EXPERIMENT

4.3.1 Interaction Region and Detectors

The interaction region is identical to the one used to detect metastable atoms, with the following exceptions:

(1) The gas beam was moved from the y-axis to the x-axis so that gas would not be effusing straight into the photon detector sitting above the interaction region. This modification reduced the chances of radiation trapping of the photons by the gas.

(2) The metastable detector was replaced by a polarized photon detector, consisting of a reflection polarizer and a channeltron(see Fig. 4.4(a) and Fig. 4.4(b)). This detector could be rotated automatically through 90 degrees by a synchronous motor attached to it.

(3) The analyzer half of the spectrometer was used to perform energy loss measurements on the scattered electrons as discussed in Chapter 2. The analyzer could be rotated about the y-axis to detect electrons scattered into non-zero angles.

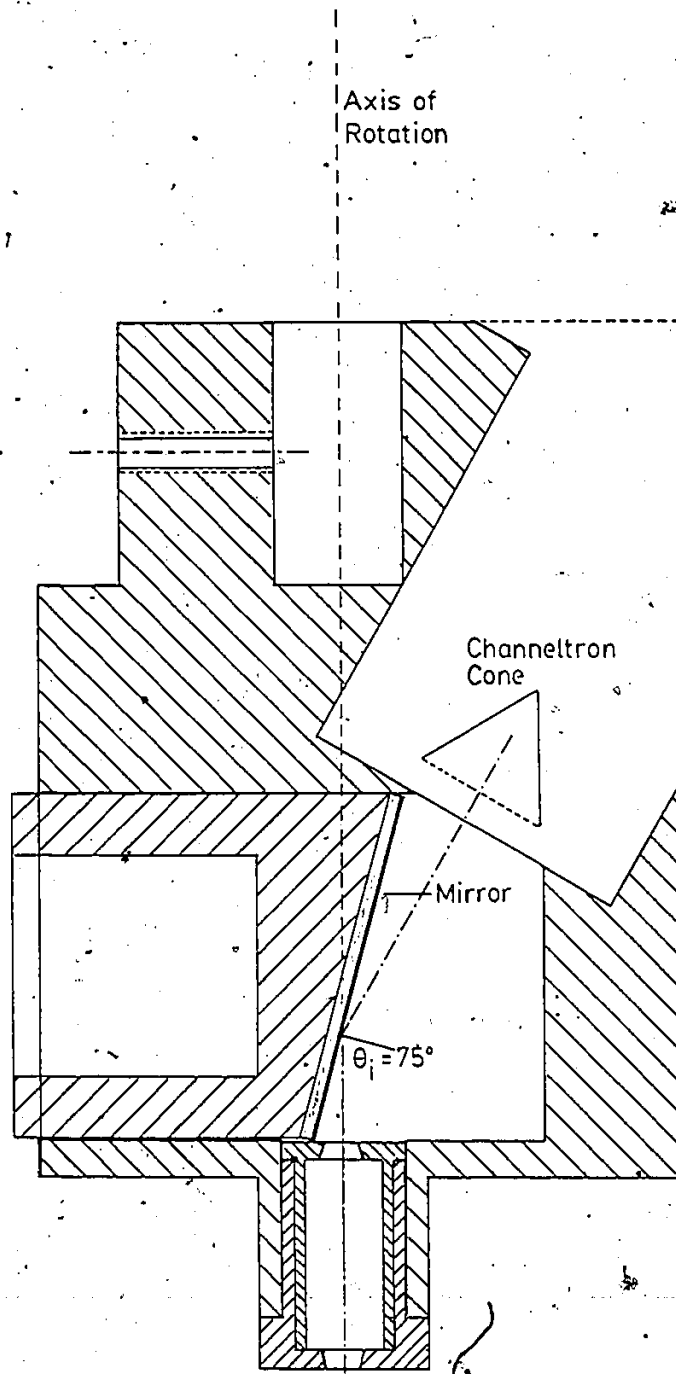A schematic diagram of the experimental geometry has already been discussed in section 4.2.3(see Fig. 4.2), so we need not discuss this further.

Polarized Photon Detectors

Axis of Rotation

Mirror 2

Mirror 1

θ_1

θ_2

Channeltron Cone

$\theta_1 = \theta_2 = 70°$

-2 MIRROR POLARIZER

FIG 4.4(a)

Axis of
Rotation

Channeltron
Cone

Mirror

$\theta_i = 75°$

SINGLE MIRROR
POLARIZER

FIG 44(b)

Fig's. 4.4(a) and 4.4(b) show diagrams of the two polar-
ized photon detectors used in this work. Fig. 4.4(a) illus-
trates a double-reflection device identical to the one used
by Malcolm and McConkey[60], except that aluminum mirrors
coated with MgF_2 were used instead of gold mirrors. The
reason for this is that any mercury vapour (from the diffu-
sion pumps) reaching the gold surface would attack it and
severly reduce the reflectivity of the surface. The double-
reflection polarizer was used to perform the polarization
correlation experiments in N_2. The polarization sensitivity
of the device was measured, and found to be 0.40 for the N_2
emissions.

Fig. 4.4(b) shows a single-reflection polarized photon
detector, used for the measurements with H_2. It was found
that the double-reflection polarizer had a polarization sen-
sitivity of 0 for the H_2 emissions, so a new device had to
be used. The mirror in the single-reflection polarizer was
made out of glass, which was found to have significant
polarization sensitivity over a large wavelength range[83].
For the H_2 emissions, the polarization sensitivity of this
device was measured and found to be 0.55.

No wavelength selection was performed in the photon chan-
nel other than that which occured due to the decrease in the
channeltron sensitivity toward longer wavelengths. For this
reason, a number of vibrational bands contributed to the
observed signal in the photon channel. However, this is not
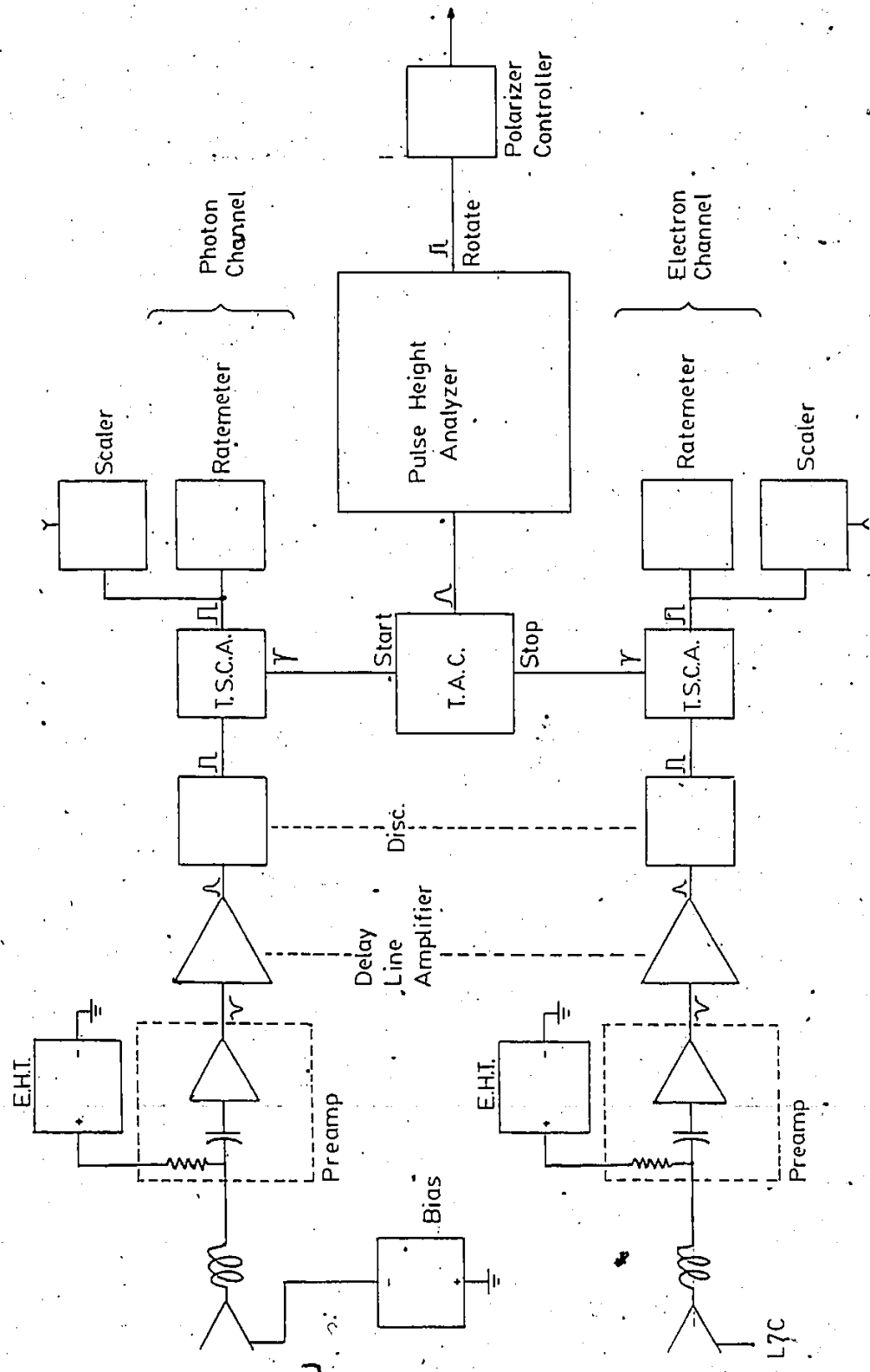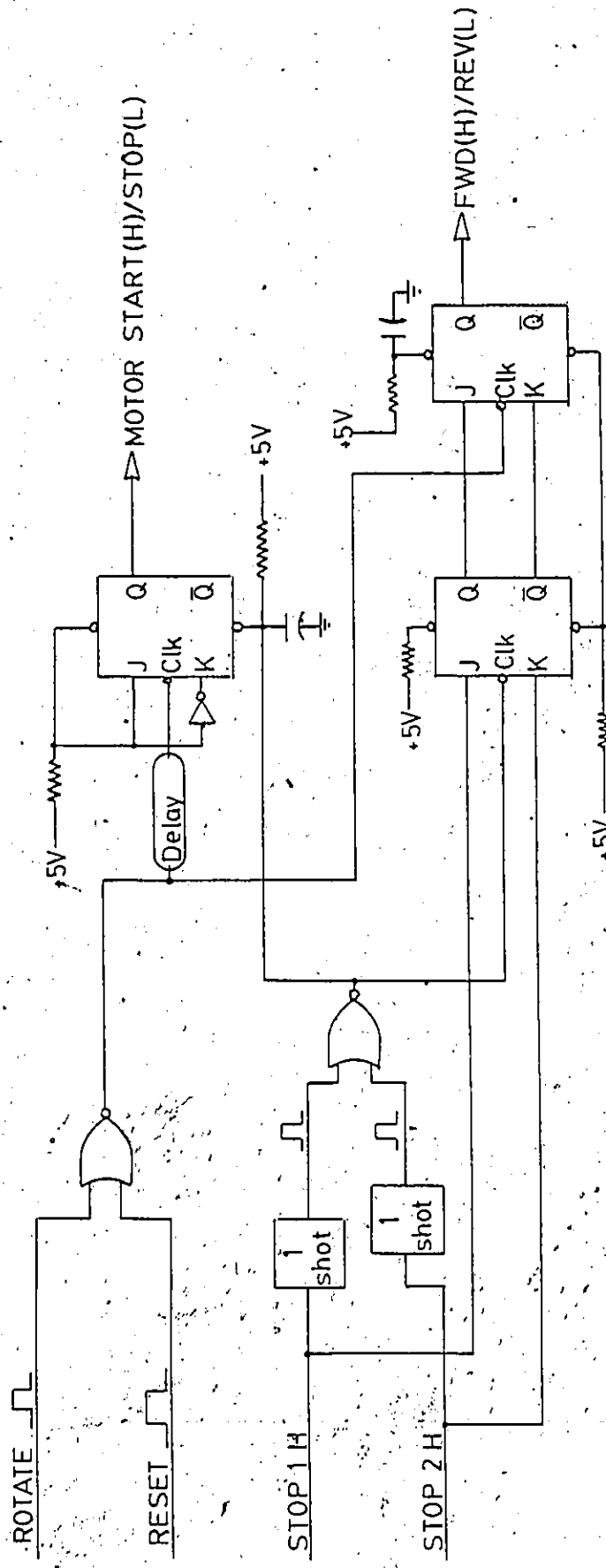expected to be a problem, since vibrational transitions do

FIG 4.5 COINCIDENCE ELECTRONICS

MOTOR START(H)/STOP(L)

FWD(H)/REV(L)

ROTATE

RESET

STOP 1 H

STOP 2 H

POLARIZER CONTROLLER LOGIC CIRCUIT

FIG 4.6

not contribute any angular momentum to the excitation or
decay processes, and will not affect the polarization. In
fact, straightforward polarization measurements using differ-
ent vibrational bands in H_2 confirmed this aspect[73].

Coincidence Counting Electronics

The coincidence counting electronics are shown in Fig.
4.5 and Table 4.2 lists the components used. Note that the
photon channel is used to start the time-to-amplitude con-
verter(TAC) and the electron channel is used to stop it.
The timing single channel analyzers have adjustable delays
which were used to vary the overall relative delay between
the photon and electron channels. The position of the coin-
cidence peak in the time spectrum could be adjusted in this
way. Normally, the integral discriminators are not neces-
sary, since the TSCA's(*) have constant fraction discrimina-
tors built in, but it was found that the timing resolution
of the electronics could be improved significantly by
including them. Output pulses from the TAC were fed into a
TN-1710 pulse height analyzer which was used to obtain the
coincidence spectrum(more will be said about this later).

Fig. 4.6 shows a logic diagram of the electronics used to
rotate the polarized photon detector. The TN-1710 issued a
TTL pulse to the device, telling it to rotate the polarizer
through 90 degrees. Microswitches on the motor mounting
were used to signal the controller that rotation was com-

(*) Timing Single Channel Analyzers

Table 4.2
Coincidence Counting Electronics

Module	Function
Tennelec AEC-5000	Channeltron High Voltage Supply
Kepco HB2AM	Photon Channeltron Bias Supply
Ortec 461	Delay Line Amplifier
Ortec 421	Integral Discriminator
Ortec 551	Timing Single Channel Analyzer
Ortec 467	Time to Pulse Height Converter
Ortec 441	Ratemeter
Ortec 484	Scaler
Tracor Northern TN-1710 TN-1710-4	PHA Mainframe 200MHz ADC

plete.

4.3.2 Data Collection and Analysis

The steps necessary to produce polarization correlation data are relatively straightforward and are as follows:

(1) An energy loss spectrum was acquired (as outlined in Chapter 2) over an energy range which covers the transition to be studied. This was normally done at a scattering angle of ·0 degrees to obtain the maximum amount of signal, and at an energy well above the excitation threshold. Acquisition times were on the order of 1-2 hours, since the electron count rates were on the order of 20kHz or more for the largest energy loss peaks. From the energy loss spectrum, an estimate of the overall resolution of the spectrometer could be obtained. The signal to noise ratio in the electron channel could also be maximized this way. Once the energy loss spectrum was obtained, the peak corresponding to the desired transition was identified, and the analyzer was tuned to that energy.

(2) The coincidence electronics was then set up to provide optimum timing resolution and the relative delay between the photon and electron channels was adjusted so that the coincidence peak appeared approximately in the middle of a

512 channel spectrum. This was to ensure that a reliable value for the background would be obtained on both sides of the peak. The timing range of the TAC was chosen to be 400ns in the present work.

(3). The TN-1710 PHA was then programmed to acquire data in both halves of its memory; the first half corresponding to the polarizer at the angle β and the second half corresponding to the polarizer rotated to the angle $\beta+90$. Coincidence counts were accumulated in each half of memory for a preset amount of _live_ _time_, after which it sent a pulse to 'the polarizer controller, telling it to rotate the polarizer. After a suitable delay (allowing the rotation to complete), the TN-1710 switched memory halves and resume counting.' This sequence was repeated until sufficient statistics were accumulated. Systematic variations in beam current and target gas pressure were averaged out in this way, and the two coincidence spectra were automatically normalized to the total live time. Because of the low coincidence rates, typical data collection times were 30 to 80 hrs, and the statistics were then only about 3 percent at best.

Before using N_2 or H_2 as target gases, the operation of the system was checked out using He. This was done to

ensure that reliable results could be obtained and to determine the orientation of the polarization ellipse. Also, any asymmetry in the polarization ellipse could be estimated from this. This was necessary since the measurements were made at only 2 angles instead of all four. Thus any asymmetry would affect the measured value of the polarization and would have to be corrected for. It was found that the asymmetry in the polarization ellipse was negligible in the present work. Of course, it would have been better to measure the coincidence data at all four angles β, $\beta+90$, $\beta+180$ and $\beta+270$, since this would average out any asymmetry. This modification is being planned for future experiments of this type.

Another experimental parameter which had to be determined was the acceptance angle (angular resolution) of the analyzer. This was done by observing the electron signal with no target gas present as a function of the angular position of the analyzer. It has been shown by Hertel and Ross[84] that the angular resolution of the analyzer is given by the angle at which the electron signal disappears. In the present work, this occured at about 2 degrees.

Analysis of the Coincidence Data

Fig. 4.6 shows a typical set of coincidence spectra obtained in the present work. The peak in the spectrum comes from electron-photon pairs which are correlated. Uncorrelated electron-photon pairs produce chance coinicidences which appear as a uniform background in the spectrum.
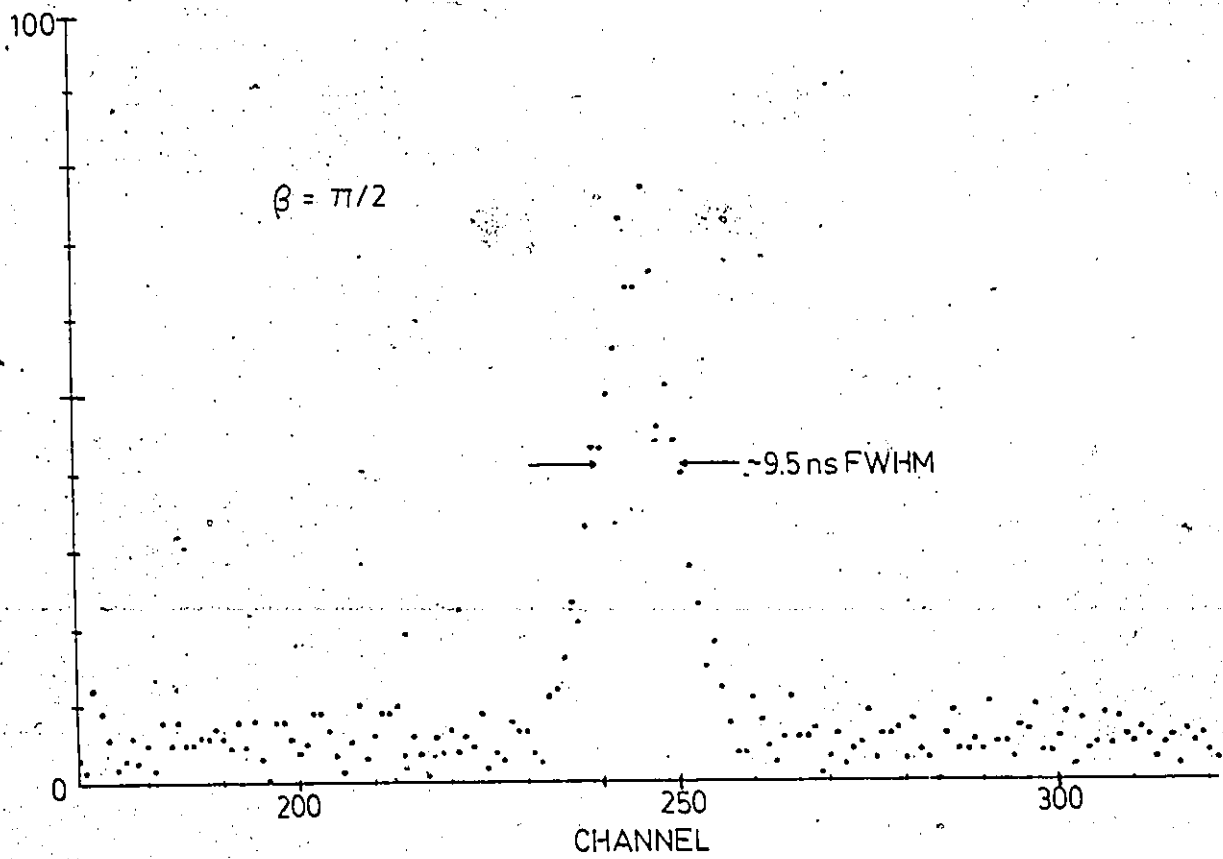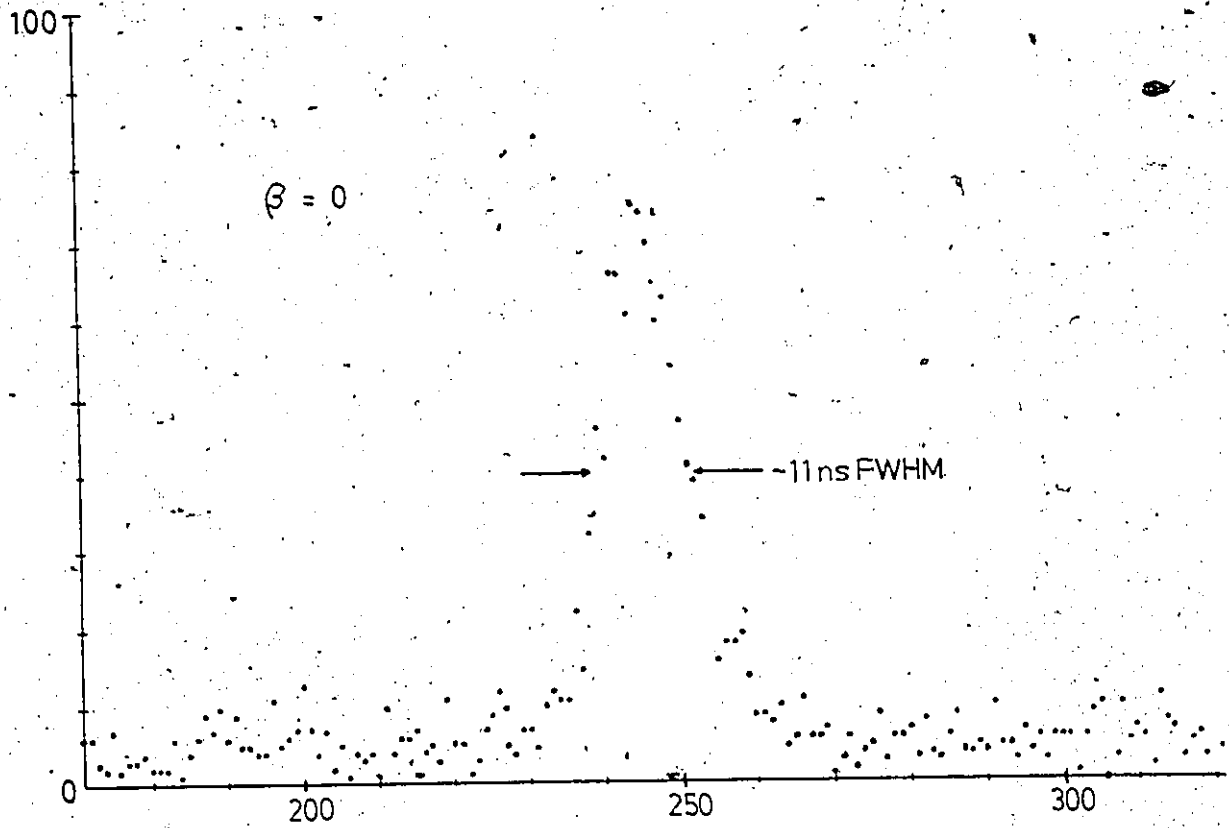
FIG 4.7 Typical Coincidence Spectra

The number of true coincidences is then the area under the peak minus the number of chance coincidences which contribute to the peak. The polarization is then defined as:

$$P_C(\beta) = \frac{1}{\alpha} \frac{N_C(\beta) - N_C(\beta+90)}{N_C(\beta) + N_C(\beta+90)} \qquad (4.3.2.1)$$

where $N_C(\beta)$ is the number of true coincidences obtained with the polarizer set to the angle β and α is the polarization sensitivity of the polarizer. With this definition, the Stokes' parameters that were measured are:

$$s_3 = P_C(0)$$
$$s_1 = P_C(45)$$

Assuming Poisson statistics, the error in $P_C(\beta)$ can be determined, and is given by:

$$\sigma(P_C(\beta)) = \frac{2(N_C^2(\beta+90)(N_C(\beta)+2N_b(\beta))+N_C^2(\beta)(N_C(\beta+90)+2N_b(\beta+90)))^{1/2}}{\alpha(N_C(\beta) + N_C(\beta+90))^2} \qquad (4.3.2.2)$$

where $N_C(\beta)$ is the number of true coincidences and $N_b(\beta)$ is the number of chance coincidences obtained at the polarizer angle β.

The pseudo-threshold polarization was obtained by measuring $P_C(0)$ at a scattering angle of 0 degrees.

For lack of a better model, the polarization correlation data was analyzed in terms of two dipole oscillators as discussed in section 4.2.2. This is bound to have its shortcomings, of course, since this model necessarily implies complete coherence. There is no reason to suppose that this will be the case for molecules when the rotational structure is not resolved, as dicussed in section 4.2.4. The follow-

ing equations list the various parameters deduced from the polarization correlation data and the associated errors.

$$R = \frac{a_x}{a_z} = \frac{1 - P_C(0)}{1 + P_C(0)}^{1/2} \qquad (4.3.2.3a)$$

$$\sigma(R) = \frac{P_C(0)}{1 + P_C(0)} \frac{\sigma(P_C(0))}{(1 - P_C^2(0))^{1/2}} \qquad (4.3.2.3b)$$

$$\delta = \cos^{-1}(P_C(45)/(1-P_C^2(0))^{1/2}) \qquad (4.3.2.4a)$$

$$\sigma(\delta) = \frac{180}{\pi} \frac{(\sigma^2(P_C(45))+(P_C(0)P_C(45)/(1-P_C^2(0))^2\sigma^2(P_C(0)))^{1/2}}{(1 - P_C^2(0) - P_C^2(45))^{1/2}} \qquad (4.3.2.4b)$$

$$\theta_{min}^{\gamma} = \frac{1}{2} \tan^{-1} \frac{P_C(45)}{P_C(0)} \qquad (4.3.2.5a)$$

$$\sigma(\theta_{min}^{\gamma}) = \frac{180}{\pi} \frac{(P_C^2(0)\sigma^2(P_C(45)) + P_C^2(45)\sigma^2(P_C(0)))^{1/2}}{2(P_C^2(0) + P_C^2(45))} \qquad (4.3.2.5b)$$

The shape of the radiation pattern in the scattering plane was determined by making the arbitrary normalization:

$$a_z^2 + a_x^2 = 1$$

and solving for a_z and a_x from equation 4.3.2.3a. These values were then used in the following equation:

$$I(\theta) = a_z^2 \sin^2\theta + a_z a_x \cos\delta \sin2\theta + a_x^2 \cos^2\theta \qquad (4.3.2.6)$$

The direction of momentum transfer is given by:

$$\theta_k = \tan^{-1}(((\sin\theta_e(1-\Delta E/E)^{1/2})^{-1}-\cot\theta_e)^{-1}) \qquad (4.3.2.7)$$

The derivation of this is given in Appendix 4.6.2.

4.4 RESULTS AND DISCUSSIONS

4.4.1 Nitrogen Data

Figures 4.8-4.16 present the results obtained for the excitation of the $C_1^1\Sigma_u^+(v'=0)$ state of N_2. Fig. 4.8 shows the energy loss spectrum obtained at an incident energy of 80 eV and a scattering angle of 0 degrees. The C state is indicated on the diagram and occurs at 12.93 eV. The estimated energy resolution of the spectrometer is 100 meV. Typical electron count rates at the peak varied from 60kHz at $\theta_e=0$ to about 10kHz at $\theta_e=15$ degrees, and the photon count rates were about 10-30 Hz, reflecting the low transmission of the polarizer (about 10 percent). Not resolved in this spectrum are the peaks on the low energy flank of the C peak due to excitation of other states. This is not a problem, however, as the recent measurements performed by Read and co-workers(*) show that the main contribution to the coincidence rate comes from the C feature. They performed coincidence gated energy loss measurements in this energy region and found that the C state is the dominant contribution to the photon signal; contributions from the $b^1\Pi_u$ state are negligible.

Figure 4.9 shows the variation of $P_C(0)$ with gas pressure at an energy of 35 eV and $\theta_e=0$ degrees. Table 4.3 lists the data. Note that at pressures above 2 torr there is a significant decrease in the polarization due to resonance trap-

_____

(*) G.C. King, private communication

$X^1\Sigma_g^+(v''=0) \longrightarrow C_4'^1\Sigma_u^+(v'=0)$

FIG 4.8

$e^- + N_2$ ENERGY LOSS SPECTRUM

$E_{inc} = 80\ eV;\ \theta_e = 0°$

ENERGY LOSS (eV)
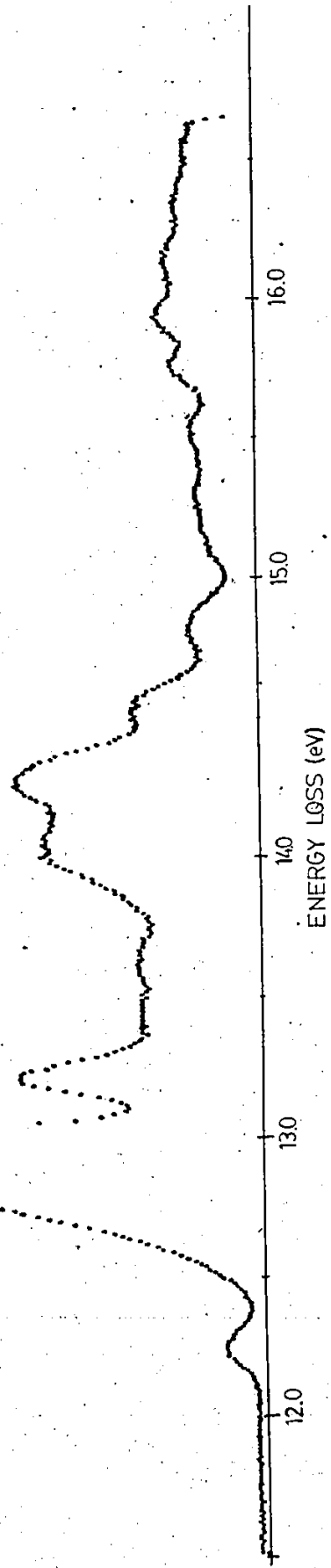
FIG 4.9
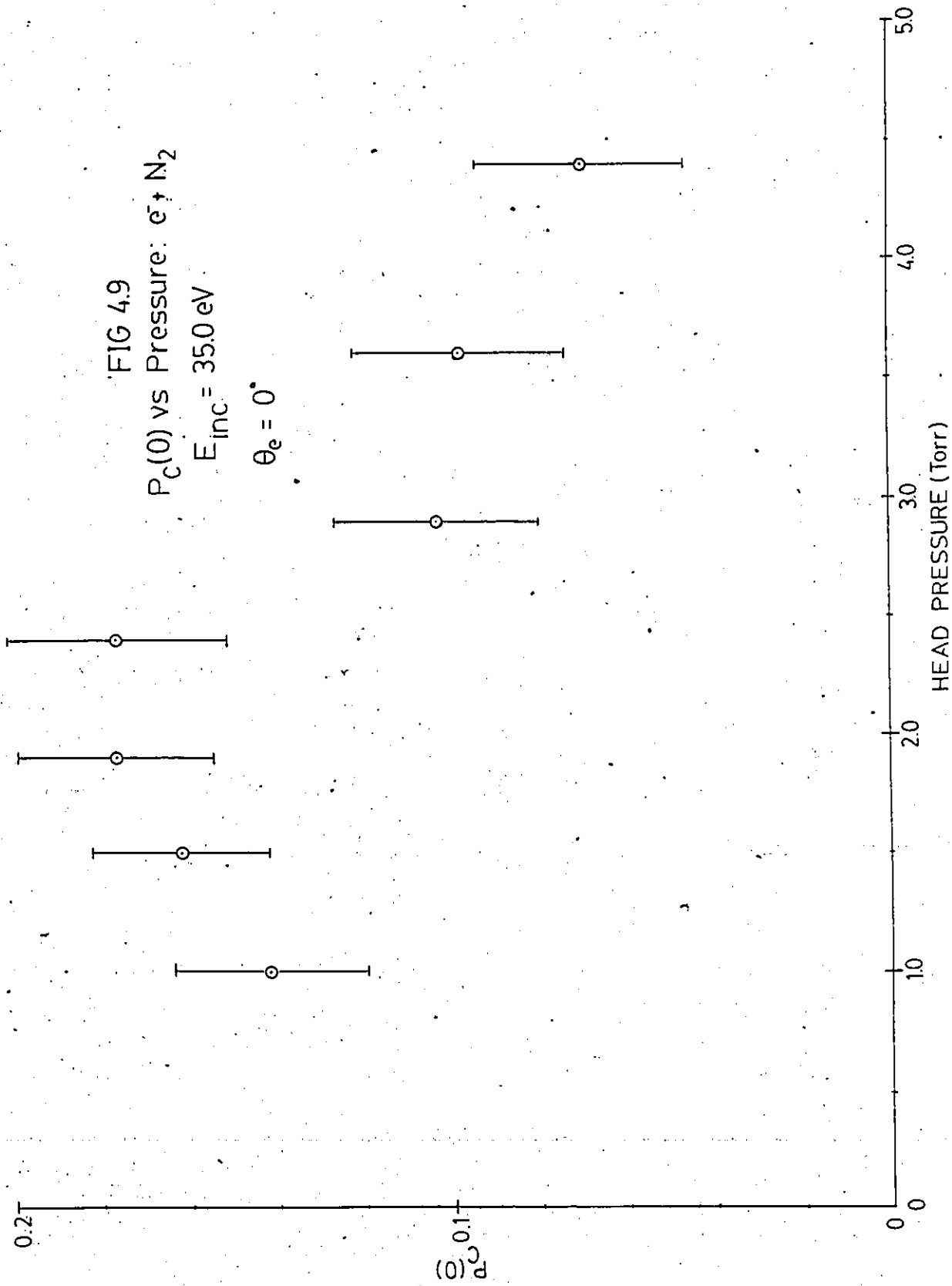$P_C(0)$ vs Pressure: $e^- + N_2$
$E_{inc} = 35.0$ eV
$\theta_e = 0°$

Table 4.3
$P_C(0)$ vs Pressure: N_2

Incident Energy = 35.0 eV, Electron Scattering Angle = 0

| Head Pressure(torr)	Polarization
1.0±0.1	0.14±0.02
1.5±0.1	0.16±0.02
1.9±0.1	0.18±0.02
2.4±0.1	0.18±0.03
2.9±0.1	0.10±0.02
3.6±0.1	0.10±0.02
4.4±0.1	0.07±0.02

---

ping or collisional effects. To ensure that subsequent measurements were free from such effects, a pressure of 1.5 torr was chosen as the working pressure throughout the rest of the experiment.

Pseudo-threshold Polarization Measurements

Fig. 4.10 shows the variation of $P_C(0)$ with incident energy at a scattering angle of 0 degrees, and Table 4.4 lists the results. This is the first such pseudo-threshold polarization measurement made in N_2. The data indicates a pseudo-threshold polarization value of 0.18 ± 0.04. Arrow a indicates the predicted threshold polarization using results of section 4.2.5 (equation 4.2.5.12), with a value of 0.19. Arrow b indicates the predicted polarization when hyperfine structure effects were taken into account (see details in ref 85). This has a value of 0.17. The experimental value is in good agreement with these, but the statistical uncertainty in the data precludes a further distinction between the two approaches. The experimental value of P_{th} is certainly above the predicted value of 0.143 using the semi-classical approach[80] (arrow c), and more than a factor of 2 above the extrapolated threshold polarization obtained by Huschilt et al[85], with a value of 0.07 (arrow d). The lack of agreement between the pseudo-threshold value and the predicted polarizations with the direct polarization measurements of Huschilt et al is rather puzzling, particularly since resonances or electron correlation effects do not appear to be dominating the excitation process in the near

FIG 4.10
$e^- + N_2$
$P_c(0)$ vs Energy
$\theta_e = 0°$
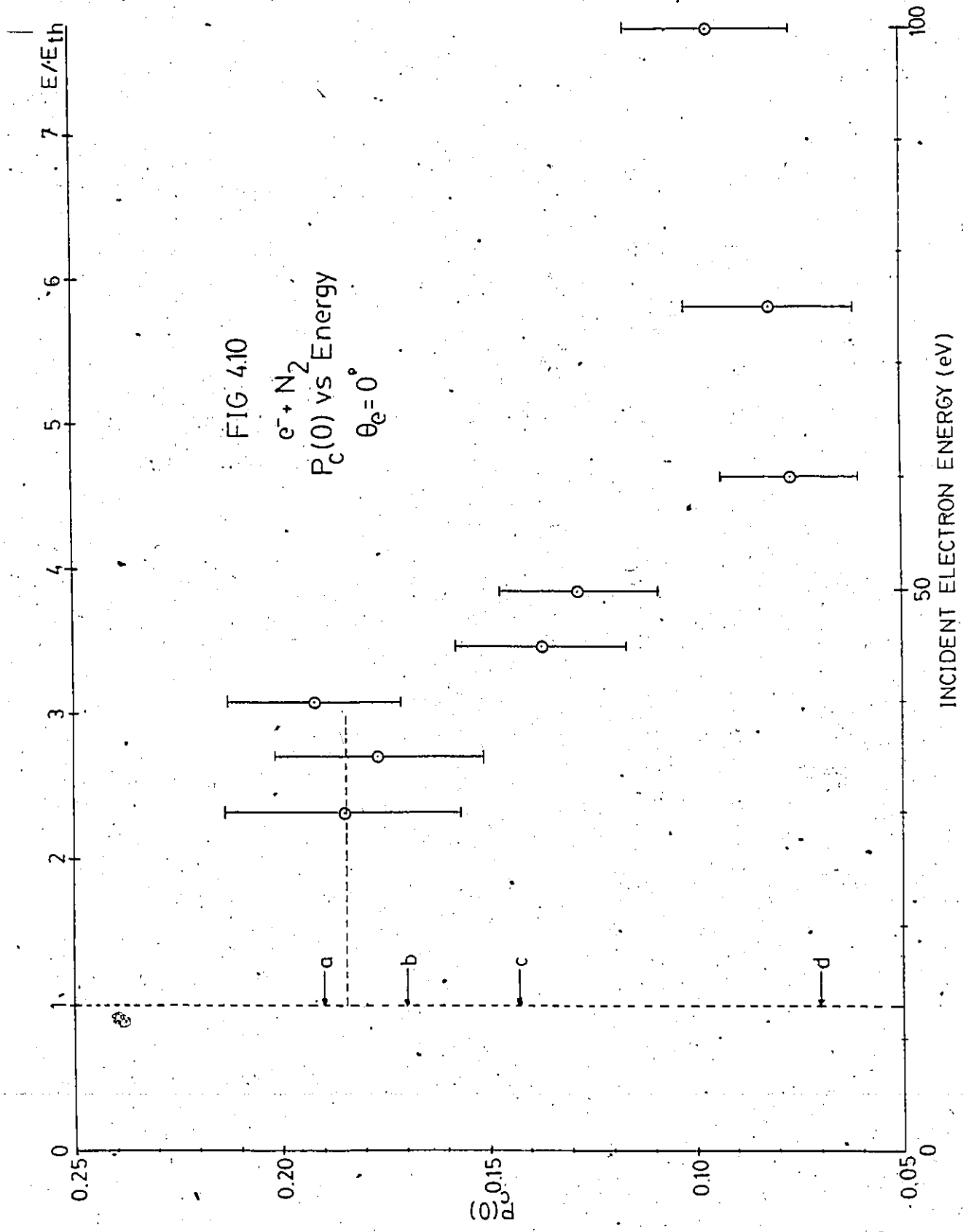
threshold region in N_2. The influence of non-dipole terms in the excitation process was suggested by Huschilt et al, and the recent work of Hernandez et al[86] lends support to this. These authors used a supersonically cooled N_2 beam and observed rotational transitions in the excitation process with changes in rotational quantum number of as much as 15. Since the entire ensemble was initially in the rotational ground state, this implies that non-dipole transitions were occuring in the excitation process. They found that these non-dipole effects were particularly significant at energies below 100 eV. The agreement of the pseudo-threshold polarization with theoretical predictions(where dipole excitation was assumed) is then probably due to the fact that dipole excitation dominates the scattering process in the forward direction. Strong configuration interaction effects[87] associated with the excitation of the C1 state may also be involved.

It is interesting to note that the measurements of Huschilt et al[85] on the polarization of radiation emitted from the $b^1\Pi_u$ state of N_2 also showed a discrepancy between the theoretical predictions and the value they obtained. This result, along with the present results, suggests that non-dipole excitation is occuring for the $b^1\Pi_u$ state also.

Note the decrease in $P_c(0)$ at about 3 times the threshold energy in Fig. 4.10. This is due to the finite acceptance angle of the analyzer[82]. This can be understood as follows. Assuming for the moment that the Born approximation is valid

Table 4.4
$P_c(0)$ vs Incident Energy: N_2

Head Pressure = 1.5 torr, Electron Scattering Angle = 0

Incident Energy (eV)	Polarization
30.0	0.19 ± 0.03
35.0	0.18 ± 0.03
40.0	0.19 ± 0.02
45.0	0.14 ± 0.02
50.0	0.13 ± 0.02
60.0	0.03 ± 0.02
75.0	0.08 ± 0.02
100.0	0.10 ± 0.02

at all energies, the momentum transfer vector is the
quantization axis. The finite angular resolution of the
analyzer means that there will be a distribution in the
direction of momentum transfer, and hence, a depolarization
in the measured value of $P_c(0)$. At low energies, the momen-
tum transfer vector is practically in the forward direction,
and the quantization axis lies very close to the z axis: no
significant depolarization would be observed. At higher
energies, however, the momentum transfer vector rotates away
from the z axis, and results in a larger angular distribu-
tion of this vector, even though the scattered electrons are
detected close to $\theta_e = 0$. This causes the observed depolari-
zation in the data at higher energies.

Polarization Correlation Data

Figure 4.11 shows the variation of $P_c(0)$ and $P_c(45)$ with
incident energy at a scattering angle of 5 degrees, and
Table 4.5 lists the data. Several points should be noted
about Fig. 4.11:

    (1) The small value of $P_c(0)$. It has an essen-
        tially constant value of about 0.06 over the
        whole energy range studied, whereas the pseu-
        do-threshold polarization measurement had a
        value of 0.18.

    (2) The dip in $P_c(0)$ towards 0 at an energy of
        about 67.5 eV is probably significant (see
        later). It appears that a minimum in $P_c(0)$
        occurs whenever $P_c(45)$ goes through 0.

FIG 4.11

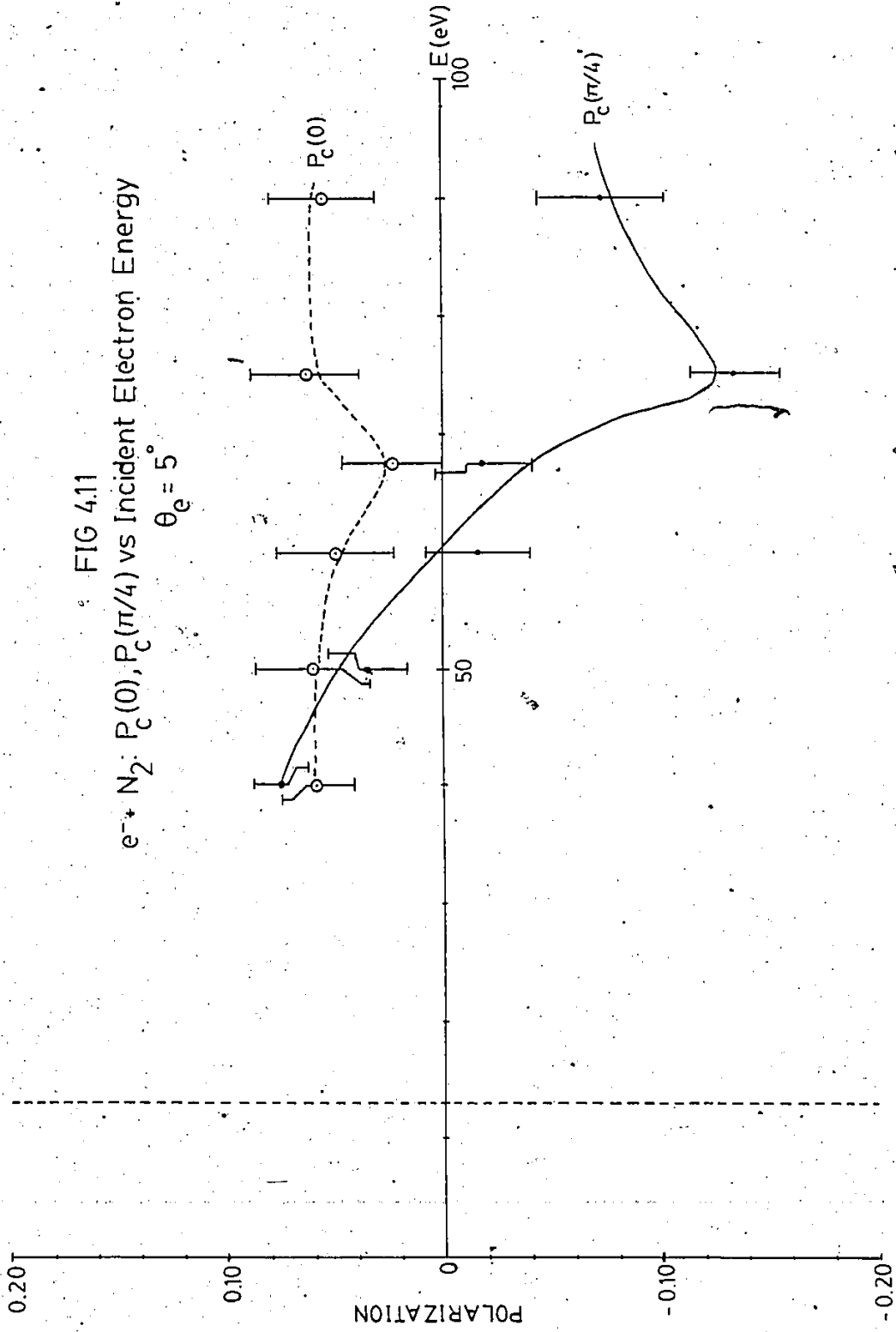$e^- + N_2$: $P_c(0)$, $P_c(\pi/4)$ vs Incident Electron Energy

$\theta_e = 5°$

POLARIZATION

Table 4.5
Polarization Correlation Data vs Energy: N_2

Electron Scattering Angle = 5 degrees, Pressure = 1.5 torr

| E (eV)	$P_C(0)$	$P_C(45)$	a_x/a_z	Phase (deg)	θ^γ_{min} (deg)	θ_k (deg)
40.0	0.06±0.02	0.08±0.01	0.94±0.02	85.7±0.7	-25.9±4.4	21.7
50.0	0.06±0.03	0.04±0.02	0.94±0.03	88.0±1.0	-15.1±8.4	27.8
60.0	0.05±0.03	-0.02±0.02	0.95±0.03	90.9±1.4	9.0±13.5	33.3
67.5	0.02±0.02	-0.02±0.02	0.98±0.02	91.1±1.3	19.8±4.5	36.9
75.0	0.06±0.03	-0.14±0.02	0.94±0.02	97.8±1.2	32.5±4.7	40.2
90.0	0.06±0.02	-0.07±0.03	0.95±0.02	94.2±1.7	26.5±8.1	45.9

(3) $P_c(45)$ is small and positive below 60 eV and then decreases rapidly to about -0.10 at 75 eV, after which it increases slowly again. The rapid variation of $P_c(45)$ near 67.5 eV, along with the decrease in $P_c(0)$ at this energy, suggests that something interesting is happening in the scattering process around 67.5 eV.

Fig. 4.12 shows a typical radiation pattern deduced from the Stokes' parameters, as discussed in section 4.2.2. Indicated on the diagram is the electron scattering angle θ_e, the direction of momentum transfer θ_k, and the orientation of the pattern θ^γ_{min}.

Fig. 4.13(a) shows the variation of θ_k and θ^γ_{min} with incident energy at a scattering angle of 5 degrees. The horizontal error bars reflect the angular resolution of the spectrometer. Note that θ_k and θ^γ_{min} do not seem to be related in any way to each other. This is distinctly differ- rent from the atomic case, where these angles should agree with each other for high energies and small scattering angles. Below 55 eV, θ^γ_{min} and θ_k are on opposite sides of the z axis.

Fig. 4.13(b) shows the variation of the phase angle, δ, with incident energy. Note that between 60 and 67.5 eV the phase angle is close to 90 degrees, suggesting that a signi- ficant component of circular polarization is present in the
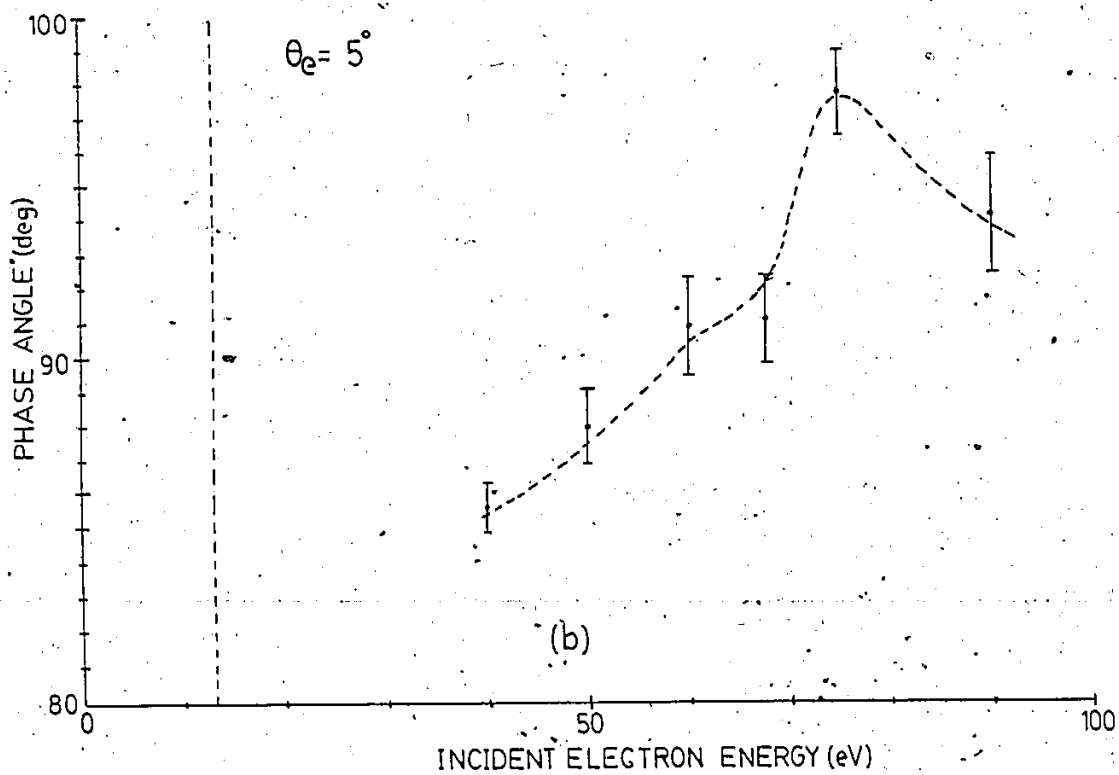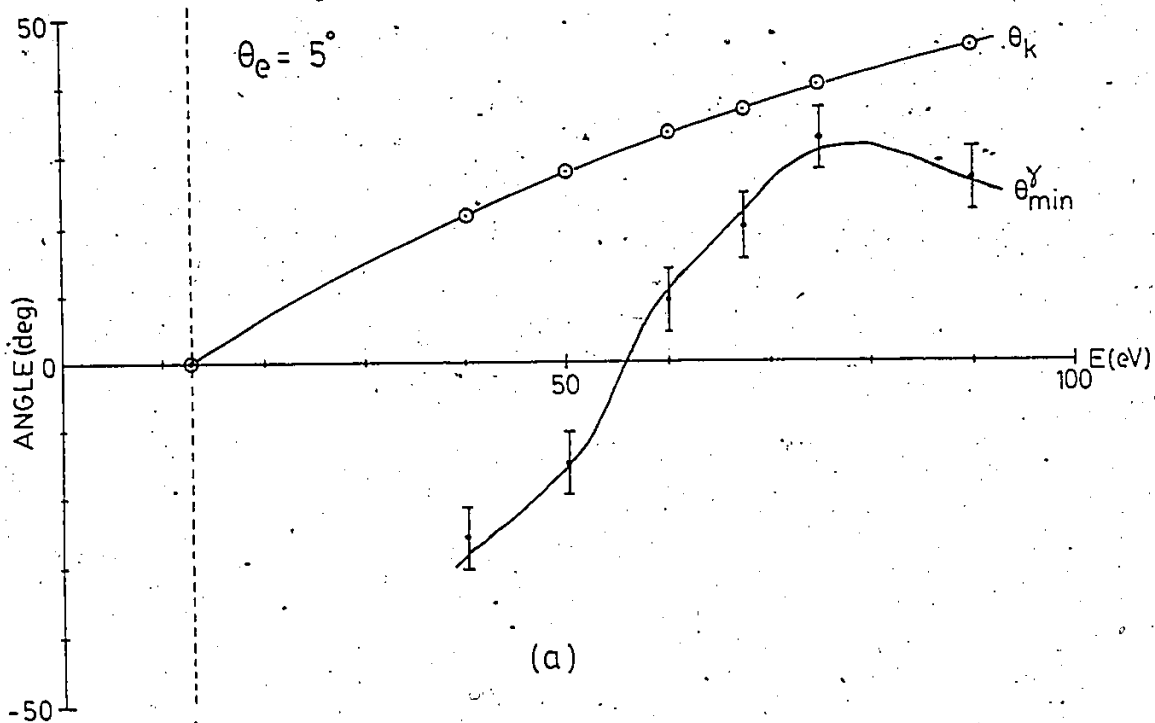
FIG 4.12
N_2 $E = 40\,eV$; $\theta_e = 10°$
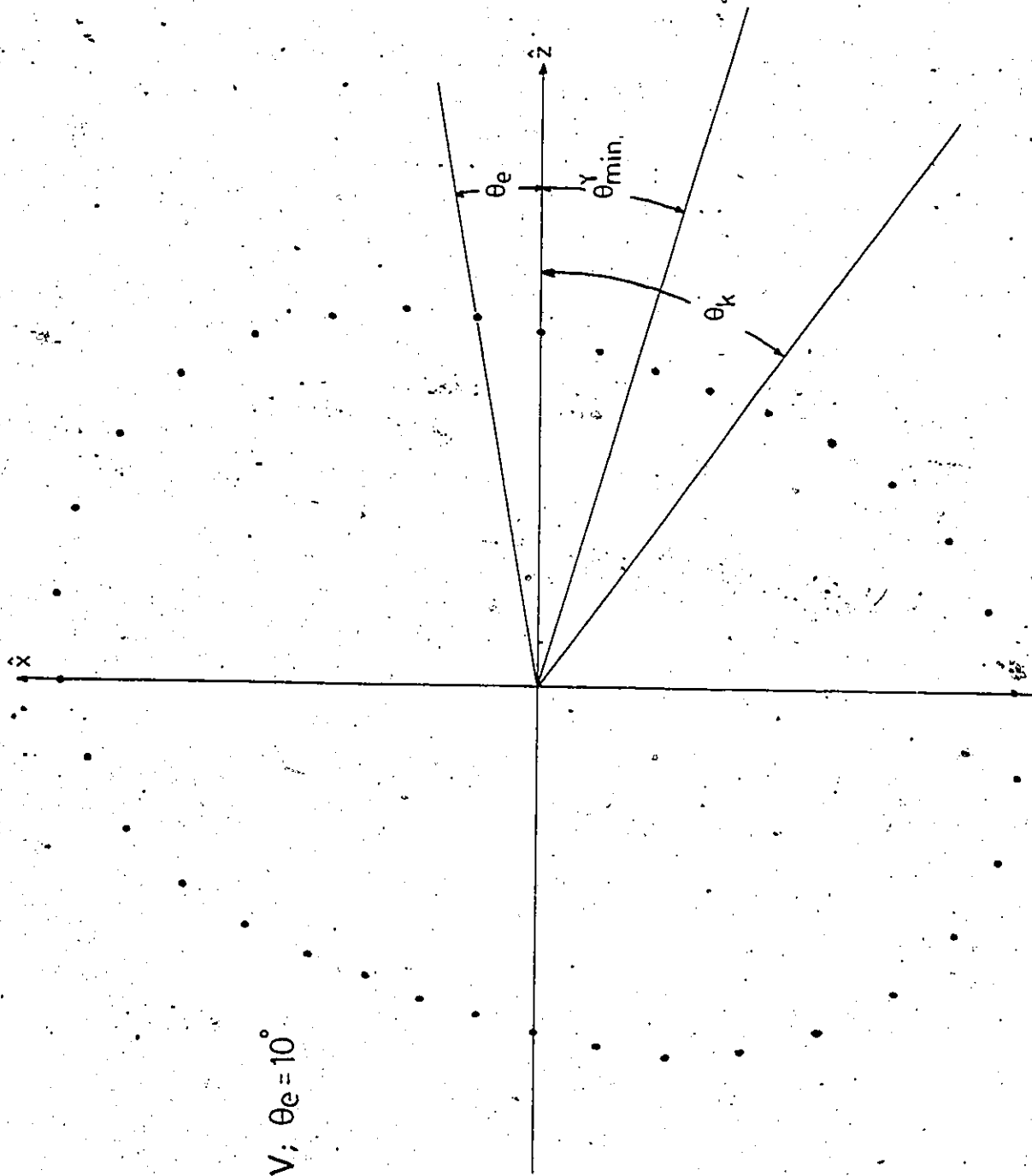
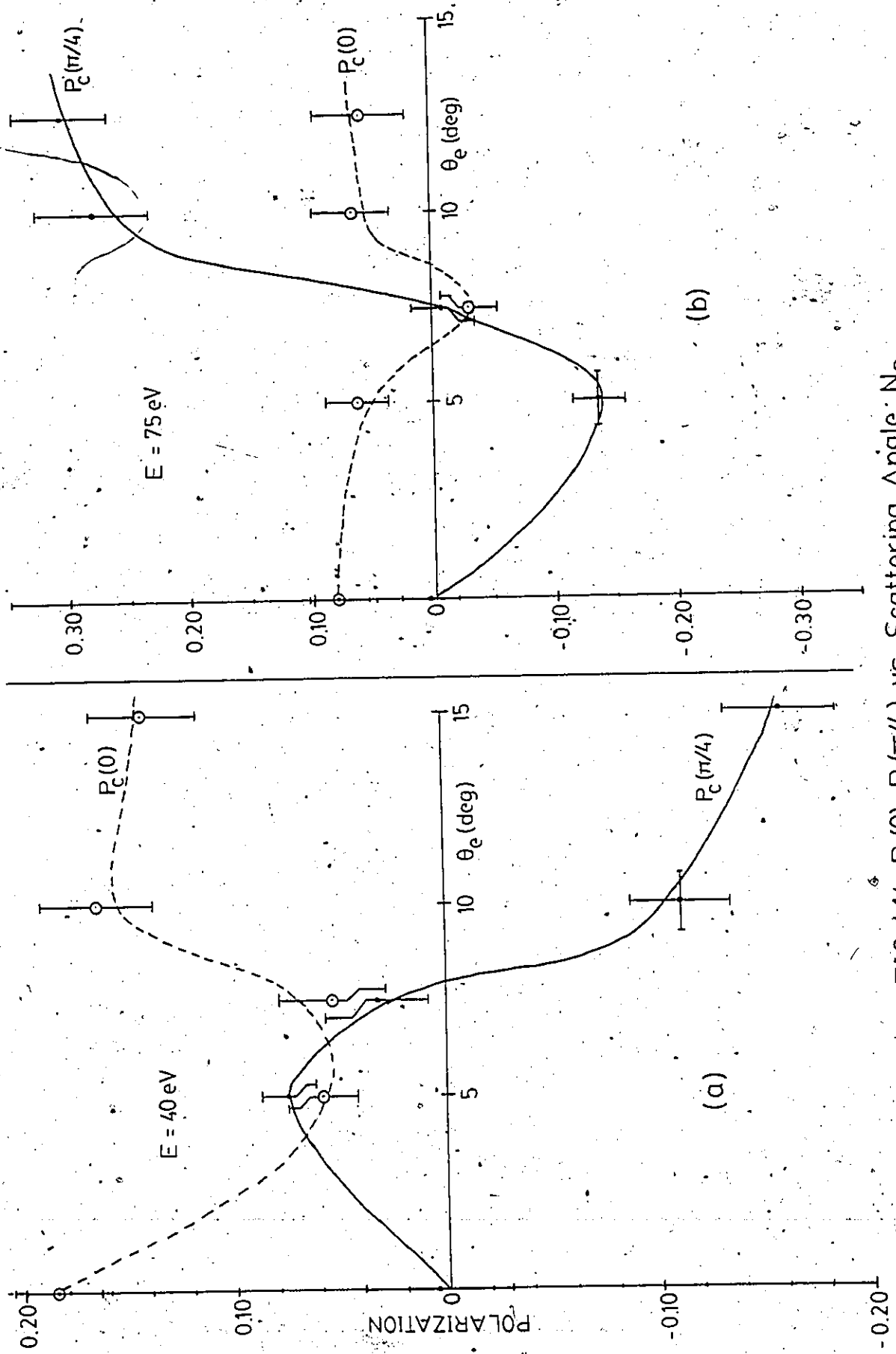FIG 4.13

θ_k, θ_{min}^Y and Phase vs Energy: N_2.

FIG 4.14 $P_C(0)$, $P_C(\pi/4)$ vs Scattering Angle: N_2

Table 4.6
Polarization Correlation Data vs Scattering Angle: N_2

Incident Energy = 40.0 eV, Pressure = 1.5 torr

θ_e (deg)	$E_C(0)$	$E_C(45)$	a_x/a_z	Phase (deg)	θ^γ_{min} (deg)	θ_k (deg)
0.0	0.18±0.02	0.01±0.04	0.83±0.02	89.6±2.0	-0.9±5.4	0.0
5.0	0.06±0.02	0.08±0.01	0.94±0.02	85.7±0.7	-25.9±4.4	21.7
7.5	0.05±0.02	0.03±0.02	0.95±0.02	88.1±1.4	-15.7±4.5	30.2
10.0	0.16±0.03	-0.11±0.02	0.85±0.02	96.4±1.3	16.9±3.5	36.6
15.0	0.14±0.02	-0.16±0.03	0.87±0.02	99.2±1.5	24.1±3.4	46.0

Incident Energy = 75 eV, Pressure = 1.5 torr

θ_e (deg)	$E_C(0)$	$E_C(45)$	a_x/a_z	Phase (deg)	θ^γ_{min} (deg)	θ_k (deg)
0.0	0.08±0.02	0.00±0.02	0.92±0.02	89.7±1.3	-1.8±4.5	0.0
5.0	0.06±0.02	-0.14±0.02	0.94±0.02	97.8±1.2	32.5±4.7	40.2
7.5	-0.03±0.02	-0.01±0.03	1.03±0.02	90.5±1.5	-8.1±4.5	50.4
10.0	0.07±0.03	0.28±0.05	0.94±0.03	73.8±2.8	-38.3±3.3	56.6
12.5	0.06±0.04	0.30±0.04	0.94±0.04	72.3±2.4	-39.6±3.5	60.4

emitted radiation.

Fig's. 4.14(a) and (b) show the variation of the Stokes' parameters with electron scattering angle at 40 and 75 eV, respectively. Table 4.6 lists the data. The following points should be noted from these figures:

(1) The rapid decrease in $P_C(0)$ to the minimum which occurs at about 7.5 degrees. Note also that $P_C(45)$ goes through 0 at about this angle. At larger scattering angles, $P_C(0)$ remains essentially constant, but $P_C(45)$ shows large variations.

(2) The behaviour of $P_C(45)$ at 40 eV is almost exactly opposite to the behaviour at 75 eV. $P_C(45)$ goes through 0 at about 7.5 degrees, independent of energy, and the extremum (maximum or minimum) in $P_C(45)$ occurs at about 5 degrees, again independent of energy.

(3) $P_C(0)$ appears to be close to 0 at 7.5 degrees at the incident energy of 75 eV.

(4) Attention should be drawn to the large variations in $P_C(45)$. These are much larger than what was observed in H, (see section 4.4.2).

It would appear from this data that $P_C(0)$ goes through a minimum each time $P_C(45)$ goes through 0. This suggests that there is some sort of correlation between these Stokes' parameters, an effect which would not be expected from the simple model discussed in section 4.2.2.
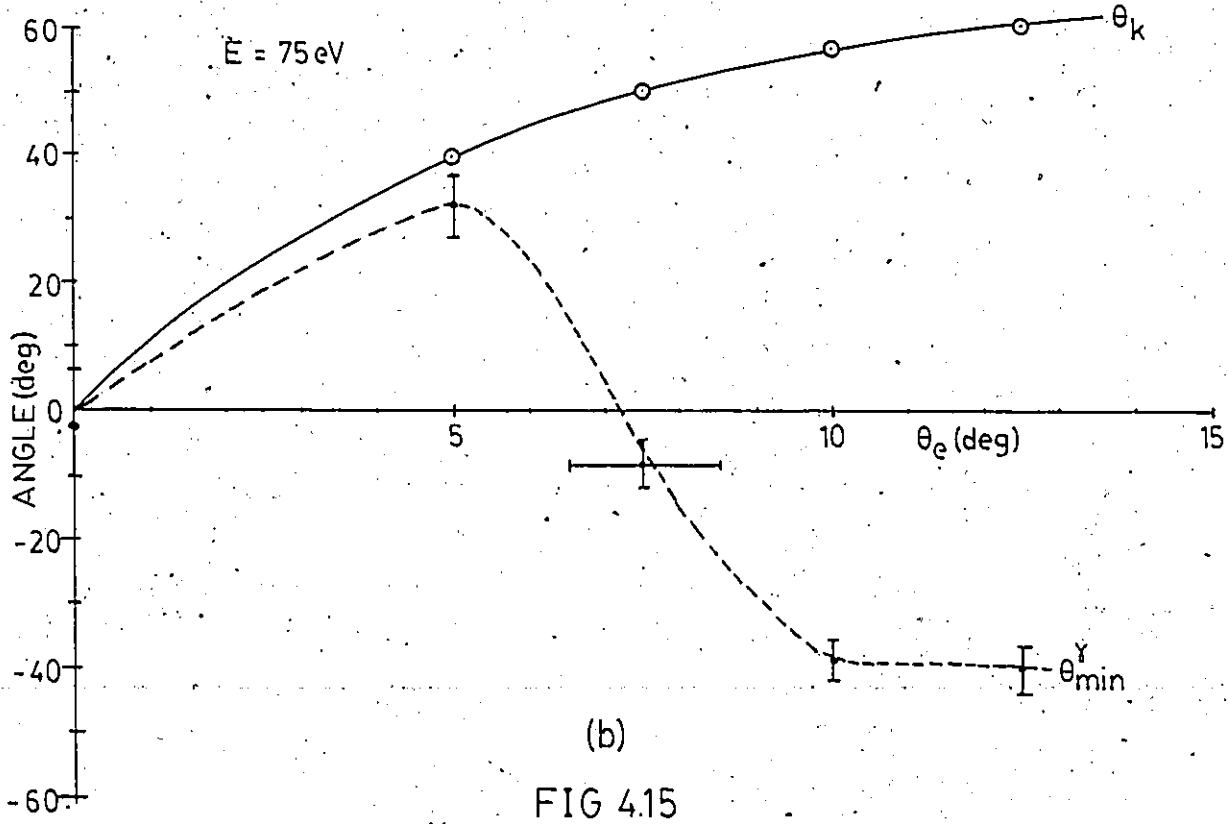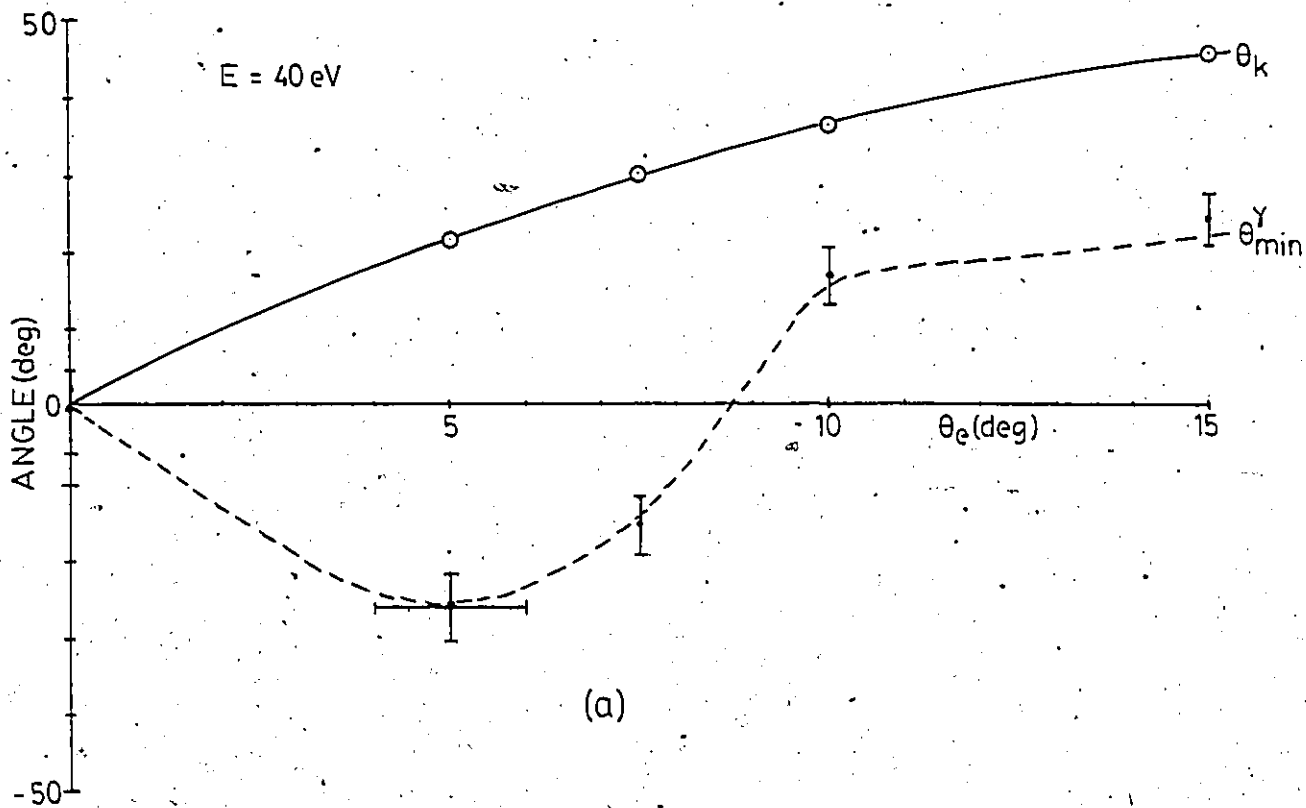
FIG 4.15

θ_k, θ_{min}^Y vs Scattering Angle: N_2

Figures 4.15(a) and (b) show the variation of θ_k and θ_{min}^{γ} with electron scattering angle at 40 and 75 eV, respectively. It can be seen at once that θ_{min}^{γ} bears no relationship to θ_k whatsoever, suggesting that the Born approximation is clearly inadequate to describe the scattering process for N_2. The significant difference in the behaviour of θ_{min}^{γ} at 40 and 75 eV should be noted also.

Figure 4.16 shows the variation of the phase angle, δ, with electron scattering angle at 40 and 75 eV. Note once again the opposite behaviour of δ at the two energies. The phase angle is about 90 degrees at a scattering angle of 7.5 degrees, suggesting that a significant component of circular polarization may be present.

Because of the large number of rotational states contributing to the observed radiation, it is not possible to extract information about the scattering amplitudes from the present data. Also, it is not possible to extract information about the state multipoles $\langle T_{KQ}^{\dagger} \rangle$ from the Stokes' parameters, except to say the following. Recall from the discussion of section 4.2.4 that the Stokes' parameters are given by:

$$P_C(0) = (-\langle T_{22}^{\dagger} \rangle + \sqrt{3/2} \, \langle T_{20}^{\dagger} \rangle)/I$$

$$P_C(45) = -2\langle T_{21}^{\dagger} \rangle/I \qquad \text{where}$$

$I = (-2\langle T_{00}^{\dagger} \rangle/\sqrt{3} + \langle T_{22}^{\dagger} \rangle + \langle T_{20}^{\dagger} \rangle/\sqrt{6})$. At a scattering angle of 7.5 degrees, where both $P_C(0)$ and $P_C(45)$ are essentially zero, $\langle T_{21}^{\dagger} \rangle = 0$ and $\langle T_{22}^{\dagger} \rangle = \sqrt{3/2} \, \langle T_{20}^{\dagger} \rangle$.

FIG 4.16 Phase vs Scattering Angle : N$_2$

E = 40 eV

E = 75 eV

θ_e (deg)

PHASE ANGLE (deg)
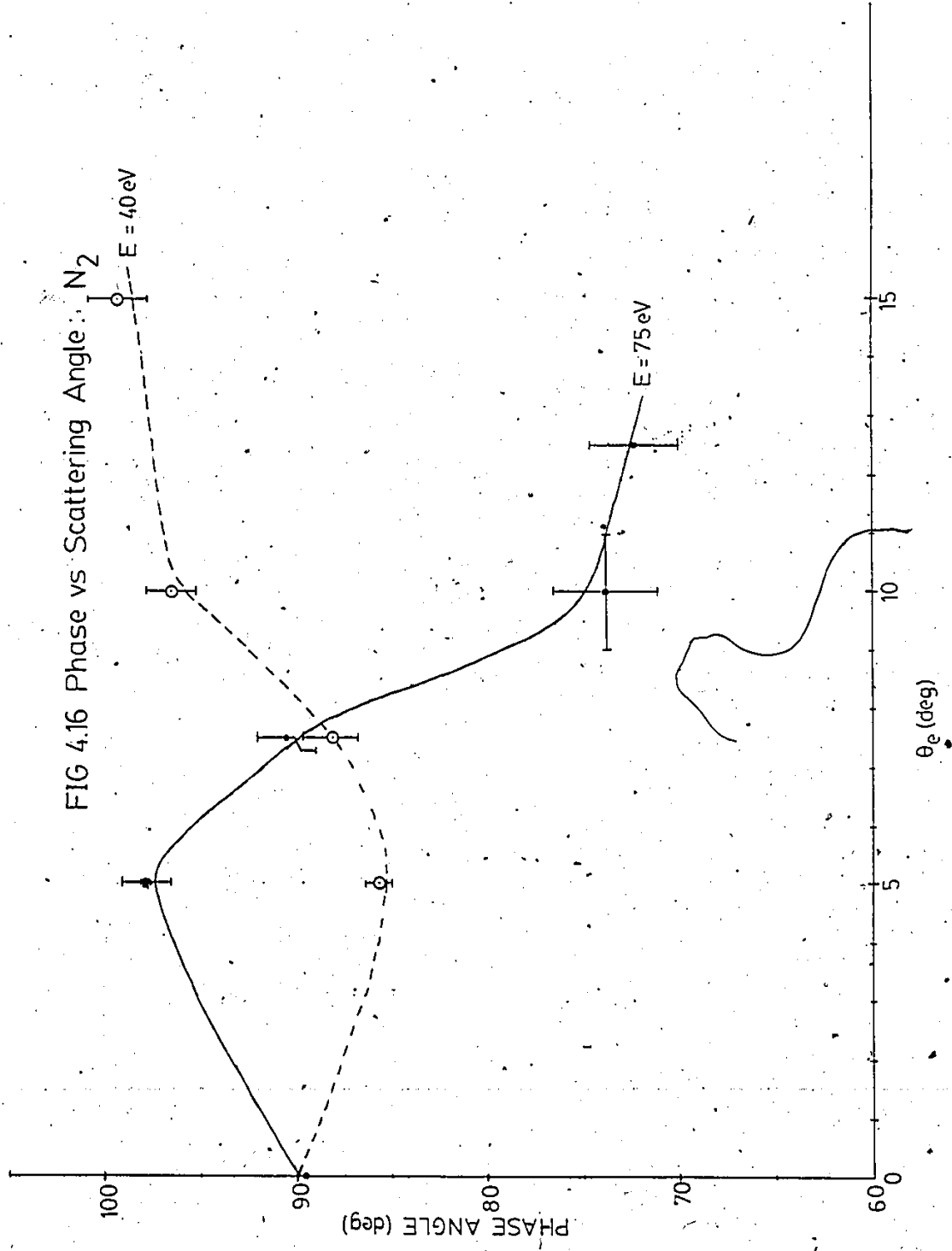
One may however, point out the following. Since the excitation and decay processes are independent the value of $P_C(0)$ is determined soley by the relative populations of the different magnetic sublevels, and hence by the selection rules governing the excitation of these. If dipole selection rules are dominant it is difficult to see how $P_C(0)$ could vary much, given the selection rules for homonuclear diatomic molecules. However, if non-dipole excitation is favoured at certain scattering angles and incident energies, then significant depolarization may occur, forcing $P_C(0)$ to 0 or even negative. As pointed out previously, non-dipole excitation is certainly occuring in N_2, particularly at the low energies used in the present work. Next, even though a large number of rotational levels contribute to the observed coincidence signal and the coherence between states of different N_1 is not observed, it may still be possible that a reduction in $P_C(0)$ may occur due to the effects of coherent excitation of the rotational levels. The amount of coherence is of course limited by the rigorous selection rule sym $<-\not\to->$ antisym in the total wavefunction. Thus only states with even N_1 can interfere with each other, and similarly, only states with odd N_1 interfere with each other. There is no coherence between states of even and odd N_1. Just as the influence of fine and/or hyperfine structure causes a reduction in the measured polarization even though the coherence between fine(or hyperfine) structure levels is not observed, the coherence between rotational levels could also reduce the measured polarization in the present case.

4.4.2 Hydrogen Data

The results of the polarization correlation experiments
with H_2 are shown in Figures 4.17 to 4.22. Fig. 4.17 shows
the energy loss spectrum obtained in H_2 at an incident
energy of 80 eV and electron scattering angle of 0 degrees.
Indicated on the diagram are the Lyman $(X^1\Sigma_g^+(v''=0)$ ->
$B^1\Sigma_u^+(v'))$ bands and the Werner $(X^1\Sigma_g^+(v''=0)$ -> $C^1\Pi_u(v'))$
bands. The estimated energy resolution of the spectrometer
was about 100 meV, as it was in N_2. Note that this is
insufficient to resolve the overlap of the higher lying
Lyman bands with the Werner bands, so the observed coinci-
dence signal contained contributions from the Lyman (7,0)
and (8,0) bands. However, these are so much weaker than the
Werner (0,0) band which was studied that their contribution
was considered negligible. Also, it is very probable that
the Lyman (7,0) and (8,0) bands do not decay back to the
$v''=0$ state, but to higher vibrational states, and hence the
wavelengths of photons emitted in these transitions are bey-
ond the cutoff limit of the channeltron sensitivity.

Electrons which lost 12.29 eV (corresponding to the Wer-
ner (0,0) band) were detected in coincidence with the emit-
ted photons. Typical count rates in the electron channel
varied from about 50 kHz at $\theta_e=0$ to about 6 kHz at $\theta_e=25$
degrees, and in the photon channel, typical count rates were
about 10-40 Hz. In order to obtain reasonable statistics,
data acquisition times were about 30 to 80 hours.

Werner Bands

$X^1\Sigma_g^+(v''=0) \to C^1\Pi_u(v')$

Lyman Bands

$X^1\Sigma_g^+(v''=0) \to B^1\Sigma_u^+(v')$

FIG 4.17

$e^- + H_2$ ENERGY LOSS SPECTRUM

$E_{inc} = 80$ eV; $\theta_e = 0°$

ENERGY LOSS (eV)
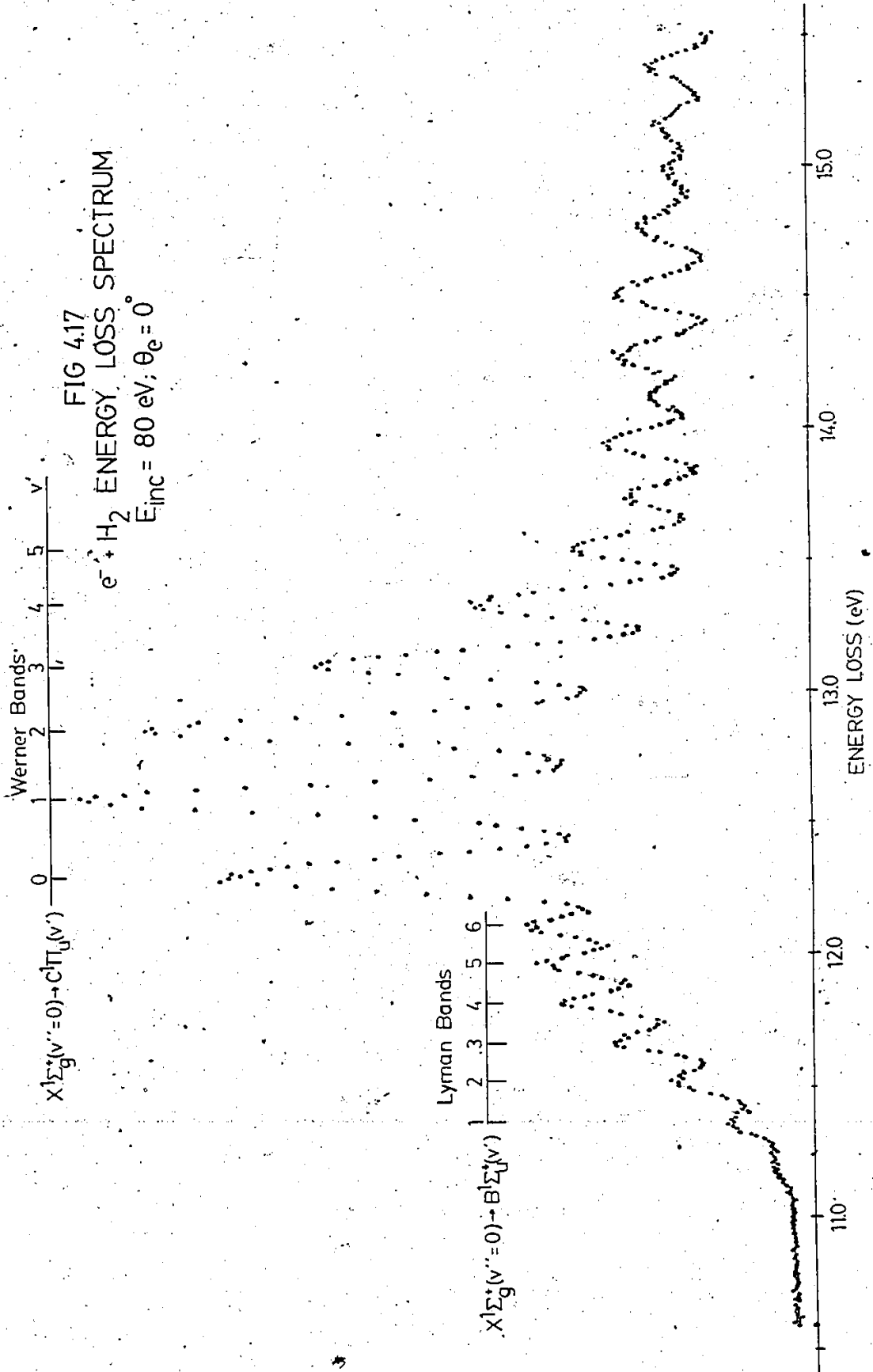
FIG 4.18

$P_C(0)$ vs PRESSURE: $e^- + H_2$

$E_{inc} = 50\,eV,\ \theta_e = 0°$

HEAD PRESSURE (Torr)

$P_C(0)$
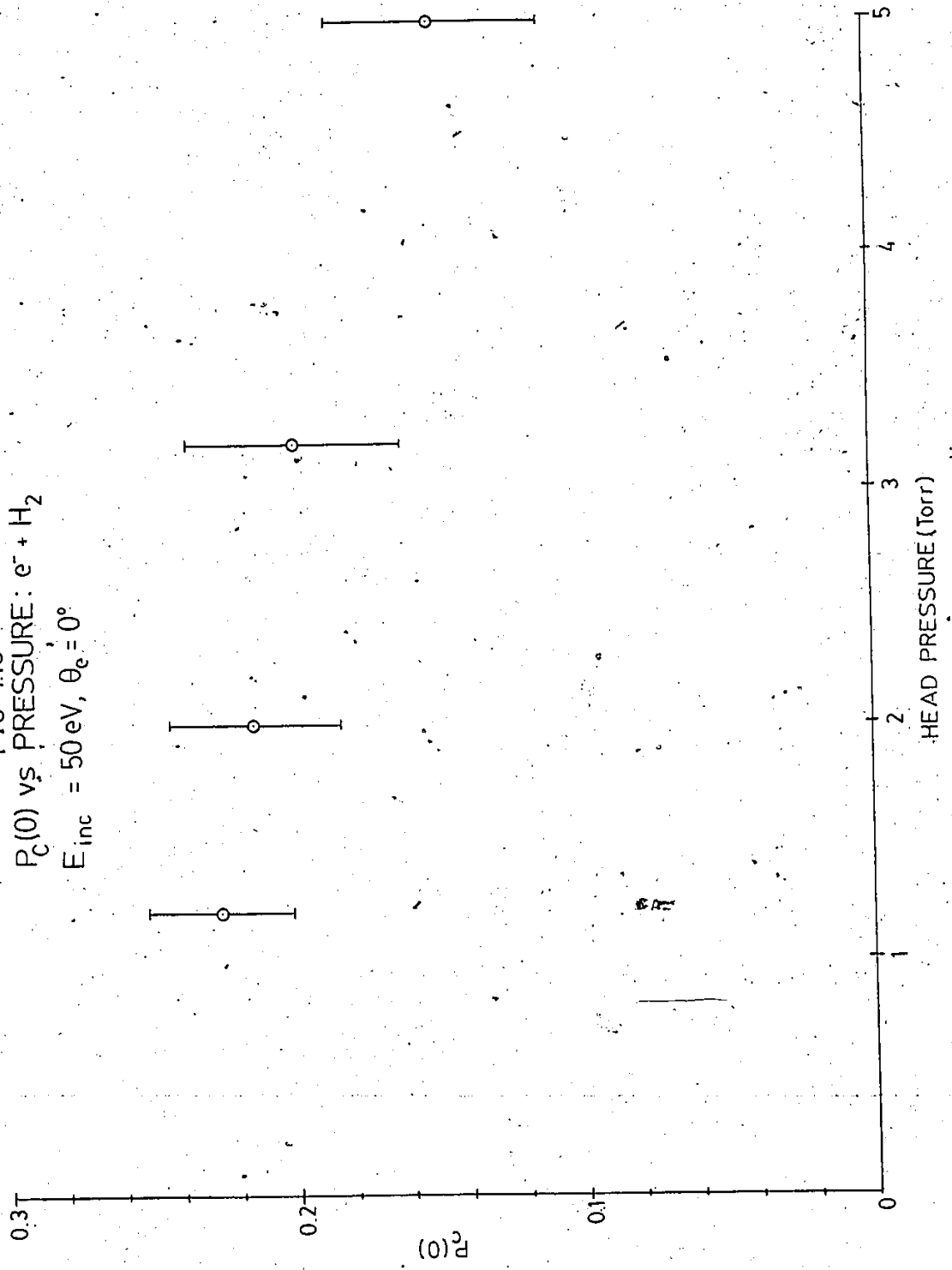
Table 4.7
$P_c(0)$ vs Pressure and Energy: H_2

Incident Energy = 50.0 eV, Scattering Angle = 0

Head Pressure(torr)	Polarization
1.2±0.1	0.23±0.05
2.0±0.1	0.21±0.05
3.2±0.1	0.20±0.07
5.0±0.1	0.15±0.07

Pseudo-Threshold Polarization Measurements
Electron Scattering Angle = 0, Pressure = 1.5 torr

Energy(eV)	Polarization
40.0	0.19±0.05
50.0	0.22±0.02
80.0	0.20±0.05

Figure 4.18 shows the variation of $P_C(0)$ with gas pressure for a scattering angle of 0 degrees and an incident energy of 50 eV, and Table 4.7 lists the data. To ensure that radiation trapping was not causing a depolarizing effect, a pressure of 1.5 torr was used throughout the experiment. It can be seen from Fig. 4.18 that the polarization is essentially constant near this pressure. A comparison of Fig. 4.18 with the polarization vs pressure data obtained in N_2 shows that the pressure dependence of $P_C(0)$ is not as strong in H_2.

Pseudo-threshold Polarization Measurements

The only other pseudo-threshold polarization measurements available in H_2 are those of Malcolm and McConkey[60,61]. The present results are listed in Table 4.7. For the H_2 Werner bands, they measured a pseudo-threshold polarization of 0.17 ± 0.03, and the present measurements indicate a value of about 0.20 ± 0.03, both of which are in disagreement with the direct polarization measurements on the integrated Werner (0,1) band[75], which indicate an extrapolated threshold polarization of about 0.3 (assuming the rapid decrease near the threshold is due to resonance effects and electron correlations). The theoretical predictions of section 4.2.5 give a value of 0.35 for the threshold polarization, which is about 100 percent higher than the pseudo-threshold values. Note that the situation in H_2 is reversed from that of N_2. In the latter gas, there was agreement between the theory and pseudo-threshold value. More will be said about

this in section 4.4.3.

Polarization Correlation Results.

Fig. 4.19 shows the variation of $P_c(0)$ and $P_c(45)$ with electron scattering angle for incident electron energies of 50 and 80 eV. The smooth curves drawn through the data points are suggestive of the trends in the data only. Table 4.8 lists the data obtained at these energies. The following points should be noted from Fig. 4.19.

(1) The slight increase in $P_c(0)$ between 0 and 5 degrees at 50 eV. This behaviour was also observed by Malcolm and McConkey[60], but was not observed in N_2.

(2) $P_c(0)$ reaches a miniumum value at about 12.5 degrees for both 50 and 80 eV. The rather deep minimum which occurs at 50 eV as compared to the shallow one at 80 eV should be noted. $P_c(0)$ is probably 0 at 15 degrees for 80 eV.

(3) $P_c(45)$ is less than zero for all scattering angles observed, except at 0 and 15 degrees, where it is close to 0 (E=50 eV). A minimum in $P_c(45)$ occurs at a scattering angle of 10 degrees at both energies. Also, $P_c(45)$ increases faster from the minimum with increasing scattering angle at 50 eV than at 80 eV.

Fig. 4.20 shows a typical radiation pattern deduced from $P_c(0)$ and $P_c(45)$. Fig. 4.21 shows the variation of θ_k and
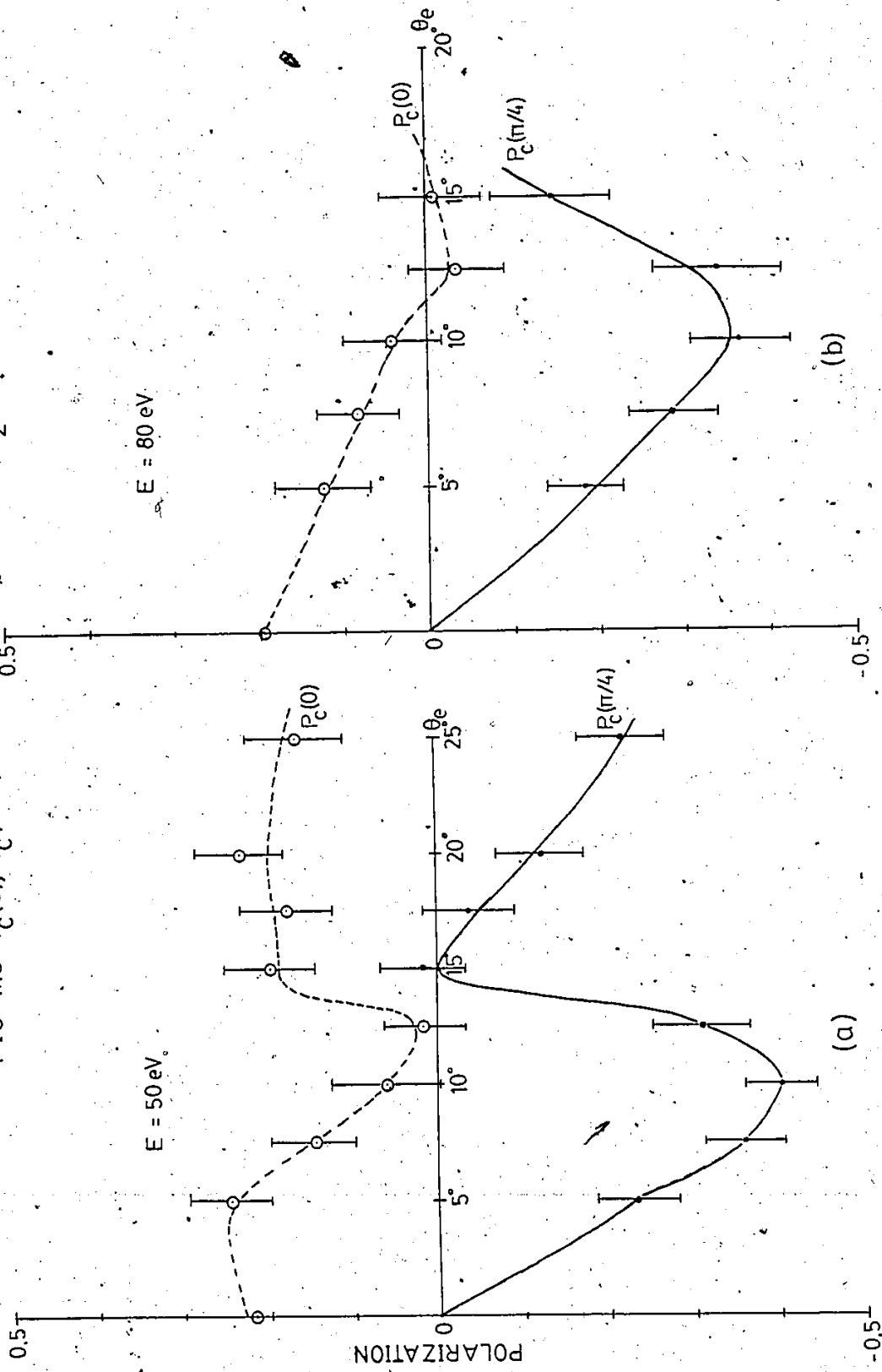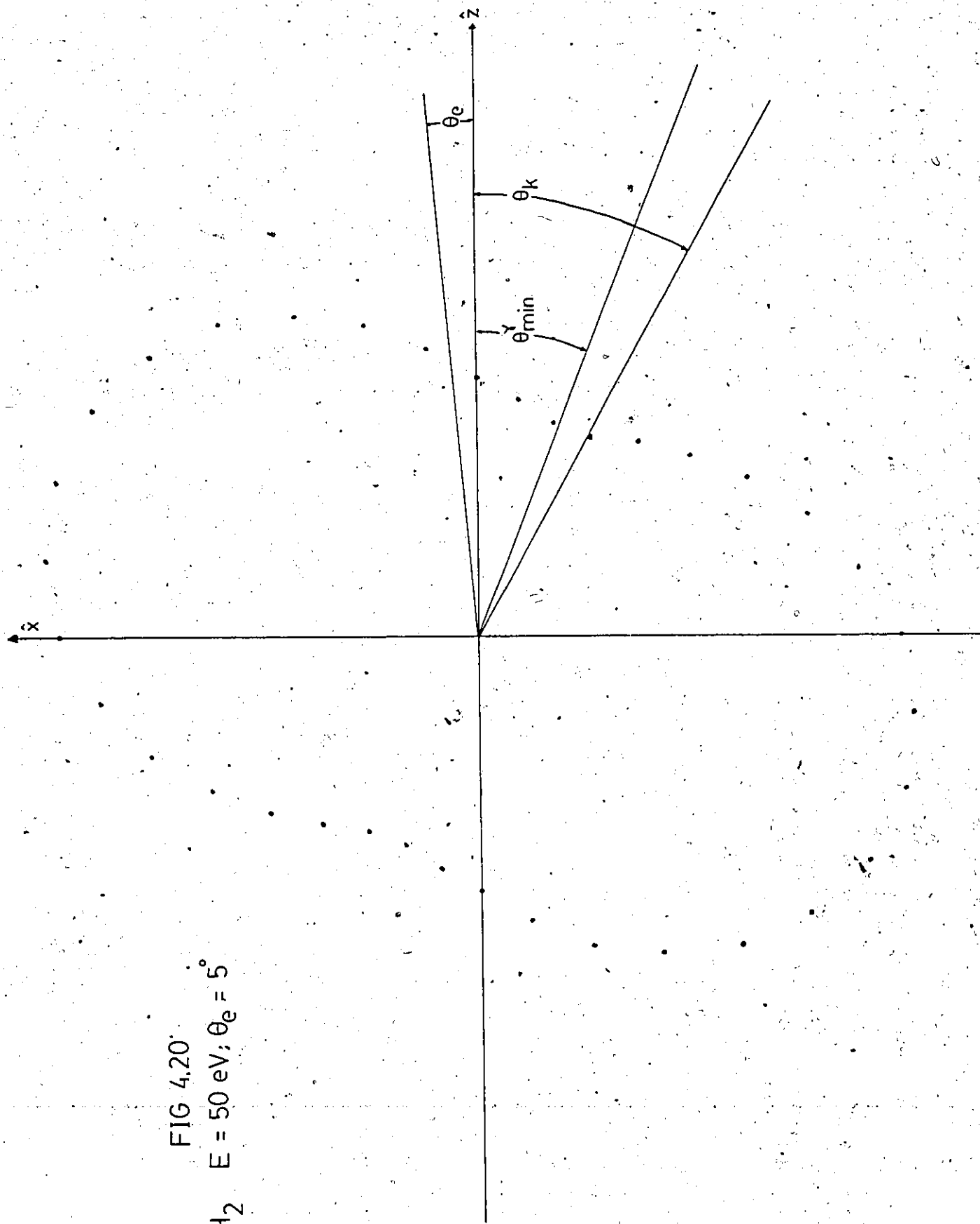
FIG 4.19 $P_c(0)$, $P_c(\pi/4)$ vs Scattering Angle: H_2
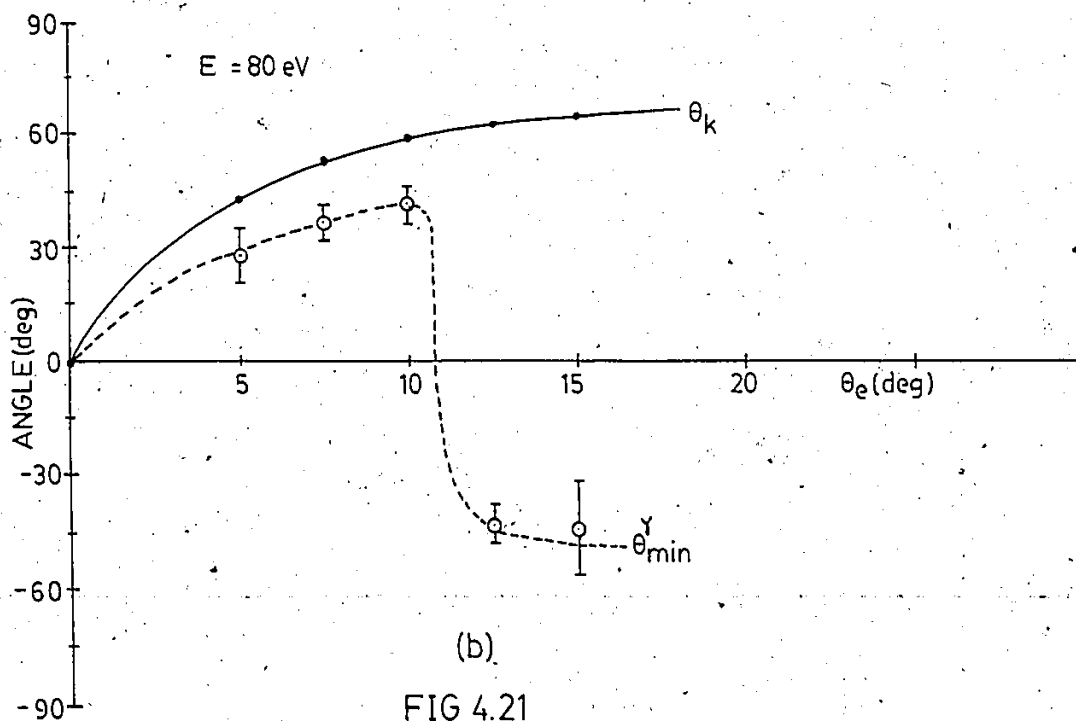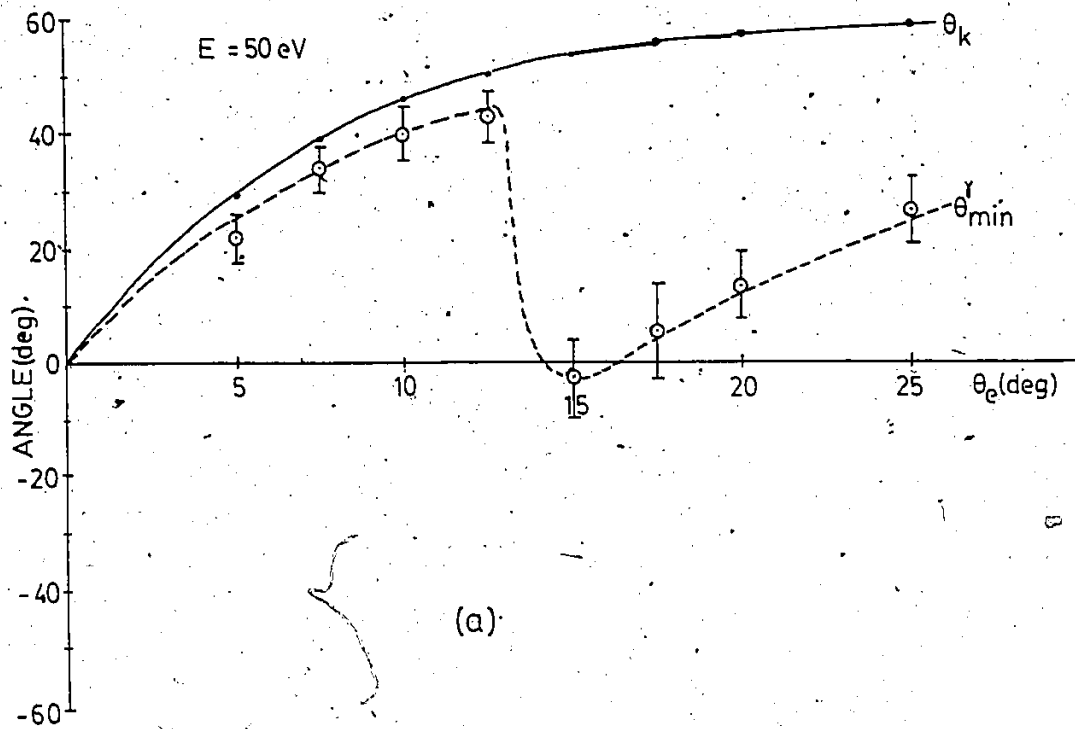
FIG 4.20

H_2 $E = 50$ eV; $\theta_e = 5°$

FIG 4.21
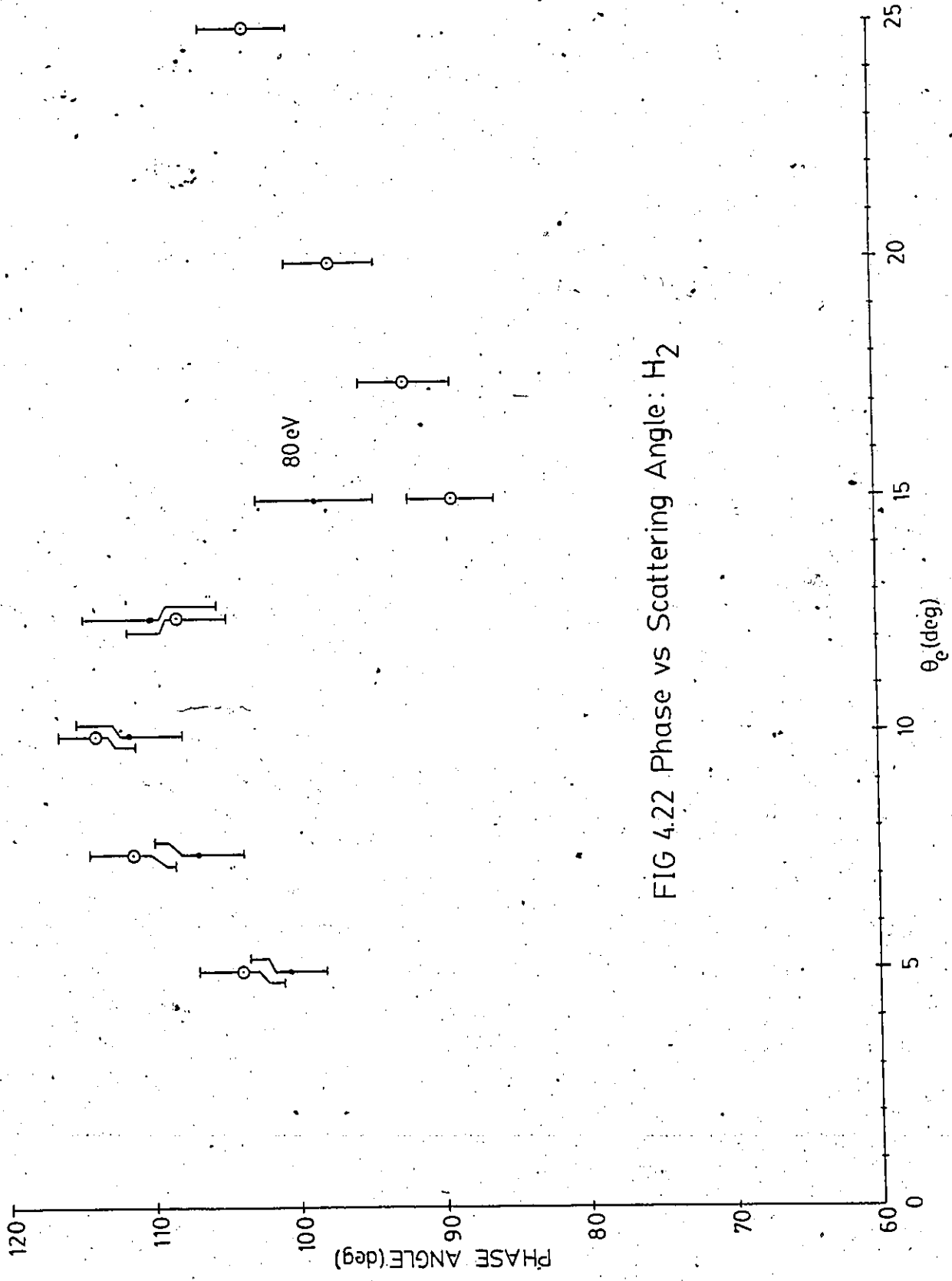
θ_k, θ_{min}^Y vs Scattering Angle: H_2

FIG 4.22 Phase vs Scattering Angle: H_2

Table 4.8
Polarization Correlation Data vs Scattering Angle: H_2

Incident Energy = 50.0 eV, Pressure = 1.5 torr

× θ_e (deg)	$F_C(0)$	$F_C(45)$	a_x/a_z	Phase (deg)	θ_{min} (deg)	θ_k (deg)
0.0	0.22±0.02	—	0.80±0.02	90.0 →	0.0	0.0
5.0	0.24±0.05	−0.23±0.05	0.78±0.04	103.9±2.9	21.8±4.1	29.3
7.5	0.14±0.05	−0.36±0.05	0.87±0.04	111.3±2.9	34.2±3.4	39.2
10.0	0.06±0.06	−0.40±0.01	0.94±0.06	113.7±2.6	40.7±4.4	46.2
12.5	0.02±0.05	−0.31±0.06	0.98±0.05	108.0±3.4	43.5±4.5	51.0
15.0	0.20±0.05	0.02±0.05	0.82±0.04	89.1±2.9	−2.3±7.2	54.4
17.5	0.18±0.05	−0.04±0.05	0.84±0.05	92.2±3.1	6.0±8.5	56.7
20.0	0.23±0.05	−0.12±0.05	0.79±0.04	97.2±3.1	13.8±5.7	58.2
25.0	0.16±0.06	−0.22±0.05	0.85±0.05	102.8±3.0	26.9±5.8	59.9

Incident Energy = 80 eV, Pressure = 1.5 torr

θ_e (deg)	$F_C(0)$	$F_C(45)$	a_x/a_z	Phase (deg)	θ_{min} (deg)	θ_k (deg)
0.0	0.20±0.05	—	0.82±0.04	90.0	0.0	0.0
5.0	0.12±0.06	−0.18±0.04	0.88±0.05	100.7±2.6	28.1±6.9	43.8
7.5	0.08±0.05	−0.29±0.05	0.92±0.04	106.8±3.1	37.1±4.5	53.8
10.0	0.04±0.06	−0.36±0.06	0.96±0.06	111.4±3.6	41.7±4.6	59.5
12.5	−0.03±0.06	−0.34±0.08	1.04±0.06	109.9±4.6	−42.2±4.6	62.9
15.0	−0.01±0.06	−0.15±0.07	1.01±0.06	98.4±4.0	−43.8±5.0	64.9

θ_{min}^{γ} with electron scattering angle for 50 and 80 eV. As can be seen, θ_{min}^{γ} appears to follow θ_k up to about 12.5 degrees at 50 eV (Fig. 4.21(a)), and then drops sharply to a slightly negative value at 15 degrees. (Recall that this small angle agreement between θ_k and θ_{min}^{γ} was not at all observed in N_2). It increases after this, but is not related to θ_k. At 80 eV (Fig. 4.21(b)) θ_{min}^{γ} follows θ_k up to about 10 degrees and then drops quickly down to a large negative value at 12.5 degrees, after which it appears to remain constant.

Fig. 4.22 shows the variation of the phase angle, δ, with electron scattering angle. The phase is about the same at both energies up to 12.5 degrees. The 50 eV data then drops quickly to about 90 degrees at a scattering angle of 15 degrees before increasing slowly, whereas the 80 eV data decreases more slowly and not as far.

4.4.3 Discussion of the Results

Pseudo-threshold Polarization

The pseudo-threshold polarization measurements in N_2 and H_2 provide the following information:

(1) The measured pseudo-threshold polarization agrees rather well with theoretical predictions for N_2 but not for H_2.

(2) A comparison of the pseudo-threshold polarization data with the results of direct polarization measurements[75,65] indicates that there is disagreement between them for both H_2 and N_2.

In addition to the above two facts, the results of direct polarization measurements on the resolved rotational structure in $H_2^{171,73}$ indicate that the extrapolated threshold polarizations agree with the predicted values using the results of section 4.2.5.

The disagreement between the pseudo-threshold measurement and the direct polarization measurements in N_2 has already been discussed, and the possibility of non-dipole excitation is most probably the cause of this, especially in the light of the results of Hernandez et al[86]. Dipole excitation dominates the forward scattering, so this effect would not be observed in a pseudo-threshold measurement, giving agreement with theory. In addition, the agreement between theory and the pseudo-threshold measurements in N_2 indicates that the relative intensities of the P and R branches of the (0,0) band are predicted correctly by theory, even at energies well above the excitation threshold. This also suggests that the configuration interaction effects associated with the C' state[87] are not altering the relative intensities of the P and R branches significantly at the energies used in the present experiment.

The disagreement between the pseudo-threshold measurement and theory for H_2 is rather puzzling. With the present data all that can be done is to suggest possible reasons for the discrepancy. It will not be possible to decide which reason is actually responsible without further detailed measurements.

Suppose that the theoretical predictions of the threshold polarization are indeed correct. Then the discrepancy is due to some experimental effect. Suppose further that $P_c(0)$ varies rapidly near 0 degrees; that is to say, it decreases sharply from a value of about 0.35 to a very small value before rising again to about 0.20 at 5 degrees. If this variation occurs over 2 degrees or less, chances are that it would not be observable because of the finite angular resolution of the spectrometer. Instead some average value (integrated over the angular resolution of the spectrometer) which was lower than the 'true' value at 0 degrees would be observed. This may also account for the apparent increase in $P_c(0)$ between 0 and 5 degrees. Such variations can be expected in the atomic case (see the paper by Wykes[33]), but they occur over a much larger range of scattering angles. However, a comparison with He[69] and with H[49] indicates that everything seems to happen at much smaller scattering angles for molecules than for atoms (the minimum in $P_c(0)$ is an example of this). Not much can be said for or against this hypothesis from a theoretical point of view; the large number of interference terms between states of the same N_1 and different M_{N_1} appearing in the state multipoles (cf equation 4.2.4.8) could either cause such a rapid variation or wash it out, depending on the relative phases of each scattering amplitude. The agreement between theory and experiment for the pseudo-threshold measurements in He[82] where there are only two scattering amplitudes to consider suggests that the above-mentioned interference effects are a

real possibility. If the above discussion is correct, then
it implies that $P_c(0)$ does not behave in this fashion for
N_2, at least not at the energies used in the present work.
It could be that any interference effects conveniently can-
cel out in N_2, leaving a smooth behaviour, and agreement
with theory. The only way to test this suggestion is to
repeat the polarization correlation measurements with a sig-
nificant improvement in the angular resolution of the spec-
trometer.

The other possibility which could account for the discre-
pancy is that the theory incorrectly predicts the relative
intensities of the P, Q and R branches of the Werner bands
in H_2. Thus the experimental value could be correct. Note
that this does not contradict the statements made earlier
about the agreement between theory and experiment for the
resolved rotational lines. These measurements were made at
energies approaching the excitation threshold, whereas the
pseudo-threshold measurement was carried out at energies
well away from the threshold. The relative intensities are
crucial when an estimate of the polarization is to be made.
It may be that the deviation in the relative intensities
from the theoretical values (at threshold) becomes signifi-
cant only at energies well above the threshold. One possi-
ble reason for incorrect relative intensities is the known
perturbations on the P and R branches of the Werner system
by mixing with the $B'^1\Sigma_u^+$ state[e8]. These effects would com-
plicate the calculation of the threshold polarization and
are not taken into account in the discussions of section

4.2.5. Another possibility has to do with the fact that the pseudo-threshold polarization measurements do not reproduce the threshold conditions exactly. First of all, the scattered electron does not leave the collision with 0 angular momentum as in the threshold case. Thus the calculation of Blum[70] as discussed in section 4.2.5 in connection with Dunn's symmetry rules would have to be modified to take this into account. Secondly, in a pseudo-threshold measurement, it is the differential cross-sections which are involved, and not the total cross-sections. In the case of He n^1P excitation, this does not matter since all dependence on the dynamics of the scattering process cancels out anyway. This is certainly not the case for molecules. It could be that a combination of the above two facts could cause the relative intensities of the P, Q and R branches to differ significantly from the expected values. If the P branch contributes more to the emitted radiation than the Q or R branches, then, since the predicted polarization of the P branch is much less than the R or the Q branches, an overall reduction of the observed polarization would occur.

Another possibility might be the effects of non-dipole excitation, as discussed for N_2. However, the agreement between the extrapolated threshold polarizations and theoretical predictions[73] for H_2 would seem to preclude this. Further work is necessary to determine which, if any, of the above suggestions are correct.

Polarization Correlation Data

It is interesting to compare the N_2 data with the H_2 data. Of course, a strict comparison between H_2 and N_2 is unjustified because of the different electronic transitions involved (Σ to Σ in N_2 and Σ to Π in H_2). Similar features are observed in both gases, but there are some rather striking differences.

(1) In both cases $P_c(0)$ is approximately constant except where it dips toward 0. The scattering angle at which this occurs seems to be independent of energy within a particular gas, but occurs at smaller scattering angles in N_2.

(2) In both gases, variations in $P_c(45)$ were much more significant than those in $P_c(0)$. This probably reflects the fact that $P_c(45)$ carries phase information which is significant. Note also that $P_c(45)$ changed sign in N_2, but not in H_2.

(3) The Born approximation was inadequate to describe the scattering process in N_2, but appeared to work fairly well for small scattering angles in H_2 (this can be seen from the graphs of θ_k and θ^γ_{min} for these gases).

(4) In N_2 the 'effective' phase deduced from the data was always close to 90 degrees, whereas in H_2, much larger deviations from 90 were observed.

It is suprising that the phase is non-zero, given the large number of interference terms in the state multipoles. One would expect a net phase of 0 from this. Clearly there must be some simplifying factors involved which produce a net phase as large as was observed in the present results. Is it possible, for example, that there could be a relatively constant phase relationship between terms in the state multipoles with $\Delta M_N = 0$ and $\Delta M_N = \pm 1$? Further experimental work is clearly necessary to shed light on this problem, and some suggestions are put forward in section 4.5.2.

4.5 CONCLUSIONS AND SUGGESTIONS

4.5.1 Conclusions

Pseudo-threshold polarizations in N_2 and H_2 have been measured and compared with the results of direct polarization measurements and theoretical predictions. This is the first such measurement performed in N_2. It was found that the pseudo-threshold measurements in N_2 for the $X^1\Sigma_g^+ \rightarrow C^1\Sigma_u^+$ system was consistent with theoretical predictions, with a value of 0.18 ± 0.04, but not with the direct polarization measurement, which suggested a value of 0.07. The discrepancy between the two measurements has been attributed to the possibility of non-dipole excitation channels. In the H_2 $X^1\Sigma_g^+ \rightarrow C^1\Pi_u$ system, it was found that the pseudo-threshold measurement was also inconsistent with the direct polarization measurement, with a value of 0.20 ± 0.03, thus verifying the earlier work of Malcolm and McConkey[60]. Theoretical predictions indicated that a value of about 0.35 should have been measured. Reasons for these discrepancies have been discussed.

Polarization correlation data were also obtained for N_2 and H_2. It was found that there were dramatic differences in the behaviour of the two Stokes' parameters $P_c(0)$ and $P_c(45)$ between the two gases. The Stokes' parameters have been analyzed in terms of two perpendicular dipole oscillators with a relative phase between them. Based on this oversimplified treatment, the parameters describing the radiation in the scattering plane were deduced from

the data. The orientation of the radiation pattern, speci-
fied by the angle θ^{γ}_{min}, was compared to the predictions of
the Born approximation (momentum transfer direction). It was
found that the Born approximation was inadequate to describe
the results in N_2, but seemed to work for very small scat-
tering angles in H_2. The relative phase between the dipole
oscillators was found to be large and close to 90 degrees in
both gases, suggesting that a significant component of cir-
cular polarization is present in molecular radiation. It
was suggested that the presence of an overall phase could be
due to the possibility that the relative phase between each
scattering amplitude is related only to the change in the
magnetic quantum number M_N in going from the initial state
to the excited state. Of course, the presence of a large
unpolarized component in the emitted radiation may also
account for this, so such a conclusion must be taken as very
tentative. Clearly an actual measurement of the circular
polarization is needed to sort this out.

The model used to analyze the polarization data is
clearly not adequate to describe the situation in the mole-
cular case, so further work will require the use of a more
general description of polarized light.

On the theoretical side, the results of the density
matrix formalism[67] have been applied to some simple cases in
H_2 excitation. It was found that information about the
scattering amplitudes could only be extracted from the
Stokes' parameters if single rotational lines could be

resolved or if the initial molecular ensemble is prepared so
that all molecules are in the $N_0=0$ state.

4.5.2 <u>Suggestions</u> <u>for</u> <u>Future</u> <u>Research</u>

Based on the discussion of the the pseudo-threshold
polarization measurements and the difficulties encountered
there, it is possible to suggest ways in which one should
proceed in dealing with electron-molecule excitation.

(1) Experiments in which single rotational lines
can be resolved should be carried out. This
involves working in the visible region and
using narrow band filters. In this way single
decay channels can be isolated. Such experi-
ments are currently being developed, and have
the distinct advantage that the circular
polarization can be measured.

(2) To reduce the number of excitation channels,
new developments in supersonic beam technology
can be used to cool the molecular ensemble so
that only the lowest rotational level is popu-
lated. This would enable actual scattering
amplitudes to be extracted from the Stokes'
parameters. This type of experiment is being
planned here at the present time.

(3) A further possibility arises using the super-
sonic expansion technique. By obtaining a
Hydrogen target with all molecules in the $N_0=0$
level and using very high resolution electron

spectroscopy it should be possible to do differential inelastic scattering involving selected rotational transitions. This would allow some of the ideas regarding non-dipole excitation channels to be checked directly. Collaboration between the Windsor and Manchester groups is already underway on this problem.

(4) It might be possible to use the time inverse approach in which electrons are superelastically scattered from molecules prepared in selected magnetic substates. This awaits the development of suitable ultraviolet lasers.

(5) Prior to these developments it would be interesting to look for isotope effects. In this regard the $X^1\Sigma_g^+ \rightarrow C^1\Pi_u$ excitation in D_2 will be investigated in the very near future, and the results will be compared with the present H_2 data.

4.6 APPENDICES

### 4.6.1 Hund's Case (b) Coupling

Hund's case (b) coupling is as follows:
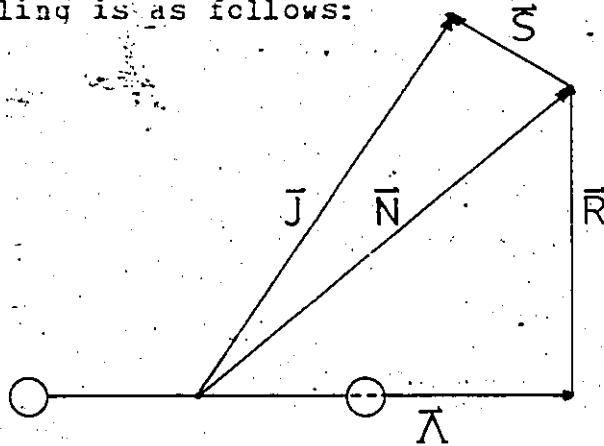
$\bar{\Lambda}$ is the component of the total electronic orbital angular momentum along the internuclear axis; $\vec{N}$ (with z component M_N) is formed by coupling the rotation with $\bar{\Lambda}$. N then couples with the total electronic spin $\vec{S}$ (with z component M_N) to give a total angular momentum $\vec{J}$ (with z component M_J). Note that in this coupling scheme the spin is coupled weakly to the internuclear axis.

4.6.2 The Momentum Transfer Direction

Consider the diagram shown below:
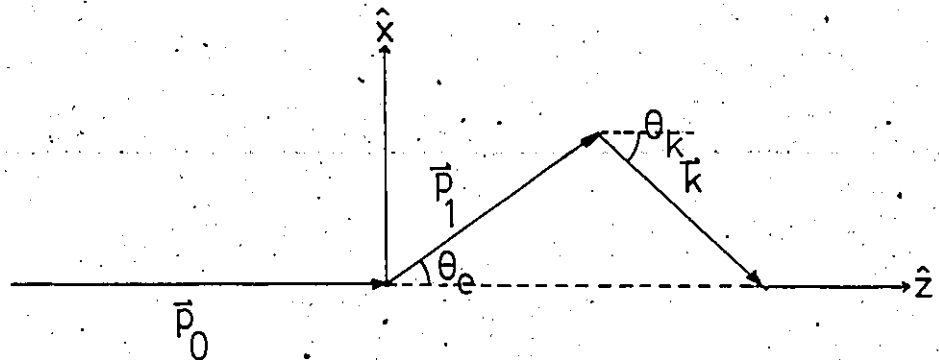
The incident electron has momentum $\vec{p}_0$ along the z axis, and final momentum $\vec{p}_1$. The electron is scattered into the angle θ_e (in the scattering plane). The momentum transfer vector $\vec{k}$ is given by:

$$\vec{k} = \vec{p}_0 - \vec{p}_1$$

$$(4.6.2.1)$$

Now

$$\vec{p}_0 = p_0\hat{z}$$
$$\vec{p}_1 = p_1\cos\theta_e\hat{z} + p_1\sin\theta_e\hat{x}$$
$$\vec{k} = k\cos\theta_k\hat{z} - k\sin\theta_k\hat{x}$$

Using these in equation 4.6.2.1 yields:

$$p_0 = p_1\cos\theta_e + k\cos\theta_k$$
$$0 = p_1\sin\theta_e - k\sin\theta_k$$

Multiplying the first equation by $\sin\theta_k$ and the second by $\cos\theta_k$ and subtracting yields the result:

$$p_0/p_1 = \cos\theta_k + \cot\theta_k\sin\theta_e$$

Solving for $\cot\theta_k$:

$$\cot\theta_k = p_0/(p_1\sin\theta_e) - \cot\theta_e$$

Now $p_0 = (2mE_0)^{1/2}$ and $p_1 = (2mE_1)^{1/2}$. Then the momentum transfer direction is given by:

$$\cot\theta_k = \frac{1}{\sin\theta_e}\left(\frac{E_0}{E_1}\right)^{1/2} - \cot\theta_e \qquad (4.6.2.2)$$

Using conservation of energy,

$$E_1 = E_0 - \Delta E$$

where ΔE is the amount of energy lost by the electron in the collision, the momentum transfer direction is:

$$\tan\theta_k = ((\sin\theta_e(1-\Delta E/E_0)^{1/2})^{-1} - \cot\theta_e)^{-1} \qquad (4.6.2.3)$$

REFERENCES

1 Brunt, J.N.H. Ph.D. Thesis 1975
   Univ. of Manchester, Manchester, England

2 Read, F.H., Comer, J., Imhoff, R.E., Brunt, J.N.H. and Harting, E.
   J. Elec. Spec. Rel. Phen. 4(1974), p293-312

3 Brunt, J.N.H., Read, F.H. and King, G.C.
   J. Phys. E: Sci. Instr. 10(1977), p134-9

4 Harting, E. and Read, F.H.
   Electrostatic Lenses, Elsevier Press, 1976

5 Brunt, J.N.H., King, G.C. and Read, F.H.
   J. Phys. B: Atom. Molec. Phys. 9(1976), p2195-207

6 Bolduc E., Quemener, J.J. and Marmet, P
   J. Chem. Phys. 57(1972), p1957-66

7 Roy, D., Delage, A. and Carette, J.D.
   Phys. Rev. A 12(1975), p45-51

8 Sanche, L. and Schulz, G.J.
   Phys. Rev. A 5(1972), p1672-83

9 Grissom, J.T., Garrett, W.R. and Compton, R.N.
   Phys. Rev. Letts. 23(1969), p1011-14

10 Spence, D.
    J. Phys. B: Atom. Molec. Phys. 13(1980), p1611-24

11 Veillette, P. and Marmet, P.
    Can. J. Phys. 54(1976), p1208-15

12 Huard, D., Marmet, P. and Bolduc, E.
    Can. J. Phys. 56(1978), p82-85

13 Roy, D. and Carette, J.D.
    J. Phys. B: Atom. Molec. Phys. 8(1975), pL157-66

14 Roy, D., Delage, A. and Carette, J.D.
    J. Phys. B: Atom. Molec. Phys. 9(1976), p1923-31

15 Delage, A., Roy, D. and Carette, J.D.
    J. Phys. B: Atom. Molec. Phys. 10(1977), p1487-96

16 Nesbet, R.K.
    Phys. Rev. A 14(1976), p1326-31

17 Marchand, P. and Cardinal, J.
    Can. J. Phys. 57(1979), p1624-33

18 Dassen, H.W., Helbing, R.K.B., Huschilt, J.C. and McConkey, J.W.
    Abstracts XIII I.C.P.E.A.C. 1(1981), p196-7 (Gatlinburg)

19 Dassen, H.W., Gomez, R., King, G.C. and McConkey, J.W.
J. Phys. B: Atom. Molec. Phys. 16(1983), p

20 Taylor, J.R.
Scattering Theory, Wiley and Sons, New York, 1972

21 Spence, D.
Phys. Rev. A 15(1977), p 883-7

22 Heddle, D. in Electron and Photon Interactions with Atoms
Plenum Press, N.Y. 1976, H. Kleinpoppen and M. McDowell, Eds.

23 Read, F.H.
J. Phys. B: Atom. Molec. Phys. 10(1977), p449-58

24 Codling, K., Madden, R.P. and Ederer, D.L.
Phys. Rev. 155(1967), p23-37

25 Codling, K. and Madden, R.P.
Phys. Rev. A 4(1971), p2261-70

26 Codling, K. and Madden, R.P.
J. Res. Nat. Bur. Stand. 26A(1972), p1-12

27 Madden, R.P., Ederer, D.L. and Codling, K.
Phys. Rev. 177(1969), p136-51

28 Lin, C.D.
Phys. Rev. A 25(1982), p76-87

29 Boulay, M. and Marchand, P.
Can. J. Phys. 60(1982), p855-64

30 Read, F.H., Brunt, J.N.H. and King, G.C.
J. Phys. B: Atom. Molec. Phys. 9(1976), p2209-19

31 Valin, M. and Marmet, P.
J. Phys. B: Atom. Molec. Phys. 8(1975), p2953-67

32 Spence, D.
J. Phys. B: Atom. Molec. Phys. 14(1981), p129-47

33 Spence, D.
Invited Papers, IX I.C.P.E.A.C, Univ. Wash. Press, Seattle, 1976

34 Lefaivre, D. and Marmet, P.
Int. J. Mass Spec. Ion Phys. 18(1975), p153-64

35 Moore, C.E. 'Atomic Energy Levels' Vol. 1-3
NSRDA-NBS 35, 1971, U.S. Gov't. Printing Office, Wash., D.C.

36 Carbonneau, R., Bolduc, E. and Marmet, P.
Can. J. Phys. 51(1973), p505-9

37 Macek, J. and Jaecks, D.H.
Phys. Rev. A 4(1971), p2288-2300

38 Wykes, J.
   J. Phys. B: Atom. Molec. Phys. 5(1972), p1126-37

39 Fano, U. and Macek, J.
   Rev. Mod. Phys. 45(1973), p553-73

40 Blum, K. and Kleinpoppen, H.
   J. Phys. B: Atom. Molec. Phys. 8(1975), p922-5

41 Eminyan, M., MacAdam, K.B., Slevin, J. and Kleinpoppen, H.
   Phys. Rev. Letts. 31(1973), p576-9

42 Eminyan, M., MacAdam, K.B., Slevin, J. and Kleinpoppen, H.
   J. Phys. B: Atom. Molec. Phys. 7(1974), p1519-42

43 Eminyan, M., MacAdam, K.B., Slevin, J., Standage, M.C.
   and Kleinpoppen, H. J. Phys. B: Atom. Molec. Phys. 8(1975), p2058-66

44 Standage, M.C. and Kleinpoppen, H.
   Phys. Rev. Letts. 36(1976), p577-80

45 Tan, K.H., Fryar, J., Farago, P.S. and McConkey, J.W.
   J. Phys. B: Atom. Molec. Phys. 10(1977), p1073-82

46 Ugbabe, A., Teubner, P.J.O., Weigold, E. and Arriola, H.
   J. Phys. B: Atom. Molec. Phys. 10(1977), p71-9

47 Sutcliffe, V.C., Haddad, G.N., Steph, N.C. and Golden, D.E.

   Phys. Rev. A 17(1978), p100-7

48 Arriola, H., Teubner, P.J.O., Ugbabe, A. and Weigold, E.
   J. Phys. B: Atom. Molec. Phys. 8(1975), p1275-9

49 Williams, J.F., in The Physics of Electronic and Atomic Collisions
   p139-150, Univ. Wash. Press, Seattle, Wash., 1975

50 Dixon, A.J., Hood, S.T. and Weigold, E.
   Phys. Rev. Letts. 40(1978), p1262

51 Hertel, I.V. and Stoll, W.
   J. Phys. B: Atom. Molec. Phys. 7(1974), p570-92

52 Macek, J. and Hertel, I.V.
   J. Phys. B: Atom. Molec. Phys. 7(1974), p2173-88

53 Thomas, L.D., Csanak, G., Taylor, H.A. and Yarlaggada, B.S.
   J. Phys. B: Atom. Molec. Phys. 7(1974), p1719-33

54 Flannery, M.R. and McCann, K.J.
   J. Phys. B: Atom. Molec. Phys. 8(1975), p1716-33

55 Bransden, B.H. and Winters, K.H.
   J. Phys. B: Atom. Molec. Phys. 9(1976), p1115-20

56 Scott, T. and McDowell, M.R.C.

J. Phys. B: Atom. Molec. Phys. 9(1976), p2235-54

57 Meneses, G.D., Padial, N.T. and Csanak, G.
J. Phys. B: Atom. Molec. Phys. 11(1978), L237-42

58 Madison, D.H. and Shelton, W.N.
Phys. Rev. A 7(1973), p499-513

59 King, T.C.F., Williams, J.F. and Crowe, A.
Abstracts XII I.C.P.E.A.C. 1(1981), p233 Gatlinburg

60 Malcolm, I.C. and McConkey, J.W.
J. Phys. B: Atom. Molec. Phys. 12(1979), p511-9

61 McConkey, J.W. and Malcolm, I.C. Coherence and Correlation in
Atomic Collisions, p145-66, Plenum Press, 1980

62 Nishimura, H., Danjo, A. and Koike, Y.
Abstracts XII I.C.P.E.A.C. 1(1981), p235 Gatlinburg

63 McGregor, I., Hils, D., Hippler, R., Malik, N.A.,
Williams, J.F., Zaidi, A.A. and Kleinpoppen, H.
Abstracts XII I.C.P.E.A.C. 1(1981), p225 Gatlinburg

64 Bartschat, K., Blum, K., Hanne, G.F. and Kessler, J.
Abstracts XII I.C.P.E.A.C. 1(1981), p224 Gatlinburg

65 Slevin, J., Eminyan, M., Woolsey, J.M., Vassilev, G.,
Porter, H.Q. and Back, C.
Abstracts XII I.C.P.E.A.C. 1(1981), p231 Gatlinburg

66 Zaidi, A.A., McGregor, I. and Kleinpoppen, H.
Abstracts XII I.C.P.E.A.C. 1(1981), p227 Gatlinburg

67 Blum, K. and Jakubowicz, H.
J. Phys. B: Atom. Molec. Phys. 11(1978), p909-25

68 Blum, K. Density Matrix Theory and Applications
Plenum Press, New York, 1981

69 Blum, K. and Kleinpoppen, H.
Physics Reports 52(1979), p205-261

70 Blum, K. in Coherence and Correlation in Atomic Collisions
p133-44, eds H. Kleinpoppen and J.F. Williams, Plenum Press 1980

71 Dassen, H.W. and McConkey, J.W.
J. Phys. B: Atom. Molec. Phys. 14(1981), p3777-88

72 Feofilov, P.P. The Physical Basis of Polarized Emission
Consultants' Bureau Enterprises, New York, 1961

73 Dassen, H.W. Master's Thesis
Univ. of Windsor, Windsor, Ont. 1980

74 McConkey, J.W. 12th I.C.P.E.A.C. 1980, Invited Papers, p225-36

eds N. Oda and K. Takanayaqi, North Holland Pub., Amsterdam

.75 Malcolm, I.C., Dassen, H.W. and McConkey, J.W.
J. Phys. B: Atom. Molec. Phys. 12(1979), p1003-18

76 Jette, A.N. and Cahill, P.
Phys. Rev. 176(1968), p186-

77 Baltayan, P. and Nedelec, C.
J. Phys. B: Atom. Molec. Phys. 4(1971), p1332-

78 Baltayan, P. and Nedelec, C.
J. Physique 36(1975), p125-

79 Dunn, G.H.
Phys. Rev. Letts. 8(1962), p62-64

80 Macpherson, M.T., Simons, J.P., and Zare, R.N.
Mol. Phys. 38(1979), p2049-55

81 Heideman, H., van der Water, W., van Eck, J. and van
Moergestel, L., in Electronic and Atomic Collisions,
eds N. Oda and K. Takayanaqi, North Holland, Amsterdam, 1980

82 King, G.C., Adams, A. and Read, F.H.
J. Phys. B: Atom. Molec. Phys. 5(1972), L254-7

83 Zetner, P.W., Pradhan, A., Westerveld, W.B. and McConkey, J.W.
J. Applied Optics (1983), in press

84 Hertel, I.V. and Ross, K.J.
J. Phys. B: Atom. Molec. Phys. 2(1969), p285-

.85 Huschilt, J.C., Dassen, H.W. and McConkey, J.W.
Can. J. Phys. 59(1981), p1893-901

86 Hernandez, S.P., Dagdiqian, P.J. and Doering, J.P.
J. Chem. Phys. 1983 in press

87 Hazi, A.U.
Phys. Rev. A 23(1981), p2232-40

88 Stone, E.J. and Zipf, E.C.
J. Chem. Phys. 56(1972), p4646-52

VITA AUCTORIS

I was born on October 18, 1955 in Tilburg, the Nether-
lands. My family came to Canada in 1959 and settled in
Windsor, Ontario. After graduating from Assumption College
School in 1974, I entered the University of Windsor, where I
obtained an Honours B.Sc in Physics in 1978. During my
fours years as an undergraduate I was given the opportunity
to gain research experience under the supervision of Dr.
J.W. McConkey, whom I continued on with to obtain a Master's
degree in Physics in 1980. I was funded by an NSERC Post-
graduate Scholarship from 1978 to 1982, after which I
received a University of Windsor Postgraduate Scholarship.